

**From the Department of Clinical Radiology
Ludwig-Maximilians-Universität, Munich
Director: Prof. Dr. med. Dr. h.c. Maximilian Reiser, FACR, FRCR**

**Development of X-ray phase-contrast imaging
techniques for medical diagnostics: towards clinical
application**

**Thesis Submitted for to obtain a doctoral degree in Natural Sciences
at the Medical Faculty of
the Ludwig-Maximilians-University of Munich**

**Submitted by
Alberto Mittone**

**From
Cuneo, Italy**

2014

**With the permission from the Faculty of Medicine,
University of Munich**

Supervisor/Examiner: Prof. Dr. Paola Coan

Second reviewer: Prof. Dr. Horst Zitzelsberger

Dean: Prof. Dr. med. Dr. h.c. Maximilian Reiser, FACR, FRCR

Date of examination: 27.01.2015

Acknowledgment

It is with great pleasure that I wish to thank all people who contributed and accompanied me during this Ph.D. Thesis work.

First of all I would like to thank my supervisor Prof. Paola Coan for the help, the patience in correcting my writings and for leading me during the years of my work.

I wish to express my full gratitude to Dr. Alberto Bravin, for being always available for discussions and for the precious hints that allowed me to improve my knowledge.

A special thanks to Dr. Sergei Gasilov whose help was fundamental for a deeper scientific understanding and in finding solutions concerning the topics on which I worked during these years.

I would like to thank my former colleagues Paul and Emmanuel and all the people with whom I spent many hours for work and not work reasons.

My gratitude goes also to all the collaborators of the department of physics of the LMU, the ESRF (in particular the ID17 team and Claudio Ferrero) the team of Lyon (CREATIS, INSA). A big thank goes also to all my friends now spread around the whole Europe.

Un ringraziamento molto speciale a tutta la mia famiglia, il cui supporto è stato fondamentale per la riuscita di questo lavoro. Un grazie a tutti gli amici che mi hanno aiutato e pazientemente sopportato, in particolare Fabri, Gabri, Fra e Stefano e tutta la compagnia dei PmT.

Now, the most important, I would like to give a big спасибо to Irina whose support was and is priceless.

My acknowledgement goes also to the financial support provided by the DFG-Cluster of Excellence Munich-Centre for Advanced Photonics (EXE158) and for the provision of computational and experimental resources by the European Synchrotron Radiation Facility (ESRF).

Table of contents

List of the publications produced in the framework of this PhD Thesis	9
Summary	10
Zusammenfassung	12
Introduction	14
I.1 Phase-contrast imaging for biomedical applications	14
I.2 The problem of radiation dose	16
I.3 Why using the Analyser-Based Imaging (ABI) technique?	16
I.4 Objectives of the Thesis work	17
I.5 The structure of Thesis	18
Chapter 1 - Biomedical imaging and Phase-Contrast Imaging Techniques	20
1.1 Biomedical imaging techniques	21
1.2 Biomedical applications	22
1.2.1 Breast tissue	22
1.3 Phase-contrast imaging: physical principles and techniques	23
1.3.1 Index of refraction	23
1.3.2 X-ray beam coherence	26
1.3.3 Phase-contrast imaging techniques	26
1.3.3.1 The Analyzer based imaging	27
1.3.3.2 Propagation based imaging	35
1.3.3.3 Grating interferometry	37
1.3.3.4 Edge-illumination or Coded aperture imaging	39
1.3.3.5 Comparison between the PCI techniques	41
1.3.4 Recent state of art of phase-contrast imaging for breast tissue	41
Chapter 2 - Experimental setups and equipment	45
2.1 Introduction to synchrotron radiation	46
2.1.1 Synchrotron radiation sources	46
2.1.1.1 Radiofrequency cavities	47
2.1.1.2 SR beam characteristics	48
2.2 The European Synchrotron Radiation Facility and the biomedical beamline (ID17)	49
2.3 Description of the experimental setups	51

2.4 ID17 Image acquisition equipment	56
Chapter 3 - Different approaches for phase-contrast computed tomography	58
3.1 Analyser-Based Imaging: quantitative imaging method.....	59
3.1.1 Diffraction-enhanced imaging (DEI)	60
3.1.2 Extended DEI (E-DEI).....	61
3.2 Phase-contrast CT reconstruction techniques	63
3.2.1 Filtered back projection algorithm (FBP)	63
3.2.1.1 Fourier slice theorem	64
3.2.2 Filtered back-projection for gradient projections (GFBP)	65
3.2.3 Refractive-index gradient vector field method (RGVF)	68
3.2.4 CT reconstruction based on a phase-retrieval method	71
3.2.4.1 Boundary conditions	72
3.3 Different ABI CT geometries: a simulation study	72
3.3.1 Simulation code	72
3.3.2 Simulation parameters.....	74
3.3.3 Simulations of experimental errors	78
3.3.3.1 Discontinuities between materials with very different optical constants	80
3.3.4 Comparison between the out-of-plane and in-plane CT geometries.....	83
3.4 Conclusions.....	88
Chapter 4 - Phase-contrast tomography: experimental results	90
4.1 Experimental acquisitions	91
4.1.1 Comparison between the index of refraction CT and the absorption CT.....	92
4.1.2 Comparison of the two different CT acquisition geometries	94
4.2 The problem of image deconvolution	99
4.2.1 The deconvolution algorithm	100
4.2.2 Point Spread Functions	101
4.2.3 Application of the deconvolution procedure on experimental images.....	101
4.2.3.1 Wavelet denoising.....	104
4.3 Conclusions.....	109
Chapter 5 - Fast and accurate simulations of the deposited radiation dose in CT	111
5.1 Introduction.....	112
5.2 Interactions of X-rays with matter	113
5.2.1 Physical processes involved in X-ray biomedical imaging.....	113

5.3 Introduction to Monte Carlo methods	115
5.3.1 The PENELOPE physic model	116
5.3.2 Photon cross section and transport algorithm	117
5.3.2.1 The interaction length or Mean Free Path	118
5.3.2.2 Determination of the interaction point	119
5.3.3 Acceleration of the simulations - Variance reduction techniques (VRT)	120
5.4 The TLE method	120
5.4.1 Local energy deposition by secondary electrons	121
5.4.2 Energy-absorption tables.....	121
5.4.3 Implementation of the TLE in GATE	124
5.4.4 Benchmarking of the TLE implementation in GATE against MC simulation.....	124
5.4.5 Experimental validation of the TLE.....	125
5.4.5.1 Photon flux measurement protocol	125
5.4.5.2 Dose measurement protocol.....	126
5.4.5.3 Simulation parameters.....	127
5.4.6 Performances comparison between TLE and MC dose deposition simulations in complex cases	127
5.5 Results.....	128
5.5.1 Benchmarking against MC simulation.....	128
5.5.2 Accuracy test of the TLE method against measurements	130
5.5.3 Performances comparison in anatomically complex cases	131
5.6 Conclusions.....	133
Chapter 6 - Radiation dose in breast CT imaging with monochromatic X-rays: a simulation study and database	135
6.1 Introduction.....	137
6.2 Dose database for breast CT	137
6.2.1 Instruments and methods	138
6.2.2 Simulations parameters	139
6.2.2.1 General parameters	139
6.2.2.2 Derivation of a reference dose database.....	141
6.2.2.3 Energy optimization with Gadox- and CdTe-based detection systems.....	141
6.2.2.4 Study of the sample thickness influence	141
6.2.2.5 Study of the tissue composition influence	141

6.2.2.6 Study of the influence of skin and/or PMMA wall to the dose calculation	142
6.2.2.7 Estimation of the accuracy of the approximation factors.....	142
6.2.3 Results.....	142
6.2.3.1 Derivation of a reference dose database.....	142
6.2.3.2 Minimization of the ratio dose/transmittance D_t	144
6.2.3.3 Energy optimization with Gadox-, CdTe-, CsI-based and a-Se imaging detectors	145
6.2.3.4 Study of the sample thickness influence	148
6.2.3.5 Study of the tissue composition influence	150
6.2.3.6 Skin and PMMA wall influence.....	151
6.2.3.7 Calculation of the deposited dose	152
6.2.3.8 Comparison between simulations of test cases and approximated values	152
6.3 Optimization of the radiation dose by adapting the exposure time to sample geometry	153
6.3.1 Instruments and methods:	154
6.3.2 Results and discussion	155
6.3.2.1 Dose and time reduction	155
6.3.2.2 Image quality	159
6.4 Conclusions.....	164
6.4.1 Dose database study.....	164
6.4.2 Optimization of the detector integration time	165
Conclusions.....	166
References.....	173
Appendix.....	186

List of the publications produced in the framework of this PhD Thesis

- [1] F. Baldacci, **A. Mittone**, A. Bravin, P. Coan, F. Delaire, C. Ferrero, S. Gasilov, J. M. Létang, D. Sarrut, F. Smekens, and N. Freud, “A track length estimator method for dose calculations in low-energy X-ray irradiations: implementation, properties and performance”, *Z. Med. Phys.*, Jun. 2014.
- [2] E. Brun, S. Grandl, A. Sztrókay-Gaul, **A. Mittone**, S. Gasilov, A. Bravin and P. Coan, “Breast Tumor Segmentation in High Resolution X-ray Phase Contrast Analyzer Based Computed Tomography”, *Medical Physics*. Med. Phys. 41, 111902, 2014.
- [3] S. Gasilov, **A. Mittone**, E. Brun, A. Bravin, S. Grandl, and P. Coan, “On the possibility of quantitative refractive-index tomography of large biomedical samples with hard X-rays”, *Biomed. Opt. Express*, vol. 4, no. 9, pp. 1512–8, Jan. 2013.
- [4] S. Gasilov, **A. Mittone**, E. Brun, A. Bravin, S. Grandl, A. Mirone, and P. Coan, “Tomographic reconstruction of the refractive index with hard X-rays: an efficient method based on the gradient vector-field approach”, *Opt. Express*, vol. 22, no. 5, pp. 5216–5227, 2014.
- [5] A. Horng, E. Brun, **A. Mittone**, S. Gasilov, L. Weber, T. Geith, S. Adam-Neumair, S. D. Auweter, A. Bravin, M. F. Reiser, and P. Coan, “Cartilage and Soft Tissue Imaging Using X-rays: Propagation-Based Phase-Contrast Computed Tomography of the Human Knee in Comparison With Clinical Imaging Techniques and Histology”, *Invest. Radiol.*, May 2014.
- [6] **A. Mittone**, F. Baldacci, A. Bravin, E. Brun, F. Delaire, C. Ferrero, S. Gasilov, N. Freud, J. M. Létang, D. Sarrut, F. Smekens, and P. Coan, “An efficient numerical tool for dose deposition prediction applied to synchrotron medical imaging and radiation therapy”, *J. Synchrotron Radiat.*, vol. 20, no. Pt 5, pp. 785–92, Sep. 2013.
- [7] **A. Mittone**, A. Bravin, and P. Coan, “Radiation dose in breast CT imaging with monochromatic X-rays: simulation study of the influence of energy, composition and thickness”, *Phys. Med. Biol.*, vol. 59, no. 9, pp. 2199–2217, May 2014.
- [8] Y. Zhao, E. Brun, P. Coan, Z. Huang, A. Sztrókay, P. C. Diemoz, S. Liebhardt, **A. Mittone**, S. Gasilov, J. Miao, and A. Bravin, “High-resolution, low-dose phase contrast X-ray tomography for 3D diagnosis of human breast cancers”, *Proc. Natl. Acad. Sci. U. S. A.*, vol. 109, no. 45, pp. 18290–4, Oct. 2012.

Summary

The X-Ray phase-contrast techniques are innovative imaging methods allowing overtaking the limitations of classic radiology. In addition to the differential X-ray absorption on which standard radiology relies, in phase-contrast imaging the contrast is given by the effects of the refraction of X-rays inside the tissues. The combination of phase-contrast with quantitative computer tomography (CT) allows for a highly accurate reconstruction of the tissues' index of refraction. Thanks to the high sensitivity of the method, tomographic images can be obtained at clinically compatible dose. For all these reasons phase-contrast imaging is a very promising approach, which can potentially revolutionize diagnostic X-Ray imaging. Several techniques are classified under the name of X-Ray phase-contrast imaging. This Thesis focused on the so-called analyzer-based imaging (ABI) method. ABI uses a perfect crystal, placed between the sample and the detector, to visualize the phase effects occurred within the sample. The quantitative reconstruction of the refraction index from CT data is not trivial and before this Thesis work it was documented only for small size objects. This Thesis has focused on two main scientific problems: (1) the development of theoretical and calculation strategies to determine the quantitative map of the refraction index of large biological tissues/organs (>10 cm) using the ABI technique; and (2) the preparation of accurate and efficient tools to estimate and simulate the dose deposited in CT imaging of large samples.

For the determination of the refraction index, two CT geometries were considered and studied: the out-of-plane and the in-plane configurations. The first one, the most used in the works reported in the literature, foresees that the rotation axis of the sample occurs in a plane parallel to that of the sensitivity of the analyzer crystal; while, in the second CT geometry, the rotation axis is perpendicular to that plane. The theoretical study, technical design and experimental implementation of the in-plane geometry have been main tasks of this Thesis. A first experiment has been performed in order to compare the results obtained with in-plane quantitative phase contrast CT with the absorption-based CT ones. An improved accuracy and a better agreement with the theoretical density values have been obtained by exploiting the refraction effect while keeping the dose to sample low.

A second campaign of experiments has been performed on large human breasts to investigate the efficiency of the in-plane and out-of-plane CT geometries and the performances of the associated image reconstruction procedures. The same experimental conditions were also studied by numerical simulations and the results were compared. This analysis shows that the in-plane geometry allows producing more accurate quantitative three dimensional maps of the index of refraction, while the out-of-plane case is preferable for qualitative investigations.

A study for developing advanced procedures for improving the quality of the obtained CT images has been also conducted. As a result, a two-step procedure has been tested and identified: first the noise level of the experimental images is reduced by applying a wavelet decomposition algorithm and then a deconvolution procedure. The obtained images show an enhanced sharpness of the interfaces and of the object edges and high signal to noise ratio values are preserved.

The second problem of this Thesis was to find strategies to calculate, in a fast way, the delivered dose in CT imaging of complex biological samples. For this purpose an acceleration method to speed-up the convergence of Monte Carlo simulations based on the Track Length Estimator method has been computed and included in the open-source software GATE. Results show that this method can lead to the same accuracy of conventional Monte Carlo methods while reducing the required computation time of up to two orders of magnitude, with the respect to the considered geometry. A database of dose curves for the case of monochromatic breast CT has been produced: it allows for a quick estimation of the delivered dose. A way to choose the best energy and the optimal photon flux was also proposed, which leads to a significant reduction of the delivered dose without any loss in terms of image quality.

Most of the experimental and data reconstruction methods developed within this Thesis work can be applied also to other phase-contrast techniques. This Thesis shows that high resolution three dimensional diagnostic imaging of large and complex biological organs can, in principle, be performed at clinical compatible doses; this is the most significant contribution of the Thesis towards the clinical implementation of phase-contrast CT.

Zusammenfassung

Auf Phasenkontrast basierende Röntgentechniken sind innovative bildgebende Methoden, welche die Limitierungen der klassischen Radiologie überschreiten. Außer der differentiellen Röntgenabsorption, auf der die herkömmliche Radiologie beruht, ist der Kontrast bei Phasenkontrast-Bildgebung durch die Brechungseffekte der Röntgenstrahlen innerhalb eines Gewebes gegeben. Die Kombination zwischen Phasenkontrast und quantitativer Computertomographie (CT) erlaubt eine höchstgenaue Rekonstruktion der Brechzahl der Gewebe. Aufgrund der hohen Empfindlichkeit dieser Methode, können tomographische Bilder mit einer klinisch verträglichen Dosis erzeugt werden. Aus all diesen Gründen, stellt Phasenkontrast-Bildgebung einen vielversprechenden Ansatz dar, welcher die diagnostische Röntgenbildgebung revolutionieren könnte. Verschiedene röntgenbildgebende Techniken werden als Phasenkontrast-Verfahren bezeichnet. Die vorliegende Doktorarbeit befasst sich mit der sogenannten Bildgebungsmethode mithilfe eines Analysatorkristalls (auf englisch: analyser-based imaging (ABI)). ABI benutzt ein perfektes, zwischen der Probe und dem Detektor angeordnetes Kristall, um in der Probe stattfindenden Phaseneffekte zu veranschaulichen. Die quantitative Rekonstruktion des Brechungsindex aus den CT-Daten ist jedoch nicht trivial und war vor dieser Arbeit nur für kleine Gegenstände beschrieben. Im Mittelpunkt dieser Dissertation stehen folgende wissenschaftliche Fragestellungen: (1) die Entwicklung theoretischer und rechnerischer Strategien, um die quantitative räumliche Verteilung des Brechungsindex in größeren Organen aus biologischen Geweben (10 cm) unter Verwendung der ABI-Technik zu bilden und (2) die Vorbereitung von genauen und leistungsfähigen Rechenmitteln zur Abschätzung und Simulation der in größeren Proben bei einem CT-Bildgebungsversuch abgelagerten Strahlendosis zu treffen. Für die Bestimmung des Brechungsindex wurden zwei geometrische Anordnungen in Betracht gezogen und untersucht, und zwar die Konfiguration außerhalb (out-of-plane) bzw. in der Ebene (in-plane) der Probe. Erstere wird am häufigsten in der Fachliteratur zitiert und sieht vor, dass die Probe-Drehachse sich in der parallelen Ebene zur Achse des Analysatorkristalls befindet, wobei in der zweiten Geometrie die Drehachse orthogonal zu jener Ebene ist. Die theoretische Studie, der technische Entwurf und die experimentelle Umsetzung der geometrischen Anordnung in der Probe-Ebene stellen die Hauptaufgaben dieser Arbeit dar. Ein erstes Experiment wurde durchgeführt, um die durch quantitative Phasenkontrast-CT nach in-plane-Modus erlangten Ergebnisse mit entsprechenden, auf Absorption basierenden CT-Versuchen zu vergleichen. Eine höhere Genauigkeit sowie eine bessere Übereinstimmung mit den theoretischen Dichtewerten

wurden dadurch erzielt, dass man sich die Brechungseffekte zunutze macht, indem man die an die Probe gelieferte Dosis niedrig hält.

Eine zweite Versuchsreihe wurde außerdem auf menschliche Brüste ausgeführt, um die Effizienz sowohl der in-plane- als auch der out-of-plane-CT-Geometrien sowie die Leistungsfähigkeit der entsprechenden Bildrekonstruktionsverfahren zu überprüfen. Die gleichen Experimentalbedingungen wurden auch anhand von numerischen Simulationen untersucht und die Ergebnisse miteinander verglichen. Diese Analyse zeigt, dass die in-plane-Geometrie die Erstellung genauerer dreidimensionaler Verteilungen der Brechzahl ermöglicht, während der out-of-plane-Fall eher für die Zwecke qualitativer Untersuchungen vorzuziehen ist.

Fortschrittliche Prozeduren zur Verbesserung der Qualität von aufgezeichneten CT-Bildern wurden im Rahmen dieser Doktorarbeit konzipiert und entwickelt. Das Fazit: eine zweistufige Vorgehensweise wurde ermittelt und geprüft. Zunächst wird der Rauschpegel der Meßdaten über die Anwendung eines Zerlegungsalgorithmus mittels Wavelets gesenkt, anschließend gefolgt von einem Entfaltung-Verfahren. Die damit gewonnenen Bilder weisen eine erhöhte Schärfe der Schnittstellen auf. Die Objektkanten und das Signal-zu-Rausch-Verhältnis bleiben damit erhalten. Die zweite Fragestellung dieser Arbeit war es, Lösungsansätze zu erarbeiten, um die während CT-Bildgebung-Messungen über komplexe biologische Proben abgegebene Dosis möglichst rapide zu berechnen. Zu diesem Zweck wurde ein Verfahren zur Beschleunigung der Konvergenz von Monte-Carlo-Simulationen auf der Grundlage der Track-Length-Estimator-Methode entwickelt und in die Open-Source-Software GATE eingegliedert. Die bisherigen Ergebnisse zeigen, dass dieses Verfahren zur selben Genauigkeit der herkömmlichen Monte-Carlo-Methoden bei gleichzeitiger Minderung bis zu zwei Größenordnungen der zur Berechnung einer und der selben Geometrie notwendigen Rechenzeit führt. Eine Datenbank von Dosiskurven für den Fall von monochromatischer Brust-CT ist erzeugt worden, die eine schnelle Schätzung der abgegebenen Dosis erlaubt. Darüber hinaus wurde ein Lösungsweg zur Auswahl der besten Energie und des optimalen Photonenflusses vorgeschlagen, welcher eine bedeutende Abnahme der abgelieferten Dosis zur Folge hat, und zwar ohne Bildqualitätsverluste.

Die meisten, im Rahmen dieser Doktorarbeit entwickelten Experimental- und Datenrekonstruktion-Verfahren können freilich auch an andere Phasenkontrast-Techniken angewendet werden. Es wird hiermit gezeigt, dass hochauflösende dreidimensionale bildgebende Verfahren zur Diagnostik größerer und komplexer biologischer Gegenstände bei klinisch verträglichen Dosen grundsätzlich eingesetzt werden können. Dies ist der nennenwerteste Beitrag dieser Dissertation zur klinischen Umsetzung der Phasenkontrast-CT.

Introduction

Since the first radiographic image has been acquired by Röntgen in the 1895, X-rays have been widely used in different fields. In medicine X-ray imaging techniques are an indispensable diagnostic tool. Many improvements have been achieved during the last century; in particular they have focused on technical developments concerning the radiation sources (*i.e.* X-ray tubes) and detectors. A fundamental step came from the introduction by Hounsfield, in the 1970's, of computed tomography (CT) that allows the three-dimensional (3D) imaging of the inspected object. Despite all these improvements the main physical principles upon which these techniques rely remained the same. The image contrast arises from the variations in the X-ray absorption caused by differences in the density, composition and thickness within the sample. As a result, when imaging soft tissues like breast or articular cartilage, the contrast in conventional radiography can be intrinsically limited. A series of techniques based on a different approach have been developed over the last decades to overcome these limitations. These imaging methods are known as phase-contrast imaging (PCI) techniques.

I.1 Phase-contrast imaging for biomedical applications

In life sciences, the samples to be investigated very often consist of weakly absorbing tissues and structures which are mainly formed of low Z elements (hydrogen, carbon, nitrogen and oxygen). In these cases, the sensitivity of conventional radiography may drastically decrease because of the small differences in the X-ray absorption coefficients, μ , of the materials composing the object. For instance, the absorption coefficients of soft tissues (ICRU 1989) are in the order of $\mu_{E=10} \approx 5 \text{ cm}^{-1}$ and of $\mu_{E=60} \approx 0.2 \text{ cm}^{-1}$ in the range of energies commonly used in radiology (10-60 keV, in case of breast tissue, 5-150 keV in general medical diagnostics), with differences of few percents between the different tissues. The use of high-efficiency and low-noise digital detectors has led to an improvement of the image quality, as the use of highly collimated and monochromatic X-ray beams (Lewis 1997).

A completely different approach, based on a different physical phenomenon, has been proposed and developed in the last years with the aim of overcoming the present limitations of clinical X-ray diagnostics. The basic idea is to detect and record the phase variations occurring when X-rays pass through the matter in addition to the absorption signal.

The behaviour of X-rays as they travel through an object can be described in terms of a complex index of refraction defined as $n = 1 - \delta + i\beta$, whose real part, δ , and imaginary part, β , are related to the X-ray

phase shifts and attenuation in the object, respectively. In the energy range 10-100 keV, the phase term is orders of magnitude higher than the absorption one (figure I.1); therefore, radiographic techniques sensitive to variations of the δ term may potentially provide an increased image contrast with respect to those methods based only on the X-ray absorption process.

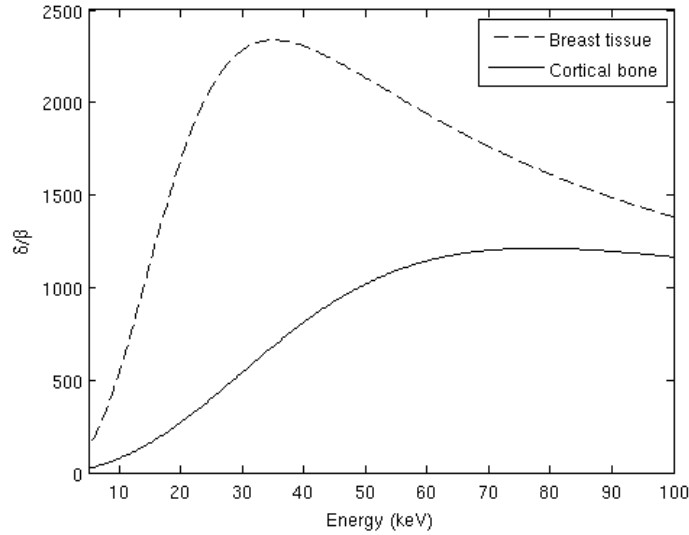


Figure I.1: ratio δ/β for breast tissue and cortical bone. The values have been calculated using the EPDL97 database (Cullen et al. 1997) and the formula presented in the Appendix. The compositions have been taken from NIST (NIST).

Several techniques have been developed (Bravin et al. 2013) for exploiting the phase effects in X-ray imaging. They include the propagation-based imaging (PBI) technique (Snigirev et al. 1995; Cloetens et al. 1996), the analyser-based imaging (ABI) technique (Förster et al. 1980; Davis et al. 1995; Bravin 2003), the interferometric modalities (Momose et al. 1996; David et al. 2002) and the non-interferometric method (Olivo et al. 2001).

In order to detect phase-contrast effects, the X-ray beam needs to fulfil certain requirements in terms of temporal and spatial coherence, two properties which are linked to the X-ray monochromaticity and to the angular source size, respectively. The introduced coherent imaging modalities have significant application in various fields such as material science (Cloetens et al. 2002; Tsai et al. 2002), sub-micron imaging (Lagomarsino et al. 1997; Hignette et al. 2003) and biomedical imaging (Arfelli et al. 2000). In this Thesis work the PCI technique which has been principally investigated and used is the analyser-based imaging (ABI); for this reason, it will be more extensively described.

One of the most promising applications of X-ray PCI is the quantitative and accurate 3D CT reconstruction of the index of refraction. However, owing to the complexity of the experiments, the reconstruction of the index of refraction has been usually performed on small samples and/or portion of tissues. The

demonstration of the high potential of the method on large medical samples has been experimentally obtained for the first time in this Thesis work.

I.2 The problem of radiation dose

The problem of the delivered radiation dose is an important issue when imaging biological tissues. The common way to calculate the dose, when direct measurements are not possible, is to perform Monte Carlo (MC) simulations. These simulations usually require long computational time to reach a reasonable level of accuracy, especially when a large number of voxels is considered.

Many MC codes are available to simulate the radiation transport: Geant4 (Agostinelli et al. 2003; Allison et al. 2006), MCNPX (Pelowitz 2005), Fluka (Battistoni et al. 2007; Ferrari et al. 2005), EGSnrc (Fragoso et al. 2008), PENELOPE (Salvat et al. 2009; Salvat et al. 2011). They are commonly used for research purposes, either in simulation mode or in combination with various acceleration techniques, such as condensed history methods or variance reduction techniques (VRT). However a method allowing performing fast simulations of the dose deposited in case of large volumes, without losing in accuracy, was missing before this Thesis work.

I.3 Why using the Analyser-Based Imaging (ABI) technique?

This Thesis work is focused on the optimization and application of the ABI technique for biomedical imaging. The principles of the method are described in Chapter 1. We choose to use the ABI technique because earlier studies demonstrated the possibility to perform ABI both in planar and tomographic mode at clinically compatible radiation doses. This was obtained by also using higher X-ray energies with respect to those used in clinical radiology. Previous works within the group had shown that the signal to noise ratio of the ABI technique is inversely proportional to the photon energy (E^{-1}), while for other PCI techniques the dependence on the energy is more unfavourable (*i.e.* E^{-2}) (Diemoz et al. 2012a; Diemoz et al. 2012b). Thus this technique appears particularly suitable when high photon energies are used, with a consequent benefit in terms of dose to the tissue/object. It has been also demonstrated that the ABI approach outperforms the other PCI techniques in the case of samples showing large density variations (Akio et al. 2008). Moreover most of the developments performed in this Thesis can be partially adapted and applied also to other PCI techniques. For all these reasons, the ABI was selected for the work of this Thesis and for investigating the feasibility of PCI of large, clinical like samples for application such as breast imaging. All

the experiments and simulations presented in this Thesis have been performed by using synchrotron radiation X-rays, which are considered the gold standard radiation for the development and optimization of new X-ray imaging strategies and modalities.

I.4 Objectives of the Thesis work

This Thesis work has been dedicated to the development and optimization of dose estimation and quantitative imaging aspects in phase-contrast tomography of clinical like biological samples. The main aim was to demonstrate the feasibility and diagnostics relevance of PCI for an accurate 3D investigation of complex and large biological tissues as those used in clinical diagnostics and therefore to extend the results previously published in the literature.

The aims of the Thesis works were, in detail:

- to provide a tool (open source and easy to use) for a fast and accurate estimation of the dose deposited in CT imaging together with the overcoming of the problem of the long computational time required by standard MC simulations;
- to present a database of dose curves that can be used for breast CT study with synchrotron radiation without the necessity of performing simulations for each case;
- to optimize and to study the contributions of several experimental parameters to the image quality and to the delivered radiation dose in phase-contrast CT;
- to develop technical methods and reconstruction procedures for quantitative index of refraction imaging of large object (> 10 cm);
- to compare the results obtained with the ABI CT methods by using two different CT acquisition geometries.

I have collaborated in the implementation of an computation acceleration module in the open-source MC code GATE/Geant4, in particular for the creation of a database of mass-energy absorption coefficients based on the EPDL97 data (Cullen et al. 1997). I validated and compared the obtained results versus standard MC and versus experimental measurements (Mittone et al. 2013). I have created a database of dose curves that can be used in preclinical breast CT studies for an estimation of the dose delivered to the sample when monochromatic parallel X-ray beams are used. I have derived a practical procedure which offers the possibility to adapt the presented results for different parameters like the sample compositions, thickness and presence of skin/container wall (Mittone et al. 2014). A study for determining the optimal photon energy depending on the specific experimental case is presented as well as the comparison in terms

of radiation dose requirement with and without modulation of the detector integration time according to the sample thickness.

I collaborated in the optimization and implementation of the CT reconstruction of the index of refraction distribution for complex and large biomedical samples (> 10 cm diameter) (Gasilov et al. 2013). Thanks to the higher sensitivity of this method, the improved precision was obtained using an incoming photon fluence on the sample several times smaller than in the case of absorption imaging.

Two different CT acquisition geometries, combined to the ABI technique, have been studied by means of simulations and experiments. Results have been analysed and compared using different image reconstruction techniques. The experimental setups have been implemented at the biomedical beamline (ID17) of the European Synchrotron Radiation Facility (ESRF, Grenoble, France). The geometry based on the rotation of the inspected object around an axis perpendicular to the plane of sensitivity of the used PCI technique (*i.e.* in-plane geometry) has been implemented *ex novo* at ID17. The description of the experimental setup and the advantages of the usage of the in-plane geometry are included in the Thesis.

I performed several simulations of ABI experiments by using a dedicated software developed within our group. The aim of these simulations was to compare the theoretical results obtained by using the two considered CT acquisition geometries and correlate them to experimental data. Simulations and experimental data have also been used to study methods to improve the quality of the reconstructed images (deblurring and dishing artefact correction).

I collaborated in the analysis of the experimental results produced during various experiments performed at the ID17 of the ESRF.

I.5 The structure of Thesis

The Thesis work is structured in the following way:

Chapter 1: it provides a brief description of the main conventional biomedical imaging techniques and of the quantitative PCI techniques. A brief overview on the state of art of breast imaging is presented as well as the main properties and issues related to this type of tissues.

Chapter 2: the properties of the synchrotron radiation are discussed and a description of the biomedical beamline (ID17), where all the experiments described in this Thesis have been performed, is reported. The experimental set-ups used and implemented in the framework of the Thesis are also described.

Chapter 3: two different approaches for ABI CT to be applied to biomedical samples are presented and the quantitative methods implemented to retrieve the index of refraction described. Numerical simulations have been performed to study the two CT geometries in the case of homogenous (e.g. human breast model) and inhomogeneous (*e.g.* human knee bone model) samples. A description of the development of advanced

methods for image reconstruction is also presented. The methods are based on the filtered back projection for gradient projections (Faris & Byer 1988), on phase-retrieval and on the work of (Maksimenko et al. 2005).

Chapter 4: The experimental results of the comparison of the two studies CT geometries for ABI are reported. The results of the reconstruction of the index of refraction in complex and large biological samples are presented as well. I show also the results of studies which I have performed to improve the final quality of the reconstructed ABI CT images.

Chapter 5: in this chapter the implementation of the computational acceleration (Track Length Estimator) method in the GATE framework is presented. The validation of the code versus experimental measurements and versus the conventional MC method is also reported. A brief description of the performance of the method is described.

Chapter 6: the development of a dose database for breast CT acquisitions with monochromatic X-rays is presented as well as a study to optimize the dose versus the photon energy. The study of the influence on the deposited dose of the imaging detector efficiency is reported.

Conclusions: summary and discussion of the Thesis work and results.

Chapter 1 - Biomedical imaging and Phase-Contrast Imaging Techniques

1.1 Biomedical imaging techniques	21
1.2 Biomedical applications	22
1.2.1 Breast tissue	22
1.3 Phase-contrast imaging: physical principles and techniques	23
1.3.1 Index of refraction.....	23
1.3.2 X-ray beam coherence	26
1.3.3 Phase-contrast imaging techniques	26
1.3.3.1 The Analyzer based imaging.....	27
1.3.3.2 Propagation based imaging	35
1.3.3.3 Grating interferometry	37
1.3.3.4 Edge-illumination or Coded aperture imaging.....	39
1.3.3.5 Comparison between the PCI techniques.....	41
1.3.4 Recent state of art of phase-contrast imaging for breast tissue.....	41

1.1 Biomedical imaging techniques

With the terminology Biomedical Imaging the techniques and the processes used to create images of the human body, animal models and biological samples for clinical and pre-clinical purposes are indicated. Many different imaging modalities like Radiography, Magnetic Resonance Imaging, Nuclear medicine, Ultrasound, Elastography, Thermography and Tomography are included (Dhawan 2003).

- **Conventional radiography and Computed Tomography (CT)** employs X-rays to investigate the property of the matter related to the distribution of the absorption coefficient μ in the imaged object. Radiography includes two 2D techniques (Fluoroscopy and Projectional radiographs). The advantages of using 2D techniques, instead of the 3D tomography, consist in the low cost, high resolution and lower radiation dosage. CT belongs to the more general Tomography techniques; it is based on the use of X-rays to image a single plane or slice within the object.
- **Magnetic Resonance Imaging (MRI)** is based on the polarization and excitation of hydrogen nuclei (single proton) in the water molecules. The signal produced is detectable, and it results in images of the body/tissue. The MRI machine emits a radio frequency pulse that specifically binds the hydrogen. This technique does not employ ionizing radiation, and therefore is not associated with the same health hazards of CT. The appearance of the obtained images differs markedly from the one produced in CT, because the two techniques are sensitive to different tissue properties.
- **Nuclear medicine** is based on the emission of energetic particles from radioactive materials injected/inserted into the body to diagnose or treat different pathologies. Images are acquired after collimated photons are detected by a crystal that gives off a light signal. This signal is subsequently amplified and converted into count data.
- **Ultrasonography** uses sound waves in the range of MHz that are reflected by tissues at varying degrees to produce images. It provides less anatomical details compared to MRI and CT, but it can be used to study the motions of moving structures.

The performance of a technique is measured in terms of contrast, delivered dose, spatial and temporal resolutions. Among the conventional techniques above listed, no one can simultaneously satisfies all these requirements. For example, conventional radiography satisfies the dose requirement but its sensitivity with respect to soft tissues is limited. Another disadvantage is related to the problem of the overlapping of the 3D structures of the object which are all projected on the same plane onto the detector. While the latter issue is solved by using the CT technique, the contrast related limitation remains because the image formation mechanism is the same as the one used in conventional radiography.

MRI can provide a good contrast for soft tissues with the advantage of the usage of not ionizing radiation but the obtainable spatial resolution is not always satisfactory. The same limitation is also encountered in nuclear medicine and ultrasonography.

To overcome these limitations, the so called X-ray Phase-contrast Imaging (PCI) techniques have been introduced for medical imaging. The PCI techniques aim to provide a high resolution and contrast while keeping low the delivered dose. These techniques can be used in both planar/projectional and CT modes. The advantages of such approach are described in the next sections.

1.2 Biomedical applications

Over the past 15 years, PCI has been tested and used for several and diverse biomedical applications; an overview can be found in Bravin et al. 2013. In this Thesis work I mainly focused on breast CT imaging. Only one model of human knee, obtained from real experimental data, has been used in a simulation study to consider the case of non-homogeneous samples. A brief description of the main features of the breast tissues and the main limitations encountered in conventional diagnostics are presented hereafter.

1.2.1 Breast tissue

Breast cancer is the first cause of cancer decease in women. It accounts for the 23% of the new total cancer cases and 14% of the total cancer death in 2008. The breast cancer incidence increase, as observed in many Western countries in the late 1980s and 1990s, likely results from changes in reproductive factors (including the increased use of postmenopausal hormone therapy) as well as an increased screening intensity (Jemal et al. 2010). According to statistics, the 5-years survival rates in women diagnosed of breast cancers has considerably improved in the last years, with a 75% survival rate in 1975, a 79% survival rate in 1985 and 89% survival rate in 2003 registered in USA (Ries et al. 2004). It becomes clear that an early detection of breast cancer plays a fundamental role.

Despite the technical improvements in X-ray sources and digital detector, a considerable fraction (10-20%) of palpable tumours go unnoticed in screening mammography (Durfee et al. 2000; Schulz-Wendtland et al. 2009), which is presently the gold standard diagnostic technique for breast cancer. Considering the large number of patients affected by breast cancer pathologies, such percentage implies a strong necessity of improvements of the existing method for breast cancer diagnose.

The breast consists of lobes of glandular tissue with associated ducts for transfer the milk to the exterior, surrounded by supportive fibrous and fatty tissues. During the reproductive years about 80-85% of an average breast consists of fat tissue. Several kinds of tumours can interest the breast and they are normally linked to the glandular fraction of tissue. They are subdivided in benign and malign tumours.

Conventional mammography is the gold standard technique for breast cancer screening, as already mentioned. However, the method is affected by several limitations mainly deriving from the fact that breast tissues are composed of light elements and present small density variations. The consequence is that a small absorption contrast occurs between the different tissues. Low photon energies (mean energy $\sim 20\text{keV}$) are employed for optimizing the image contrast, but this leads to a consequent increase of the delivered radiation dose to the tissue (as it is shown in Chapter 6). Due to the high radiation sensitivity of the breast (in particular of the glandular fraction, while the remaining tissues, *i.e.* skin and fat, are not considered to be at risk) the dose has to be kept low: as a result, the obtainable contrast is limited.

A possible alternative of such technique is the usage of MRI, but the high costs, the bulkiness of the machine and the long acquisition time make preferable to find other solutions. As demonstrated by earlier studies, the use of PCI techniques may provide a fundamental tool to overcome the limitations of conventional mammography thanks to the high sensitivity of the methods, which is not purely based on the X-ray absorption mechanism. The development of advance technical and image processing aspects is therefore fundamental for a future implementation in clinical routine of the PCI.

1.3 Phase-contrast imaging: physical principles and techniques

1.3.1 Index of refraction

The propagation of X-rays through the matter is generally described with reference to the complex refractive index n , which can be expressed as (Jackson 1975):

$$n = 1 - \delta + i\beta \quad (1.1)$$

δ represents the refractive index decrement, which is related to the phase shifts of the electromagnetic wave in the matter and, therefore, its deviation from the incident direction due to the scattering with electrons of the medium (Azároff 1968). β is the absorption term which is linked to the absorption of X-rays into the matter, mainly due to the photoelectric effect for low X-ray energies ($< 20\text{ keV}$ for oxygen, lower energies in case of lighter elements) and also Compton scattering in the other cases.

Under the influence of the electromagnetic field of the incident radiation, the polarization of the medium, for hard X-rays and far from the absorption edges, is well described by the free-electrons model where the electric susceptibility χ is proportional to the electron density ρ_E . The terms δ and β are related to the real and imaginary part of χ , respectively, by the following expressions (Zachariasen 1945):

$$\delta = -\frac{1}{2}\chi_{0r} \quad (1.2)$$

$$\beta = \frac{1}{2}\chi_{0i} \quad (1.3)$$

Such relations can be otherwise written as (Jackson 1975):

$$\delta = \frac{r_e \lambda^2 \rho_e}{2\pi} \quad (1.4)$$

$$\beta = \frac{r_e \lambda^3 \rho_e}{4\pi^2 c} \sum_j \frac{f_j \gamma_j}{Z} \quad (1.5)$$

where r_e is the electron radius, λ the X-rays wavelength, f_j is the number of electrons per atom with damping constant γ_j , and Z is the atomic number that gives the total number of electrons per atom; the sum is over all the j electrons of the atom.

The quantity ρ_e is linked to the macroscopic mass density of the medium ρ by the relation $\rho_e = Z/V = Z\rho N_A/A$ where V is the volume of reference, N_A the Avogadro's number and A the atomic weight.

The refractive index decrement can be generally expressed also as:

$$\delta = \frac{r_e \lambda^2}{2\pi V} \sum_j (Z + f'_j) \quad (1.6)$$

with f'_j the real part of the wavelength-dependent dispersion correction of the atomic scattering factor.

Similarly, the absorption index β can be also written in terms of the imaginary part of the wavelength-dependent dispersion correction, f''_j , as:

$$\beta = \frac{r_e \lambda^2}{2\pi V} \sum_j f''_j \quad (1.7)$$

For energies far from the absorption edges, f'_j is approximately zero, whereas f''_j dominated by the absorption process, behaves with the energy as E^{-m} , with $m \in [3,4]$.

β is related to the linear absorption coefficient μ , through the relation (Raven et al. 1996):

$$\mu = \frac{2\pi\beta}{\lambda} \quad (1.8)$$

The quantities δ and β are functions of the spatial coordinates (x, y, z) because of local changes in the matter.

In the case of a crystalline medium, the scattering properties of the radiation are generally described by means of the structure factor. If the Bragg reflection is not satisfied, the wave propagation is not influenced

by the crystalline structure. In this case, the refractive index may be expressed in terms of the (complex) structure factor F_0 as:

$$n = 1 - \frac{r_e \lambda^2 F_0}{2\pi V} \quad (1.9)$$

Numerically, n deviates only slightly from unity, δ and β being extremely small. The δ term is much larger than β in the energy range normally used in radiology and differs at least by three orders of magnitude from β , as shown in figure I.1 (Introduction), where the ratio δ/β as function of the X-ray energy in the range [5,100] keV is reported for breast tissue and cortical bone.

This large difference between δ and β is the reason for the advantages of PCI with respect to absorption-based radiology; the phase contribution being an additional and important source of contrast when the absorption counterpart is very weak or undetectable.

The energy dependence of the two terms δ and β , for energies far from the absorption edges and for low Z materials, is approximately given by $\delta \sim E^{-2}$ and $\beta \sim E^{-4}$.

Since the X-ray phase φ is related to δ by $\varphi = -2\pi\delta t/\lambda$, where t is the thickness traversed by X-rays, the energy dependence of the phase and of the linear attenuation coefficient may be expressed as $\varphi \sim E^{-1}$ and $\mu \sim E^{-3}$.

Let us now consider a thin object described by $n(x, y, z)$, illuminated by a monochromatic wave field of wavelength λ propagating along the z -axis. The wave exiting the sample can be expressed by:

$$\Psi_{obj}(x, y) = T(x, y)\Psi_{in}(x, y) \quad (1.10)$$

where $\Psi_{in}(x, y)$ represents the incident wave on the sample and $\Psi_{obj}(x, y)$ the wave at the exit surface. The interactions between the wave and the object can be described by the object complex transmission function $T(x, y)$:

$$T(x, y) = A(x, y)e^{i\phi(x, y)} \quad (1.11)$$

The amplitude modulation is given by the projection of β of refractive index distribution along the beam direction z .

$$A(x, y) = e^{-B(x, y)} \quad \text{with} \quad B(x, y) = \frac{2\pi}{\lambda} \int \beta(x, y, z) dz \quad (1.12)$$

The phase modulation is provided by the projection along z of δ :

$$\phi(x, y) = -\frac{2\pi}{\lambda} \int dz [1 - \delta(x, y, z)] = \phi_0 - \frac{2\pi}{\lambda} \int dz \delta(x, y, z) \quad (1.13)$$

The integrations along the propagation direction z are made along the entire object thickness.

An important effect of the distortion of the wavefront due to the phase shifts introduced by the object is that the X-rays which passed through the sample are locally refracted by an angle $\Delta\alpha$ that can be expressed as (Born & Wolf 1999):

$$\Delta\alpha(x, y; \lambda) \simeq -\frac{\lambda}{2\pi} \vec{\nabla}_{x,y} \phi(x, y; \lambda) \quad (1.14)$$

1.3.2 X-ray beam coherence

The concepts of spatial and temporal coherence are very important for PCI. The coherence can be seen as the property that makes a wave capable to produce observable interference and diffraction effects. For example a monochromatic plane wave is in this sense perfectly coherent, while the light emitted by a standard light bulb is completely incoherent. In the between we have states of partial coherence. The coherence properties of a wave field can be described using correlation functions (Born & Wolf 1999), space and time dependent, linked to the X-ray and to the angular source size and the monochromaticity, respectively.

- **Spatial (transverse) coherence:** indicates the correlation of the wave amplitudes between different points transverse to the propagation direction, between a wave $\Psi(x)$ and $\Psi(x + \Delta x)$. The lateral coherence length is defined as $l_t = \lambda L/2S$, where L and S represent the source-to-object distance and the transverse dimension of the source (Born & Wolf 1999).
- **Temporal (longitudinal) coherence:** implies a phase relationship between the wave $\Psi(t)$ and the wave $\Psi(t + \Delta t)$ separated by a short time delay. The longitudinal coherence length is defined as $l_t = \lambda^2/\Delta\lambda$, where λ is the wavelength, and it is the distance covered by a wave during a time delay over which the correlation remains high. It is associated to the monochromaticity $\Delta\lambda/\lambda$ of the X-ray beam.

It is possible to find a more complete and general description of the spatial and temporal coherence, given in terms of the mutual coherence function in Paganin 2006.

1.3.3 Phase-contrast imaging techniques

X-ray PCI techniques are all those imaging methods which exploit the phase shifts occurring when an X-ray beam passes through the matter in addition to the signal originated by the photon absorption (*i.e.* changes in the X-ray wave amplitude). These phase shifts, linked to variation in the value of δ , determine extremely small angular deviations $\Delta\alpha$ (*i.e.* refraction angles). As a highly collimated monochromatic beam traverses the sample, photons are deviated according to the gradient of the real part of the refractive index

as previously shown (eq. 1.13, 1.14). Several techniques exist: the propagation-based (free-space propagation) imaging, the analyser-based imaging, the interferometric-based techniques (*i.e.* crystal and grating interferometry) and the non-interferometric (*e.g.* the edge-illumination) imaging methods. In this section a general description of these PCI techniques is provided by focusing in particular on the analyser-based imaging (ABI) which is the most used method in this Thesis work.

1.3.3.1 The Analyzer based imaging

The ABI technique consists in the use of a parallel quasi-monochromatic X-ray beam to irradiate the sample and of a perfect crystal, called analyser crystal (AC), placed between the sample and the detector, to analyse the radiation exiting the sample (Förster et al. 1980; Somenkov et al. 1991; Ingal & Beliaeskaya 1995; Davis 1996; Chapman et al. 1997).

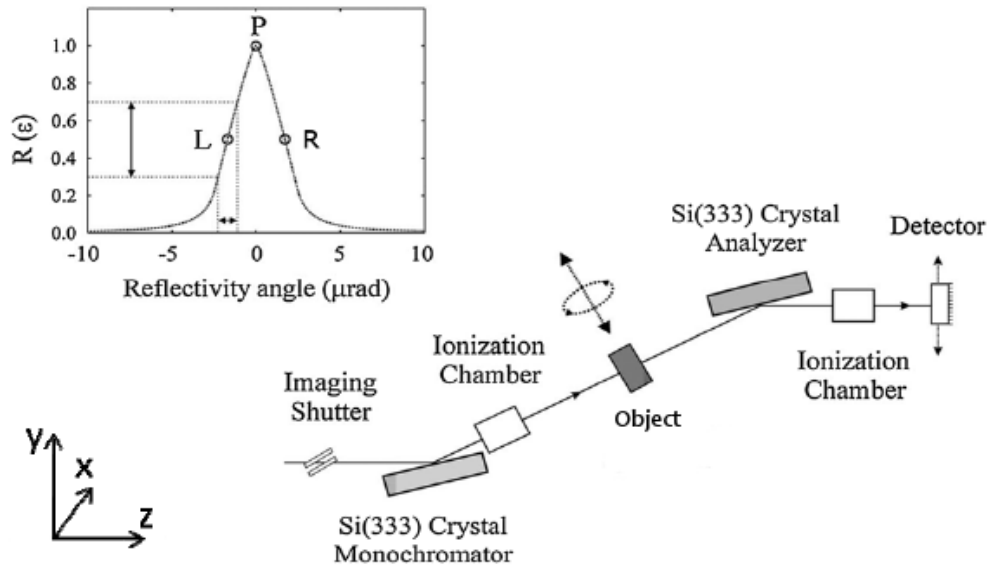


Figure 1.1: Schematic diagram of an ABI set-up. The diffraction optics includes a monochromator and an analyser crystal. The graph shows the reflectivity curve, $R(\epsilon)$, of a silicon crystal 333 (Si 333) reflection at 30 keV and the principle of the analyser-based X-ray imaging method. The reflectivity curve demonstrates the conversion between the angular X-ray deviations (horizontal axis) and the intensity changes (vertical axis), as shown by the arrows. P, L, and R indicate the peak, left-angle, and right-angle positions on the reflectivity curve, respectively. The system of coordinates used is the same considered in all this work. Image from Keyriläinen et al 2008.

The AC (figure 1.1) acts as an angular filter selectively accepting only the photons satisfying the Bragg law for diffraction $2d \sin \theta_g = \lambda$, where d is the crystal d-spacing, θ_g is the grazing angle of incidence to the crystal and λ the radiation wavelength. A narrow range of X-rays can reach the detector and contribute to

the image formation (Podurets et al. 1989; Bravin 2003). The monochromator and analyser form a non-dispersive pair of crystals, where the reflecting planes are parallel.

The Rocking Curve (RC) of the AC, that represents the filter function, actually corresponds to the convolution of the monochromator and analyser reflectivity curves. It presents an angular acceptance (given by the RC Full-Width at Half Maximum, FWHM) of a few μrad or tens of μrad , (for example 1.4 μrad for Si(333) at 52 keV).

Two different AC configurations are possible: Bragg geometry (Förster et al. 1980; Somenkov et al. 1991; Chapman et al. 1996; Bushuev et al. 1997) or Laue geometry (Ingal & Beliaeskaya 1995; Chapman et al. 1996).

The parameters that influence the image contrast are the RC width of the analyser, the crystal composition and quality, the X-ray energy, the X-ray divergence and the diffraction order. After setting up all these parameters, the image contrast ultimately depends on the angular position of the AC with respect to the Bragg angle corresponding to the energy of the X-ray beam impinging on the sample. Due to the presence of the AC, the ABI technique is sensitive to angular deflections caused by the X-ray refraction within the object only in the direction parallel to the crystal diffraction plane (please refers to figure 1.1 for the coordinate system):

$$\Delta\alpha \simeq -\frac{\lambda}{2\pi} \frac{\partial\phi(x, y; \lambda)}{\partial y} \quad (1.15)$$

Under the geometrical optics approximation and considering a slowly varying function over the length scale on the order of the crystal extinction length, it is possible to express the intensity on each detector pixel as (if the crystal diffraction plane is assumed to be parallel to the (x, y) plane):

$$I_{ABI} = M^{-2} M_{asym} I_0 TR(\theta_{an} + \Delta\alpha) \quad (1.16)$$

where M is the magnification due to the divergence of the beam, M_{asym} is applied in case of asymmetric cut of the AC and θ_{an} is the angular deviation of the AC from the Bragg angle.

Several algorithms have been developed for separating the different contribution to the image signal. The most common algorithms are: the Diffraction Enhanced Imaging (DEI) method (Chapman et al. 1997; Zhong et al. 2000), the Extended-DEI (Maksimenko 2007; Hu et al. 2008), the Generalized-DEI (Chou et al. 2007; Rigon et al. 2007), the Multiple image Radiography (MIR) algorithm (Pagot et al. 2003; Wernick et al. 2003) and the Gaussian curve fitting (GCF) procedure (Nesterets et al. 2006). New mathematical methods for image processing that deal more specifically with ultra-small-angle scattering (USAXS) have been recently introduced by (Oltulu et al. 2003; Pagot et al. 2003; Rigon et al. 2003; Wernick et al. 2003).

Other procedures have been instead proposed for quantitatively computing mass-density maps from refraction-angle images (Hasnah et al. 2005, Wernick et al. 2006; Gasilov et al. 2013).

However the exploitation of simply ABI images recorded at different angular positions of the analyser can alone provide qualitative important information on the sample/tissue (Sztrókay et al. 2012).

The image formation in ABI can be described using two different approaches:

- **Geometrical optics (GO) approach:** the ray tracing of the radiation from the source to the detector can be performed by calculating the refraction angle (point by point) in the sample and by weighting the intensity of the refracted X-ray by the RC of the AC calculated at the point $\theta + \Delta\alpha$, where θ is the analyzer angular position and $\Delta\alpha$ is the refraction angle. This approach gives results in good agreement with the experimental data for simple objects (Keyriläinen et al. 2002; Rigon et al. 2002).
- **Wave optics approach:** in this approach less stringent assumptions have to be considered (Bushuev et al. 1997), for that reason more precise results are provided. The use of the *Takagi-Taupin* equations to compute the intensity of the electric field outgoing a crystal is necessary for perfect and flat or cylindrically bent crystals; in these cases the equations even have analytical solutions (Authier 2001).

The general limits of utilization of the two approaches have been identified by differentiating the case of an area contrast (the image contrast far from the object edges, where weak phase variation occur) from the case of the edge contrast, occurring at the interfaces between different materials (Gureyev & Wilkins 1997).

1.3.3.1 Theoretical description of ABI

The theoretical description of the ABI technique is based on the dynamical diffraction theory for perfect crystals (Zachariasen 1945; Authier 2001). In the following we consider the case of a thick, non-absorbing crystal set in symmetrical Bragg geometry and we neglect all propagation effects.

The coordinate system is the one shown in figure 1.1; the axis z is the X-ray propagation axis while the plane (y, z) is the AC diffraction plane.

Let us consider a monochromatic plane wave with unitary amplitude, incident onto the sample which is placed upstream the AC (figure 1.1). The wave incident onto the crystal is given by:

$$\Psi_{obj}(x, y) = \Psi_{in}(x, y)T(x, y) = \Psi_{in}(x, y)\exp[i\phi(x, y) - B(x, y)] \quad (1.17)$$

The amplitude of the wave diffracted by the AC can be expressed by means of a convolution integral as:

$$\Psi_{an}(x, y; \theta_{an}) = \int_{-\infty}^{+\infty} dy' G(y'; \theta_{an}) \Psi_{obj}(x, y - y') \quad (1.18)$$

where $G(y'; \theta_{an})$ is the Point Spread Function (PSF) of the AC and θ_{an} is the angular deviation of the crystal from the Bragg position θ_B . The convolution is performed only in one direction (*i.e.* the direction of the sensitivity of the crystal). In the Fourier space eq. 1.18 becomes:

$$\tilde{\Psi}_{an}(x; v; \theta_{an}) = r(\theta_{an} + \lambda v) \tilde{\Psi}_{obj}(x; v) \quad (1.19)$$

where v is the spatial frequency coordinate corresponding to y , $\tilde{\Psi}_{obj}$ and $\tilde{\Psi}_{an}$ are the forward Fourier transform of the complex amplitudes of the waves incident onto and diffracted from the AC, respectively. The amplitude reflection coefficient of the AC is represented by $r(v; \theta_{an})$, which is equivalent to the forward Fourier transform of the analyser PSF: $r(\theta_{an} + \lambda v) = \tilde{G}(v; \theta_{an})$. The function $r(v; \theta_{an})$ that represents the transfer function of the analyzer is also called *Takagi propagator*.

In the case of a semi-infinite perfect crystal, the crystal amplitude reflection coefficient can be expressed analytically (Afanas'ev & Kohn 1971) as:

$$G_{\infty}(y, \theta) = i \frac{\sigma_h}{\sigma} \exp(i\alpha\eta y) \frac{J_1(2\alpha\sigma y)}{y} H(y) \quad (1.20)$$

where J_1 is the Bessel function of the first kind and first order, H is the Heaviside step function, $\alpha = \gamma^2 / \sin(2\theta_B)$, with $\gamma = \sin(\theta_1)$, θ_1 is the angle between the wavevector \vec{k} of the incident wave and the perfect crystal surface, $\eta = 2\sigma_0 + k\gamma\theta_{an}/\alpha$, $\sigma^2 = \sigma_h\sigma_{-h}$, $\sigma_0 = \pi\chi_0/(\lambda\gamma)$, $\sigma_{\pm h} = \pi C\chi_{\pm h}/(\lambda\gamma)$, $\chi_{0,\pm h}$ are the Fourier components of the crystal susceptibility and C is the polarization factor.

The crystal amplitude reflection coefficient can be then expressed as:

$$r_{\infty}(\theta) = \begin{cases} \frac{\sigma_h}{\xi_1}, & \text{Im}(\xi) < 0 \\ \frac{\sigma_h}{\xi_2}, & \text{Im}(\xi) < 0 \end{cases} \quad (1.21)$$

where $\xi_{1,2} = (-\eta \pm \xi)/2$ and $\xi = (\eta^2 - 4\sigma^2)^{1/2}$.

To simplify eq. 1.18 and to find an analytical solution for the inverse problem of calculating the absorption and phase related properties of the object from the intensity recorded on the detector, different approximations have been proposed. The most common methods are based on the GO approximation. Other methods based on the weak object approximation (Nesterets et al. 2004; Nesterets et al. 2006) and on the linear transfer function approximation (Paganin et al. 2004; Pavlov et al. 2004) have also been developed.

The weak object assumes that the variations in the object absorption are weak and that the phase is either weak or slowly varying across the characteristic length scale of the system PSF (*i.e.* on the length scale of the crystal extinction length). Under these assumptions, the object complex transmission function (eq. 1.17) can be safely linearized (Nesterets et al. 2004).

Using the linear transfer function approach, the imaging system transfer function is linearly approximated under the assumption that the spatial Fourier spectrum of the wave incident onto the analyser is non-negligible over a frequency range for which the amplitude reflection coefficient of the analyser is well approximated by a linear function (Paganin et al. 2004; Pavlov et al. 2004).

In the GO approximation (Gureyev & Wilkins 1997; Bushuev et al. 1998) the condition of validity is that the phase of the wave incident onto the crystal is a slowly varying function over a length scale which is in the order of the crystal extinction length; this is equivalent to:

$$N_T = (h/\lambda)^2 \left| \frac{r(\theta_{an})}{r''(\theta_{an})} \right| \gg 1 \quad (1.22)$$

where h is the size of the smallest feature in the object or the resolution limit of the imaging system if this is larger, and $r''(\theta_{an})$ denotes the second derivative of the Takagi propagator, the term N_T is called *Takagi number*. More complex formulations of the Takagi number taking into account the quasi-monochromaticity and divergence of the beam, the source size and the detector resolution have also been derived (Nesterets et al. 2006; Kitchen et al. 2007). If the condition in eq. 1.22 is satisfied, eq. 1.18 can be approximated, by using the stationary phase method (Gureyev & Wilkins 1997), as:

$$\Psi_{an}(x, y; \theta_{an}) = r \left(\vartheta_{an} - k^{-1} \frac{\vartheta \phi(x, y)}{\vartheta y} \right) \Psi_{obj}(x, y) \quad (1.23)$$

Using eq. 1.15 for the refraction angle and taking the square modulus of eq. 1.23, the intensity of the diffracted wave at a point (x, y) onto the detector plane can be related to the intensity of the wave exiting the sample at a corresponding point in the plane object:

$$I(x, y; \theta_{an}) = I_T(x, y) R_{an}[\theta_{an} + \Delta\alpha(x, y)] \quad (1.24)$$

where I_T represents the intensity transmitted through the object and R_{an} is the reflectivity curve of the crystal. R_{an} corresponds to the square modulus of the *Takagi propagator*: $R_{an} = |r(\theta)|^2$. Normally, in an experimental case, one or more crystals need to be used before the object for collimation/monochromatization purposes. However the beam illuminating the object is not perfectly monochromatic and parallel (a small degree of polychromaticity and divergence is always present), which depends on the used crystals and on the chosen reflections. By indicating with $d_i(\theta')$ the intensity

distribution of the beam incident on the first monochromator crystal, such that $I_i(x, y) = \int_{\theta_{min}}^{\theta_{max}} d\theta' d_i(x, y; \theta')$, where θ' is the detuning angle from Bragg condition and $I_i(x, y)$ is the integral intensity incident on the first monochromator crystal, the following expression can be written for the intensity distribution $d_0(\theta')$ incident onto the object:

$$d_0(x, y; \theta') = d_i(x, y; \theta') \prod_{j=1 \dots N} R_j(\theta') \quad (1.25)$$

where $\prod_{j=1 \dots N} R_j(\theta')$ indicated the product of the reflectivity curves of the N used monochromators. The integrated intensity incident onto the object can be calculated as:

$$I_0(x, y) = \int d\theta' d_i(x, y; \theta') \prod_{j=1 \dots N} R_j(\theta') = d_i(x, y; \theta' = 0) \int d\theta' \prod_{j=1 \dots N} R_j(\theta') \quad (1.26)$$

where it is assumed, in the second equation, that the intensity distribution is constant over the narrow angle range where the reflectivity of the crystal is non-negligible.

We can rewrite eq. 1.24 in the case of a quasi-monochromatic and slightly divergent beam, to express the intensity of the wave diffracted by the analyser as a function of the intensity of the wave exiting the object as:

$$I(x, y) = I_T(x, y) R(\theta_{an} + \Delta\alpha(x, y)) \quad (1.27)$$

where R is the analyser RC, *i.e.* convolution of the reflectivity curves of the AC and of the monochromators. R is defined as the ratio between the intensity diffracted by the analyser and the intensity incident on it:

$$R(\theta) = \frac{\int d\theta' d_i(\theta') (\prod_{j=1 \dots N} R_j(\theta')) R_{an}(\theta - \theta')}{\int d\theta' d_i \prod_{j=1 \dots N} R_j(\theta')} \quad (1.28)$$

Eq. 1.27 can be reduced to eq. 1.24 in the ideal case of a perfectly parallel and monochromatic beam incident onto the first monochromator, that is $I(\theta') = \delta(0)$, where $\delta(0)$ is the Dirac delta function centered on the Bragg angle.

Using the GO approximation it is possible to relate in a simple way the intensity recorded by the detector to the intensity transmitted through the sample. In particular, under this approach and for a given orientation of the analyser, the intensity recorded at a point (x, y) on the detector depends only on the absorption and refraction introduced at the corresponding point (x, y) in the object. Eq. 1.27 represents the starting point of various extraction algorithms that are based on the GO approximation and aim at solving the inverse

problem of calculating the absorption, refraction and scattering related properties of the object from the recorded ABI images.

1.3.3.1.2 The phase filtering and amplitude modulation properties of the analyzer crystal

The X-rays impinging onto the AC and satisfying the Bragg law are diffracted with an intensity modulated by the RC. Different mechanisms are at the basis of the image contrast formation:

- The phase of the waves with negative spatial frequencies is shifted by 180° . This fact results in the **inverted contrast behavior observed at opposite angular positions of the AC**.
- X-rays coming with angular deviations that are outside the small analyser angular acceptance window cannot be diffracted and do not contribute to the image formation. These missed scattered X-rays appear in the diffraction images as absorbed X-rays, generating the so-called ‘**extinction contrast**’. These rays are always contributing to the blurring of the details in conventional images. When the AC is set at the angle corresponding to the peak of the RC, it diffracts the unrefracted X-rays with full efficiency and the images appear almost scatter-free (only the small-angle scattering at angles within the RC width can reach the detector).
- When the AC is set at one of the slopes of its RC, the intensity of the X-ray beam diffracted by the AC is changed by the refraction in the sample, giving rise to the ‘**refraction contrast**’.
- By moving the AC far off the Bragg angle, inverse contrast is observed: the AC rejects the unrefracted X-rays whereas the scattered ones are recorded and contribute to the image formation (Zhong et al. 2000). For samples producing a very large amount of small angle scattering (sponge-like tissues, for instance) this case is very interesting for a high visualization of the details (Arfelli et al. 1999).

1.3.3.1.3 Beam and resolution requirements

- In order not to lose too many X-rays from the incoming beam, X-rays incident on the sample have to be monochromatic with a typical $\Delta E/E \sim 10^{-4}$ (E is the X-ray energy) of a perfect crystal, with a divergence in the diffraction plane that has to be smaller than the angular deviations to be detected. However no particular restrictions have to be fulfilled by the beam arriving on the monochromator since the ABI set-up itself generally warrants the necessary beam collimation and coherence. The advantage of the synchrotron radiation for the implementation of this technique mainly resides in

the optimization of the delivered photon flux given the unavoidable loss of photons occurring in the monochromator/analyser diffraction process.

- The presence of the AC intrinsically affects the spatial resolution of the technique. In the GO description, a point of the image corresponds to an angularly deviated X-ray from a given point of the projected object. When diffraction effects occur, anyway, either in a perfect or an imperfect crystal, the notion of wavefields which have definite propagation direction in the direct space breaks down (Authier 2001). Under the effect of an external field (incident X-rays), a perturbed electron density is developed in the crystal and it is the propagation of this perturbation that is associated with the electromagnetic wave in the crystal. In this dynamical approach, the relationship between the value of the amplitude and phase distribution at any point of the exit surface of the crystal is obtained by convolution of the Green-Riemann function (or influence function) with the amplitude and phase distribution at the entrance surface, expressed as a distribution of point sources (Pinsker 1978; Förster et al. 1980; Authier 2001). If the dynamical diffraction fringes are not disentangled, the resolution is limited to the width of the influence function, whose value (of the order of some μm) depends on the reflection geometry (Laue or Bragg geometry) and on the used photon energy.
- The effect of the finite resolution of the detector and of the finite size of the source can be considered by convoluting the signal with the PSF of the detector and with the source distribution function. Moreover, image magnification is achievable in the diffraction plane by utilizing asymmetric crystals.
- It is preferable to reduce as much as possible the analyser-to-detector distance to reduce the Fresnel diffraction occurring in the path between the sample and the detector, affecting the spatial resolution of ABI images. However, this typically undesirable effect has been demonstrated to be able to produce a signal to noise improvement in specific experimental conditions (Coan et al. 2005). Theoretical investigations on this subject have been realized by Pavlov *et al.* (Pavlov et al. 2004) and Bravin *et al.* (Bravin et al. 2007).

1.3.3.1.4 ABI sensitivity and optics

The width of the analyser RC strongly affects the sensitivity of the ABI technique: narrower is the curve width, higher is the extinction and refraction contrast. Phase sensitive techniques, as previously discussed, present advantages at X-ray energies higher than those used in conventional absorption X-ray imaging; this result is due to the weaker energy dependence of the $\delta (E^{-2})$ term with respect to $\beta(E^{-4})$. Among the others, the ABI technique particularly benefits from high energies since the RC width for a given crystal

reflection decreases linearly with increasing energy, and this partially compensates for the E^{-2} phase effect behaviour (Rigon et al. 2002; Bravin 2003). As a consequence, the ABI effectiveness is proportional to E^{-1} .

- **The width of the RC determines the sensitivity of the method.** Narrower RC can be achieved either by using higher X-ray energies or by choosing higher crystal reflections (Chapman et al. 1997; Zhong et al. 2000; Rigon et al. 2002). For instance, the use of the (333) reflection at 20 keV produces a RC which is about five times narrower than the one of the (111) reflection. Therefore, the associated improvement in refraction contrast can be 5-fold.
- Protopopov *et al.* (Protopopov et al. 2002) proposed the use of a special kind of multilayer mirror to analyse the refracted X-ray beam (technique referred as "**dark field**" imaging). For a given energy, the reflectivity curve of this multilayer has a resonant dip that is few μrad wide. If the multilayer is used as AC, it shows a minimum reflectivity for an unrefracted X-ray beam and, therefore, it acts as a perfect crystal with an 'inverse' RC. The advantage of this set-up consists in the rejection of the direct beam, with only the pure refraction information being kept.
- Ando *et al.* (Ando et al. 2001) proposed a different version of dark field imaging. The set-up in this case consisted in an asymmetric monochromator, a monolithic optics comprising a collimator and an analyser, with the sample in between.
- Other optics implementations include the **use of an asymmetric crystal as analyser**. The main advantage is the possibility of expanding the incident X-ray laminar beam in the diffraction plane. For small samples, this set-up does not require the translation of the sample, which typically may introduce blurring artefacts.

1.3.3.2 Propagation based imaging

The propagation-based imaging (PBI) is experimentally the simplest way to visualize the phase-contrast (figure 1.2). The absence of optical elements implies that such technique is intrinsically free from the usual aberrations, with achievable resolution depending largely, but not entirely, on the size of the source (Pogany et al. 1997; Arhatari et al. 2004) and on the imaging detector spatial resolution.

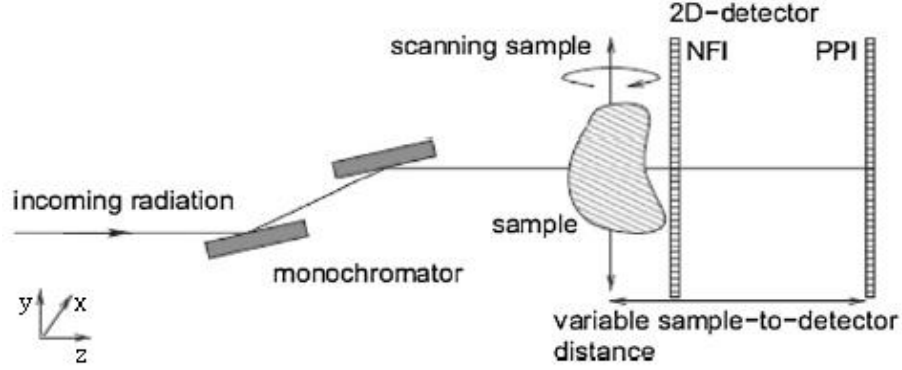


Figure 1.2: The experimental set-up of the propagation-based imaging technique. A, transversally coherent X-ray fan beam traverses the sample, and is recorded by a 2D detector positioned at a certain distance. Changing the propagation distance generates different signals on the detector, allowing investigating different spatial frequencies. The choice of the distance is related to the kind of study of interest. Image from Keyriläinen et al 2010.

When a coherent wave-front traverse the sample and the distorted wave-front propagates sufficiently far the occurred interference gives rise to a characteristic pattern that is then recorded by a detector placed at a convenient distance (Snigirev et al. 1995; Cloetens et al. 1996). Thanks to the Fresnel diffraction, the phase shifts are therefore transformed in detectable intensity variations (Born & Wolf 1999).

The PBI phase-contrast signal has an important dependence on the distance d between the sample and the detector. Three different regimes may be distinguished (Snigirev et al. 1995) varying z and considering the transverse characteristic length scale t of the object and a monochromatic plane wave: the contact regime characterized by $d \simeq 0$ (absorption regime); the near field diffraction regime when $r_F = \lambda d \leq t^2$, where r_F represents the radius in the object plane of the so-called first Fresnel zone (edge detection regime); the far field regime when $r_F = \lambda d > t^2$ (Fraunhofer regime).

The intensity recorded by the detector can be expressed in the near-field regime by the transport of intensity equation (TIE). The approximation of near-field regime is valid only for sufficiently small propagation distances and for an object inducing a slowly phase shift in the plane (x, y) , transversal to the optical axis z . Under these two assumptions the TIE can be expressed as:

$$I_{PBI} = M^{-2} I_0 T \left(1 - \frac{\lambda D}{2\pi} \nabla^2_{\perp} \phi \right) \quad (1.29)$$

where $M = (r + l)/l$, with l being the source-to-sample distance, is the magnification factor which takes into account the beam divergence; I_0 indicates the intensity incident onto the object; T is the object transmission; $d = r/M$ is the so-called defocusing distance and ϕ is the phase shift introduced by the object. It is possible to notice that under these approximations, the intensity modulation is proportional to the Laplacian of the phase shift.

Since at every propagation distance there are frequency components of the object that do not contribute to the image, the retrieval of the phase cannot be simply performed with a single image without strong constraints on the object characteristics (Gureyev et al. 2004). A way to retrieve the phase is to acquire several images at variable distances and suitably combine them (Cloetens 1999). Recently Paganin reported a method to retrieve the phase using a single defocused distance in homogenous (Paganin et al. 2002) and in multi-material objects (Beltran et al. 2010). Algorithms for quantitatively phase-retrieval may be based on the Fresnel approximation of the Kirchoff diffraction formula (Op de Beeck et al. 1996) or on the TIE equation (Gureyev et al. 1999).

The X-ray beam has to be (partially) laterally coherent and quasi-monochromatic. The first condition, linked to the angular source size, is the more stringent in the case of the PBI technique and it is easily fulfilled by using synchrotron sources or microfocus X-ray tubes with source size of the order of 10 to 20 μm . With a classical laboratory X-ray source, the effect of the finite size of the source consists in the blurring of the interference pattern. The degree of monochromaticity of the beam is instead less important as proven by Wilkins who obtained PBI images even with a polychromatic spectrum generated by a conventional micro-focus X-ray tube (Wilkins et al. 1996).

1.3.3.3 Grating interferometry

Grating-based imaging (GI) or X-ray Talbot interferometry is an X-ray PCI technique based on the use of grating interferometers. Since the first X-ray grating interferometer consisting of two phase gratings and an AC (David et al. 2002) was built, various slightly different setups have been developed. Nowadays the standard method consists of a phase grating and an analyser grating (Momose 2003). The technique is based on an optical phenomenon discovered by H.F. Talbot in the 1830s (Talbot 1836). The image of the grating is repeated at a regular distance behind the grating: $d_T = 2p^2/\lambda$, where p is the period of the grating.

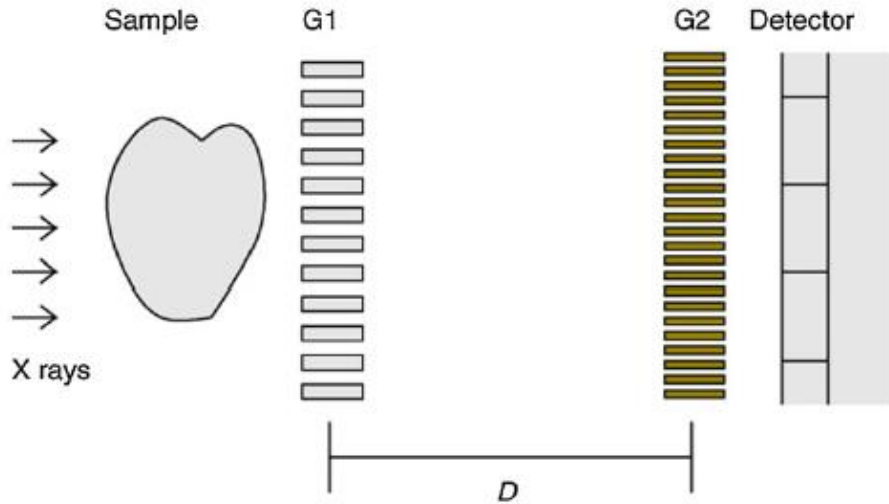


Figure 1.3: Schematic set-up of GI. A pattern of X-ray interference fringes is formed downstream a linear diffraction grating G1 (beam splitter); its local distortions from its ideal regular shape contain information on the sample structure. Since the fringes are too closely spaced to be resolved by the pixel detector used to record images, an additional absorption grid (G2, analyser grating) in front of the detector is needed to transform fringe-position information into intensity values on the detector pixels. Image from Weitkamp et al 2008.

The interference pattern is modified by the presence of the sample, due to its X-ray absorption, refraction and scattering. The angular deviations result into changes of the locally transmitted intensity. These changes in position of the interference pattern can be retrieved by performing measurements with and without the sample. To resolve the period of the interference pattern (few micrometers of range) high resolution detectors in combination with high flux sources are required, which limits significantly the field of view (Takeda et al. 2007). For this reason a second grating, typically an absorption grating, is placed at a fractional Talbot length to analyse the interference pattern (Momose 2003).

Two methods exist to separate the different contributions to the signal: the technique called “phase-stepping” (Weitkamp et al. 2005) and the approach which uses the Moiré fringes (Momose 2003). These two methods can be used in both planar and tomographic mode and allow reconstructing the real and imaginary part of the refractive index (Weitkamp et al. 2005; Momose et al. 2009). The dark field signal (scattering component of the signal) can be reconstructed as well using the phase-stepping technique (Bech et al. 2010) and the Moiré pattern (Bevins et al. 2012).

A good spatial coherence of the X-ray beam is required. To overcome this problem, for instance when using conventional X-ray tubes, a third grating (known as Talbot-Lau interferometer) can be added close to the X-ray source.

The grating interferometer in phase-stepping configuration can be used efficiently with polychromatic radiation because the position of the interference fringes formed behind the source grating is independent of the wavelength over a wide X-ray energy range (Weitkamp et al. 2005). Using the Moiré pattern

configuration only a moderate polychromaticity is allowed because the use of a finite bandwidth of energy decreases the visibility of the Moiré fringes and thus the image quality (Momose et al. 2006).

1.3.3.4 Edge-illumination or Coded aperture imaging

The Coded aperture (CA) imaging or Edge Illumination (EI) method has been developed recently by Olivo *et al.* (Olivo et al. 2001; Olivo & Speller 2007) and it is based on the use of coded apertures. The principle at the basis of this method is that the phase sensitivity of an imaging system can be strongly enhanced by illuminating only the edge of the active surface of a detector pixel, with a small fraction of the beam cross section falling outside the pixel edge itself (Olivo & Speller 2007).

The setup (figure 1.4) consists in pre-sample coded apertures and post-sample coded apertures. The pre-sample coded aperture (sample mask) is placed immediately before the sample; it creates an array of individual beams each one impinging the edge of the detector pixels, as defined by the post-sample coded apertures. The post-sample coded aperture system (detector mask) is placed in contact with the detector. Its purpose is to create totally insensitive regions along the separation between adjacent pixel rows. The sample mask prevents unnecessary radiation from traversing the sample, thus ensuring efficient dose delivery.

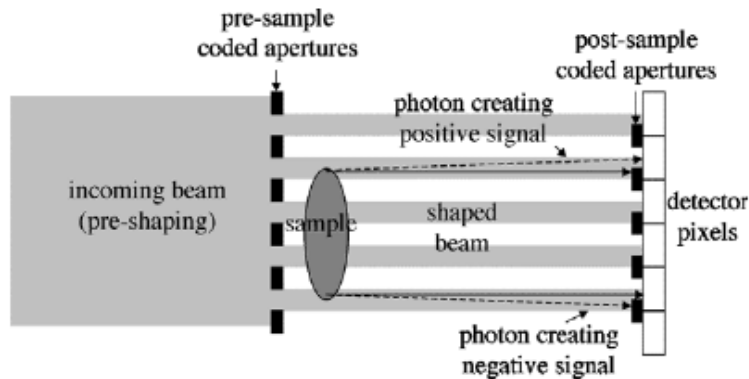


Figure 1.4: schematic of the concept of the coded-aperture imaging technique. Image from Olivo et al, 2007.

Photons, which normally would not hit the detector active surface, can be deviated inside it, as a consequence of the interaction with the sample; this leads to an increase in the number of counts. In the same way photons originally impinging immediately inside the detector active surface can be deviated outside it, with a consequent reduction in the number of counts. Thanks to these effects, negative and positive peaks are generated in the acquired signal, with results very similar to the ones obtained with the ABI technique. The reduction of the beam cross section hitting the active surface of the detector results in a strong increase of the system sensitivity, again in a similar way as in ABI when the AC is rocked off,

progressively, its Bragg position. The analogies with the ABI were more recently formally demonstrated (Munro et al. 2013).

The absence of crystal means that this technique can be implemented with divergent (by scaling down the sample mask dimensions in order to take the beam divergence into account) and polychromatic beams, like those generated by a conventional rotating-anode X-ray tube. The EI technique can be used in the laboratory practice, substituting the sample scanning normally performed using the Synchrotron Radiation (SR), with a detector with a proper area.

Due to the plurality of individual beamlets, no scanning of the sample through a 2D beam is required. The sample is instead placed downstream of the sample mask and imaged with a single shot, or two if the phase-retrieval is performed (Munro et al. 2012).

The EI technique seems promising and suitable for overcoming some of the major limitations of other PCI methods. For instance, in the case of ABI, a significant fraction of the radiation is absorbed in the crystal after having crossed the sample, with a consequent reduction of the dose efficiency. A similar problem is encountered with the grating interferometer method, because of the presence of grating elements downstream of the sample. The described system is sensitive to phase effects in one direction only (*i.e.* upward/downward photon deviation only if pixel rows are used, and left/right deviation with pixel columns).

The EI differs from the grating interferometric method, because the individual beams defined by the sample mask are separated by a distance of the order of half pixel or more (tens of μm), and thus do not interfere with each other.

The thickness of the mask can be kept smaller than the aperture dimension, with a consequence that almost no angular filtering is applied to the radiation beam. Assuming a typical fill factor of 50% for the sample mask, the technique imposes an overall increase in the exposure time of about 2 in order to achieve the same statistics on the detector.

The method has been successfully demonstrated in areas such as security scanning (Ignatyev et al. 2011), biological imaging (Zhifeng et al. 2007; Marenzana et al. 2012), material science (Endrizzi et al. 2013), paleontology (Olivo et al. 2012). The adaptation to CT was also demonstrated (Diemoz et al. 2013).

1.3.3.5 Comparison between the PCI techniques

Technique	Pros	Cons
ABI	<ul style="list-style-type: none"> -Suitable for large range of energies (20-100 keV). -Large field of view of the AC (up to 15 cm). -The problems of stability of the AC are solved by using fast reacting feedback systems. -One single image may be diagnostically meaningful (Sztrókay et al. 2012). 	<ul style="list-style-type: none"> -Strong requirements in terms of X-ray beam properties (intense and monochromatic X-rays) -To separate the different contributions to the signal, two or more images acquired at different position of the AC RC are required.
PBI	<ul style="list-style-type: none"> -Simple method, no additional X-ray optics is required. -The technique shows a weak sensitivity to the beam spectrum and it works also with polychromatic beams. -The beam divergence and size are not limiting factors. -One single image may be diagnostically significant (Beltran et al. 2010). -Sensitivity along 2 directions. 	<ul style="list-style-type: none"> -Limitation in the source size to guarantee a good spatial coherence and thus edge signal enhancement (high degree of spatial coherence is required). -Sufficient distance sample to detector is required.
GI	<ul style="list-style-type: none"> -Field of view up to ~5 cm, but the actual technology may cover large fields. -Demonstration of the applicability of the technique using conventional X-ray tubes. 	<ul style="list-style-type: none"> -The technique covers a narrow energy spectrum. In order to use the method at different energies different sets of grating are required. -Difficulties in the fabrication of gratings because of the small pitch (in the micron scale) -For fast imaging a sufficiently coherent source is required to avoid the usage of a third (source grating) -To separate the signals 3 or more images are required.
EI	<ul style="list-style-type: none"> -Requirements of beam monochromaticity and longitudinal coherence are among the weakest (Munro et al. 2010). -High energy imaging (energies close to 100 keV) has been demonstrated (Olivo et al. 2012) 	<ul style="list-style-type: none"> -The technique is still at an early stage.

Table 1.1: Comparison between the PCI techniques.

1.3.4 Recent state of art of phase-contrast imaging for breast tissue

Over the last years several works have been published on the application of PCI techniques to the study of biological tissues. According to the theoretical predictions the published works show a considerable increase in the image contrast for such tissues compared to conventional absorption imaging. A review of

some of the most relevant studies concerning the breast is reported in this section. Imaging of the breast has been one of the first applications of X-ray PCI (Pisano et al. 2000; Arfelli et al. 2000). An extensive review on PCI mammography has been provided recently (Coan et al. 2013). The most used techniques for breast imaging are so far PBI and ABI. PBI has been used in planar mode, for comparison with the clinical absorption-contrast mammography. The improved contrast on excised breast samples has been demonstrated Arfelli *et al.* (Arfelli et al. 1998; Arfelli et al. 2000). These studies have led to the first clinical trials performed at the ELETTRA SR facility in Trieste, Italy (Castelli et al. 2007; Castelli et al. 2011). It was concluded that the PBI with SR is successful in the challenging case of clarifying diagnoses of questionable or suspicious breast anomalies detected via digital mammography. The comparison between digital mammography and SR PBI is shown in figure 1.5.

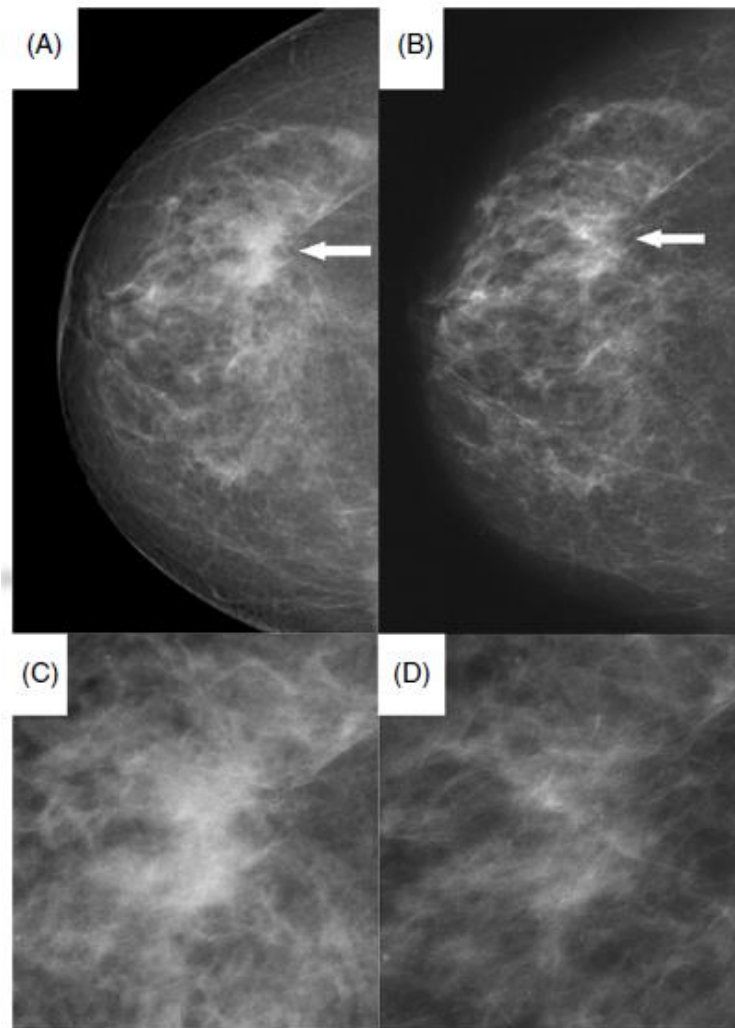


Figure 1.5: PBI images of right breast in 60-year-old woman with suspicious mass identified at DM. (a) Craniocaudal DM image and (b) corresponding digital zoom image show mass with architectural distortion (arrow) (BI-RADS category 4) in upper outer quadrant. (c) Findings on SR mammographic

image and (d) corresponding digital zoom image do not confirm any suspicious breast masses (BI-RADS category 1). Imaging follow-up findings did not confirm any breast lesion. Image from Castelli et al 2011.

Studies comparing clinical radiographies of thick excised human samples with ABI mammograms using laboratory X-ray sources have been reported (Parham et al. 2009) showing that high contrast images can be obtained at very low doses. Several studies suggest that ABI-CT may provide a “histo-pathology” both in partial (Keyriläinen et al. 2008) and in full and large (15 cm of diameter) breasts (Sztrókay et al. 2012). The radiation doses used to acquire the CT images on portions of excised human breast in the work of Keyriläinen (Keyriläinen et al. 2008) and in the case of a full breast (Zhao et al. 2012, within this PhD Thesis) are comparable with those used in a dual-view digital mammography (Mean Glandular Dose ~2 mGy). A histological section and the ABI-CT image of a same breast tissue are overlaid in figure 1.6.

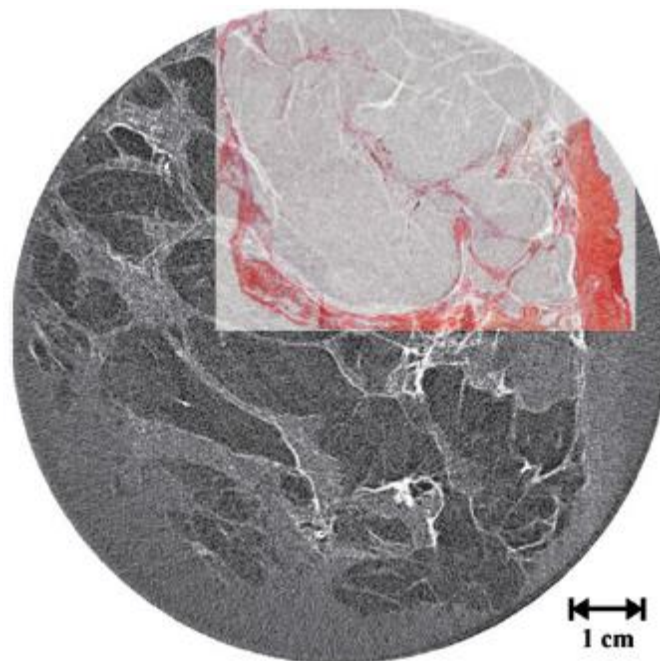


Figure 1.6: ABI-CT peak image of a 30 mm thick human breast tissue specimen with multifocal lobular carcinoma, obtained at 30 keV and with a mean glandular dose of 1.9 mGy. The ABI image is shown with an overlaid (50% transparent) optical image of the histopathologic whole-mount slide on the right upper quadrant of the specimen (Herovici stain; original magnification X1). The mature collagen appears red, and adipocytes appear white. Image from Keyriläinen et al 2008.

The variant of ABI where non-deviated and refracted beams are separated by a thin Laue-type crystal is presented in Ando (Ando et al. 2008) to image a small sample of breast tissue with ductal carcinoma *in situ*. The GI method has been used for studies performed on freshly dissected mastectomy samples and the obtained planar images have been compared with the conventional techniques (Stampanoni et al. 2011). The Mean Glandular Dose was 26 mSv, but with possibility of reductions. By combining absorption,

refraction and scattering images a better detection of mammographic signs are obtained, especially in case of dense breast tissue.

Dark signal (scattering) images revealed scar tissue and associated cancer invasion. It has been proved that an increase of the Small Angle X-ray Scattering signal arises from malignant changes in granulation and in the fibrous collagen structures (Fernández et al. 2005; Fernández et al. 2008). Due to the high radiation dose delivered with this technique, it could be used on biopsied to provide decisive information for breast cancer diagnosis.

Chapter 2 - Experimental setups and equipment

2.1 Introduction to synchrotron radiation	46
2.1.1 Synchrotron radiation sources.....	46
2.1.1.1 Radiofrequency cavities.....	47
2.1.1.2 SR beam characteristics	48
2.2 The European Synchrotron Radiation Facility and the biomedical beamline (ID17)	49
2.3 Description of the experimental setups.....	51
2.4 ID17 Image acquisition equipment.....	56

2.1 Introduction to synchrotron radiation

The electromagnetic radiation emitted from charged particles travelling at quasi-relativistic speed in a magnetic field is called Synchrotron Radiation (SR). In the case of sufficiently high electron energies and magnetic field, the emitted radiation can lie in the X-ray region of the electromagnetic spectrum. This phenomenon was observed the first time in 1947 at the General Electric synchrotron in the USA (Elder et al. 1947). At the beginning this phenomenon was considered as a nuisance, but successively in the 1960s, the important properties like the high brightness, a wide energy spectrum and the high polarization of this radiation were recognized.

The major applications of synchrotron light are in the field of condense matter physics, in the material science, in biology and in medicine. Currently the top most powerful synchrotrons are the Advanced Photon Source in the USA, the European Synchrotron Radiation Facility in France and the SPring-8 facility in Japan.

2.1.1 Synchrotron radiation sources

The ring tube consists of straight sections and curved sections (figure 2.1a). Inside the tube a state of ultrahigh vacuum is kept (10^{-13} atmospheres). In the straight sections special insertion devices (ID), *i.e.* *undulators* and *wigglers* are installed. Many experiments can be supported simultaneously thank to the presence of multiple emitting devices.

Electrons are produced, pre-accelerated and injected into the storage ring by a device called *injector* that can be either a synchrotron or a linear accelerator (LINAC). In the storage ring, electrons are kept circulating and their trajectories are periodically deflected by the bending magnets (figure 2.1a), which consist in big dipole electromagnets placed in the curved sections of the ring. The Lorentz force acting on the electrons is responsible of the deflection of their trajectory. The magnetic dipoles in the case of storage rings are also one type of SR light sources. Other kinds of magnets, like quadrupole magnets, are used to focus the electrons and thus to improve the geometrical characteristics of the electron beam.

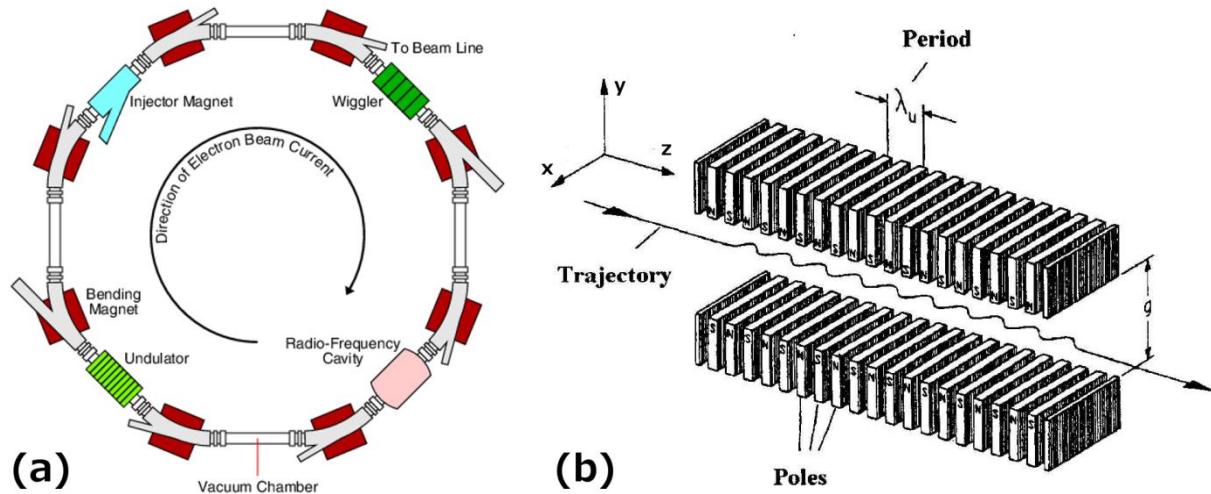


Figure 2.1: (a) Schematic representation of the electron ring in a synchrotron (Image from pd.chem.ucl.ac.uk); (b) representation of a wiggler (Image from www.project.slac.stanford.edu).

Wigglers and undulators consist of a sequence of dipole magnets of alternating polarities. The electrons are then forced to oscillate around a straight-line trajectory, and the radiation cone emitted at each curve superimpose. The undulator emissions are collected by the beamlines departing from the ring vacuum tube. In the case of undulators the cone of radiation presents a total divergence less than the natural $1/\gamma$ (with $\gamma = 1/\sqrt{(1 - v^2/c^2)}$, where v and c are the electron and light velocity, respectively). In this case the beams emitted by individual poles can interfere coherently, in practice this leads to a spectrum characterized by strong peaks at specific energies and their harmonics.

With wigglers the total divergence is much larger than the natural opening of the radiation, and so interference no longer occurs. The resulting emitted beam is the incoherent sum of the beams at each pole, and in this case the X-ray spectrum has a continuous distribution.

2.1.1.1 Radiofrequency cavities

Due to the emission of electromagnetic radiation the electrons circulating in the ring decrease their energy. Without correcting action the electron would rapidly become unable to circulate in the ring, because of the energy loss.

This correction action is performed by *radiofrequency* (RF) *cavities*. Passing through the RF an electron increases its energy to compensate the one lost for the emission of SR. However the electrons present different energies due to the differences in the energy loss because of the SR. In order to compensate for this effect the less energetic electrons (*i.e.* smaller velocity) are synchronously accelerated in the RF cavities. To perform this synchronization, electrons cannot circulate as a continuous flow around the ring,

but only in the form of discrete bunches. The consequence is that the synchrotron sources provide a pulsed emission.

A periodic re-injection of electron in the machine is necessary for compensating the unavoidable electron and energy losses due to effects such as the interaction with the residual gas atom (this cannot be avoided even in ultrahigh vacuum), a not-perfect compensation of the energy in the RF cavities and also the Coulomb electron-electron interactions.

2.1.1.2 SR beam characteristics

Several aspects of an X-ray source determine the quality of the X-ray beam it produces. They can be combined into a single quantity called *brilliance* B , function of the photon energy and defined as:

$$B = \frac{\text{Photons}}{\text{second} \cdot \text{mrad}^2 \cdot (\text{mm}^2 \text{source area}) \cdot (0.1\% \text{ bandwidth})} \quad (2.1)$$

More in details the beam can be described in terms of:

- **Divergence:** the angular distribution of the X-ray beam can be well approximated using a Gaussian distribution in both the orbit plane and in the perpendicular one. Depending on the experimental requirements, small source size and high divergent beam or large source size combined with a little divergent beam are available. For the first case wigglers are used, while in the second case undulators are employed.
- **Polarization:** this is an important characteristic of SR. In the case of synchrotron radiation we have a 100% linear polarized beam along the orbit plane. Using a wiggler the radiation is linearly polarized inside and outside the orbit plane.
- **Spatial coherence:** the small opening angle of the X-ray beam produced in synchrotron facilities enable to position the sample at large distances from the source while preserving a high incident intensity. This fact, together with the small size of the source, allows experiments in which a high degree of spatial coherence is required. This property is fundamental for phase-contrast imaging (PCI) techniques, for instance.
- **Parallel beam:** the emitted X-rays are almost parallel at the sample position. This is a very important property, especially in analyser-based imaging (ABI), because of the high angular selectivity of the monochromator and AC.

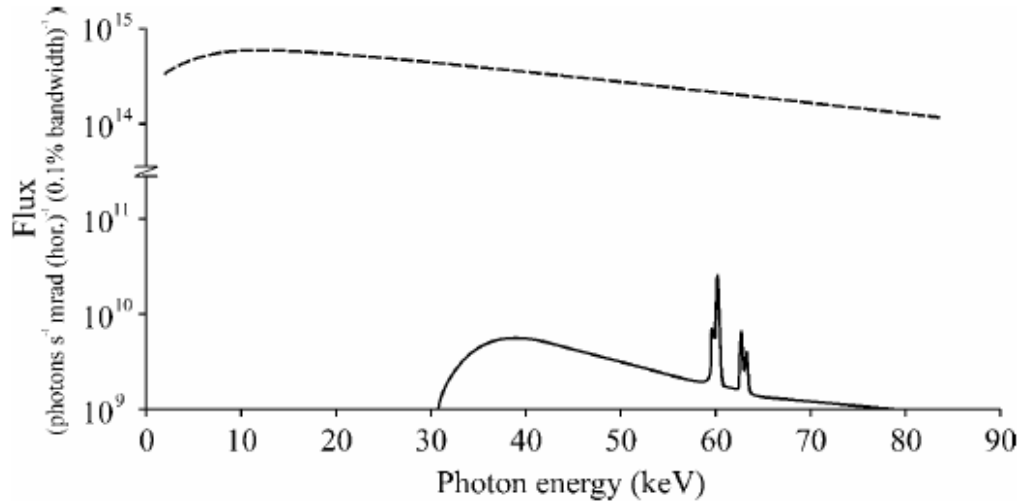


Figure 2.2: comparison between a wiggler X-ray beam spectrum (dashed line) (ESRF, ID17 at 200 mA ring current) and an X-ray tube (100 kVp – 2.5 mm Al @ 1 meter/source).

- **Monochromaticity:** the beams produced by bending magnets and wigglers present a high flux and a broad energy spectrum (figure 2.2). Owing to these properties, particular wavelengths can be selected by means of a monochromator while maintaining a high flux.

2.2 The European Synchrotron Radiation Facility and the biomedical beamline (ID17)

The European Synchrotron Radiation Facility (ESRF) of Grenoble (France) is one of the most powerful synchrotron sources of third generation in the world. It is the result of an international consortium between twenty countries founded in 1988 for scientific and technological research by means of high brilliant X-rays.

At the ESRF a beamline, ID17, is dedicated to bio-medical applications. In particular preclinical and clinical studies in radiation therapy and X-ray imaging are carried out. Several research programs are performed in this beamline: for example, PCI, bronchography, brain perfusion studies, preclinical Microbeam Radiation Therapy and Stereotactic Synchrotron Radiation Therapy.

ID17 is one of the three long ESRF beamlines: it is composed by two experimental hutches, the first located at 40 m from the source, while the second at 150 m. The aim of such high distance from the source is to achieve a sufficiently large beam for imaging purposes and to obtain a high degree of spatial coherence (Van cittert 1934). The beam in the second experimental hutch can reach $\sim 250 \times 10 \text{ mm}^2$ (horizontal x vertical) thanks to the beam divergence and the long distance from the source. However the size of the beam is reduced in practice due to optical constrains (*i.e.* monochromators and other optics). As results a

beam of about $150 \times 10 \text{ mm}^2$ is available in the second experimental hutch. All the experiments performed within this Thesis work, have been performed in this hutch.

The insertion device for the production of X-ray radiation at ID17 is a multi-pole wiggler magnet (*w150*) with an adjustable gap (21 poles, period of 15 cm and maximum magnetic field of 1.6 T at the minimum allowed gap-24.8 mm). This corresponds to a maximum critical energy of 38.1 keV (unfiltered radiation). A second wiggler (*w125*) characterized by 22 poles, with 12.5 cm of period and a maximum magnetic field of 1.8 T at a gap of 11 mm is installed with the purpose to increase the photon flux when needed. The X-ray source size calculated at a gap of 60 mm for the *w150* wiggler is $132 \mu\text{m}$ (horizontal) \times $24 \mu\text{m}$ (vertical) as FWHM. In the same conditions the beam divergence is around $735 \mu\text{rad}$ in the horizontal direction and $85 \mu\text{rad}$ in the vertical one. The transversal coherence length is of $130 \mu\text{m}$ in the vertical plane for an X-ray energy of 30 keV.

All the optical components were designed and manufactured to reduce and avoid, when possible, the spurious signals, loss of coherence on the X-ray path and/or to maintain the beam inhomogeneity at the sample position.

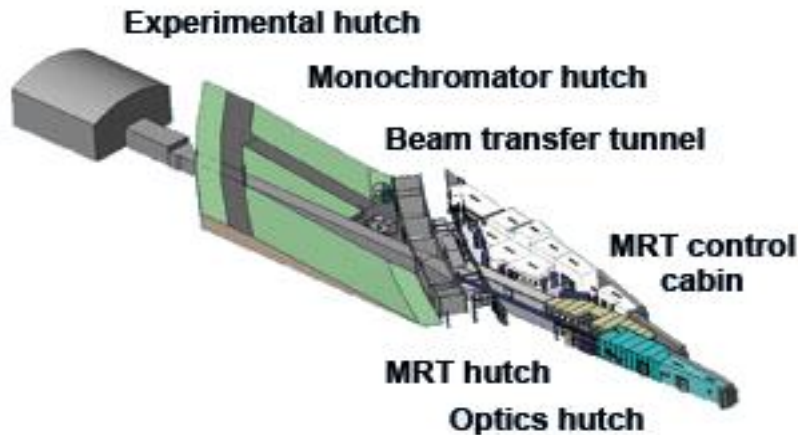


Figure 2.3: ID17 block scheme (image from www.esrf.eu).

The block scheme of ID17 is shown in figure 2.3. The beamline consists in two experimental hutches, two optical hutches containing all the necessary optical and mechanical elements for the X-ray beam geometrical and spectral definition and for performing the different kinds of experiments. A 100 m long tunnel connects the first optics and experimental hutches to the second ones. A more detailed description of the hutches where the experiments of this Thesis have been performed is here reported:

- **Second Optics Hutch (OH2):** a second set of slits, absorbers, beam monitors and monochromators are installed here. Two systems of monochromators are present: 1) a single crystal monochromator (identified as “angiography monochromator”) and a double crystal system monochromator

(identified as “computed tomography monochromator”, CTM). Both systems operate in oxygen-free helium filled chambers, at atmospheric pressure. The CTM uses two water-cooled bent Si crystals in Laue geometry producing a monochromatic beam parallel to the incident white beam, with a vertical offset of 40 mm. The central part of the crystals is 1 mm thick, 150 mm wide and 12 mm high, cut with an asymmetry angle of 15° . The X-ray energies that can be selected with this monochromator are in the range of 20-140 keV. The hutch contains also a fast shutter and a chopper. The chopper synchronized with the taper optics FReLoN camera prevents the camera from being exposed during the readout time.

- **A second Experimental hutch (EH2):** it contains different experimental setups. All the experiments presented in this Thesis work have been performed in this hutch. A second control room is located close to this hutch.

2.3 Description of the experimental setups

The ABI CT setups are located in the second experimental hutch, at a distance of about 155 m from the source. Two kind of setup are used, as shown in figure 2.4. They differ only in the sample stage, in particular in the orientation of the axis of rotation of the sample. In the first case, referred as out-of-plane geometry (figure 2.4a), the sample rotates around a vertical axis, while in the second case (figure 2.4b), referred as in-plane geometry, the rotation of the sample is performed along an axis parallel to the ground and perpendicular to the analyser crystal (AC) sensitivity plane. A detailed description underlining the differences between these two setups is presented in Chapter 2.

The in-plane setup has been designed *ex-novo* in the framework of this Thesis work to validate and compare the results obtained by using this geometry with respect to the out-of-plane one. The part composing the sample stage frame has been designed, and then manufactured at the ESRF, while most of the motors can be exchanged with the out-of-plane geometry setup.

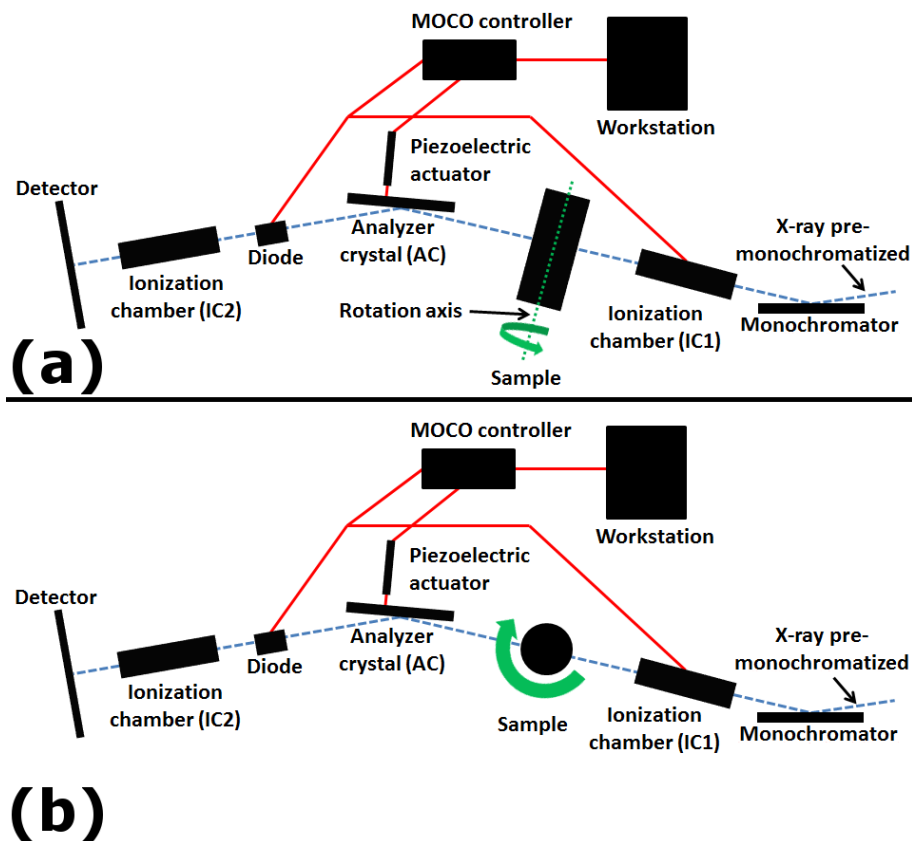


Figure 2.4: block scheme of the two ABI CT setups. (a) out-of-plane geometry; (b) in-plane geometry.

The beam incoming in the experimental hutch from the Laue double Si(111) crystal is monochromatized to a narrower bandwidth by a Si(333) Bragg crystal. After passing through the sample, the beam impinges on a second crystal (the AC), identical to the first one, which is used to filtrate the beam before it reaches the imaging detector system. The ABI crystals are mounted on a granite block screwed to the floor in order to increase the mechanical stability (figure 2.5). A first ionization chamber is set in front of the sample, while a diode and a second ionization chamber are placed behind the analyser (figure 2.4).

The monochromator crystal stage, shown in figure 2.6a, consists of a tower bearing the crystal and is mounted on a vertical translation motor and a double tilt motor (“theta” and “roll” cradle). The “theta” motor defines the angle in the diffraction plane with respect to the X-rays propagation direction, while the “roll” is used to align the angle in a plane perpendicular to the propagation direction. The two tilt motors have a resolution of $0.25 \cdot 10^{-3}$ degrees. The monochromator stage is mounted on the first of the two columns of the granite block (figure 2.5).



Figure 2.5: overview of the setup: (1) granite block; (2) monochromator crystal stage; (3) first ionization chamber; (4) sample stage; (5) analyser crystal stage; (6) diode; (7) second ionization chamber; (8) imaging detector system. Image from Diemoz 2011.

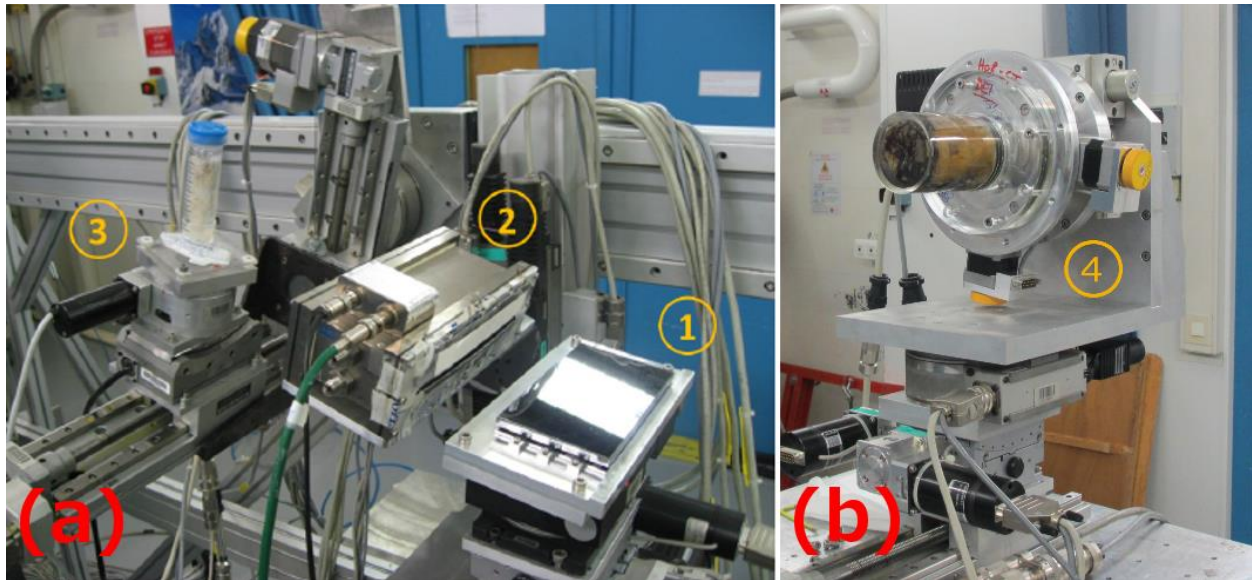


Figure 2.6: (a)-1 monochromator stage; (a)-2 Ionization chamber; (a)-3 out-of-plane geometry sample stage; (b)-4 in-plane geometry sample stage. Image (a) from Diemoz 2011.

The sample stage, for both projection and CT imaging, is mechanically decoupled from the granite block, in order not to transmit vibrations from the sample movements to the ABI crystals. The sample stage is anchored to a transverse bar directly fixed on the floor. In the case of the out-of-plane geometry (figure 2.6a), it consists of:

- A high resolution vertical translation motor to scan the sample through the laminar beam.
- A horizontal translation motor (motion perpendicular to the X-rays direction) to center the sample with respect to the center of the beam and put it in/out of the beam for reference images acquisitions (along the x-axis).
- A rotation stage for tomography imaging (resolution 0.01 degrees). In this geometry, the rotation axis of the sample is parallel to the y-axis.
- A “theta” tilt motor for angularly aligning the sample with respect to the X-ray beam direction, in particular to position the whole sample stage perpendicular to the X-rays.
- A “roll” tilt motor to align the sample for CT along the x-axis.

In the case of the in-plane geometry (figure 2.6b), the sample stage consists of:

- A high resolution vertical translation motor to scan the sample through the laminar beam (y-axis). This motor can be also used also to acquire the reference images, by moving the sample out of the beam.
- A “roll” tilt motor to align the sample, with respect to the beam, along the x-axis.

- A “theta” motor to align the sample, with respect to the X-ray beam, along the z-axis (propagation axis).
- A rotation stage for horizontal tomography imaging. In this geometry, the rotation axis of the sample is parallel to the x-axis (rotation resolution 0.01 degrees).
- A horizontal translation motor (along the x-axis). This motor can be used also to acquire the reference images, by moving the sample out of the beam.



Figure 2.7: The analyser stage.

The AC stage is shown in figure 2.7. The crystal is fixed at a 25 cm long arm which is angularly controlled by means of a piezoelectric motor which is used for the angular tuning of the analyser (the piezoelectric resolution of $0.02 \mu rad$ is limited in practice by the mechanics so that the final minimum step is about $0.1 \mu rad$). Like for the monochromator, the tower bearing the AC is placed on a double cradle (“theta” and “roll” tilt) for alignment and acquisition purposes. The crystal stage is mounted on the second column of

the granite block. The two columns of the granite blocks can be independently moved in the beam direction in order to align the monochromator and the analyser with the beam for different X-ray energies and crystal reflections configurations.

Ensuring the crystal stability is the main challenge in this kind of experiment setup due to the very small angular acceptance of the monochromator and AC. The effect of possible AC vibrations are studied by means of simulations and showed in Chapter 3. A device called monochromator controller (MOCO) is integrated into the ABI setup to improve the stability of the AC. The MOCO consists of a feedback system that permits to dynamically tune the analyser piezoelectric actuator in order to keep the ratio between the intensity incident on the analyser and the diffracted intensity at a given fixed value. The intensity before the analyser is measured with the first ionization chamber, placed before the sample (figure 2.6), while the diffracted intensity is measured by the diode, which is paced in a portion of the beam outside the footprint of the sample. This system yielded to considerable improvements in terms of the AC stability.

2.4 ID17 Image acquisition equipment

The detector systems used for the measurements performed at the ID17 beamline, and presented in this Thesis work, are.

- **The taper optics FReLoN camera:** this detector system (figure 2.8a) is based on a Fast-Readout Low-Noise (FReLoN) CCD camera coupled to a fiber optic taper (Coan et al. 2006). It has been developed at the ESRF for a broad range of applications; its specifications were initially tailored for CT applications in ABI mammography (Bravin 2003). The FReLoN taper optics shows an active input surface of $94 \times 94 \text{ mm}^2$ where X-rays are converted to visible light by a fluorescent screen; this secondary radiation is then guided by a fiber optics taper with a 3.2:1 reduction ratio and extra-mural absorption (Schott) onto the 2048×2048 pixels $14 \times 14 \mu\text{m}^2$ CCD (Atmel Corp, USA). This reduction allows an effective pixel size of about $46 \times 46 \mu\text{m}^2$ to be achieved. The FReLoN camera is cooled by using a Peltier-type cooling system. For this detector both the readout and dark signal (signal in absence of X-rays) levels are kept low. The maximum readout speed is of 20 Mpixels/s through four outputs provides the possibility of high frame rate imaging (4.2 frames/s) in full size image mode without binning. The gain is constant and it is 23 electrons/ADU (analog-to-digital unit); the maximum analog-to-digital readout of 214 bits corresponds to $3 \cdot 10^4$ electrons whatever the binning applied.
- **The high resolution FReLoN optics:** in order to cope with experiments requiring higher resolution, a FReLoN camera coupled to an optical system made of de-magnifying lenses has also been developed. The CCD camera and the electronics are the same as those used for the taper optics

FReLoN camera. This optical system allows obtaining an effective pixel size of about $7.5 \mu\text{m}$, but the available field of view is consequently reduced to $15.3 \times 15.3 \mu\text{m}^2$.

- **X-rays conversion screens:** the X-ray conversion can be optimized by changing the fluorescent screen according to the kind of applications. Among others, powder phosphor screens ($\text{Gd}_2\text{O}_2\text{S:Tb}$, 5g/cm^3 density) of $40 \mu\text{m}$, $100 \mu\text{m}$ and $200 \mu\text{m}$ thicknesses can be coupled with the FReLoN detection system. The spatial resolution is higher in case of usage of thinner screens, but at the expenses of absorption efficiency. All these screens consist in an active phosphor layer deposited on a thin plastic film substrate. The active layer is in direct contact with the input surface of the fiber-optic taper.
- **Germanium detector:** (figure 2.8b) this detector is made from a monolithic high purity p-type Ge (B doped with a rate of 10^{18} ion/cm^3) crystal 2 mm thick, 160 mm long, 10 mm high and electrically segmented into two rows of 432 parallel strips each (0.35 mm pitch). It is protected by a 0.5 mm thick beryllium window and cooled at liquid nitrogen temperature (EurisyS Mesures) (Elleaume et al. 1999). The 16-bit electronics works in charge integration mode. The efficiency is of nearly 100% at 33 keV and 45% at 90 keV (Peterzol et al. 2003).



Figure 2.8: (a) The ID17 taper optics FReLoN camera; (b) ID17 Germanium detector.

Chapter 3 - Different approaches for phase-contrast computed tomography

3.1	Analyser-Based Imaging: quantitative imaging method.....	59
3.1.1	Diffraction-enhanced imaging (DEI)	60
3.1.2	Extended DEI (E-DEI).....	61
3.2	Phase-contrast CT reconstruction techniques	63
3.2.1	Filtered back projection algorithm (FBP)	63
3.2.1.1	Fourier slice theorem	64
3.2.2	Filtered back-projection for gradient projections (GFBP)	65
3.2.3	Refractive-index gradient vector field method (RGVF)	68
3.2.4	CT reconstruction based on a phase-retrieval method	71
3.2.4.1	Boundary conditions	72
3.3	Different ABI CT geometries: a simulation study	72
3.3.1	Simulation code	72
3.3.2	Simulation parameters	74
3.3.3	Simulations of experimental errors	78
3.3.3.1	Discontinuities between materials with very different optical constants	80
3.3.4	Comparison between the out-of-plane and in-plane CT geometries.....	83
3.4	Conclusions.....	88

3.1 Analyser-Based Imaging: quantitative imaging method

The recorded analyser-based imaging (ABI) signal is given by a mixture of absorption, refraction, ultra small-angle X-ray scattering (USAXS) and small-angle X-ray scattering rejection (SAXS). As described in Chapter 1 the absorption and refraction components are related to the real and imaginary part of the index of refraction. The USAXS signal is produced by structures ranging in the order of magnitude of hundreds of nm up to μm , and it occurs at angles at angle of several μrad . In part the signal falls within the acceptance of the analyser crystal (AC), resulting in a broadening of the measured rocking curve (RC). In the $mrad$ range diffuse scattering originated by structures of nm scale (SAXS signal) is instead rejected and gives rise to the extinction contrast.

In order to separate the different physical effects and accurately quantify them, several mathematical methods have been proposed. In all cases, a multi (2 or more)-image set has to be acquired at different angular positions of the AC RC. Most of the proposed methods are based on the geometrical optics (GO) approximation (see Chapter 1). This approximation is valid only if the phase of the incident wave on the AC is a slowly varying function on the length scale of the extinction length of the crystal. This condition is equivalent to say that $NT \gg 1$, where NT is the Takagi number (Chapter 1) (Pavlov et al. 2004; Nesterets et al. 2006). Other methods based on different approximations (weak object and linear transfer function) have been introduced. In the case of the weak object approximation, the condition is that the phase shift of the object is small (Nesterets et al. 2004), while for using the linear transfer function approximation (Paganin et al. 2004) it is required that the transfer function of the imaging system can be linearized in the Fourier space. Both the last two methods require the knowledge of the Point Spread Function (PSF) of the imaging system, which requires specific measurements and calculations. Additional terms to the expression of the imaging PSF need to be included in order to take into account the not perfect parallelism and monochromaticity of the X-ray beam (Nesterets et al. 2005). Contrariwise, when using methods which are based on the GO approximation only the knowledge of the RC of the imaging system is required. Several GO based algorithms have been proposed and developed over the past twenty years. They are:

- Diffraction-enhanced imaging (DEI) (Chapman et al. 1997): it is the simplest method. It is described in section 3.1.1.
- Extended DEI (EDEI) (Maksimenko 2007; Hu et al. 2008): this method aims at overcoming the intrinsic limitations of the DEI algorithm in terms of accuracy of the results and range of applicability. This algorithm is the one used in this Thesis work to extract the distribution of the refraction angle and is described in section 3.1.2.

- Generalized DEI (G-DEI) (Chou et al. 2007; Rigon et al. 2007): this approach allows separating not only the refraction and absorption signal, but also the USAXS, using three images. This is of particular importance when the investigated sample presents a not negligible amount of scattering. This method assumes that the refraction and scattering angle are small compared to the Full Width at Half Maximum (FWHM) of the AC RC.
- Multiple image radiography (MIR) (Pagot et al. 2003; Wernick et al. 2003): this method requires a number of images ≥ 3 to separate the absorption, refraction and USAXS signals. The MIR is a statistical method that allows for reconstructing the RC pixel-by-pixel basis by combining several images acquired at different positions along the RC of the AC. The MIR presents several limitations: large refraction angles can be underestimated (Zhifeng et al. 2007), as well as the signal of USAXS. This method is very stable with respect to noise, but on the other hand the high number of images that need to be acquired increase both the dose and acquisition time, which represent an important issue in case of biological tissues.
- Gaussian curve fitting (GCF) (Nesterets et al. 2006): this method is similar to the MIR but it consists in fitting, pixel-by-pixel, the ‘reference’ and ‘object’ RCs with a Gaussian function in order to recover the different contributions of the refraction, absorption and USAXS components.

In order to keep low the dose the EDEI algorithm has been chosen because only two images are required to separate the refraction and absorption signals. For this reason only the DEI and EDEI algorithms are described in the next sections.

3.1.1 Diffraction-enhanced imaging (DEI)

The simplest extraction method is the DEI algorithm that was developed by Chapman et al. (Chapman et al. 1997). The basic idea is to linearize the imaging system RC recorded without the sample at its two slopes (where the second derivative is equal to zero). When the object is in the beam we can express the intensity equations by using a first order Taylor approximation of the RC, for each image pixel as:

$$I_{L,R} = I_T \left(R(\theta_{L,R}) + \frac{dR}{d\theta}(\theta_{L,R})\Delta\alpha \right) \quad (3.1)$$

In this equation we refer to the two symmetric positions on slopes of the RC as the ‘left’ (L) and ‘right’ (R). Eq. 3.1 represents a linear system with two unknown quantities: I_T and $\Delta\alpha$. To solve analytically this equation on a pixel-by-pixel basis, two images of the sample have to be acquired, at the L and R slopes of

the RC, respectively. In this way it is possible to calculate the transmission and the refraction angle image as following:

$$I_T = \frac{I_L \frac{dR}{d\theta}(\theta_R) - I_R \frac{dR}{d\theta}(\theta_L)}{R(\theta_L) \frac{dR}{d\theta}(\theta_R) - R(\theta_R) \frac{dR}{d\theta}(\theta_L)} \quad (3.2)$$

$$\Delta\alpha = \frac{I_R R(\theta_L) - I_L R(\theta_R)}{I_L \frac{dR}{d\theta}(\theta_R) - I_R \frac{dR}{d\theta}(\theta_L)} \quad (3.3)$$

The image of I_T is referred to as the ‘absorption image’ for consistency with the terminology used in most publications, despite in practice this is the image of the transmitted intensity through the sample (dark pixels correspond to high absorption values and vice versa). The second image, $\Delta\alpha$, corresponds to the distribution of the refraction angles.

The DEI algorithm has the advantage that both the dose deposited to the sample and the acquisition time may be reduced compared to other methods because only two images are needed to solve the eq. 3.1. The drawback of this approach is that the assumptions concerning the sample are quite restrictive. The linear approximation of the RC at the two slopes is valid only if the refraction angles are small compared to the FWHM of the AC RC. Additionally, this method does not take into account the USAXS produced by the object, which has the effect of broadening the observed (with the sample in the beam) RC compared to the reference (without the sample in the beam) RC used in the calculations.

Incorrect results are obtained in the case of biological tissues giving rise to a high level of scattering or in the case of large refraction angles ($\Delta\theta \geq FWHM_{RC}$), for example at the interfaces between different materials or structures (Pagot et al. 2003; Rigon et al. 2003; Wernick et al. 2003; Zhifeng et al. 2007; Hu et al. 2008).

3.1.2 Extended DEI (E-DEI)

Two ways to overcome the intrinsic limitations of the DEI algorithm has been proposed by Maksimenko 2007 and Hu et al. 2008, respectively. In these methods, generally referred as extended-DEI (E-DEI), the separation of the absorption and refraction signals can be done using two input images, like in the DEI, but without imposing a Taylor approximation of the RC slopes.

The basic of the method (Hu et al. 2008) is to fit the system RC with a Gaussian function. It is assumed that, once the object is in the beam, its effect on the measured RC consists only in a shift of the RC center

(due to refraction), and in a decrease in intensity (due to absorption), but not in a change in the RC shape. In particular, no RC broadening due to USAXS is considered.

When two images at different angular positions of the AC RC, $\theta_{L,R}$, are acquired, the intensity recorded in each image pixel can be expressed as:

$$I_{L,R} = I_T A \exp \left[-\frac{(\Delta\alpha + \theta_{L,R})^2}{2\sigma^2} \right] \quad (3.4)$$

where A is the ‘reference’ RC peak value and σ is the standard deviation of the Gaussian function fitting the RC. The values of I_T and $\Delta\alpha$ can then be analytically calculated, on a pixel by pixel basis, by using the following expressions obtained from the equations 3.4:

$$\Delta\alpha = \frac{2\sigma^2 \log(I_L/I_R) + \theta_L^2 - \theta_R^2}{2(\theta_R - \theta_L)} \quad (3.5)$$

$$I_T = I_L \exp \left[\frac{(\theta_L + \Delta\theta_y)^2}{2\sigma^2} \right] \quad (3.6)$$

No restrictions on the values of refraction angles are imposed in this method (assuming that the conditions of the GO approximation are fulfilled). In addition, the range of refraction angles that can be calculated is wider with respect to the case of the DEI algorithm. It is also possible to acquire the two images at different positions along the slope of the RC and not necessarily at the FWHM. The RC broadening due to the USAXS is not accounted also in this method. This can be reflected in errors during the calculation of the absorption and refraction images (in the case of highly scattering samples). In the presence of large refraction angles incorrect results are obtained as in the case of DEI (an example of such behaviour is presented in section 3.3.3.1).

An error in the estimation of the angular position of the AC along its RC leads to a shift of the calculated refraction angle according to eq. 3.5. An incorrect measurement of σ of the Gaussian curve fitting the AC RC quantitatively affects the calculated values of the index of refraction; they result multiplied by a constant value which is equal to the ratio of the squares of the correct (real) and incorrect (estimated with the applied fit) standard deviations.

3.2 Phase-contrast CT reconstruction techniques

In these sections the algorithms used for the computed tomography (CT) reconstructions performed in this Thesis work are presented. All the algorithms are implemented in the simulation code we developed, called *RIPCIP* and described in section 3.3.1.

The reconstruction of the CT images can be performed by means of several algorithms based on the analytical Fourier-based method or on iterative methods (algebraic and statistical).

The analytical method includes several algorithms. The most commonly used is the filtered backprojection (FBP), (Kak & Slaney 1988; Herman 2009). A variant of it is the filtered backprojection for gradient projections (GFBP), (Faris & Byer 1988). An example of iterative algorithm used within our group based on a Fourier method, but not described here, is the Equally Sloped Tomography (EST), (Miao et al. 2005). It allows performing the CT reconstruction using a reduced number of projections without loss in the image quality (Zhao et al. 2012). In this Thesis work the algorithms allowing the reconstruction of the 3D distribution of the fluctuation of the index of refraction are described. A brief introduction of the FBP algorithm is presented as well in section 3.2.1. Three different methods are considered: 1) the GFBP method (section 3.2.2); 2) the refractive-index gradient vector field method (section 3.2.3); and 3) the application of the phase-retrieval applied on projections followed by a CT reconstruction algorithm (section 3.2.4).

3.2.1 Filtered back projection algorithm (FBP)

Let start our discussion with the simplest reconstruction method, by considering a coordinate system defined as (x', y, z') (figure 3.2a) fixed with respect to both the X-ray beam and the detector, for the so-called out-of-plane geometry (where the sample rotates around an axis parallel to the sensitivity direction of the AC, y -axis, figure 3.2a). The beam direction is represented by z' and the system is rotated of an angle θ with respect to the sample reference frame (x, y, z) (figure 3.2a). We use capital letters for functions and coordinates when working in the frequency domain and lower case for the spatial domain. Using the FBP algorithm it is possible to calculate the three-dimensional distribution of the linear attenuation coefficient μ by using:

$$\mu(x, y, z) = \int_0^\pi d\theta F^{-1}[|w|P(w, y, \theta)] \quad (3.7)$$

Where F^{-1} denotes the inverse Fourier transform, w is the spatial frequency coordinate corresponding to x' , and P represents the forward Fourier transform of the function p , which is equal to the logarithm of the normalized transmission projection:

$$p(x', y, \theta) = -\ln[I_T(x', y, \theta)/I_0(x', y, \theta)] = \int_{L_\theta(x', y)} dz' \mu(x', y, z') \quad (3.8)$$

I_0 and I_T denote the incident and transmitted intensities and $L_\theta(x', y)$ is the path of the beam inside the object.

3.2.1.1 Fourier slice theorem

The FBP is based on the Fourier Slice Theorem, also known as the *central-slice theorem* or *central-section theorem* or *projection-slice theorem*. The statement of this theorem is as follows: denoting with $p_\theta(r)$ the Radon transform of $f(x, z)$, then the 1D Fourier transform of $p_\theta(r)$, indicated by $P_\theta(v)$, is equal to the slice at angle θ through the 2D Fourier transform of $f(x, z)$.

$$P_\theta(v) = \int_{-\infty}^{\infty} p_\theta(r) e^{-i2\pi vr} dr \quad (3.9)$$

Denoting with $F(u, v)$ the 2D Fourier transform of $f(x, z)$, *i.e.*,

$$F(u, v) = \int_{-\infty}^{\infty} \int_{-\infty}^{\infty} f(x, z) e^{-i2\pi(ux+vz)} dx dz \quad (3.10)$$

The Fourier-slice theorem can then be expressed mathematically as:

$$P_\theta(v) = F(v \cos \theta, u \sin \theta) \quad (3.11)$$

that is equivalent to figure 3.1. It is possible to notice that with the Fourier-slice theorem the Radon transform describes completely any (Fourier transformable) object $f(x, z)$, because there is a correspondence one to one between the Radon transform and the 2D Fourier transform $F(u, v)$, and from $F(u, v)$ the object $f(x, z)$ can be recovered by applying the inverse 2D Fourier transform.

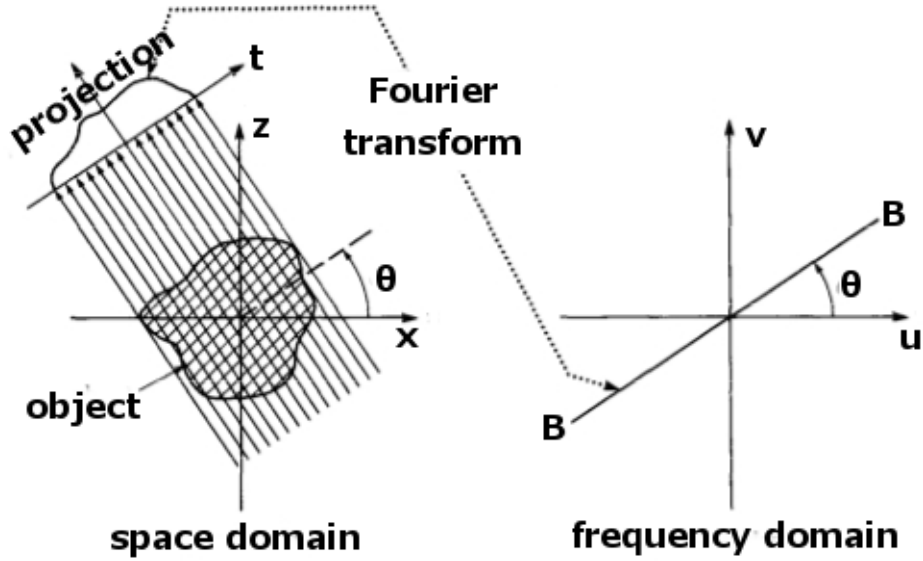


Figure 3.1: Fourier-slices theorem. Image from Kak and Slaney, 1988.

3.2.2 Filtered back-projection for gradient projections (GFBP)

This method is the variant of the FBP used in the case of the in-plane geometry (where the sample rotates around an axis perpendicular to the sensitivity direction of the AC, x-axis, figure 3.2b) whose setup has been described in Chapter 2. Let us consider an object described by the function $f(x, y, z)$. An ordinary projection in the plane defined by $x = x_0$ for an object rotated of an angle θ with respect to the y-axis can be expressed as (figure 3.2b):

$$p(y', \theta) = \int_{-\infty}^{\infty} f(y', z') dz' \quad (3.12)$$

The y' - z' axes are rotated at an angle θ with respect to the y - z axes. The 1D forward Fourier transform of a projection is given by:

$$P(Y', \theta) = \int_{-\infty}^{\infty} p(y', \theta) \exp(-i2\pi y' Y') dy' \quad (3.13)$$

It can be shown that $f(y, z)$ can be reconstructed by applying the Fourier transform to a set of projections

$$f(y, z) = \int_0^{\pi} \int_{-\infty}^{\infty} P(Y', \theta) \exp[i2\pi Y'(-z \sin \theta + y \cos \theta)] |Y'| dY' d\theta \quad (3.14)$$

By using the convolution theorem and inverting the 1-D Fourier transform in the variable Y' we obtain

$$f(y, z) = \int_0^{\pi} [p(y', \theta) * k(y')]_{y' = -z \sin \theta + y \cos \theta} d\theta \quad (3.15)$$

where * indicates the convolution operator and $k(y')$ is the inverse Fourier transform of $|Y'|$. Equation 3.15 represents the convolution backprojection integral.

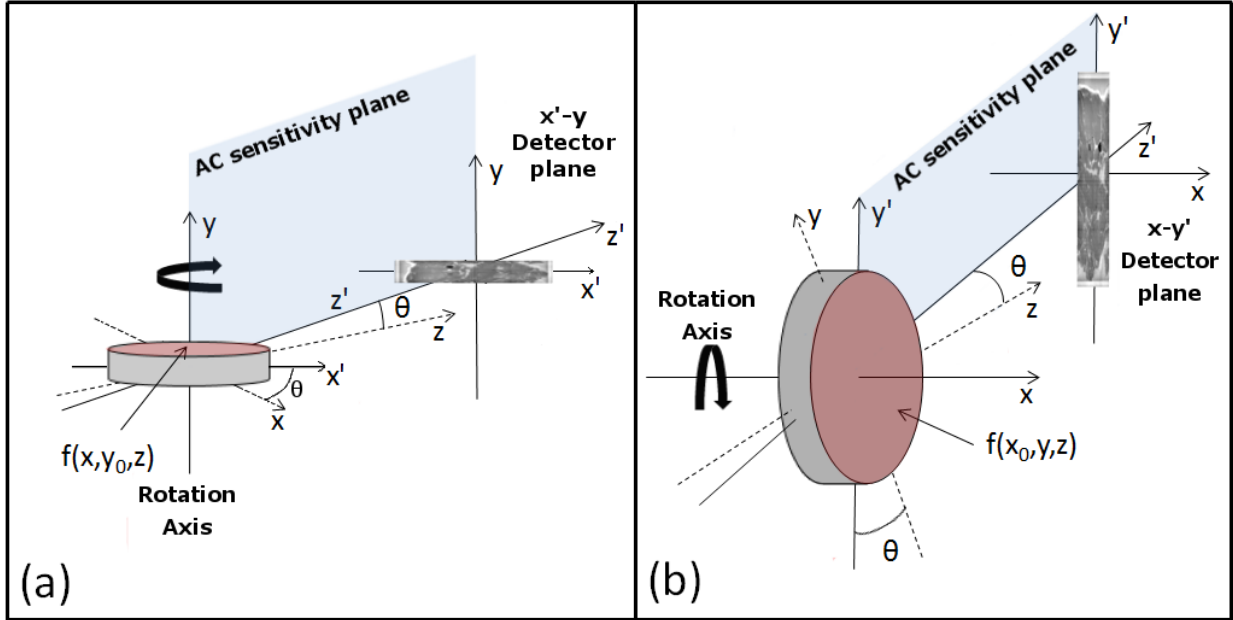


Figure 3.2: schematic of the coordinate systems of: (a) the out-of-plane geometry; and (b) the in-plane geometry. In the first case the sample rotation axis is parallel to the y-axis, while in the case of in-plane geometry is parallel to the x-axis. The blue plane represents the AC sensitivity plane, while the red one the image reconstruction plane. It is possible to notice that in (a) these two planes are perpendicular to each other, while in (b) they are parallel.

Experimentally, projections have a finite sampling spacing due to the finite spatial resolution of the imaging detector. If the projections are sampled at a spacing $\Delta y'$, only frequencies below the Nyquist frequency $1/2\Delta y'$ are adequately sampled and represented. In the frequency space the filter function becomes

$$K(Y') = \begin{cases} |Y'| & |Y'| < \frac{1}{2\Delta y'} \\ 0 & |Y'| > \frac{1}{2\Delta y'} \end{cases} \quad (3.16)$$

The convolution backprojection algorithm, eq. 3.15, may be extended to operate in the case of beam-deflection measurements (*i.e.* refraction signal). Let consider an index of refraction which is characterized by the following spatial distribution:

$$n(\mathbf{r}) = n_0[1 + \hat{n}(\mathbf{r})] \quad (3.17)$$

where n_0 represents the uniform background index of refraction and \hat{n} is a localized normalized variation in the index of refraction. For a slowly varying inhomogeneous non-absorbing medium, the propagation of a Gaussian X-ray beam is governed by the paraxial ray equation:

$$\frac{d}{dz} \left[n_0 \frac{d\mathbf{r}}{dz} \right] = n_0 \nabla_{\perp} \hat{n}(\mathbf{r}) \quad (3.18)$$

where \mathbf{r} is the displacement perpendicular to the direction of propagation z . Integrating along the ray path gives:

$$\frac{d\mathbf{r}}{dz} = \int \nabla_{\perp} \hat{n}(\mathbf{r}) dz \quad (3.19)$$

This equation can be approximated, for small deflections, as a straight line, and the two orthogonal deflections can be considered independently. The deflection angle of a Gaussian beam in the y - z plane is then approximately given by:

$$\alpha \approx \tan \alpha = \frac{dy}{dz} = \int \frac{d\hat{n}(y, z)}{dy} dz \quad (3.20)$$

For the rotated coordinates (figure 3.2b) we have:

$$\alpha(y', \theta) = \int \frac{d\hat{n}(y', z')}{dy'} dz' \quad (3.21)$$

where $\alpha(y', \theta)$ is the projection at the angle θ . Assuming that the optical path is straight, we can change the order of differentiation and integration:

$$\alpha(y', \theta) \approx \frac{d}{dy'} \int \hat{n}(y', z') dz' \quad (3.22)$$

We refer to a projection of this type as a transverse gradient projection. If $p(y', \theta)$ is an ordinary projection as eq. 3.12:

$$p(y', \theta) = \int \hat{n}(y', z') dz' \quad (3.23)$$

then using the derivative theorem and indicating with $P(Y', \theta)$ the forward Fourier transform of the ordinary projection, the Fourier transform of $\alpha(y', \theta)$ is:

$$A(Y', \theta) = i2\pi Y' P(Y', \theta) \quad (3.24)$$

From eq. 3.17 we know that:

$$\hat{n}(y', \theta) = \int_0^\pi \int_{-\infty}^{\infty} P(Y', \theta) \exp[i2\pi Y'(-x \sin \theta + y \cos \theta)] |Y'| dY' d\theta \quad (3.25)$$

and using the last two equations we find:

$$\hat{n}(y, z) = -\frac{i}{2\pi} \int_0^\pi \int_{-\infty}^{\infty} A(Y', \theta) \exp[i2\pi Y'(-z \sin \theta + y \cos \theta)] \text{sgn}(Y') dY' d\theta \quad (3.26)$$

where $\text{sgn}(Y')$ is the sign function:

$$\text{sgn}(Y') = \begin{cases} -1 & Y' < 0 \\ 1 & Y' > 0 \end{cases} \quad (3.27)$$

By performing an inverse Fourier transform of eq. 3.26 we obtain:

$$\hat{n}(y, z) = \int_0^\pi [\alpha(y', \theta) * k(y')]_{y' = -z \sin \theta + y \cos \theta} d\theta \quad (3.28)$$

where $k(y')$ is the inverse Fourier transform of $-i \text{sgn}(Y')/2\pi$. Eq. 3.28 represents the FBPG approach. It allows reconstructing the index of refraction in one step from a CT data set of deflection angle projections. Note that instead of the index of refraction decrement, only the fluctuating component \hat{n} is recovered from eq. 3.17. In order to obtain the constant component of n , an additional prior information about boundary values must be taken into account.

3.2.3 Refractive-index gradient vector field method (RGVF)

The basic principles in X-ray CT are founded on the relationship between the ray-propagation path and the physical quantities on the path to be depicted. Let us begin by examining the ray equation:

$$\frac{d}{ds} [n(\mathbf{r}) \mathbf{t}(\mathbf{r})] = \nabla n(\mathbf{r}) \quad (3.29)$$

where s is an arc length parameter along a ray from an origin to a point of interest, \mathbf{r} is a spatial coordinate; $\mathbf{r}(s)$ signifies a curve in space. If we indicate with n , \mathbf{t} and \mathbf{v} the refractive index distribution and the tangential and normal ray vectors with respect to a point along $\mathbf{r}(s)$, and we consider the 2D case, then we can write:

$$n \frac{d\alpha}{ds} \mathbf{v} + \frac{\alpha}{ds} \mathbf{t} = \nabla_{yz} n \quad (3.30)$$

$$n \frac{dn}{ds} = \nabla_{yz} \mathbf{t} \quad (3.31)$$

$$n \frac{d\alpha}{ds} = \nabla_{yz} \boldsymbol{\nu} \quad (3.32)$$

where α is an angular deflection from the propagation direction that satisfies the following relationship from differential geometry: $dt/ds = da/dsv$ and with $n \sim 1$ and $\beta = 0$ (no absorption by the medium). If Ψ is the angle between $\nabla_{yz} n$ and \boldsymbol{t} , then we can write

$$n \frac{dn}{ds} = |\nabla_{yz} n| \cos \Psi \quad (3.33)$$

$$n \frac{d\alpha}{ds} = |\nabla_{yz} n| \sin \Psi \quad (3.34)$$

Under the paraxial-ray approximation that the ray approximately propagates along a line in an object because $n \sim 1$, one can integrate n along a line S to obtain:

$$\int_S \frac{dn}{ds} ds = \int_S dn = \int_S |\nabla_{yz} n| \cos \Psi ds = 0 \quad (3.35)$$

$$\int_S \frac{d\alpha}{ds} ds = \int_S d\alpha = \int_S |\nabla_{yz} n| \sin \Psi ds = \Delta\alpha_{yz} \quad (3.36)$$

where we use the approximation $\int_S dn = 0$ and where $\Delta\alpha_{xy}$ corresponds to an in-plane angular deviation of the beam. If the yz -coordinate system is fixed with respect to an object and is rotated by θ about the origin, then:

$$\int_{-\infty}^{\infty} |\nabla_{yz} n(\mathbf{r}_l)| \cos[\varphi(\mathbf{r}_l) - \theta] dq = 0 \quad (3.37)$$

$$\int_{-\infty}^{\infty} |\nabla_{yz} n(\mathbf{r}_l)| \sin[\varphi(\mathbf{r}_l) - \theta] dq = \Delta\alpha_{yz}(p, \theta) \quad (3.38)$$

where, in the pq -coordinate system, $\mathbf{r}_l = (p \cos \theta - p \sin \theta, p \sin \theta + q \cos \theta)$ and $\varphi(\mathbf{r}_l)$ is the angle between $\nabla_{yz} n(\mathbf{r}_l)$ and the z -axis, that is the phase angle of the vector $\nabla_{yz} n(\mathbf{r}_l)$ in the yz -coordinate system. By adding eq. 3.37 to eq. 3.38 multiplied by i , we obtain:

$$\int_{-\infty}^{\infty} |\nabla_{yz} n| \exp[i\varphi(\mathbf{r}_l)] dq = i\Delta\alpha_{yz}(p, \theta) \exp(i\theta) \quad (3.39)$$

It is possible to express ∇_{yz} in the complex number formalism by using the following relations:

$$\nabla_{yz} n = \frac{\partial n}{\partial z} + i \frac{\partial n}{\partial y} \quad (3.40)$$

$$\frac{\partial n}{\partial z} = |\nabla_{yz} n| \cos \Psi \quad (3.41)$$

$$\frac{\partial n}{\partial y} = |\nabla_{yz} n| \sin \Psi \quad (3.42)$$

eq. 3.39 becomes:

$$\int_{-\infty}^{\infty} |\nabla_{yz} n(\mathbf{r}_l)| \cos \varphi(r) + i |\nabla_{yz} n(\mathbf{r}_l)| \sin \varphi(r) dq = i \Delta \alpha_{yz}(p, \theta) \cos \theta - \Delta \alpha_{yz}(p, \theta) \sin \theta \quad (3.43)$$

$$\int_{-\infty}^{\infty} \left[\frac{\partial n}{\partial z} + i \frac{\partial n}{\partial y} \right] dq = i \Delta \alpha_{yz}(p, \theta) \cos \theta - \Delta \alpha_{yz}(p, \theta) \sin \theta \quad (3.44)$$

Separating the real and imaginary components, one obtains:

$$\int_{-\infty}^{\infty} \frac{\partial n}{\partial z} dq = -\Delta \alpha_{yz}(p, \theta) \sin \theta \quad (3.45)$$

$$\int_{-\infty}^{\infty} \frac{\partial n}{\partial y} dq = \Delta \alpha_{yz}(p, \theta) \cos \theta \quad (3.46)$$

To perform the CT reconstruction of the images containing the information of the derivative of n along the z and y directions (eq. 3.45, eq. 3.46) any CT algorithm can be used. The CT images so obtained are then combined together, as in eq. 3.49, in order to obtain the distribution of n . The method to solve this problem and its implementation has been proposed by Gasilov et al (Gasilov et al. 2014) within our team. By using $\nabla n = \mathbf{f}$, then

$$\nabla \cdot \nabla n = \nabla \cdot \mathbf{f} \quad \nabla^2 n = \nabla \cdot \mathbf{f} \quad (3.47)$$

One possible way to practically calculate the divergence is the following. We apply first the definition of divergence and we define the scalar quantity Φ . Then we perform our calculation on a discrete grid of points and we obtain:

$$\nabla \cdot \mathbf{f} = \oint_{\Gamma} \mathbf{F} \cdot \mathbf{n} ds = \Phi \quad (3.48)$$

where Γ is a line on a grid cell (*i.e.* perimeter of the cell). By interpolating:

$$\oint_{\Gamma} \mathbf{F} \cdot \mathbf{n} ds = \sum_{l_1, l_2, l_3, l_4} \left(\frac{F_{l_1} + F_{l_2}}{2}, \frac{F_{l_3} + F_{l_4}}{2} \right) \cdot (n_y, n_z) = \Phi \quad (3.49)$$

where $F_{l_{n=1,4}}$ represents the values of the function at the corners of the cell. From this equation we obtain the so-called Poisson equation (elliptic equation):

$$\frac{\partial^2 \varphi}{\partial z^2} + \frac{\partial^2 \varphi}{\partial y^2} = \nabla \cdot \mathbf{f} = \Phi \quad (3.50)$$

with the boundary condition $\varphi_r = 0$. To solve eq. 3.48 the multigrid method has then been used (Press et al. 1992; Fedorenko 1962; Gasilov et al. 2014). The FBP algorithm has been employed in this Thesis work to perform the CT reconstruction of the quantities of eq. 3.45 and eq. 3.46.

3.2.4 CT reconstruction based on a phase-retrieval method

Another approach can be used to retrieve the distribution of the index of refraction decrement. This method consists in first performing the phase-retrieval on the projections of the calculated refraction angle and then performing the CT reconstruction. The reconstruction can be done with any CT algorithm; the one used in this work is the conventional FBP with the ramp filter.

The increment of the phase delay due to the interaction of the X-rays with an object is linearly proportional to the value of the decrement of the refractive index in the considered object volume: $\phi(z) = k \cdot \delta(y)dz$, where k is the wavenumber and the same coordinate system of section 3.2.2 is used. It is possible to express the total phase delay, by using the ordinary Radon transform:

$$\phi(y', \theta) = k \int \delta(y', z') dz' \quad (3.51)$$

The spatial derivative of the phase at the exit plane of the object can be written as:

$$\frac{\partial \phi(x, y', \theta)}{\partial y'} = k \alpha(x, y', \theta) \quad (3.52)$$

By using eq. 3.51 it is then possible to convert the refraction angle into a phase delay. A significant problem when performing the integration of eq. 3.51 is related to the presence of noise in the experimental data, resulting in strong streak artefacts along the integration direction (y' -axis). Several methods have been proposed to suppress these streak artefacts, for example eq. 3.52 can be converted to a constrained minimization problem (Wernick et al. 2006; Thüring et al. 2011). In this approach, a constraint, expressed by a regularization term, is introduced to suppress the variations of the phase in the direction perpendicular to the integration (x -axis in this notation). Here the method we proposed and implemented in the code (Gasilov et al. 2014) is instead followed. The basic idea is to convert the boundary value problem by differentiating both sides of eq. 3.51 over y' :

$$\frac{\vartheta^2 \phi(x, y', \theta)}{\vartheta y'^2} = k \frac{\vartheta \alpha(x, y', \theta)}{\vartheta y'} \quad (3.53)$$

A regularization term is then introduced and weighted by a factor γ . In this way an approximate solution of eq. 3.51 is obtained.

$$\frac{\vartheta^2 \phi(x, y', \theta)}{\vartheta y'^2} + \gamma \frac{\vartheta^2 \phi(x, y', \theta)}{\vartheta x^2} = k \frac{\vartheta \alpha(x, y', \theta)}{\vartheta y'} \quad (3.54)$$

With this method is possible to include both the boundary conditions and other a-priory information about the sample. In this work it has been taken into account the natural fact that at the interface between air and the object the derivative of the phase has very high value. In order to solve eq. 3.54 the finite elements method is then applied (Zienkiewicz & Morgan 2006, Gasilov et al 2014).

3.2.4.1 Boundary conditions

Two different kinds of boundary conditions have been considered in both simulations and experimental data (Chapter 4). Let us consider for example a problem defined in an interval $[a, b]$:

$$y''(x) + y(x) = 0 \quad (3.55)$$

The boundary conditions, considered in our cases, can be expressed in the following two ways:

- Dirichlet boundary conditions: $y(a) = \alpha$ and $y(b) = \beta$
- Neumann boundary conditions: $y'(a) = \alpha$ and $y'(b) = \beta$

where α and β are known values. These boundary conditions imply the knowledge of the values of the function or of its derivative at the extreme of the function domain that is, in our case, the extremes of the integration to retrieve the phase.

3.3 Different ABI CT geometries: a simulation study

3.3.1 Simulation code

The simulations code developed and used in this work is called *RIPCIP*. This software was initially based on the existing code X-TRACK written by Gureyev *et al* (X-TRACK: <http://www.ts-imaging.net/Services/AppInfo/X-TRACT.aspx>), but it has been then totally rewritten within our group.

Today only two classes of the original code are still used as the core of the data structures for 1D and 2D matrices and operations. I contributed in the development of several parts of the code, especially in those concerning the processing and reconstruction of the experimental CT data. The code is entirely implemented in ANSI/ISO C++ programming language following an object-oriented approach. The simulation code is subdivided in three separated parts:

- **RI-pcip:** in this part of the code the simulation of the interactions between X-rays and the sample is performed under the GO approximation. This is equivalent to the calculation of the Radon integral of projections, according to the definition of this transformation.
- **ri-PC-ip:** the purpose of this second step of the code is to model the X-ray intensity measurement of PCI experiments. Different PCI techniques (*i.e.* ABI and PBI, Chapter 1) are included.
- **rip-IP:** the last part of the code is dedicated to the solution of the inverse problem, in order to find the distribution of a given physical property of the sample starting from experimental measurements acquired in different modes (e.g. with different CT configurations and imaging techniques). The algorithms presented in section 3.2 and other methods needed for image processing are implemented in this part of the code. Data from both experiments and simulations can be processed.

Each branch of the code can be run separately from the others on different platforms. All the parameters used in the simulations are defined either directly inside the code or in external ‘parameters’ files. All the simulations whose results are presented within this Thesis have been performed in part on a desktop machine, in part on the ESRF computing cluster (ESRF nice, www.esrf.eu) and in part on the LRZ cluster (Leibniz-Rechenzentrum, www.lrz.de). Several processes are parallelized in a not platform-dependent way, in order to profit of the cluster computation systems. I wrote several scripts to interface the code with the clusters used for calculations. In particular, the calculations of the Radon transform (RI-pcip) and several reconstruction procedures (for example the phase-retrieval) require heavy calculation resources to be performed in reasonable computational time (hours).

The code here presented has been used to simulate all the equivalent experimental cases considered in this Thesis work. To this end, I considered mainly simulations of ABI experiments, only one simulation of a PBI experiment is presented in the Chapter 6. For this reason the description of the simulations presented in the next section is focused on the ABI technique. All the simulation parameters described in the next sections has been chosen following the experimental conditions of our experiments performed at ID17 (ESRF).

3.3.2 Simulation parameters

Beam parameters: The X-ray beam characteristics (*i.e.* divergence, polychromaticity) can be defined in the code, as well as the photon flux, which has been set to 2000 photons per pixel for all simulations (this value has been chosen to represent a realistic case). After several tests, we saw that including the divergence and polychromaticity of the beam does not visibly influence the results, while it leads to longer computational times and other additional complications related to data treatment. For these reasons, we decided to work by assuming a perfectly parallel and monochromatic X-ray beam.

The X-ray beam intensity profile is simulated as a 2D Gaussian distribution with different standard deviations σ_x, σ_y . It is possible to specify the coordinates of the center of this distribution. The shape of the beam can play an important role in terms of image quality and accuracy of the reconstructions. For instance, in the case of an ABI experiment if the wavefront impinging on the AC is distorted, we have that the signal in different regions of the image is produced by X-rays which have been modulated in different way by the AC. In the in-plane geometry this means that certain slices of the reconstructed volume are acquired at different positions on the RC. The beam shape can also be loaded as an external input data (*i.e.* white field from an experiment).

The photon energy has been set equal to 52 keV in all the simulations presented in the next sections. This energy value is determined by considering a Gadolinium based scintillator for the imaging detector (as used in our experiments) and it allows optimizing the obtainable signal while minimizing the dose delivered to the sample (for more details please refer to Chapter 6).

Simulated sample models: The geometry and characteristics of the input sample models can be defined in two ways in the first part of the code (RI-pcip): 1) by defining it directly by using the Visualization Toolkit (VTK) library (<http://www.vtk.org/>); or 2) by uploading an external input volume. The first way is preferable for very simple geometries. In the second case the volume has to be “prepared” by properly segmenting the experimental data in order to provide the material spatial distribution within the object under study. In all simulations a sample holder consisting of PMMA plastic cylinder with 5 mm thick walls has been considered and included in the definition of the object geometry.

The compositions of the different biological tissues and materials of the simulated sample models and the related optical constants $\delta(E)$ and $\beta(E)$ for the selected X-ray energy (their calculation is described in detail in the Appendix) are reported in tables 3.1 and 3.2, respectively.

Material	H	C	N	O	Na	P	S	Cl	K	Ca
Adipose tissue	0.120	0.640	0.008	0.229	0	0.002	0	0	0	0.001
Glandular tissue	0.102	0.184	0.032	0.677	0	0.005	0	0	0	0
Formaline 10% solution	0.115	0.040	0	0.845	0	0	0	0	0	0
Skin	0.100	0.204	0.042	0.645	0.002	0.001	0.002	0.003	0.001	0
Muscle	0.102	0.143	0.034	0.710	0.001	0.002	0.003	0.001	0.004	0
Cortical bone	0.034	0.155	0.042	0.435	0.001	0.103	0.003	0	0	0.226
Cartilage	0.096	0.099	0.022	0.744	0.005	0.022	0.009	0.003	0	0
Polyethylene (PE)	0.134	0.856	0	0	0	0	0	0	0	0
Polymethylmethacrylate (PMMA)	0.080	0.600	0	0.320	0	0	0	0	0	0

Table 3.1: fractions of the single elements composing the different biological tissues and materials considered in the simulations. The compositions for the breast refer to the work of Hammerstein et al. 1979, while the others are taken from (NIST) . The composition of formalin has been calculated using the manufacturer specifications.

Material	δ_{52}	β_{52}	ρ (g/cm ³)
Air	0	0	1.20e-3
Adipose tissue	7.88e-8	3.65e-11	0.95
Glandular tissue	8.77e-8	4.28e-11	1.04
Formalin 10% solution	9.21e-8	4.53e-11	1.08
Skin	9.16e-8	4.49e-11	1.09
Muscle	8.82e-8	4.34e-11	1.05
Cortical bone	1.52e-7	1.44e-10	1.92
Cartilage	9.22e-8	4.74e-11	1.10
PE	8.13e-8	3.63e-11	0.93
PMMA	9.84e-8	4.60e-11	1.19

Table 3.2: values of the real and imaginary part of complex index of refraction of the materials considered in the simulations calculated for a photon energy of 52 keV and by using the data of table 3.1. The values have been calculated using the software presented in Appendix. For simplicity both the optical constants of air is set to zero.

Three of the presented sample models are obtained directly from the results of PCI CT experiments while the last one (phantom) is mathematically defined directly inside the code (table 3.3). In the case of the three sample models derived from experimental data, a segmentation procedure has been applied to the CT image sets and converted to spatial distributions of the different materials composing the samples (*i.e.* assignment of a defined material to each voxel of the geometry). This part of the procedure was performed by following the indications of the radiologists of the Institute for Clinical Radiology of the Ludwig-Maximilians-University Hospital. An overview of the sample models considered in this work is hereafter presented:

Human knee (figure 3.4a)	<ul style="list-style-type: none"> -This set has been obtained from a PBI-CT data set. -The sample model consists of 1520x1520x17 voxels of size 100x100x100 μm^3. -The segmentation has been performed using a simple thresholding method. -1000 angular projections have been simulated and used for the CT reconstruction. -This sample model is used to compare the out-of-plane and in-plane ABI CT geometries in the case of inhomogenous samples (figure 3.9).
---------------------------------	--

<p>Simple breast (figure 3.4b)</p>	<p>-This sample model is obtained from an ABI-PC data set. -The sample model consists of 620x620x150 voxels of size 50x50x50 μm^3. -A statistical region merging algorithm (Nock & Nielsen 2004) has been used to perform the segmentation. -500 angular projections have been considered. -This sample model has been used in the study of the comparison between the two acquisition geometries presented in section 3.3.4.</p>
<p>Complex breast (figure 3.4c)</p>	<p>-This sample model is obtained from an ABI-PC data set. -The sample model consists of 250x250x10 voxels of size 100x100x1000 μm^3. The volume consists in one slice of 1 mm of thickness. -A statistical region merging algorithm (Nock & Nielsen 2004) has been used to perform the segmentation. -200 angular projections have been simulated. -This sample model has been used in the study of the reconstruction artefacts associated to the use of the EDEI algorithm, and presented in section 3.3.3.</p>
<p>Plastic phantom (figure 3.4d)</p>	<p>-This sample model has been defined considering two coaxial cylinders, and used for simple tests (errors study, figure 3.5). The internal cylinder is made of PE and has a diameter of 6.5 mm and the external one of PMMA with a 15 mm diameter. -The total simulated-imaged height of the phantom has been defined equal to 5 mm. -The voxel size is 50x50x50 μm^3. -250 projections have been simulated and used in the CT reconstructions. -This sample geometry is based on an experimental phantom that we normally use to check the alignment of the experimental set-up in the case of in-plane configuration.</p>

Table 3.3: Sample models used in this work.

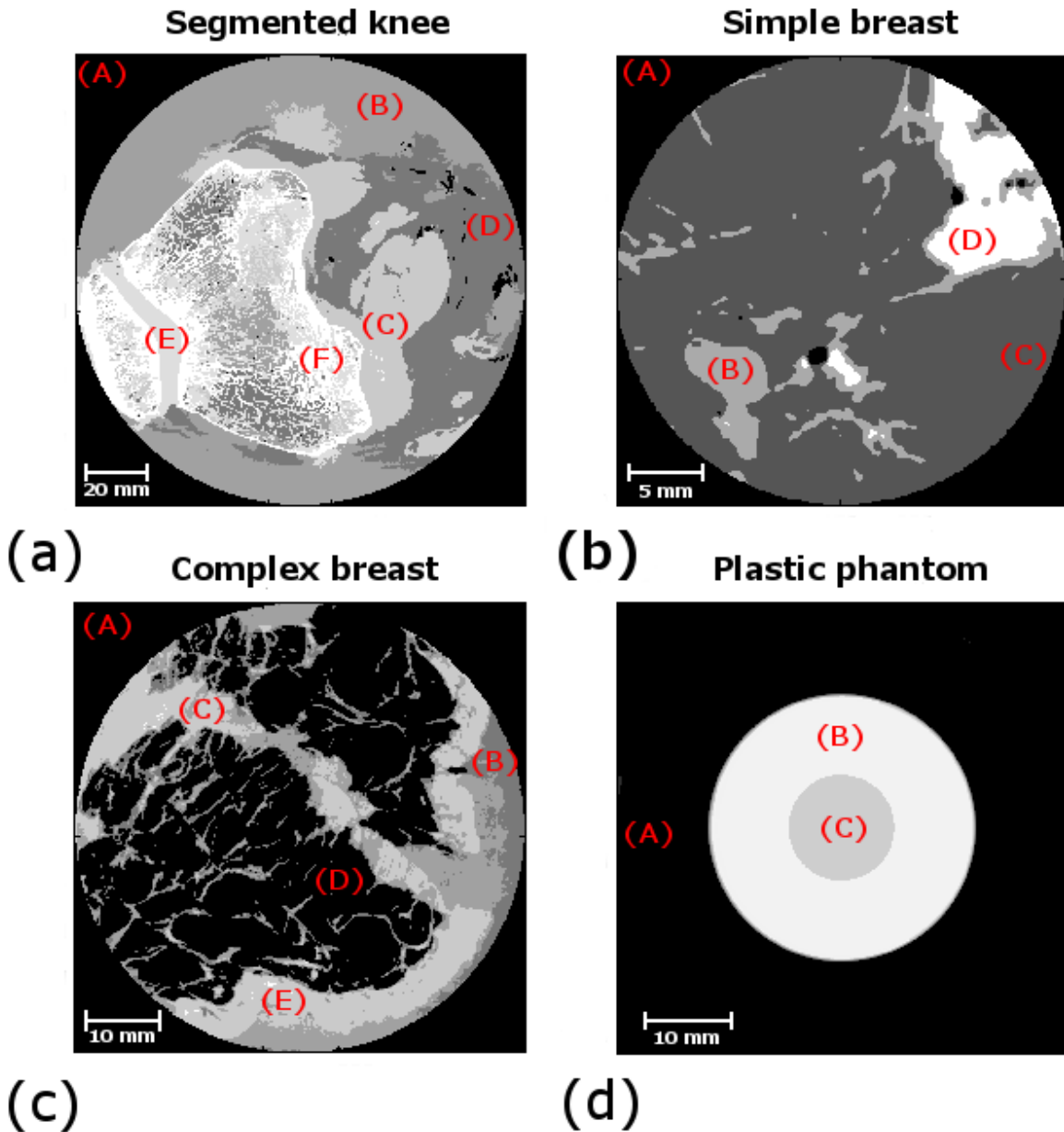


Figure 3.4: Sections of the sample models used in this simulation work. (a) Segmented human knee: (A) is the air, (B) formaline solution, (C) muscle, (D) adipose tissue, (E) cartilage and (F) cortical bone. (b) Segmented “Simple” breast: (A) air, (B) glandular tissue, (C) adipose tissue and (D) skin. (c) Segmented “complex” breast: (A) air, (B) formalin solution, (C) glandular tissue, (D) adipose tissue and (E) skin. (d) plastic phantom, (A) air, (B) PMMA and (C) PE.

Parameters of the X-ray imaging technique (ABI): a symmetrically cut Silicon perfect crystal with Miller index [333] has been used as AC. The system RC (figure 3.3) has been experimentally measured at ID17 and inserted in the code.

Imaging detector: For simplicity the conversion efficiency of the detector has been considered equal to 1.

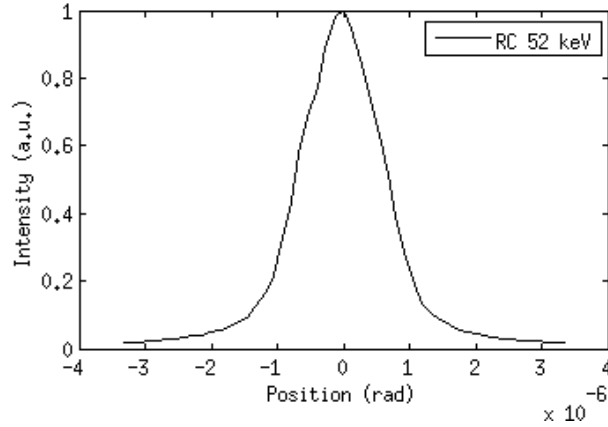


Figure 3.3: experimental RC of the ABI system for an X-ray energy of 52 keV. The RC is approximated with a Gaussian distribution with $\sigma^2 = 3.534e^{-13}$ rad². The curve presents a slightly asymmetry that has to be accounted when experimental data are treated to avoid shifts or stretching of the reconstructed refraction angles when applying the EDEI algorithm.

The simulations are structured and performed following the three separate parts of the RIPCIP, according to the description in section 3.3.1 and in general it can be resumed as:

- Simulation of the interaction between the X-ray and the considered sample model as described previously in section 3.3.2.
- Simulation of the phase-contrast imaging (PCI) experiment: in case of ABI experiment two sets of images are generated at two positions on the slope of the RC. The AC RC is the one of figure 3.3 and the parameters of the crystal are the ones described in section 3.3.2. In case of ABI experiment a different function is used and only the propagation distance has to be defined.
- Application of the EDEI algorithm using the set of two images previously produced and reconstruction of the images following one of the approaches described in section 3.3.2.

The most time consuming parts of the simulations are the calculation of the Radon integrals (*i.e.* X-ray-matter interaction) and the image reconstruction based on the use of a phase-retrieval method. For these steps we generally use the computation resources of ESRF or LRZ clusters and parallelization methods.

3.3.3 Simulations of experimental errors

A class of operations dedicated to the simulations of experimental errors has been implemented in the code. The sources of errors which have been included and studied are:

- **Detector blurring.** This effect is simulated by convolving a user-defined detector PSF and the amplitude of the signal impinging the detector.
- **Detector noise.** This effect has been simulated considering a Poisson distribution.
- **Hotspots:** Detector dead pixels are another problem, which determines the presence of hotspots in the acquired images and, therefore, lead to ring artefacts in the reconstructed CT data. To simulate this effect, a random number generator is used to define the coordinates and the magnitude of the hotspots.
- **Beam intensity drift.** The natural decay of the electron current in the storage ring at synchrotron facilities determines a decrease of the intensity of the X-ray beam over time. During the experiments at the ESRF (and considering filling modes providing the highest electron current), we have a decrease of about $\sim 1.5\%$ per hour of the total intensity. This effect is corrected by regularly acquiring series of white fields (reference images) with a sufficiently time frequency to normalize images.
- **Crystal vibrations.** Crystal vibration in the monochromator system can be another origin of X-ray intensity variations. As for the previous case, this effect can be often corrected by normalization with whitefields. In the case of the ABI technique or other PCI methods based on the use of an analyser optical system (e.g. AC, gratings, coded apertures...), instabilities of this additional element may affect the results. In ABI, we consider that the deviations of the AC from the selected position on the RC follow a Gaussian distribution. An example of the effect produced by this error is shown in figure 3.5b.

The normalization performed using the white field may correct most of the above listed errors. The beam blurring and the detector noise can be reduced by introducing denoising procedures (Chapter 4). The effect of the vibrations of an additional optical element (e.g. AC) cannot be easily corrected. An example of the effect of this error source on the reconstructed images is presented in figure 3.5b. According to the magnitude of the vibrations, this effect can be neglected or not. The vibrations have been simulated by considering a Gaussian distribution for the angular positions of the AC along its RC with a $\sigma = 0.14 \mu rad$; this Gaussian function is centered in the nominal AC angular positions defined in the EDEI algorithm. The simulations of the effects on the reconstructed image of the different error sources have been performed on a test object, which is in our case the plastic phantom previously described. The RGVF approach is used for reconstructing the CT images. All the simulations of this Thesis have been carried out by including all these errors. All simulated data have been linearly normalized using a reference material (usually the PMMA of the container).

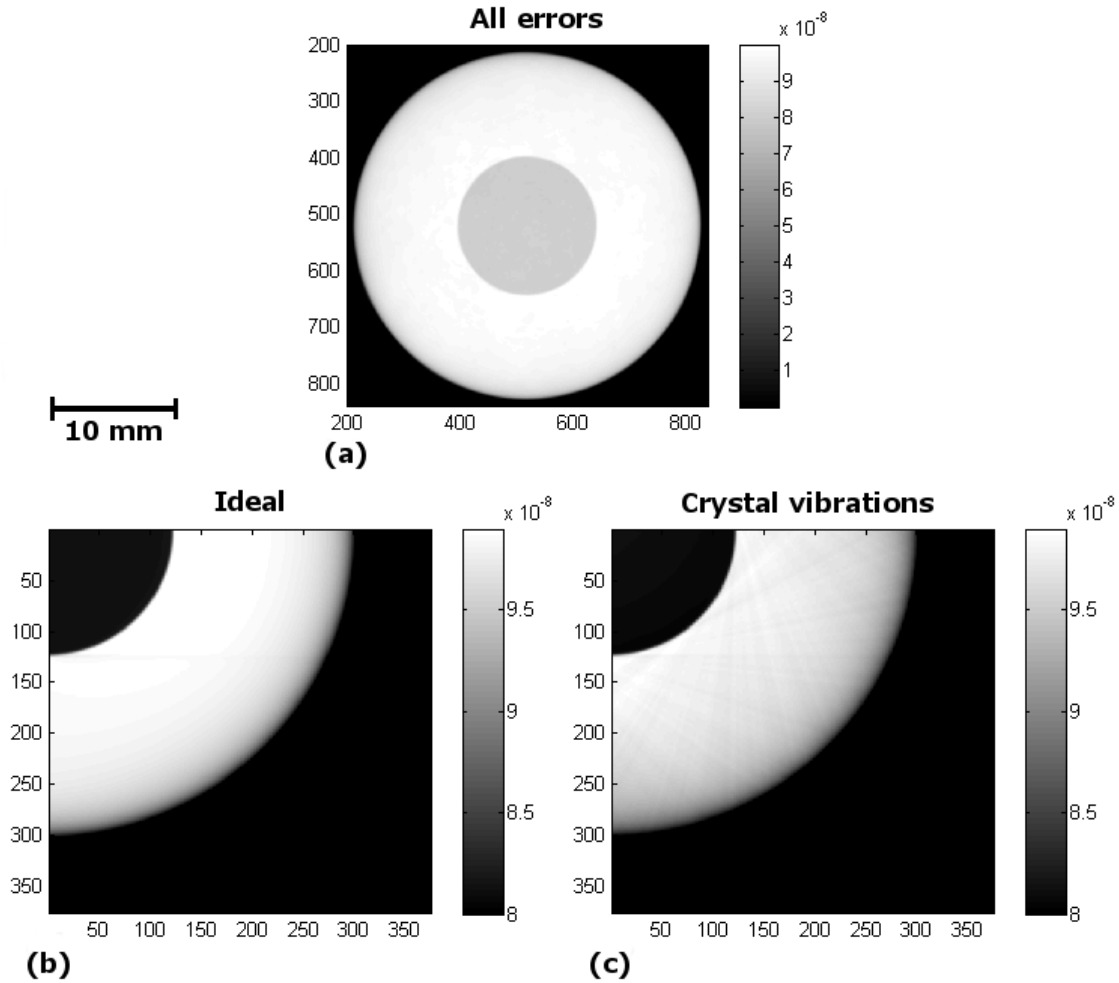


Figure 3.5: Zoomed views (b, c) in a portion of a reconstructed axial CT slice of the plastic phantom. (a) overview of the entire plastic phantom simulated with all the errors active; simulated image obtained (b) without considering any error source and (c) with the effect of the crystal vibrations. It is possible to see the streak artefacts induced by the instability of the optical element (AC). The different layers visible in (b) are due to the so-called dishing artefact, which will be described in the next section. The grey colour bars represents the value of the reconstructed δ . The contrast of the images (b) and (c) has been intentionally stretched to highlight this effect. The reconstruction of the distribution of δ have been performed using the RGVF approach.

3.3.3.1 Discontinuities between materials with very different optical constants

The presence within the same sample/object of materials with very different optical properties (e.g. air and tissue) can be critical in the CT reconstruction of the index of refraction and can produce artefacts. This effect is particularly important in ABI and has been studied by comparing experimental and simulated PCI-CT images of the plastic phantom described in table 3.3. Results are shown in figure 3.6. The effect is more pronounced at the air-PMMA interface; while in the case of the PMMA-PE interface the experimental

signal is very close to the theoretical one. This effect is indicated as “dishing” effect and it appears as a sort of smoothed/reduced signal in the region close to the interface. In figure 3.7 results for the simple breast model are presented. Three different AC reflections have been considered: Si(111), Si(333) and a ‘fake’ case in which a RC with a FWHM 50 times larger than the RC for a Si(333) is used. This “exaggerated” case is included for highlighting the role of the AC characteristics in this kind of effect. The used RC curves have been theoretically calculated using the software XOP (del Río 2004).

It is possible to see how the narrower the RC is, the bigger is the artefact on the reconstructed images. Besides the experimental error source linked to the chosen AC reflection, this effect is also related to the specific algorithm employed to separate the different components of the signal, the EDEI algorithm in this work. In the case of large refraction angles (*i.e.* at interfaces), the extracted refraction angles values obtained using this method are incorrectly calculated: the signal is underestimated giving rise to the “dishing” effect. By using a very large RC (figure 3.7) it is possible to notice how the effect can be reduced. Another example is presented in figure 3.8 for the complex breast geometry described in table 3.3. The CT reconstructions presented in this section have been performed using the GFBP method previously described.

In figures 3.8a and 3.8b the results obtained without and with a PMMA container with a wall of 3 mm of thickness are reported. The profiles presented in figure 3.8c clearly show how a small layer surrounding the sample is sufficient to reduce the artefacts due to the dishing effect. As shown, these artefacts can strongly affect the signal intensity and contrast. Several features disappear due to the important smoothing of the signal caused by the interface with air. From the profiles of figure 3.6 and figure 3.8c it is possible to notice that the reconstructed values can show differences up to 50% in the region interested by this artefact. This effect is more important for sample of small dimensions (few centimeters of size).

All the simulations presented in this section have been carried out without considering the other error sources discussed in section 3.3.3.

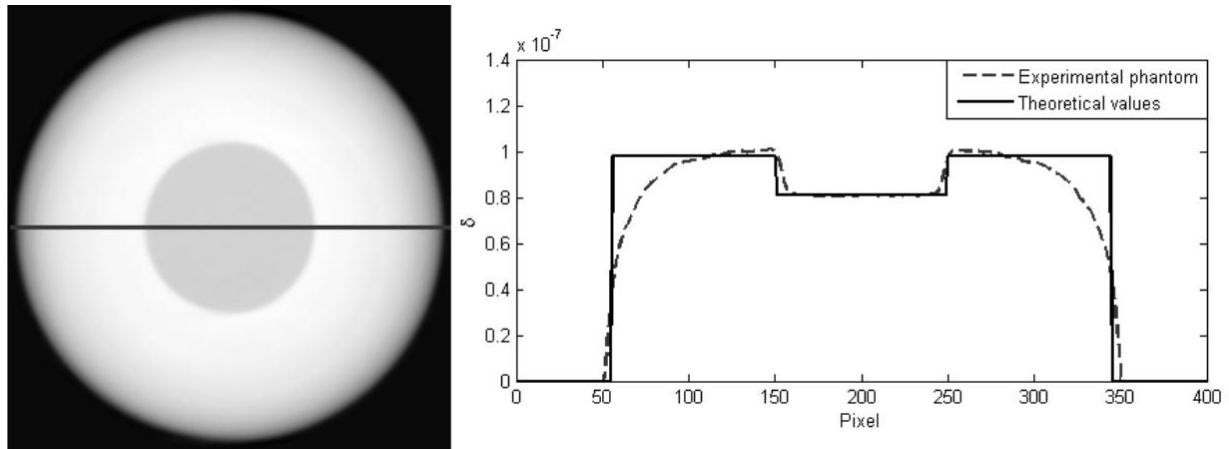


Figure 3.6: (Left) reconstructed index of refraction CT image of the plastic phantom (from experiment). The profile along the black line in the left image is compared with the simulated theoretical signal (table 4.2).

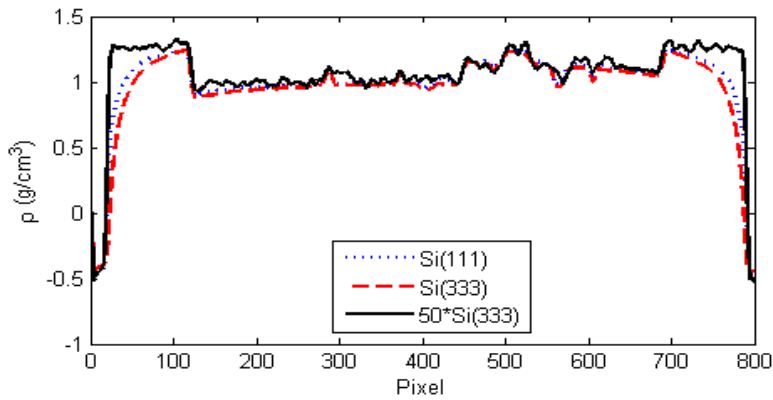


Figure 3.7: profiles along the reconstructed images, considering the complex breast sample model, using three different AC reflections: the blue dotted line correspond to a Si(111); the red dashed line to a Si(333); the continue black line to a 'fake' RC with a FWHM=50*FWHM(Si(333)). The CT reconstructions have been performed using the GFBP approach.

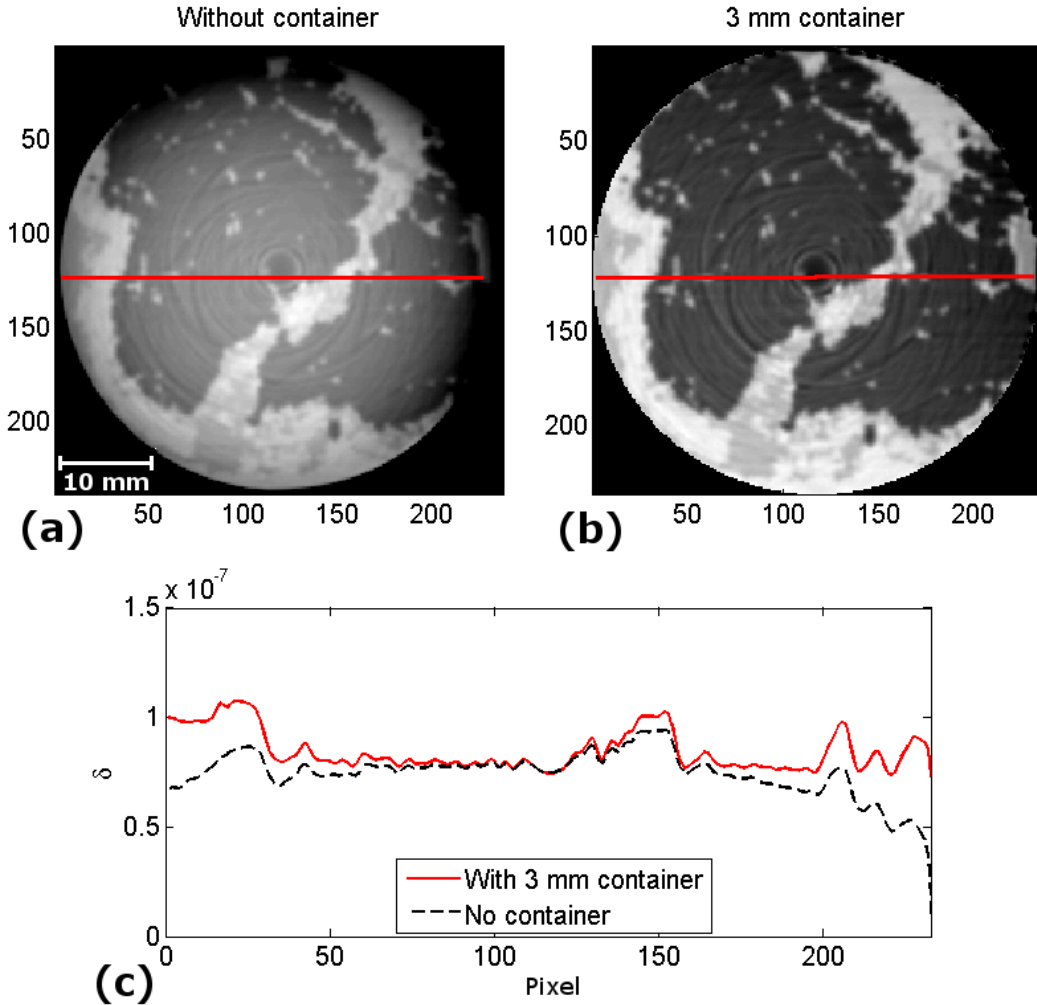


Figure 3.8: Results of a simulation performed by considering the complex breast sample without (a) and with (b) a PMMA container with 3 mm thick walls; (c) profiles along the red lines of (a) and (b). The solid red line corresponds to the image (b) while the dashed black line to image (a).

3.3.4 Comparison between the out-of-plane and in-plane CT geometries

In this section a comparison of the results obtained from the simulations performed using the in-plane and the out-of-plane acquisition geometries are presented. As study cases I have considered the human knee and simple breast modelled samples. Experimental results of this comparison are instead reported in Chapter 4 for a whole human breast specimen. The comparison is performed by reconstructing the refraction angle and the distribution of δ which has been converted into the material density by using the asymptotic electrodynamics expression $\sim k\delta$, where k is a material independent constant at a given photon energy (L. D. Landau 1974). Results are shown in figures 3.9 and 3.10 for the human knee and the simple breast, respectively. All the images have been reconstructed using the FBP algorithm with the ramp filter.

In figures 3.9c, 3.9d the distribution of δ is obtained by performing the phase-retrieval on projections, following the approach described in section 3.3.4. For both the in-plane and out-of-plane geometries the Dirichlet boundary conditions are used to perform the phase-retrieval. A regularization term, set as $\gamma=0.02$, has been used as well to suppress the streak artefacts occurring during the integration. It is possible to notice that, due to the nature of the signal (the in-plane geometry is sensible to both y, z directions, while with the out-of-plane configuration the sensitivity is only along the y direction, figure 3.2), the results obtained with the in-plane geometry lead to an evident superior depiction of the internal features of the object in both the refraction angle and the δ (or density) reconstructed CT images in both axial and sagittal slices (figures 3.9, 3.10 and 3.11). The different appearance of the same tissues and structures between the in-plane and out-of-plane cases is due to their different orientation with respect to the sensitivity plane of the AC. In the case of the knee modelled sample, the structures to be visualized are mainly oriented along a direction parallel to the sensitivity one of the AC, thus the results of the phase-retrieval for the out-of-plane geometry provide very few information compared to the in-plane geometry. From figure 3.11, it is possible to see that the reconstructed distribution of δ (converted into density) obtained with the in-plane geometry have values which are in better agreement with the theoretical values reported in table 3.2 compared to the out-of-plane geometry results. The errors in the quantitative reconstruction of the δ (density) distributions are due to the difficulties in imposing the correct boundary conditions during the phase-retrieval. Moreover the presence of artefacts related to the phase-retrieval procedure used for the out-of-plane geometry lead to different mean values of δ for the same material in different regions in the reconstructed images. It is important to notice that the results are strictly related to the kind of sample used in the simulations, how it will be discussed also in Chapter 4. The quantitative results obtained for the simple breast modelled sample after the phase-retrieval are reported in table 3.4.

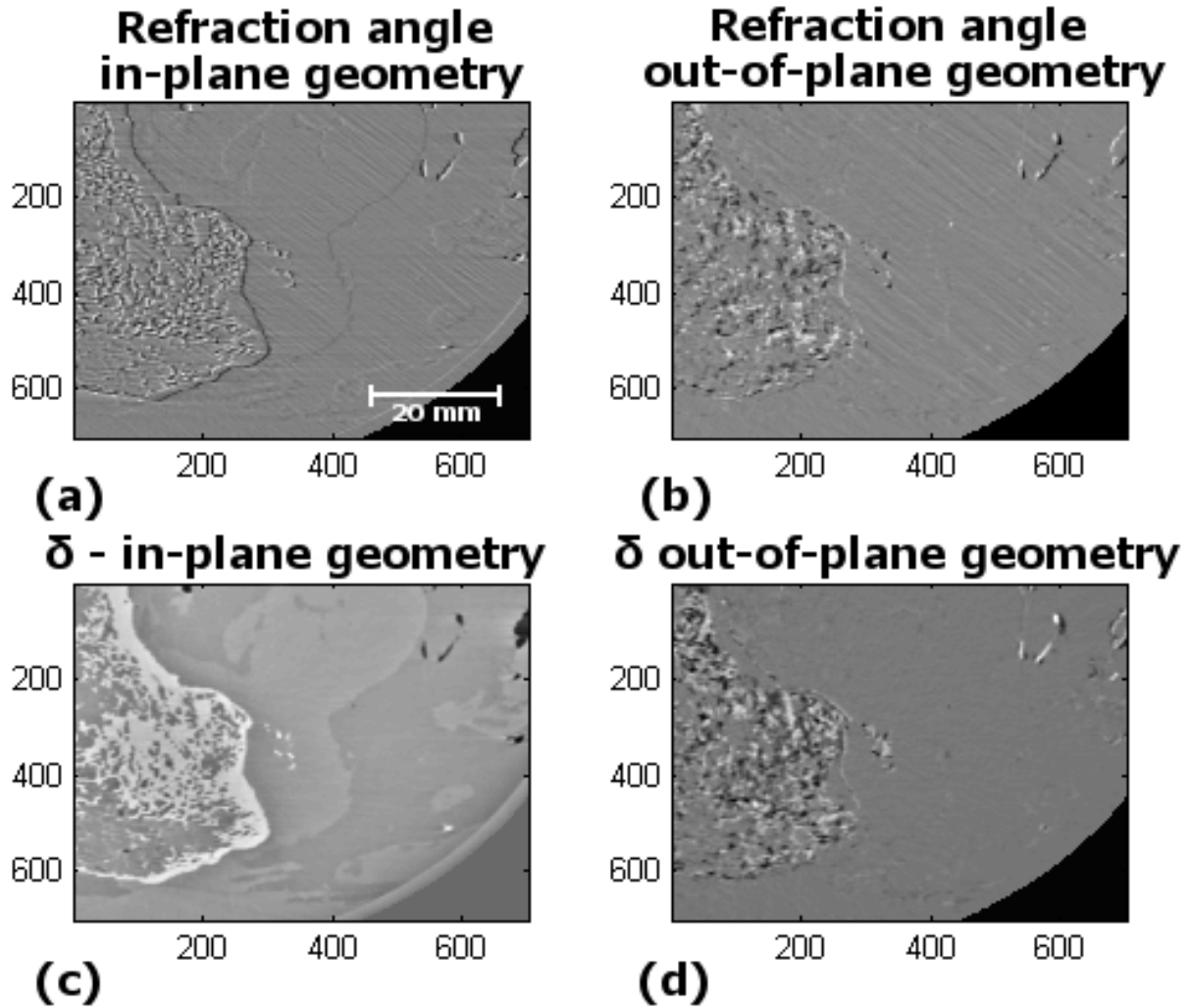


Figure 3.9: comparison of the results obtained with the in-plane and out-of-plane CT geometries for the human knee modelled sample (figure 3.4a). (a) Refraction angle distribution derived with the in-plane geometry; (b) reconstruction of δ distribution (after phase-retrieval) obtained with the in-plane geometry; (c) refraction angle distribution obtained with the out-of-plane geometry; (d) reconstruction of δ distribution (after phase-retrieval) obtained with out-of-plane geometry.

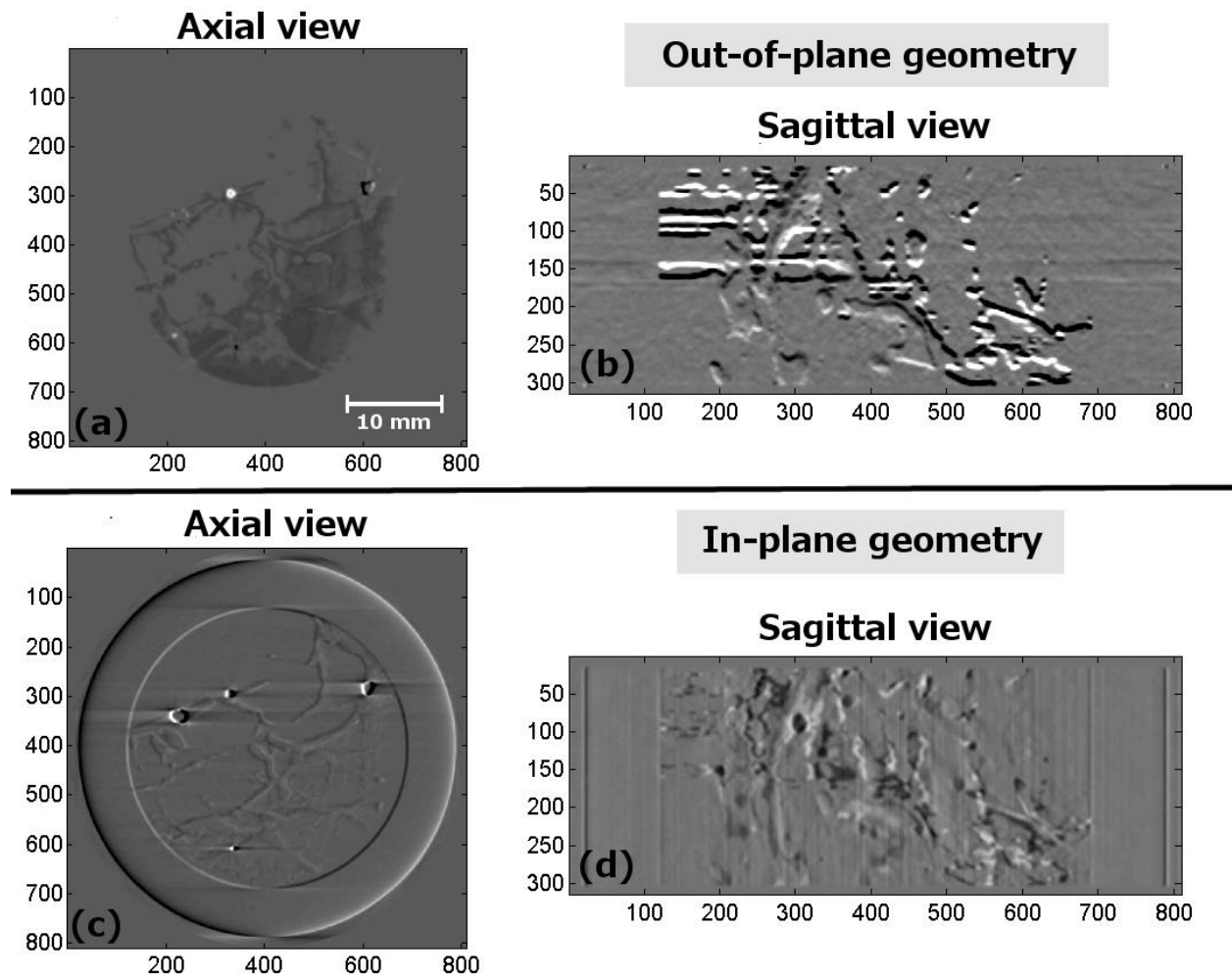


Figure 3.10: reconstruction of the refraction angle distribution in the case of the simple breast geometry (figure 3.5b). Axial (a) and sagittal (b) slices of the refraction angle distribution obtained with the out-of-plane geometry. Axial (c) and sagittal (d) slices of the refraction angle distribution obtained with the in-plane geometry. The present of air bubbles of air in the volume, lead to several streak artefacts. The boundaries of the container are not visible in the case of out-of-plane geometry because of the nature of the signal (*i.e.* sensitivity direction). The Mean Glandular Dose for these simulated results has been calculated using the database presented in Chapter 6 and is about ~ 4 mGy.

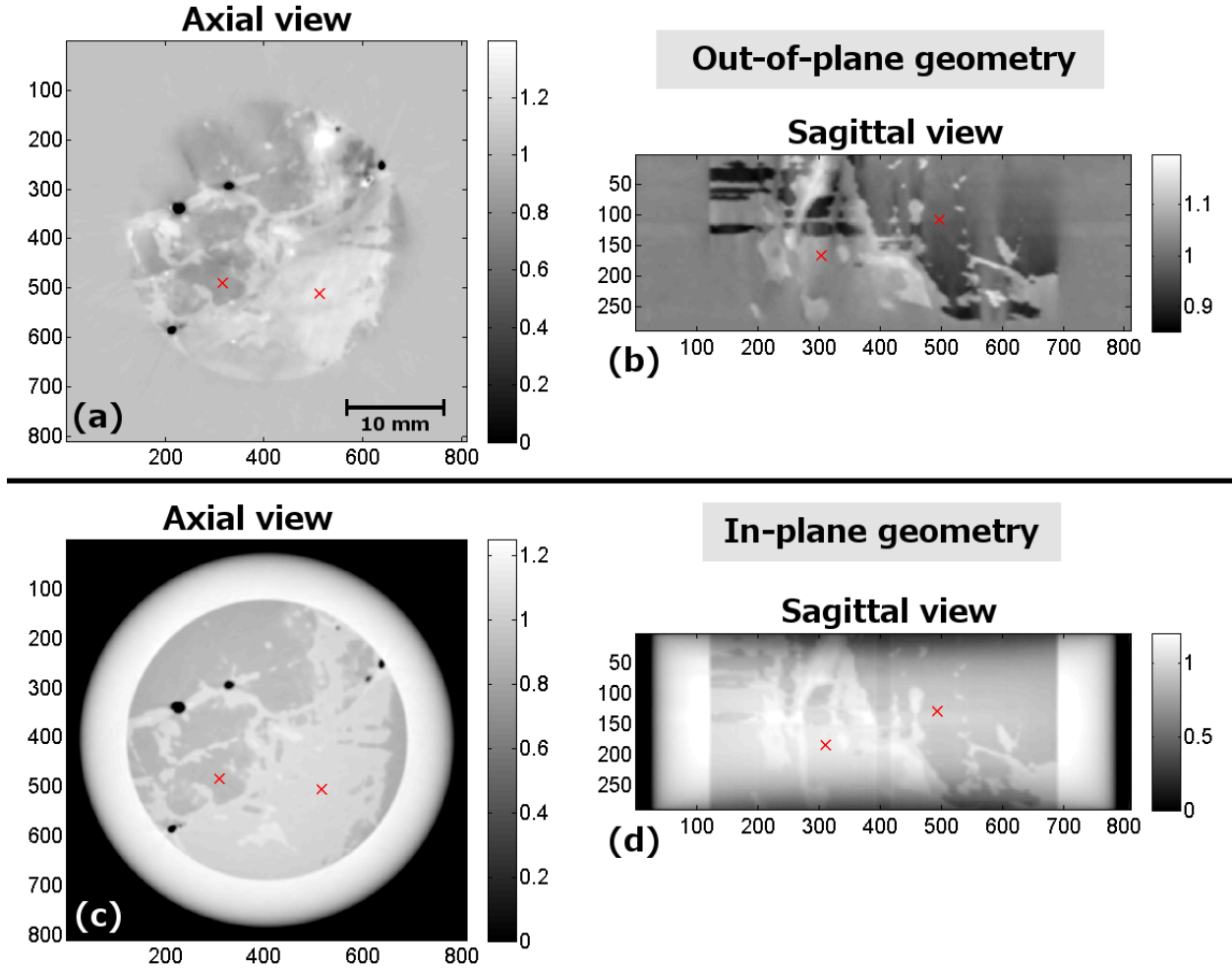


Figure 3.11: reconstruction of the δ distribution, converted into density values, in the case of the simple breast geometry (figure 3.5b). (a) Axial view and (b) sagittal view of the reconstructed density obtained with the out-of-plane geometry; (c) axial view (d) sagittal view of the reconstructed density using the in-plane geometry. The black details within the sample are air bubbles, while the brighter regions (higher density) are skin. The remaining surrounding material consists of adipose tissue. The boundaries of the container are not visible in the case of out-of-plane geometry because of the nature of the signal (*i.e.* sensitivity direction). The horizontal darker stripes visible on the top left of figure (b) and (d) are due to a defect in the segmentation.

Case	$\bar{\rho}$ adipose (g/cm^3)	STD	SNR	$\bar{\rho}$ glandular (g/cm^3)	STD	SNR
Out-of-plane axial	0.87	0.0031	281	1.22	0.0073	167
Out-of-plane sagittal	0.97	0.0007	1586	1.06	0.0034	312
In-plane axial	0.92	0.0038	242	1.05	0.0032	328
In-plane sagittal	0.96	0.0009	1067	1.11	0.0007	1586

Table 3.4: quantitative results obtained for the simple breast geometry after the phase-retrieval. The values have been measured in the regions indicated with the red crosses in figure 3.11. It is possible to notice that in the case of the out-of-plane geometry quantitative results are less accurate with respect to the ones in case of in-plane geometry. The expected theoretical values are $0.95 \text{ g}/\text{cm}^3$ for the adipose tissue and $1.04 \text{ g}/\text{cm}^3$ for the glandular tissue. STD is the standard deviation calculated in the area used

for the measurement while the SNR is the signal to noise ratio, and it has been calculated as $SNR = \mu/\sigma$, where $\mu = \bar{\rho}$ is the calculated mean value in the considered region and σ its standard deviation.

Combining the RGVF approach or the phase-retrieval not with the FBP but with more advanced CT reconstruction algorithms (like for example the Equally Sloped Tomography algorithm, Zhao et al. 2012), it is possible to decrease the dose of a factor of about ~ 4 by reducing by the same amount the number of projections required for the CT reconstruction, without any loss in the image quality.

3.4 Conclusions

The aim of this simulation study was to investigate the best experimental configuration and acquisition parameters for ABI CT experiments for biomedical applications. I have contributed in the development of a simulation code within our group by implementing a series of functions and tools for the analysis of the effects on the CT reconstructed data of different experimental error sources. This work may allow a deeper understanding of the mechanisms producing different image artefacts and development of optimized correction strategies. Among the others, the study of the **effect of interfaces between materials showing very different optical properties** (for example the interface between air and the sample) is important for PCI CT experiments. This analysis has demonstrated that **the quantitative CT reconstructions of the index of refraction may be importantly affected** (differences in the calculated density up to 50% in proximity of the interfaces) and the visibility, in terms of image contrast, is reduced. In Chapter 4 I will show that the results of these simulations are confirmed by the experimental data. The “dishing” effect may be particularly critical in ABI-CT (or gratings or coded aperture) experiments. The effect is related to both the analyser system (a perfect crystal in ABI) and the choice of the algorithm used for the quantitative analysis of the data. The EDEI algorithm, which I have applied in this work, gives incorrect results when the refraction angles are large. **This artefact is remarkably pronounced in the case of small samples; however it has been shown that it can be reduced by the use of containers with walls of few millimeters of thickness.**

By using the RIPCIP code two possible configurations for PCI CT acquisitions have been compared: the so called in-plane geometry and the out of plane geometry. These two configurations are not equivalent, since they provide a different sensitivity with respect to the variation of the index of refraction distribution in the sample. **The results of the simulations performed for the in-plane configuration present superior image quality, accuracy and therefore a better visibility of the sample details.** This evidence is due to the fact that the reconstructed CT slice in the in-plane geometry corresponds to the plane of sensitivity of the AC and contained information along two directions, while in the out-of-plane configuration the reconstructed slice is perpendicular to the AC sensitivity plane and, consequently, it is sensible only along

the direction of sensitivity of the AC. Additionally the difficulty in imposing the correct boundary conditions necessary to retrieve the phase represents an important limitation for the quantitative computation of the index of refraction when using the out-of-plane configuration. To this purpose further developments are still required. Another advantage of using the in-plane geometry is related to the possibility to reconstruct the distribution of the δ (density) by applying different CT reconstruction approaches (e.g. the GFBP, the RGVF and the one based on a phase-retrieval method...), while for the out-of-plane configuration only the phase-retrieval based CT reconstruction method can be used. The comparison of the results obtained by using the three different approaches described for the in-plane geometry has been published in Gasilov et al. 2014. As a conclusion, we can state that the choice of the best CT configuration has to be made depending on the main orientation of the structures to be visualized and study within the object.

All the simulations with modelled biological tissues have been performed considering clinical compatible doses (few mGy).

Chapter 4 - Phase-contrast tomography: experimental results

4.1 Experimental acquisitions.....	91
4.1.1 Comparison between the index of refraction CT and the absorption CT.....	92
4.1.2 Comparison of the two different CT acquisition geometries	94
4.2 The problem of image deconvolution.....	99
4.2.1 The deconvolution algorithm.....	100
4.2.2 Point Spread Functions	101
4.2.3 Application of the deconvolution procedure on experimental images.....	101
4.2.3.1 Wavelet denoising.....	104
4.3 Conclusions.....	109

4.1 Experimental acquisitions

The experimental study and optimization of the index of refraction CT imaging have been done through experiments performed using the analyser-based imaging (ABI) technique. The aims of the experiments can be resumed as follows:

- To study the performances in term of **accuracy in the detection of different biological tissues** by comparing the results of the index of refraction CT with the absorption CT (experiment 1, table 4.1).
- **To compare the two acquisition geometries** (in-plane and out-of-plane) employed for the reconstruction of the index of refraction (experiments 2, 3, table 4.1).
- **To improve the quality of the reconstructed images** by means of a deconvolution procedure (experiment 2, table 4.1).

In all the experiments a double Si(111) Laue crystal monochromator has been used to select a quasi-monochromatic ($\Delta E/E \sim 10^{-4}$) from a quasi-parallel X-ray beam issued from a 21-pole wiggler, having a divergence <1 mrad in the horizontal plan and <0.1 mrad in the vertical one. The photon energy used for the experiments was 51 keV. To analyse the X-ray beam after its propagation through the sample a 3 cm thick, symmetrical, Si (333) Bragg monochromator has been employed. A second identical crystal placed just upstream the sample has been used as pre-monochromator. The detector employed was a charge-coupled device detector (CCD) combined with a gadolinium-based fluorescent screen to convert the X-ray to visible light (Chapter 2).

Three separated experiments have been performed using two different formalin-fixed whole human breast samples presenting different diameters:

- **Breast L:** it presents an invasive breast cancer type NST (non-specific type) after neoadjuvant chemotherapy with poor treatment response (maximum diameter 6.2 cm). The sample is embedded in a 10 cm diameter PMMA container of 0.5 cm thickness.
- **Breast S:** it presents an invasive breast cancer NST of 2.6 cm diameter. The sample is embedded in a 7 cm diameter PMMA container of 0.5 cm thickness.

All the samples have been provided by the Department of Pathology of the Ludwig Maximilians University.

Experiment 1	<ul style="list-style-type: none"> -Sample: breast L. -Full Width at Half Maximum (FWHM) rocking curve (RC): 1.9 μrad. -Different sets of images have been acquired using: (a) the in-plane geometry for the index of refraction computed tomography (CT) (b) absorption setup, <i>i.e.</i> without analyser crystal (AC). -500 projections acquired at two different positions on the RC. -Effective pixel size: 96x96 μm^2.
Experiment 2	<ul style="list-style-type: none"> -Sample: breast S. -FWHM RC: 1.7 μrad. -In-plane geometry. -500 projections acquired at two different positions on the RC. -Effective pixel size: 98x98 μm^2.
Experiment 3	<ul style="list-style-type: none"> -Sample: breast S. -FWHM RC: 1.7 μrad. -Out-of-plane geometry. -500 projections acquired at two different positions on the RC. -Effective pixel size: 98x98 μm^2.

Table 4.1: Overview of the parameters and samples used in the studies presented in this Chapter.

4.1.1 Comparison between the index of refraction CT and the absorption CT

In order to evaluate the performances of the index of refraction CT in term of accuracy in the depiction of different biological tissues with the in-plane geometry, a quantitative study comparing this method with absorption tomography is presented in this section. The setup used for the acquisition of the absorption images was identical to the one used with the in-plane geometry but without the AC. Due to the small sample-to-detector distance the effects due to the Fresnel propagation can be neglected. The GFBP algorithm has been used to reconstruct the fluctuations of the index of refraction (converted in densities, see Chapter 3) and the filtered backprojection (FBP) with a ramp filter to reconstruct the absorption images. To convert the reconstructed quantity to density values in the case of the absorption images the asymptotical electrodynamics expression $\rho \sim t\mu$ is used, where t is a material-independent constant at a given X-ray energy (L. D. Landau 1974). The results of CT reconstructions are reported in figures 4.1a, b, where a zoomed view in a part of the reconstructed CT image is shown (c, d) for both the density distributions obtained from the index of refraction CT and absorption CT. The average measured values of densities $\bar{\rho}$ of the different tissues and the corresponding Signal to Noise Ratios (SNR) are reported in table 4.2. The $\bar{\rho}$ and the SNR, defined as the ratio between the calculated mean value and its standard deviation, are calculated in the coloured regions marked in figures 4.1a, b.

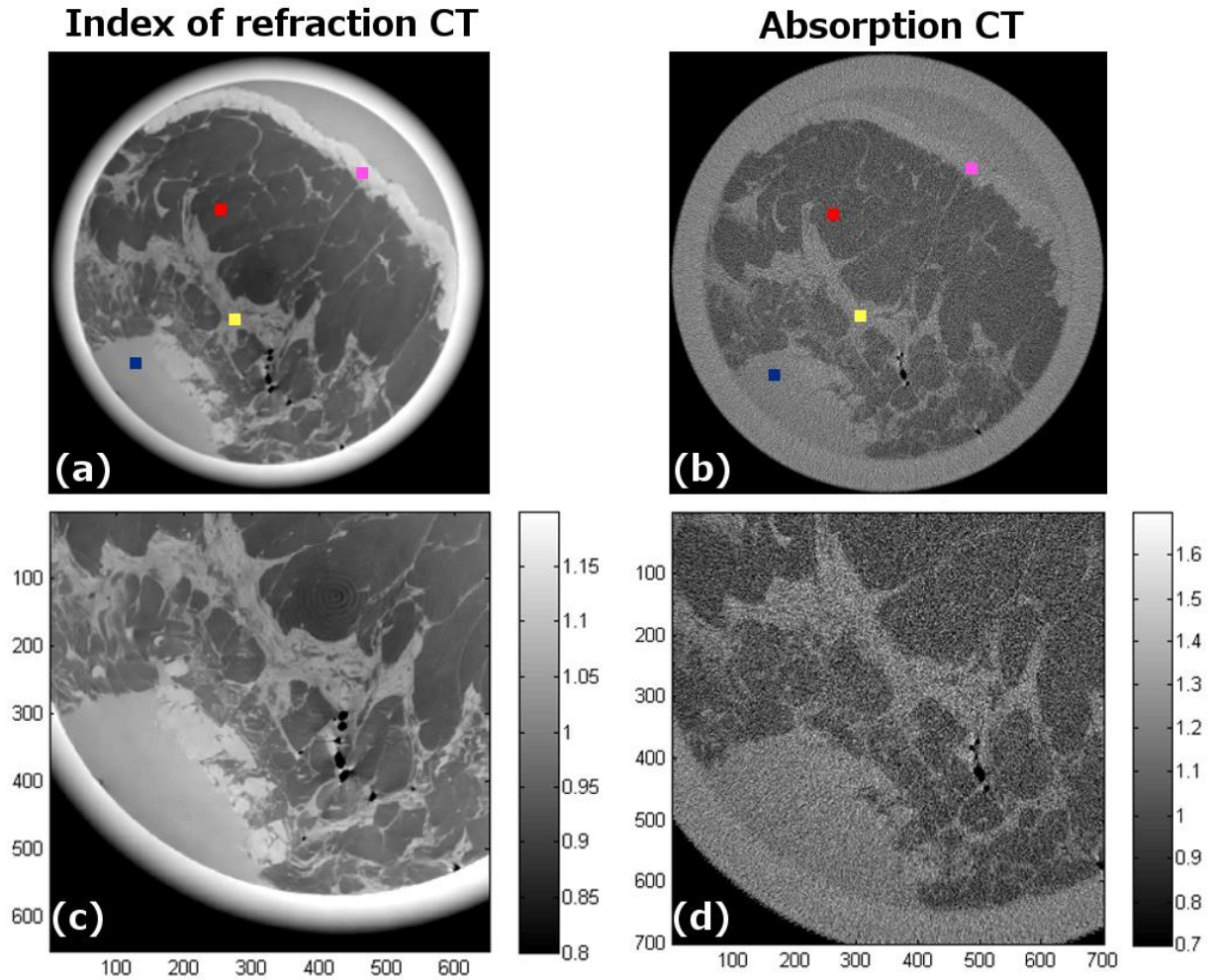


Figure 4.1: Comparison between the reconstructed images using the in-plane geometry (a) and the absorption image (b). Zoomed views within a CT slice reconstructed (c) of image (a) (d) of image (b). The grey colour bars represent the values of reconstructed densities (in g/cm^3). It is possible to notice how the level of noise and the relative incertitude of the different tissue are much higher in the absorption images (b), (d). The values of SNRs reported in table 4.1 have been calculated in the region marked by: red squares (adipose tissue); blue squares (formalin 10% in water); purple squares (skin); yellow squares (glandular tissue).

Material	Expected $\bar{\rho}$ (g/cm^3)	Measured Refraction CT $\bar{\rho}$ (g/cm^3)	Absorption CT $\bar{\rho}$ (g/cm^3)	SNR Refraction CT	SNR Absorption CT
Adipose	0.95	0.97 ± 0.01	0.94 ± 0.12	97	8
Skin	1.09	1.13 ± 0.03	1.13 ± 0.10	38	11
Glandular	1.04	1.05 ± 0.02	1.13 ± 0.13	52	9
Formalin 10%	1.08	1.10 ± 0.02	1.10 ± 0.10	55	11

Table 4.2: Estimation of the density of different materials derived using the in-plane geometry and the absorption reconstructions. The measurements are taken in different regions of the image marked in figure 4.1 by the coloured squares.

A calibrated ionization chamber (PTW 31010, PTW, Freiburg, Germany) has been used to measure the incoming fluence during the acquisitions. The measured photon fluences are $(9.72 \pm 0.04) \times 10^8$ photons/mm² for the in-plane configuration and $(3.10 \pm 0.02) \times 10^{10}$ photons/mm² for the absorption images. The simulations for the calculation of the mean glandular dose have been performed using the GATE program (Chapter 5). The obtained values are ~120 mGy for the in-plane geometry and ~340 mGy in case of the absorption images.

This study shows that, for the case considered, the index of refraction CT produces more accurate results (3-10 times larger SNR values) than the absorption tomography. The obtained values of $\bar{\rho}$ are in a good agreement with the expected values (table 4.1); these results were obtained using a dose that in the case of refraction CT was ~3 times smaller. The improved accuracy by using the index of refraction CT can be explained by making two considerations:

- The amount of the high frequency noise component is partially reduced by the inherent properties of the filter function (flat function) used in the reconstruction (Chapter 3) while in the case of absorption CT the use of the ramp filter amplifies the high frequency components of the noise.
- The presence of the AC assures in the index of refraction tomography an almost complete rejection of scattered photons that leads to an additional reduction of the noise.

The reported results have been presented in the publications by Gasilov et al. 2013.

4.1.2 Comparison of the two different CT acquisition geometries

In this section the results of the comparison using the out-of-plane and the in-plane geometries for the index of refraction CT are presented. A quantitative comparison is performed for the density distributions images by studying the average mean values and SNRs of the adipose tissue (in the axial views) and of the skin and the adipose tissue (sagittal views). The entire volume of the sample has been imaged in CT for the in-plane geometry (~8 cm in height) while a reduced region (~3 cm in height) has been investigated using the out-of-plane geometry).

The comparison of the results obtained with the two geometries, respectively, is presented in figures 4.2-4.5. Both the reconstruction of the refraction angles (figures 4.2, 4.4) and the distribution of density (derived from values of δ) have been performed (figures 4.3, 4.5). In order to reconstruct the distribution of δ the method based on phase-retrieval has been applied on the angular projections acquired in both the geometries. The phase-retrieval procedure follows the method described in the Chapter 3. The regularization term used in the phase-retrieval to suppress the streak artefacts was set as $\gamma = 0.05$ for the in-plane and $\gamma = 0.02$ for out-of-plane geometry, respectively.

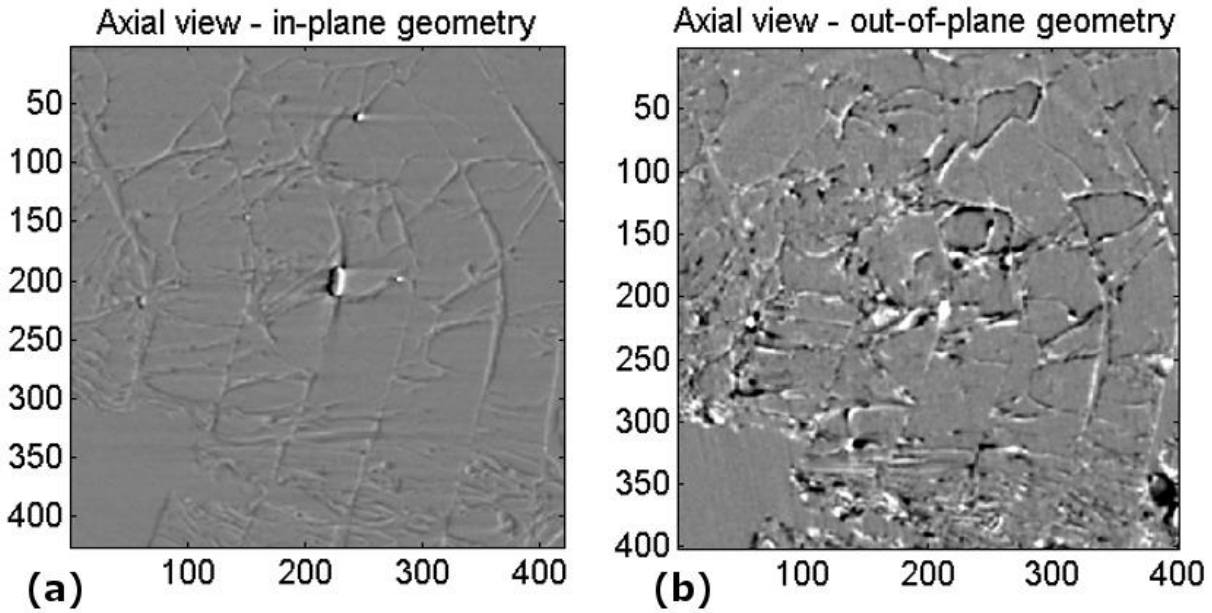


Figure 4.2: Reconstructed axial slices of the refraction angle for the in-plane and out-of-plane geometries.

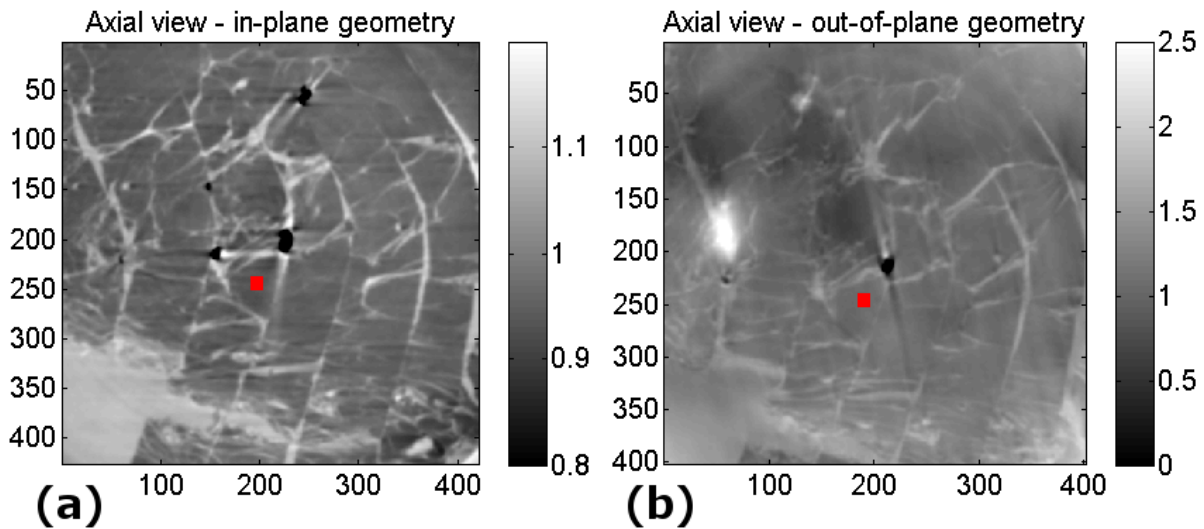


Figure 4.3: Reconstructed axial slices of the distribution of δ . Comparison between the in-plane, image (a), and out-of-plane, image (b), geometries. The white spot in figure (b) is an artefact due to a big bubble of air present in a different slice of the volume and appearing when the phase-retrieval is applied. Air bubbles are slightly different both in number and shape because the two experiments were performed at different times. The values of SNRs presented in table 4.3 are calculated in the regions marked by the red squares (adipose tissue).

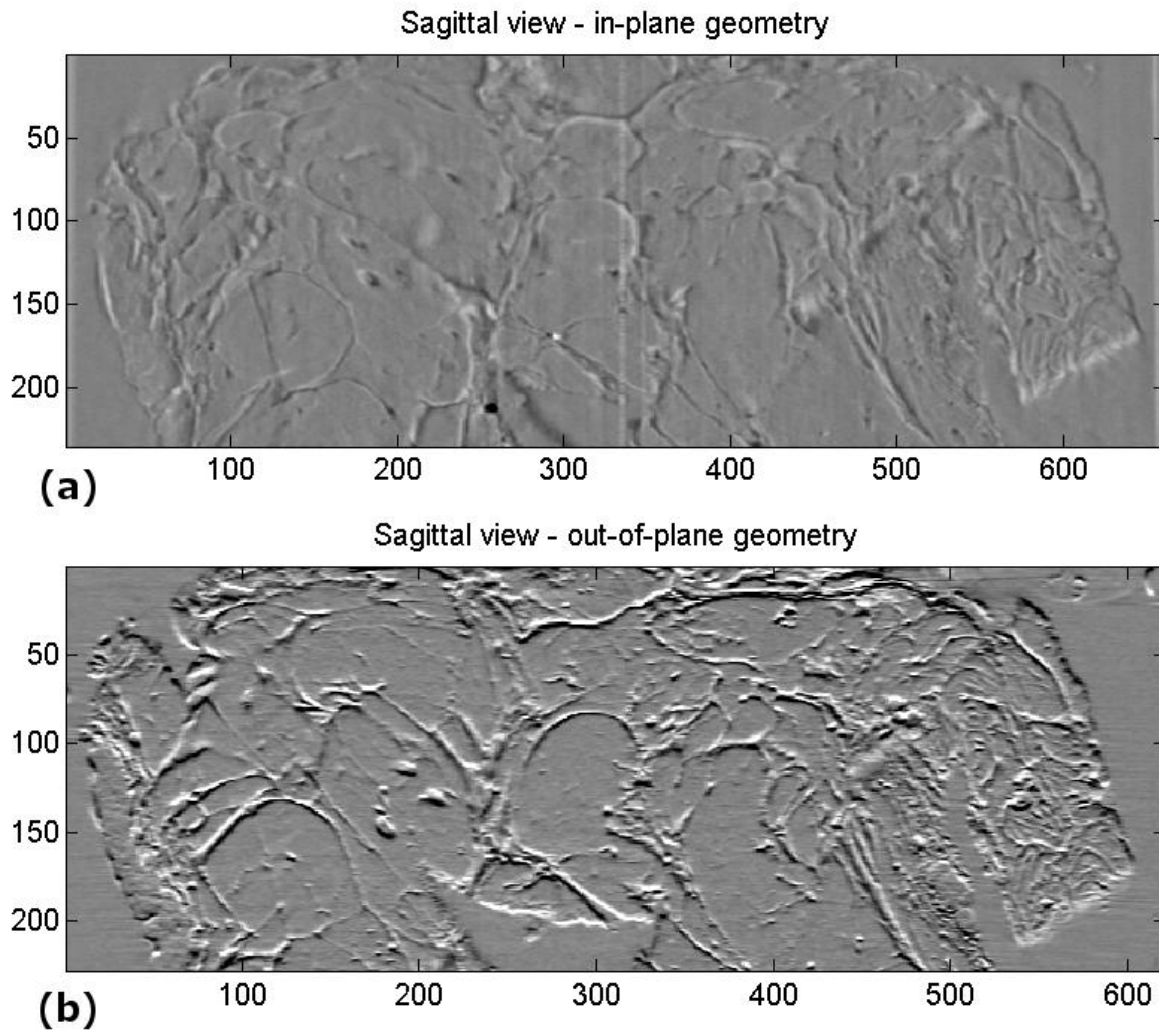


Figure 4.4: Comparison of reconstructed CT sagittal slices of the refraction angle obtained with the in-plane (a) and out-of-plane (b) geometries. The out-of-plane configuration allows in this case a superior depiction of the internal structures of the breast tissue.

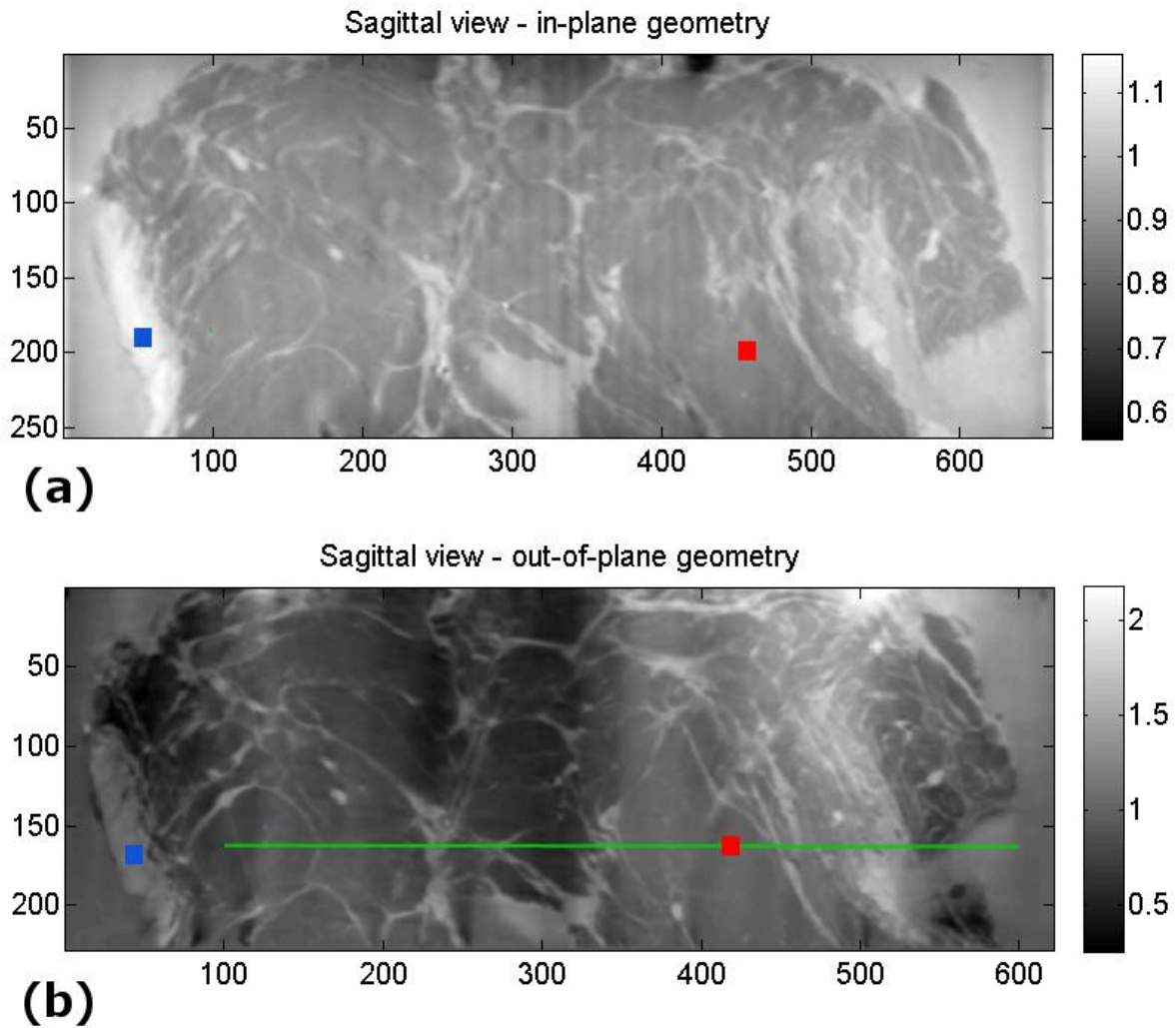


Figure 4.5: Reconstruction of the distribution of the tissue density (derived from δ values). In-plane geometry (a) and of the out-of-plane geometry (b) in the case of sagittal views. The grey bar is expressed in g/cm^3 . Several air bubbles are present in our sample but are not visible in these figures because only a portion of the reconstructed volume is shown here. The presence of such bubbles causes many artefacts, among them the appearance of darker/brighter regions (as visible from the fluctuations of the profile reported in figure 4.6) in the image (b). The values of SNRs presented in table 4.4 are calculated in the regions marked by the red squares (adipose tissue) and by the blue squares (skin). The plot of profile along the green line in (b) is reported in figure 4.6.

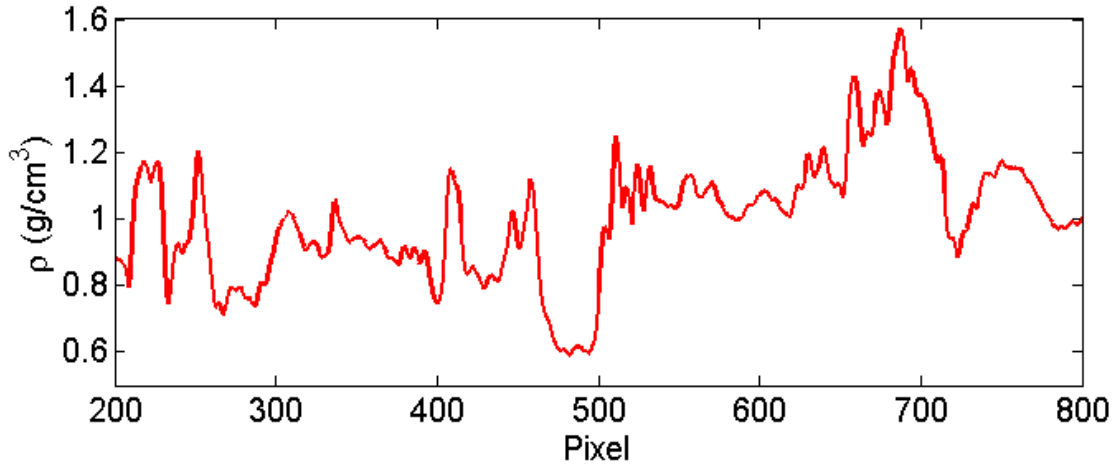


Figure 4.6: Profiles along the green line of figure 4.5. It is possible to notice how the artefacts related to an incorrect definition of the boundary conditions during the phase-retrieval and due to the presence of air bubbles (not visible in figure 4.5), lead to global shift in the values of $\bar{\rho}$. For example, it is possible to notice that average $\bar{\rho}$ when the pixel position is >500 is higher than the average values for pixels <500 .

The in-plane geometry presents a SNR ~ 3 times higher respect to the out-of-plane configuration in the case of the axial view (table 4.3), while similar SNR values (table 4.4) are obtained for the sagittal views, due to the presence of several artefacts (ring artefacts resulting in vertical stripes, figure 4.5a, and artefacts related to the presence of air bubbles). The photon fluence used to perform the CT acquisition for the in-plane case was about 25% lower with respect to the out-of-plane one. In this case the out-of-plane geometry cannot be used for an accurate quantitatively analysis, because the average values measured on the same tissue (but in different regions) show differences up to 50% (figure 4.6), due to the presence of artefacts (*i.e.* incorrect definition of the boundary conditions during the phase-retrieval and the presence of air bubbles). These global differences can be seen like a shift of the values reconstructed for an entire region of the image (figure 4.5b). Following the results reported above it is possible to make the following considerations:

- From a qualitative point of view the results obtained using the out-of-plane geometry lead to a superior depiction of the inner structures in the case of sagittal view, while the in-plane geometry provides better results in the axial view, as expected according to the directions of sensitivity of the two acquisition modalities.
- The reconstruction of the refraction angle distributions produces a superior visualization of the internal details in case of the out-of-plane geometry, especially for the sagittal view.
- The quantitative results reported (mean values and SNR, tables 4.3 and 4.4) show clearly how, for the considered experimental case, the in-plane geometry allows to obtain more accurate results with respect to the out-of-plane one.

- It is possible to notice that the $\bar{\rho}$ for the adipose tissue, for instance, are in better agreement with the expected value ($\sim 0.95 \text{ g/cm}^3$) and present higher SNRs by using the in-plane geometry with respect to the out-of-plane configuration (tables 4.3, 4.4).

Due to the important global differences in the case of the out-of-plane geometry, as previously discussed, the results of the out-of-plane geometry cannot be used quantitatively to detect possible differences related to the presence of diseases. However, a qualitative analysis can be applied to obtain useful information with both the geometries.

Case	$\bar{\rho} \text{ adipose (g/cm}^3\text{)}$	STD	SNR
In-plane geometry	0.94	0.0068	138
Out-of-plane geometry	1.05	0.0230	46

Table 4.3: Quantitative results obtained from the axial slices reconstructed from data acquired with both the CT geometries. The values refer to the region marked with the red squares in figure 4.3. The expected value is 0.95 g/cm^3 .

Case	$\bar{\rho} \text{ adipose (g/cm}^3\text{)}$	STD	SNR	$\bar{\rho} \text{ skin (g/cm}^3\text{)}$	STD	SNR
In-plane geometry	0.94	0.0100	93	1.12	0.0242	44
Out-of-plane geometry	0.98	0.0326	39	1.07	0.0285	39

Table 4.4: quantitative results obtained from the sagittal slices reconstructed from data acquired with both the CT geometries. The values refer to the region marked with the coloured squares in figure 4.5. The expected values are 0.95 g/cm^3 for the adipose tissue and 1.09 g/cm^3 in the case of skin.

4.2 The problem of image deconvolution

The image $I_{rec}(x, y)$ recorded by a detector is always the result of the convolution of the incident signal $I_{inc}(x, y)$ with the $PSF(x, y)$ (point spread function) of the acquisition system plus the noise of the detection system $\eta(x, y)$. This phenomenon can be expressed as:

$$I_{rec}(x, y) = I_{inc}(x, y) * PSF(x, y) + \eta(x, y) \quad (4.1)$$

The effect of the convolution is a smearing of the signal, but lost information can be partially recovered by applying deconvolving strategies. For this purpose, different algorithms exist and they are classified in iterative (for example the Richardson-Lucy) and non-iterative (for example the Wiener deconvolution) ones.

The PSF of the detection system can be calculated theoretically or on the basis of experimental measurements by using known probes. In addition, the PSF of the system may be non-linear; therefore its effect on the recorded images may be spatial-dependent.

If the PSF is unknown, a so-called blind deconvolution method can be applied which consists in trying deconvolving the recorded image with different PSFs and assessing whether the signal to noise ratio has (or not) been improved.

In this study, I used the deconvolution method proposed by Robert Dougherty, OptiNav, 2005 which is based on the DAMAS 3 algorithm (Deconvolution Approach for the Mapping of Acoustic Sources). I have tested the results of the deconvolution on experimental data. I have applied the algorithm to three different steps of the phase-contrast imaging (PCI) CT data reconstruction process and then compared the effects directly on the final CT reconstructed distribution of the density.

4.2.1 The deconvolution algorithm

The algorithm which has been used is an implementation of the DAMAS 3 (Robert Dougherty, OptiNav 2005; Brooks & Humphreys 2006) code for the software ImageJ. The algorithm considers a translationally-invariant *PSF*. I wrote a specific macro in order to apply the algorithm to the entire stack of images, in order to process all the reconstructed volume.

The DAMAS 3 uses a hybrid iterative technique combined with a Wiener filter and which works only for a non-negative solution. It solves the equation $PSF * q = b$. In our case q represents $I_{inc}(x, y)$ and b is the $I_{rec}(x, y)$. As first step, the algorithm performs a regularized division of the *PSF* and of the term b by the FFT of the *PSF* in the spectral domain. This results in the modified deconvolution problem $PSF_w * q = b_w$. A non-negative solution of the modified problem is sought by iteration. The sequence of steps to be applied is summarized hereafter:

- 1) Compute the forward FFT of $b(x)$ and $PSF(x)$: $\tilde{b}(k)$ and $\tilde{p}(k)$.
- 2) For each frequency k , compute $\tilde{b}_w(k) = \frac{\tilde{p}^*(k)\tilde{b}(k)}{\tilde{p}^*(k)\tilde{p}(k)+\gamma}$ and $\tilde{p}_w(k) = \frac{\tilde{p}^*(k)\tilde{p}(k)}{\tilde{p}^*(k)\tilde{p}(k)+\gamma}$, where γ is a regularization term used to avoid divisions by zero at spatial frequencies for which $|\tilde{p}(k)|^2$ is small.
- 3) Compute the inverse FFT of $\tilde{p}_w(k)$ to obtain the PSF_w .
- 4) Set $a = \sum_{x,y}|PSF_w|$.
- 5) Set solution $q(x) = 0$ for each x in the beamforming grid.
- 6) Iterate:
 - a) $\tilde{q}(k) = FFT(q)$.
 - b) Let $\tilde{r}(k) = \tilde{p}(k) \cdot q(k)$ for each k .
 - c) $r(x) = FFT^{-1}(\tilde{r}(k))$.
 - d) $q(x) \leftarrow q(x) + [\tilde{b}_w(x) - r(x)]/a$ for each x .
 - e) Replace each negative value of $q(x)$ by 0.

4.2.2 Point Spread Functions

Two PSFs have been considered in this work. The first function, indicated as PSF1, has been defined by considering a signal spread over three pixels in 2D for a point-like signal, figure 4.7a. The second PSF (figure 4.7b), here indicated as PSF2, has been extracted directly from experimental projections by calculating the first derivative of the profile along a highly X-ray opaque object (figures 4.7c, d).

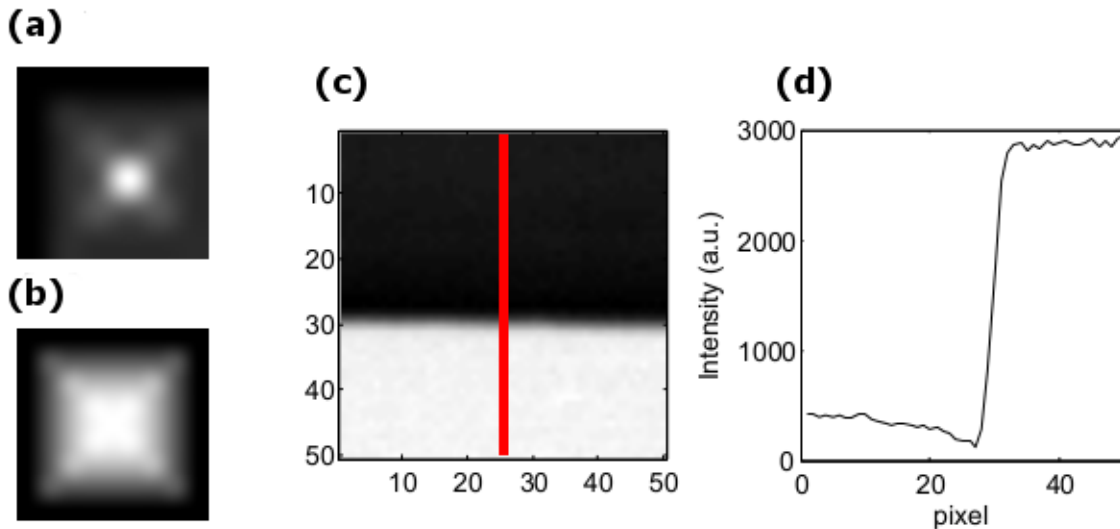


Figure 4.7: (a) PSF1; (b) estimated PSF (PSF2) from the experimental image; (c) Zoomed view of a highly X-ray opaque object used to estimate the PSF2; (d) profile along the red line of figure (c).

The two PSFs have been used in the application of the DAMAS 3 algorithm. The results are presented in the next section.

4.2.3 Application of the deconvolution procedure on experimental images

The CT data of the breast S (section 4.1) acquired by using the ABI technique, during the experiment 2, have been used for this study.

The deconvolution procedure has been applied at three different steps of the reconstruction procedure, which are below described. In this section the PSF2 has been used. All the CT reconstructions are performed following the RGVF approach.

- **Case 1:** this is the physically correct case, because the blurring of the images due to the system (optical elements) affects directly the recorded projections. It consists in applying the

deconvolution **directly on the two CT sets of angular projections** acquired at two different positions on the RC of the AC.

- **Case 2:** the deconvolution is applied **on the refraction angle projections**, obtained applying the EDEI algorithm on the two sets of images previously acquired.
- **Case 3:** the deconvolution is applied directly to the reconstructed density images.

In figure 4.8 the zoomed view of a reconstructed axial slice obtained by applying the deconvolution at different steps of the reconstruction procedure is shown. The quantitative comparison of these results is reported in table 4.5. The SNRs are again calculated as the ratio between the mean value of the signal and its standard deviation for a selected region corresponding to a particular tissue. It is possible to notice that the application of the deconvolution directly on the intensity projections (case 1) causes an increase of the image noise which reflects in reduced SNR values by a factor of ~ 20 with respect to the original non-deconvolved image. As a consequence, the obtained density values vary between the different reconstructed images (in the table the cases for the adipose and skin tissues are reported with their expected density values). The application of the deconvolution to the refraction angle projections (case 2) reduces the SNR values by a factor of ~ 3.5 while preserving the quantitative information. With a direct application of the deconvolution to the reconstructed density images (case 3) the SNR values are reduced only by a factor of ~ 2.5 and the quantitative information is again preserved. However the application of the deconvolution directly on the reconstructed images is not mathematically correct because in reality the convolution occurs during the interaction with the crystal and the imaging detector. From a practical point of view this is reflected in a difficulty to estimate the PSF for the deconvolution. The usage of a wrong PSF may erase all the advantages of the deconvolution or also lead to a degradation of the image quality and an amplification of the image noise. An example of the influence of the PSF is reported in section 4.2.3.1.

From this part of the study we can conclude that case 2 (deconvolution applied the refraction angle projections) is the most suitable for our experimental data. However a further optimization in terms of noise reduction is necessary. This aspect and the influence of the PSF used in the deconvolution process are examined in the next sections.

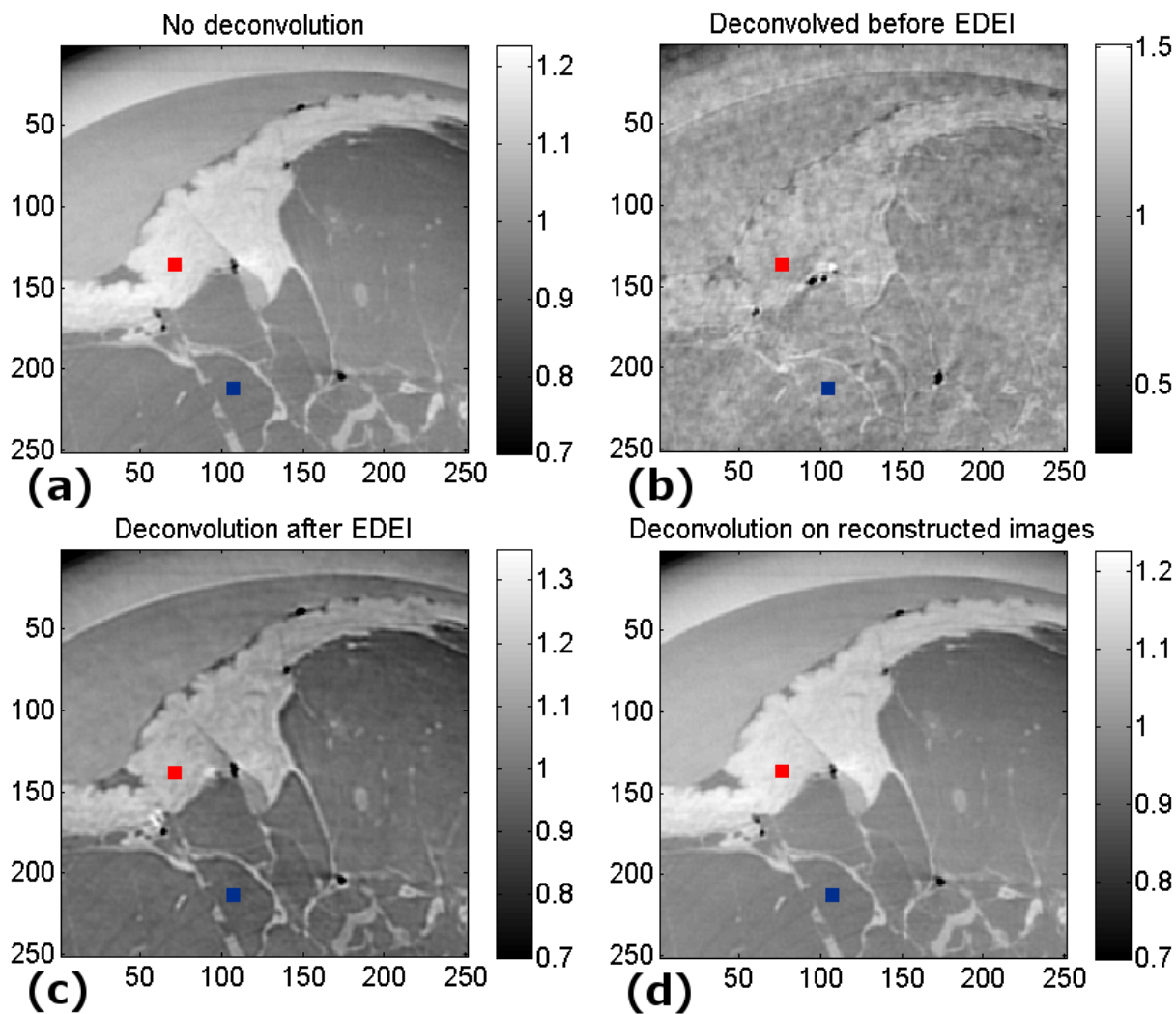


Figure 4.8: A reconstructed density slice obtained by applying the deconvolution algorithm to different steps of the reconstruction: (a) original-without deconvolution image; (b) deconvolution applied to the angular projections acquired at the two positions on the RC of the analyser crystal; (c) deconvolution applied to the refraction angle projections obtained after application of the EDEI algorithm; (d) deconvolution applied to the reconstructed density images. The quantitative results measured on the coloured squares are reported in table 4.5. The blue squares indicated the adipose tissue while the red squares the skin. The grey bar is expressed in g/cm^3 .

Case	$\bar{\rho}$ adipose (g/cm ³)	STD	SNR	$\bar{\rho}$ skin (g/cm ³)	STD	SNR
Original	0.92	0.0048	192	1.11	0.0052	213
PROJ	0.97	0.0469	21	1.14	0.0513	22
EDEI	0.92	0.0106	87	1.10	0.0073	151
REC	0.92	0.0062	149	1.11	0.0062	179

Table 4.5: quantitative results obtained on the axial view of the reconstructed images (figure 4.8). The average values, the standard deviation (STD) and the SNR are reported. The expected values for adipose and skin tissue are 0.95 g/cm³ and 1.09 g/cm³, respectively, as reported in 3.3.2 . PROJ refers to the results of application of the deconvolution on the intensity projections; EDEI deconvolution applied on the refraction angle; REC directly on the reconstructed images.

4.2.3.1 Wavelet denoising

As just mentioned, by applying the deconvolution directly on the refraction angle projections the image noise of the reconstructed CT images is amplified. To overcome this problem an effective strategy is that of first applying a denoising procedure on the images and then to apply the deconvolution. To perform the denoising, I chose the wavelet decomposition method. The denoising has been performed using the Matlab (MathWorks) wavelet Toolbox. The decomposition with wavelets is obtained by using the Coiflet 2 as a basic function with a decomposition level 3. The results of the application of this two-step approach (denoising + deconvolution) on refraction projection data of breast S are presented in figure 4.9. In figure 4.10 the results of denoising + deconvolution applied to the CT reconstruction are instead presented. The quantitative results ($\bar{\rho}$, SNR) are reported in tables 4.6 and 4.7 at the end of this section. As it results clear, both the SNR and the quantitative information of the original image are preserved, with the advantage of an increased image sharpness.

In figures 4.10 and 4.11 the SNR values have been calculated for the different cases and for the different tissues in the regions marked by the coloured squares. The red indicates the adipose tissue, the blue the skin and the yellow the glandular tissue. The profiles plotted along the red and yellow lines on the axial and sagittal views respectively, are reported in figures 4.12 and 4.13.

In the projections images (figure 4.9), the noise is highly reduced using the wavelet denoising. The SNRs have been calculated in the regions marked by the red squares, corresponding to 10% formalin solutions, and are ~25 for figure 4.9a, ~13 for figure 4.9b and ~42 for figure 4.9c. By using of the wavelet denoising the SNRs increase by a factor of ~2 with respect to the non-deconvolved images and ~3 times with respect to the images deconvolved but without denoising.

The results reported in tables 4.6 and 4.7 show how the best agreements between the obtained values of $\bar{\rho}$ with the expected ones are obtained in the case of usage of wavelet + deconvolution. The values of SNRs using this case are smaller with respect to the images without deconvolution but 2-3 times higher with respect to the results obtained applying the deconvolution without denoising.

From the profiles reported in figures 4.12 and 4.13 it is possible to see how the sharpness of the images is improved without an excessive amplification of the noise by using this two steps approach. The amplification of the noise becomes particular important in the case of sagittal views when no denoising is applied before the deconvolution (figures 4.10a, c, e).

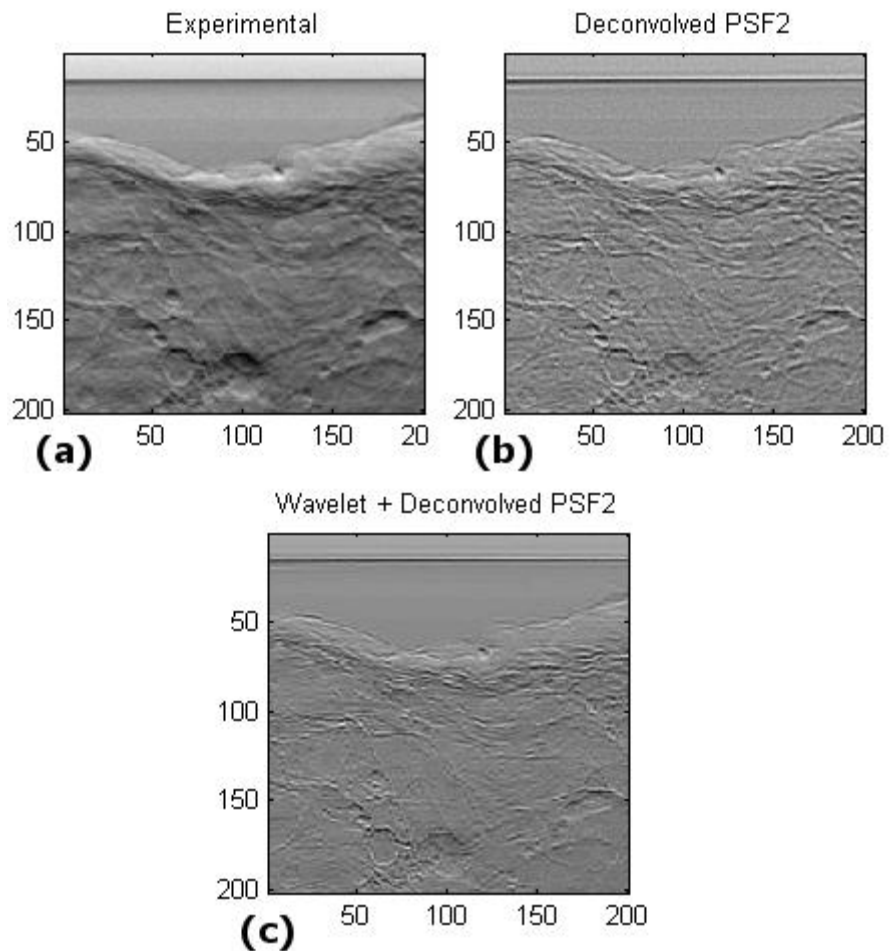


Figure 4.9: projections images of the refraction angle reconstructed using the EDEI algorithm. (a) original image; (b) projection deconvolved using the PSF2; (c) projection first denoised using the wavelet decomposition and successively deconvolved with the PSF2.

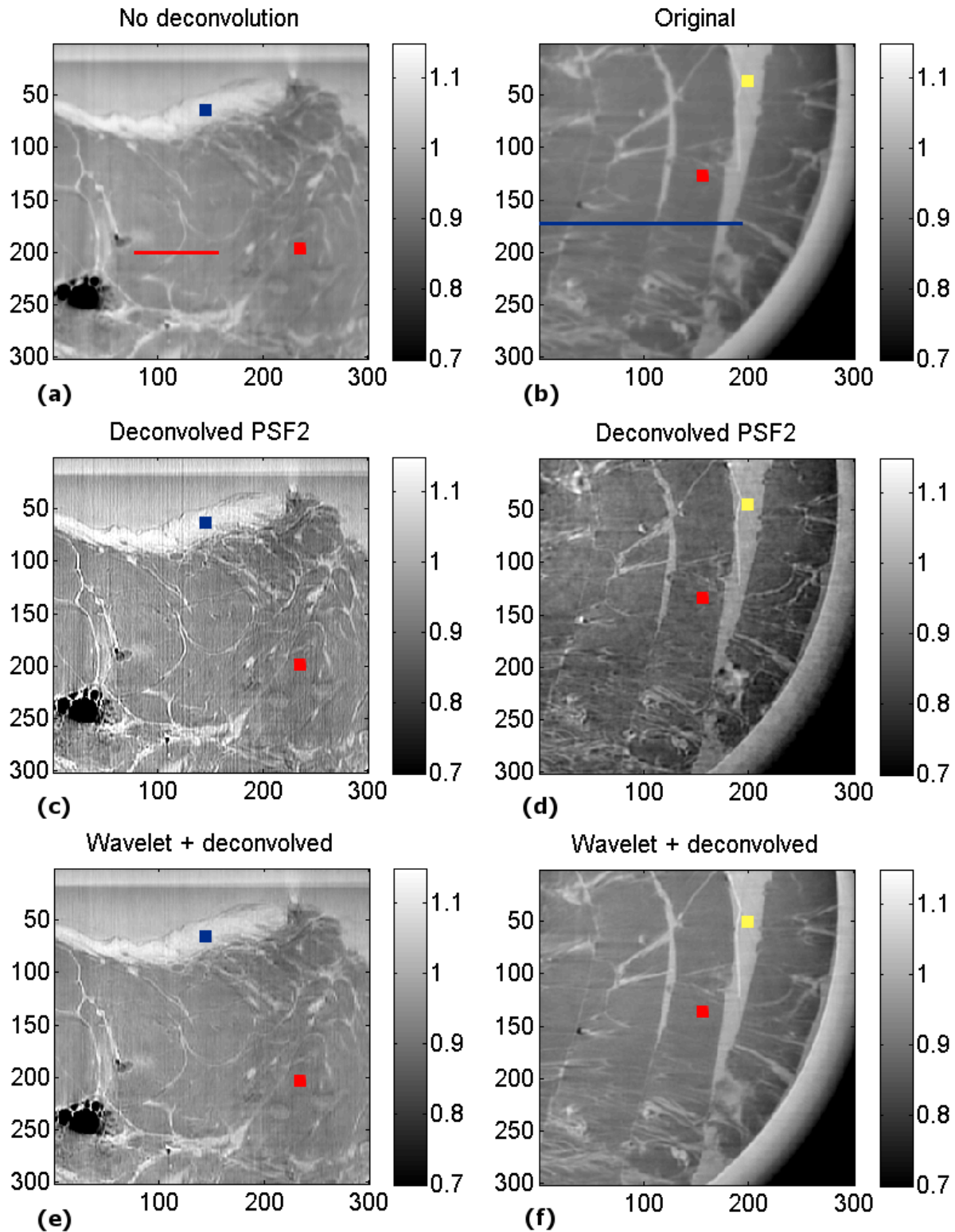


Figure 4.10: axial view of the reconstructed images. Reconstructed image without deconvolution, sagittal view (a) and axial view (b); Reconstructed image deconvolved using the PSF2, sagittal view (c) and axial view (d); Reconstructed images using the projection first denoised with wavelet approach and successively deconvolved with the PSF2, sagittal view (e) and axial view (f). The SNRs have been

calculated for different tissues in the region marked by the coloured squares. The profiles reported in figures 4.12, 4.13 have been plotted along the coloured lines. The grey bar expresses the reconstructed density in g/cm^3 .

The results obtained by using the two PSFs described in section 4.2.2, without the application of the denoising by using the wavelet decomposition in order to study the behaviour in term of noise in the deconvolved images. In figure 4.11, both the axial and the sagittal views of the reconstructed density distributions deconvolved with the PSF1 instead of the PSF2 are presented. The quantitative results of the values of $\bar{\rho}$ for two tissues and their SNRs are also reported in the tables 4.6 and 4.7.

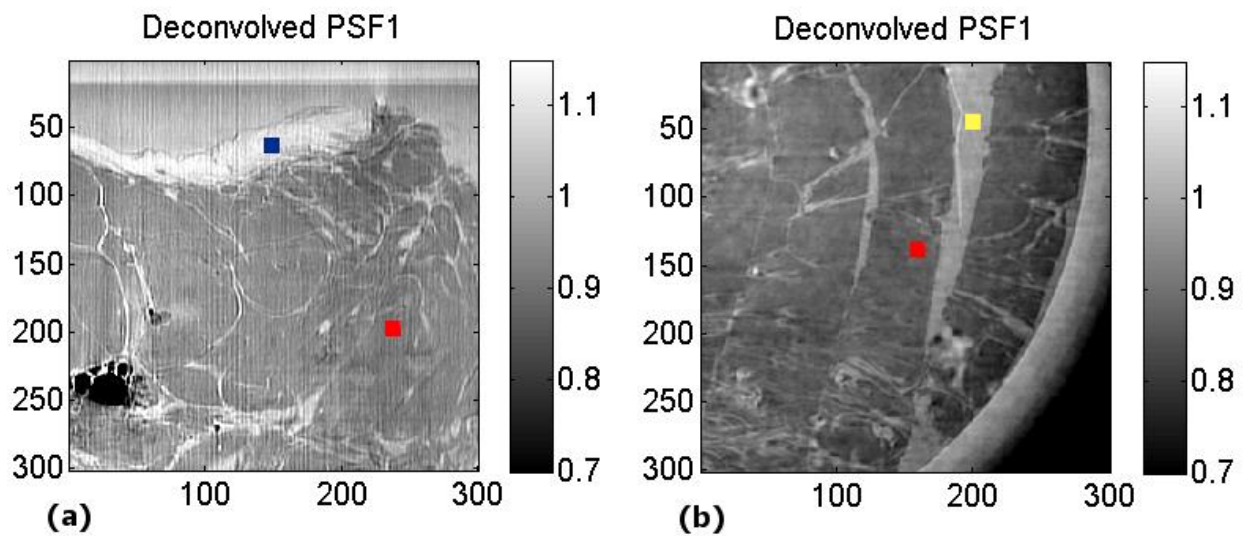


Figure 4.11: Reconstructed image deconvolved using the PSF1, sagittal view (a) and axial view (b). The SNRs have been calculated in the regions marked by the coloured squares. The grey bar expresses the reconstructed density in g/cm^3 .

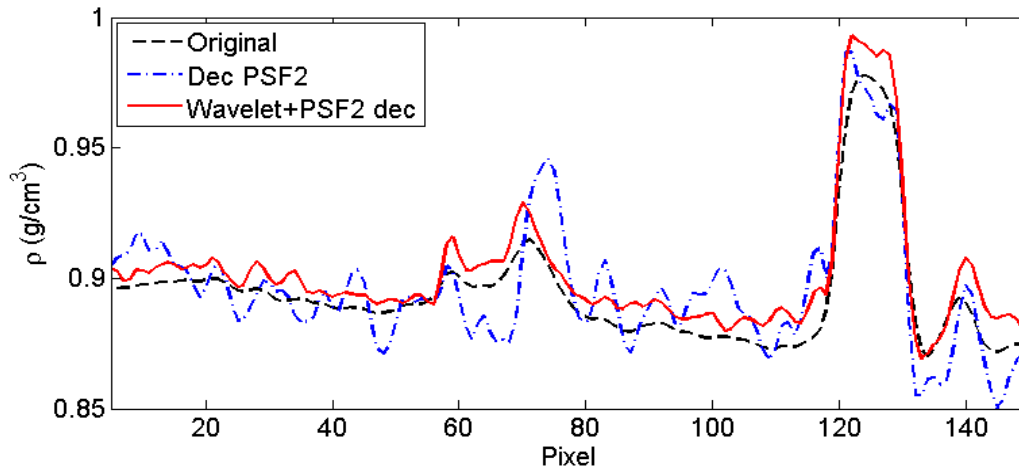


Figure 4.12: profiles along the red line indicated in figure 4.10a (and equivalent location in c and e). The dashed black line represent the profile along the original experimental data; the blue dotted line the profile along the image reconstructed using with deconvolution applied on the refraction angle projections with the PSF2; the continue red line is the profile with the additional denoising using the wavelet applied on the refraction angle projections.

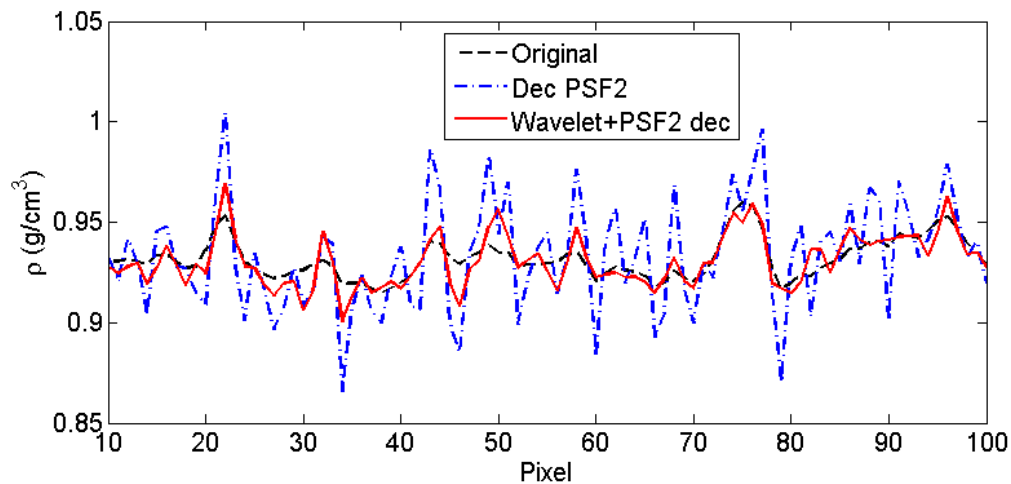


Figure 4.13: profiles along the blue line indicated in figure 4.10b (and equivalent location in d and f). For simplicity only one line has been shown in the image. The dashed black line represents the profile along the original experimental data; the blue dotted line the profile along the image reconstructed using the deconvolution method applied on the refraction angle projections (PSF2); the continue red line is the profile after the application of the additional denoising procedure using the wavelet method applied to the refraction angle projections.

It is possible to notice from figure 4.11 and from the results reported in tables 4.6 and 4.7 how the use of a different PSF (with respect to the one extracted from the experimental data) increases the noise, especially in the case of the sagittal views, and therefore decreases the SNR. For the considered tissues, the values of $\bar{\rho}$ also slightly vary depending on the PSF which is used for the deconvolution.

Case	$\bar{\rho}$ adipose (g/cm ³)	STD	SNR	$\bar{\rho}$ glandular (g/cm ³)	STD	SNR
Original	0.93	0.0025	372	1.02	0.0015	680
PSF1	0.90	0.0109	83	1.01	0.0044	230
PSF2	0.90	0.0126	71	1.01	0.0055	184
Wave	0.94	0.0044	214	1.04	0.0044	236

Table 4.6: quantitative results obtained on the axial view of the reconstructed images (figures 4.10, 4.11).

The average values, the standard deviation (STD) and the SNR are reported. The expected values for adipose and glandular tissue are 0.95 g/cm³ and 1.05 g/cm³, respectively, as reported in Chapter 3. PSF1 refers to the refraction angle projection deconvolved using the PSF1; PSF2 with the experimental PSF; Wave refers to the images previously denoised by using the wavelet decomposition and then deconvolved using the PSF2.

Case	$\bar{\rho}$ adipose (g/cm ³)	STD	SNR	$\bar{\rho}$ skin (g/cm ³)	STD	SNR
Original	0.96	0.0027	361	1.08	0.0059	190
PSF1	0.96	0.0121	79	1.10	0.0137	80
PSF2	0.96	0.0140	69	1.11	0.0160	69
Wave	0.96	0.0053	180	1.08	0.0076	142

Table 4.7: quantitative results obtained using the sagittal view of the reconstructed figures 4.10, 4.11 with the application of deconvolution. The expected value of the skin is 1.09 g/cm³. The average values, the standard deviation (STD) and the SNR are reported.

4.3 Conclusions

In this chapter I presented the results of the reconstruction of the index of refraction distribution (converted to density) for large biological samples (more than 6 cm of diameter), while the previous results reported in literature were limited to significantly smaller tissue sizes.

The comparison of the density distributions obtained from PCI CT data acquired by using the in-plane geometry with the experimental absorption-based CT images of the same breast sample shows that **a much more precise depiction of the different tissues (both in terms of average density and SNR values) is provided by PCI**. The PCI CT results (derived density values) are in good agreement with the theoretical ones (from NIST) while larger discrepancies are obtained in absorption imaging. The SNRs in the case of PCI CT are 3-10 times higher with respect to those calculated for absorption CT. Moreover the dose used for obtaining the PCI CT data set, and thus the reconstructions of the densities (derived from the δ values), is three times smaller compared to the one used for the acquisitions in the absorption modality. However, despite the dose still remains high for clinical purposes, several ways have been identified to reduce it. Examples include the use of more efficient detectors and the reduction of the number of projections required for the CT reconstruction to be used in combination with advanced and sophisticated CT reconstruction algorithms. Furthermore considering the high SNR values of the acquired images, a reduction of the photon

fluence for each projection can be applied without a significant loss in the final SNR value. This fact also implies a reduction of the exposure time and therefore of the dose.

The comparison of the two acquisition CT geometries (in-plane and out-of-plane) demonstrates that **the in-plane geometry leads to superior quantitative results with respect to the out-of-plane geometry**. In fact, by using the out-of-plane configuration, the obtained density values are 10% higher than the reference ones, as reported for example in table 4.3. For a correct and precise determination of the density distribution, a correct definition of the boundary conditions is required. When this is not possible (as those for instance caused by the air bubbles), results can be highly affected quantitatively-wise with local shifts up to 50% in our cases (figure 4.6). Contrariwise, the averaged values of the density obtained using the in-plane configuration are in better agreement with the expected values (NIST) for all the different tissues (differences < 3%). **In order to improve this quantitative approach for PCI CT and therefore be able of discriminating smaller densities variations (better than few percents) further developments are needed.**

From a qualitative point of view both CT acquisition geometries allow a good depiction of the internal features of the sample. However, for the choice of the geometry to be used it is necessary to consider the properties of the sample to be analysed and in particular the orientation of the structures of interest.

In summary, there are several advantages in using the in-plane configuration during the acquisitions:

- It allows an easier definition of the boundary conditions required for the phase-retrieval and, therefore, it provides more accurate CT density distributions (tables 4.3-4.4).
- It is possible to reconstruct the δ (or the density) by using different approaches, as reported in chapter 3, while only the method based on phase-retrieval can be used for the out-of-plane geometry.

The study of the application of the deconvolution procedure shows that it is possible to improve the sharpness of the images while keeping the SNR high. However **the deconvolution procedure requires a preliminary image denoising**. In this work I have applied the wavelet decomposition method in order to avoid the amplification of the noise during the deconvolution procedure. The best results, for the considered case, are obtained by applying the deconvolution procedure on the refraction angle projections. It is also shown, in the studied case, how the use of a slightly incorrect PSF does not produce important differences on the resulting image quality.

Chapter 5 - Fast and accurate simulations of the deposited radiation dose in CT

5.1 Introduction.....	112
5.2 Interactions of X-rays with matter	113
5.2.1 Physical processes involved in X-ray biomedical imaging.....	113
5.3 Introduction to Monte Carlo methods.....	115
5.3.1 The PENELOPE physic model.....	116
5.3.2 Photon cross section and transport algorithm	117
5.3.2.1 The interaction length or Mean Free Path.....	118
5.3.2.2 Determination of the interaction point	119
5.3.3 Acceleration of the simulations - Variance reduction techniques (VRT)	120
5.4 The TLE method.....	120
5.4.1 Local energy deposition by secondary electrons	121
5.4.2 Energy-absorption tables.....	121
5.4.3 Implementation of the TLE in GATE.....	124
5.4.4 Benchmarking of the TLE implementation in GATE against MC simulation	124
5.4.5 Experimental validation of the TLE.....	125
5.4.5.1 Photon flux measurement protocol	125
5.4.5.2 Dose measurement protocol.....	126
5.4.5.3 Simulation parameters.....	127
5.4.6 Performances comparison between TLE and MC dose deposition simulations in complex cases	127
5.5 Results.....	128
5.5.1 Benchmarking against MC simulation.....	128
5.5.2 Accuracy test of the TLE method against measurements	130
5.5.3 Performances comparison in anatomically complex cases	131
5.6 Conclusions.....	133

5.1 Introduction

Knowledge of the dose delivered during medical imaging and radiation therapy represents a considerable issue. In order to preserve the integrity of the samples, their exposure should be carefully guided following dosimetric criteria that all lead to the basic paradigm that the absorbed dose should be as low as reasonably achievable. In this respect, therapeutic and imaging doses, when combined, cannot be regarded from the same viewpoint because the imaging dose adds to an already high level of therapeutic radiation. The Monte Carlo (MC) method is often used to compute the distribution of the dose deposited in both imaging and radiotherapy applications. It provides accurate results but still requires long computation times, hindering its use in clinical routine applications. In order to accelerate the convergence, techniques such as condensed history methods or variance reduction techniques (VRT), *e.g.* splitting and Russian roulette, importance sampling, forced detection, etc, (Jenkins et al. 1988) have been introduced. These acceleration procedures provide substantial speedup but have to be used very cautiously to stay within their limits of validity. Among the VRTs, the track length estimator (TLE) method is known as a very efficient tallying method, well suited for kerma calculations at any given point during photon irradiations (Williamson 1987).

Within this Thesis work a TLE module has been coded and then implemented for the first time in the open-source MC code GATE/Geant4. We investigated the application of TLE to speed up dose calculations for low-energy (from 1 keV to a few hundred keV) photon irradiations, which include radiology, brachytherapy, synchrotron radiation-based therapy and imaging applications.

Results obtained with the TLE module and the procedures used to validate them are presented in this manuscript. A database of energy-absorption coefficients was also generated (please refer to Appendix A for more details about the calculation of these coefficients), which is used by the TLE calculations and is now also included in GATE/Geant4. The validation was carried out by comparing the TLE-simulated doses with experimental data in a synchrotron radiation CT experiment. The TLE technique shows good agreement versus both experimental measurements and the results of a classical MC simulation. Compared with the latter, it is possible to reach a pre-defined statistical uncertainty in about two to three orders of magnitude less time for complex geometries without loss of accuracy.

Before introducing the details about the implementation and the validation of the TLE, a brief description of the interactions of photons with matter is presented as well as a short introduction on MC techniques.

5.2 Interactions of X-rays with matter

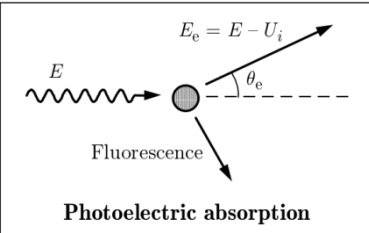
Photons are electromagnetic radiation with zero mass, zero charge, and a velocity that is always c , the speed of light. Because photons are electrically neutral, they do not steadily lose energy via coulombic interactions with atomic electrons as do charged particles.

While travelling through the matter photons are involved in several physical processes. In the energy range used in medical diagnostics and in this Thesis work, the atomic processes of interest are (I) the Photoelectric absorption, (II) the Compton scattering and (III) the Rayleigh scattering. Pair production (IV) takes place at energies ≥ 1.02 MeV and therefore it is not considered here. Other interactions, such as photonuclear absorption, occur with much smaller probability and can be disregarded for most practical purposes (Hubbell et al. 1980). The effect of the polarization of the photons is also not considered.

As long as the response of an atom is not appreciably distorted by molecular binding, the single-atom theory can be extended to molecules by using the additivity approximation, *i.e.*, the molecular cross sections for a process is approximated by the sum of the atomic cross sections of all the atoms in the molecule. The additivity approximation can also be applied to dense media whenever interference effects between waves scattered by different centres (which, for instance, give rise to Bragg diffraction in crystals) are small. We assume that these conditions are always satisfied.

5.2.1 Physical processes involved in X-ray biomedical imaging

The basics of the main X-ray-matter interaction mechanisms are described in the following table (pictorial schemes as in Salvat & Fernández-Varea 2006).

	<p>For gamma or X- rays of relatively low energy the photoelectric process is the predominant mode of interaction with matter. This effect is characterized by the absorption of the X-ray by an electron of an atomic shell. This energy transfer results in the ejection of the shell electron (photoelectron) whose energy (E_e) is</p> $E_e = h\nu - E_b$ <p>Where E_b is the binding energy of the electron in its original shell, h is the Planck constant and ν the frequency of the photon. The interaction leaves an ionized atom with a vacancy in one of its bound shell. This vacancy is quickly filled through the capture of a free electron from the medium or/and rearrangement of electrons from other shells or atoms. One or more characteristic X-ray photons may be generated consequently. In some cases the emission of Auger electrons may substitute for the characteristic X-ray carrying away the atomic excitation energy.</p>
---	--

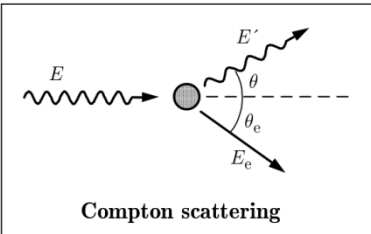
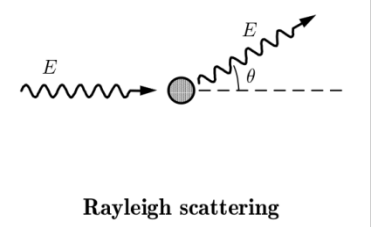
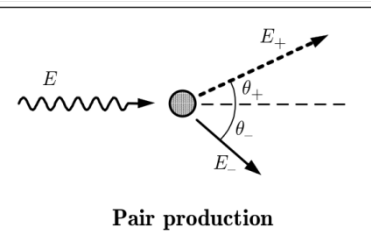
	<p>The process is also enhanced for high Z absorber materials; it scales as Z^4-Z^5, depending on the photon energy.</p>
 <p style="text-align: center;">Compton scattering</p>	<p>The Compton interaction consists in the inelastic scattering of a photon by a free charged particle, usually an electron. A scheme of the process is shown in the left panel. Part of the photon energy is transferred to the scattering electron, which is then known as <i>recoil electron</i> or a <i>Compton electron</i>. The energy transferred to the electron can vary from zero to a large fraction of the photon energy because all angles of scattering are possible. The energy transferred to the <i>recoil electron</i> is in the range:</p> $0 \leq E_e \leq h\nu \frac{1}{1 + 2\alpha}$ <p>where $\alpha = h\nu/m_e c^2$. In this case the photon wavelength varies as:</p> $\lambda' - \lambda = \frac{h}{m_e c} (1 - \cos \theta)$ <p>Where λ is the initial wavelength, λ' is the wavelength after scattering, h is the Planck constant, m_e is electron rest mass, c is the speed of light and θ is the scattering angle. Inverse Compton scattering also exists, in which a charged particle transfers part of its energy to a photon hitting the atom.</p>
 <p style="text-align: center;">Rayleigh scattering</p>	<p>The Rayleigh process is the elastic (no energy loss) scattering from atoms. Rayleigh scattering varies in a complicated way with different atoms: like Z^2 for small scattering angles and Z^3 for large ones. The scattering is qualified as “coherent” because it arises from the interference between secondary electromagnetic waves coming from different parts of the atomic charge distribution in the medium.</p>
 <p style="text-align: center;">Pair production</p>	<p>Pair production refers to the creation of an elementary particle and its antiparticle, and it usually occurs when a photon interacts with a nucleus. In this case an electron and its antiparticle, the positron, may be created. This is allowed provided that there is enough energy available to create the pair (at least the total rest mass energy of the two particles) and that both energy and momentum are conserved. All other conserved quantum numbers (angular momentum, electric charge, lepton number) of the produced particles must sum to zero. The probability of pair production in photon-matter interactions increases with increasing the photon energy and the medium atomic number (approximately as Z^2).</p> <p>The probability of this process is negligible at the X-ray energies used in the experiments of this Thesis work.</p>

Table 5.1: overview of the main X-ray-matter interaction mechanisms

5.3 Introduction to Monte Carlo methods

The name “Monte Carlo” was introduced in the 1940s by scientist working on the nuclear weapon project in Los Alamos to designate a class of methods based on the use of random numbers.

The ability of MC simulation methods to describe photon transport in complex geometries has been established through many studies during the last five decades (Hayward & Hubbell 1954; Berger & Seltzer 1972; Chan & Doi 1983; Ljungberg & Strand 1989).

The MC method is often used to compute the distribution of the dose deposited in both imaging and radiotherapy applications. It provides accurate results but still requires long computation times, hindering its use in clinical routine practice. Many MC codes are available to simulate radiation transport as listed in table 5.2.

GEANT4	Agostinelli et al, 2003, Allison et al, 2006
MCNPX	Pelowitz, 2005
FLUKA	Battistoni et al, 2007, Ferrari et al, 2005
EGSnrc	Fragoso et al, 2009
PENELOPE	Salvat et al, 2009, Salvat et al, 2011

Table 5.2: overview of the main MC codes used to simulate radiation transport.

In MC simulations of radiation transport, the history (track) of a particle is viewed as a random sequence of free flights that end with an interaction event where the particle changes its direction of movement, loses energy and, occasionally, produces secondary particles. To simulate an experimental arrangement with a MC method, a random number of histories have to be generated numerically and an interaction model, *i.e.* a set of Differential Cross Sections (DCS), for the relevant interaction mechanisms is needed. The DCSs determine the function of the probability distribution of the random variable that characterizes the track and that includes: 1) the free path between successive interaction events; 2) the type of the occurring interaction; 3) the angular deflection and energy loss in a particular event.

The MC method yields the same information as the solution of the Boltzmann transport equation, with the same interaction model and with the advantage of an easier implementation (Berger 1963).

The most accurate available DCSs are given in a numerical form, and therefore advanced MC codes make use of extensive databases.

The code implemented in this Thesis work has been integrated into the framework of the GATE (Geant4 Application for Tomography Emission) collaboration (Jan et al. 2011). All the simulations presented in this manuscript have been performed using this version of the MC code (Agostinelli et al. 2003).

The GATE code is open-source and user friendly (no knowledge in programming languages like C++ is required to use it). To set all the parameters for a simulation is sufficient to create few macros written in the interactive GEANT4 language.

Several physic models are made available for the users, in our case the employed model is the PENELOPE implementation for GEANT4 (Salvat & Fernández-Varea 2006) which is described in the next section.

5.3.1 The PENELOPE physic model

All the simulations presented in this Thesis work have been performed by using the implementation for GEANT4 of the PENELOPE (PENetration and Energy LOSS of Positrons and Electrons) model (Salvat & Fernández-Varea 2006). In the PENELOPE model, a combination of analytical DCSs and numerical tables of total cross sections are used. The model allows the user to perform simulations using different particles (γ , e^- , e^+), for a range of energy from 250 eV to 1 GeV. The range considered in this work (for the applicability of the TLE) is included between 1 and to 100 keV. A brief description of the PENELOPE model for the different physical processes is here presented.

Photoelectric effect: In PENELOPE the independent-electron model Dirac-Hartree-Fock-Slater is adopted to represent the atomic states. In this model each electron occupies a single-particle orbital with well-defined ionization energy.

The photoelectric cross sections are obtained by interpolation in a numerical table that was extracted from the Lawrence Livermore National Laboratory (LLNL) Evaluated Photon Data Library (EPDL) (Cullen et al. 1997). This library contains photoelectric cross sections for all shells of the elements with Z in the range [1-100] and photon energies from 1 eV to 1000 GeV derived from Scofield's theoretical calculations of the shell cross sections (Saloman et al. 1988). These tables are estimated to be accurate within a few percent for photon energies above 1 keV (Cullen et al. 1997). At lower energies, uncertainties in the data are much larger. The cross sections in the EPDL are based on free-atom theoretical calculations and, therefore, near-edge absorption structures produced by molecular or crystalline ordering (e.g. extended X-ray absorption fine-structure) are ignored.

For compound materials (and also for mixtures) the molecular cross section $\sigma_{pe}(E)$ is evaluated by means of the additivity approximation, that is, as the sum of the atomic cross sections of the involved elements.

Compton scattering: Compton scattering events are described by means of the cross section obtained from the relativistic impulse approximation (Ribberfors 1983). Contributions from different atomic electron shells are considered separately. After a Compton interaction with the i -th shell, the active target electron

is ejected to a free state with kinetic energy $E_e = E - E' - U_i > 0$, where U_i is the ionization energy of the considered shell, and the residual atom is left in an excited state with a vacancy in the i -th shell.

In the case of scattering by free electrons at rest, the conservation of energy and momentum implies the following relation between the energy E' of the scattered (Compton) photon and the scattering angle θ .

$$E' \equiv \frac{E}{1 + \kappa(1 - \cos \theta)} \equiv E_C \quad (5.1)$$

where $\kappa = E/m_e c^2$. The DCS for Compton scattering by a free electron at rest is given by the Klein-Nishina formula (Heitler 1954). The impulse approximation accounts for Doppler broadening and binding effects in a natural, and relatively simple, way. The DCS is obtained by considering that electrons in the i -th shell move with momentum distribution $p_i(\mathbf{p})$. For an electron in an orbital $\varphi_i(\mathbf{r})$, $p_i(\mathbf{p}) \equiv |\varphi_i(\mathbf{p})|$, where $\varphi_i(\mathbf{p})$ is the wave function in the momentum representation. The DCS for Compton scattering by an electron with momentum \mathbf{p} is derived from the Klein-Nishina formula by applying a Lorentz transformation with velocity \mathbf{v} equal to that of the moving target electron. The impulse approximation to the Compton DCS (per electron) of the considered shell is obtained by averaging over the momentum distribution $p_i(\mathbf{p})$.

Rayleigh scattering: The atomic DCS per unit solid angle for coherent scattering can be calculated using the non-relativistic perturbation theory (Sakurai 2006; Baym 1974). The most accurate form factors are those obtained from Hartree-Fock or configuration-interaction atomic-structure calculations; the non-relativistic atomic form factors from the EPDL (Cullen et al. 1997), calculated by Hubbell et al (1975) are adopted. The total atomic cross sections used in PENELOPE are from the EPDL and were calculated from the DCS given by Cromer 1970.

5.3.2 Photon cross section and transport algorithm

In order to study and model the behaviour of photons travelling through the matter is necessary to solve the problem of the photons transportation. The volume where the problem is considered is subdivided in voxels of well-defined physical dimensions.

The transportation process is responsible for determining the geometrical limit of a step. It calculates the length of the step with which a track will cross into another voxel. When the track actually arrives at the boundary of a voxel, the transportation process locates the next volume that it enters.

In GEANT4 the simulation of particle transport is performed step by step (Agostinelli et al. 2003). The true step length (*i.e.* the length of the step between two subsequent interactions, corrected for multiple scattering)

is randomly sampled using the mean free path of the interaction or by various step limitations established by different GEANT4 components. The smallest step limit defines the new true step length.

5.3.2.1 The interaction length or Mean Free Path

In GEANT4 the computation of the mean free path of a particle in a media is performed by using the cross section of a particular physical process and the density of atoms in the considered medium. In a simple material the number of atoms per volume is:

$$n = \frac{N_A}{\rho} \cdot A \quad (5.2)$$

Where N_A is the Avogadro number, ρ is the density of the medium and A it the mass of a mole.

In a compound material the number of atoms per volume of the i -th element is:

$$n_i = \frac{N_A}{\rho \cdot w_i} \cdot A_i \quad (5.3)$$

The mean free path of a process, λ , also called the interaction length, can be given in terms of the total cross section:

$$\lambda(E) = \left(\sum n_i \sigma(Z_i, E) \right)^{-1} \quad (5.4)$$

where $\sigma(Z, E)$ is the total cross section of the process per atom and the sum operator \sum runs over all elements composing the material. $\sum n_i \sigma(Z_i, E)$ is also called the macroscopic cross section. The mean free path is defined as the inverse of the macroscopic cross section.

Cross sections per atom and mean free path values may be tabulated during initialization in the code.

The photon inverse mean free path (*i.e.* $1/\lambda$) for a given mechanism is known as the partial attenuation coefficient of that mechanism. Thus the partial attenuation coefficient for photoelectric absorption is:

$$\mu_{ph} = N \sigma_{ph} \quad (5.5)$$

Where $N = N_A \rho / A_M$ is the number of atoms or molecules per unit of volume and σ_{ph} is the atomic or molecular photoelectric cross section. The photoelectric mass attenuation coefficient is defined as μ_{ph}/ρ and, therefore, is independent of the density of the material. Analogous definitions apply for the other interaction processes. The total mass attenuation coefficient is then obtained as:

$$\frac{\mu}{\rho} = \frac{N_A}{A_M} (\sigma_{Ra} + \sigma_{Co} + \sigma_{Ph} + \sigma_{pp}) \quad (5.6)$$

Where σ_{Ra} is the cross section for Rayleigh scattering, σ_{Co} Compton scattering, σ_{Ph} Photoelectric effect, and σ_{pp} the pair production (not considered in this work).

As mentioned above, PENELOPE uses table of total cross sections for photoelectric absorption and Rayleigh scattering extracted from the EPDL (Cullen et al. 1997). Cross sections of these two processes for energies different from those in the tables are calculated by a linear log-log interpolation.

Mean free paths for incoherent scattering are calculated from the DCSs given by the impulse approximation. For $E > 50$ keV, the resulting values are very close to those given by the XCOM program (Berger & Hubbell 1987), which were calculated from the Waller-Hartree theory, with the incoherent scattering functions of Hubbell *et al* (1975). At lower energies, the PENELOPE mean free path for Compton scattering deviates from that given by XCOM, because the Waller-Hartree theory neglects the Doppler broadening. The evaluation of the total atomic cross section for Compton scattering involves numerical quadrature to perform the integration of the Compton DCS (for more details check Salvat & Fernández-Varea 2006).

5.3.2.2 Determination of the interaction point

The mean free path, λ , of a particle for a given process depends on the medium and cannot be used directly to sample the probability of an interaction in a heterogeneous volume. The number of mean free paths which a particle travels is (Geant4 2013):

$$n_\lambda = \int_{x_1}^{x_2} \frac{dx}{\lambda(x)} \quad (5.7)$$

which is independent of the material traversed. If n_r is a random variable denoting the number of mean free paths from a given point to the point of interaction, it can be shown that its distribution function is given by:

$$P(n_r < n_\lambda) = 1 - e^{-n_\lambda} \quad (5.8)$$

The total number of mean free paths, n_λ , the particle travels before reaching the interaction point is assigned a given value at the beginning of the trajectory. This value is calculated as:

$$n_\lambda = -\log(\eta) \quad (5.9)$$

where η is a random number uniformly distributed in the range (0, 1). n_λ is updated after each step x according to the formula:

$$n'_\lambda = n_\lambda - \frac{\Delta x}{\lambda(x)} \quad (5.10)$$

until the step originating from $s(x) = n_\lambda \cdot \lambda(x)$ is the shortest and trigger the specific process.

The probability of occurrence of each interaction mechanism is then determined by the related cross section, which is a function of photon energy for a considered material.

5.3.3 Acceleration of the simulations - Variance reduction techniques

(VRT)

Every output random variable from a simulation is associated with a variance which limits the precision of the results. In order to obtain greater precision and smaller confidence intervals for the output random variable of interest, variance reduction techniques can be used. The main ones are: common random numbers, antithetic variates, control variates, importance sampling and stratified sampling. Under these headings are a variety of specialized methods. For example, particle transport simulations make extensive use of "weight windows" and "splitting/Russian roulette" techniques, which is a form of importance sampling. The TLE method is known as a very efficient tallying method for the calculation of the kerma at any given point during photon irradiations (Williamson 1987). In the next section the implementation and validation of the TLE method in the GATE framework (as performed within this Thesis work) is presented and discussed.

5.4 The TLE method

The TLE estimators are based upon the equivalence of particle fluence and total photon path length per unit volume. The use of a TLE technique for calculating particle fluences, kerma and absorbed doses has long been known (Carlsson. 1985; Williamson 1987). It is implemented e.g. in the MCNPX MC code (Demarco et al. 2002; Smans et al. 2010) and in some dedicated tools, notably for external radiotherapy (Zee et al. 2005) and brachytherapy applications (Chibani & Williamson 2005; Taylor et al. 2007). Considering a monoenergetic photon beam with energy E , the absorbed dose in charged particle equilibrium (CPE) is given by (Carlsson. 1985; Hubbell, J.H. and Seltzer 2004):

$$D = \phi E \frac{\mu_{en}}{\rho} \quad (5.14)$$

where ϕ is the particle fluence and μ_{en}/ρ is the mass energy-absorption coefficient. Fluence can be interpreted as the track length density of the particles at a point \mathbf{r} in space (Carlsson. 1985), *i.e.*:

$$\phi(\mathbf{r}) = \frac{dL(\mathbf{r})}{dV} \quad (5.15)$$

For a photon traversing a voxel of volume V , an estimate of the corresponding fluence is therefore given by (Williamson 1987; Demarco et al. 2002):

$$\phi = \frac{L}{V} \quad (5.16)$$

where L is the track length, *i.e.* the straight line distance travelled in the voxel between successive collisions. TLE can thus be used to determine the expected value of the dose deposited along every photon trajectory given by Eq. 5.14. With the TLE scoring method, a photon deposits its energy in all voxels it encounters between successive interaction points, instead of doing so only at interaction points as is the case in an equivalent MC simulation. The major advantage of the use of the TLE is a drastic acceleration of the convergence of the simulation.

5.4.1 Local energy deposition by secondary electrons

According to the TLE method, secondary electrons are not tracked and their energy is deposited locally (within a single voxel). This approximation is satisfactory when the CPE condition is fulfilled and the electron range remains smaller than either the voxel size or the required spatial accuracy. Comparing the electron range in the continuous-slowing-down approximation (CSDA range) to the voxel size is a conservative criterion, since the projected range is always smaller than the CSDA range (*i.e.* detour factor below 1; *i.e.* owing to the multiple scattering, the trajectory of the particle is wiggly rather than straight, and the detour factor is always smaller than unity) (Berger & Zucker 2004). For soft tissues (mass density $1.06 \text{ g} \cdot \text{cm}^{-3}$), the CSDA range stays below 1 mm up to about 300 keV (ICRU 1984).

5.4.2 Energy-absorption tables

In the energy domain of interest in this Thesis work (keV X-rays), the linear energy-absorption (μ_{en}) and energy-transfer (μ_{tr}) coefficients can be considered to be the same quantity (Attix 2004; Hubbell, J.H. and Seltzer 2004; Freud et al. 2008):

$$\mu_{en} \approx \mu_{tr} \quad (5.17)$$

For tissues composed of elements with atomic numbers $Z \leq 20$, the relative difference between μ_{tr} and μ_{en} remains below 1 % for energy values up to 1 MeV. The difference can reach a few percent at 1 MeV for

elements with $Z > 20$ (Attix 2004). In the case of a mixture of elements, the mass energy-transfer coefficient μ_{tr}/ρ satisfies the additivity rule.

The values of μ_{en}/ρ may be obtained in several ways:

- I. directly from the NIST database for elemental media and a limited number of materials of interest (Hubbell, J.H. and Seltzer 2004). In the case of compounds or mixtures, the additivity rule can be used as an approximation;
- II. by using the EPDL97 database and the approximation by eq. 5.20. Details about the calculation of the coefficients can be found on the NIST webpage (Hubbell, J.H. and Seltzer 2004);
- III. by using MC simulations (method described in Freud et al. 2008). In Geant4, several low-energy electromagnetics physic lists based on Livermore or Penelope models (Ivanchenko et al. 2011) are available for reference. Both ones use EPDL97 and EADL to describe photon interactions and atomic relaxation, respectively. As regards Compton scattering, both Livermore and Penelope models predict the ionized shell and subsequent atomic relaxation. Note, however, that the fluorescence emission following Compton scattering is a very rare process and has a negligible influence on the μ_{en} value.

Figure 5.1 presents a comparison between μ_{tr}/ρ calculated for cortical bone and lung tissue (ICRU 1989) using the EPDL97 database (Cullen et al. 1997), see II, μ_{tr}/ρ derived from Geant4 v9.5 simulations (III) with the Livermore model, and μ_{en}/ρ as from NIST (Hubbell, J.H. and Seltzer 2004), (I). No significant difference is detected between these three sets of data.

In the case of iodine (figure 5.2), slight differences are found between the μ_{tr}/ρ calculated via EPDL97 and μ_{en}/ρ from NIST, up to about 4 % at 1 MeV, corresponding to the average fraction of the kinetic energy of secondary charged particles escaping through radiative processes (Hubbell, J.H. and Seltzer 2004). Moreover, no significant difference (below about 1 %) appears between the μ_{en}/ρ values calculated through EPDL97 and estimated by Geant4, whichever model (Penelope or Livermore) is used.

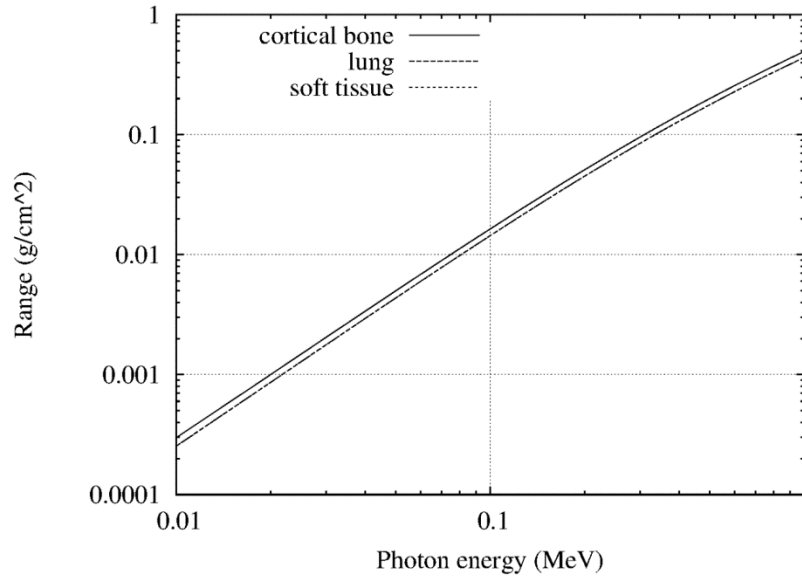


Figure 5.1: Comparison between energy absorption-to-attenuation coefficient ratios calculated for cortical bone and lung tissue (ICRU 1989) by using the EPDL97 database (Cullen et al. 1997), as derived from Geant4 v9.5 simulations with the Livermore model (according to the method described in (Freud et al. 2008)), and as given by NIST (Hubbell, J.H. and Seltzer 2004).

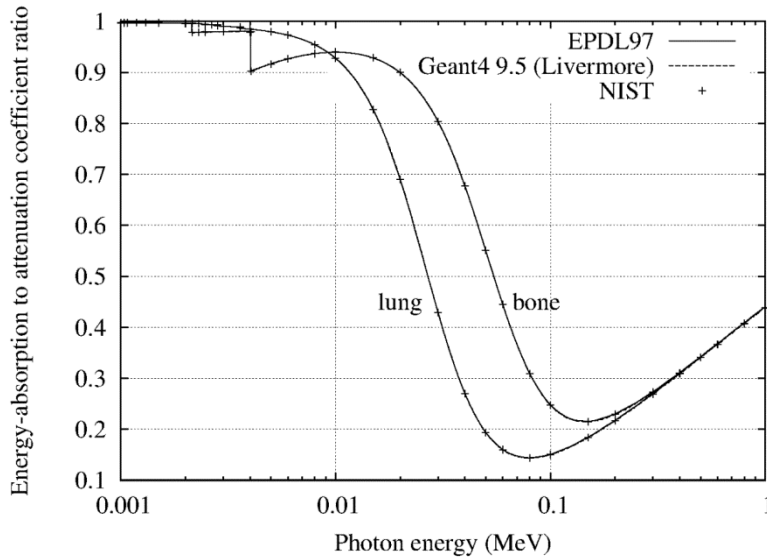


Figure 5.2: Comparison between energy absorption-to-attenuation coefficient ratios calculated for iodine using the EPDL97 database (Cullen et al. 1997), simulated using Geant4 v9.5 in conjunction with the Penelope and Livermore physics models, and as provided by NIST (Hubbell, J.H. and Seltzer 2004). The curves corresponding to the Geant4, Penelope and Livermore models can hardly be distinguished. The relative difference between EPDL97 and Geant4 stays below about 1 %. When energy increases, the difference between μ_{tr}/ρ (either from EPDL97 or Geant4) and μ_{en}/ρ from NIST increases up to about 4 % at 1 MeV. In the EPDL97 library the Doppler broadening effect is not considered. It has been shown (Ye et al. 2006) that the usage of this approximation compared to a more advanced model (impulse approximation) does not produce significant differences in the results, at least for the considered energy range.

The database I generated from the EPDL97 library and now included in the new release of GATE, incorporates the μ_{en} coefficients mentioned above for all elements with $1 \leq Z \leq 100$ in the energy range [1 keV, 1 MeV] and has been used in all TLE calculations reported here.

5.4.3 Implementation of the TLE in GATE

During the initialization of a simulation the pre-generated database, presented in section 5.4.2, is loaded. The discontinuities are treated by insertion of two identical energies with different μ_{en} values. When the energy of the photon is equivalent to the absorption edge energy the higher values of the μ_{en} is considered for the simulation.

Materials are defined as mixtures of n elements with corresponding mass fractions w_n . When an energy value used by the simulation does not appear in the database, the value of the corresponding μ_{en} is calculated on the fly by means of a logarithmic interpolation between the μ_{en} values referring to the two nearest energies. We implemented this method in GATE v6.2 and it will be available for the usage in the next release of GATE. In order to use it, it is sufficient to call the *TLEDoseActor* in a way similar to the pre-existing *DoseActor* (Jan et al. 2011). The distribution maps of the energy deposited in the volume V of interest are created if the actor is attached to V . The volume must be a matrix of voxels named *NestedParametrizedVolume*. By definition one element of the dose score matrix corresponds to one *doseL*. The implementation of a look-up table to store the tabulated values μ_{en} of the already defined materials is foreseen to accelerate the computations.

5.4.4 Benchmarking of the TLE implementation in GATE against MC simulation

The test case chosen for the comparison between TLE and equivalent classical MC simulations is a chest radiography consisting of a CT model (obtained during a real CT acquisition and provided in the set of examples distributed with GATE) of a thorax phantom (512x512x53 voxels of 0.602x0.602x3.000 mm³, see figure 5.3) irradiated by an X-ray tube, simulated as a point source with a 81 kVp polychromatic spectrum. The thorax phantom is the *Dynamic Thorax Phantom* from CIRS, Inc. It is composed of several different materials (in terms of both density and linear attenuation) included between air and metal implant. The distance from the source to the phantom centre was set to 100 cm. Simulations were carried out using Geant4 v9.5 with the Penelope physics models. The voxel size of dose and energy deposited maps was set to 3.08x3.08x9.9375 mm³.

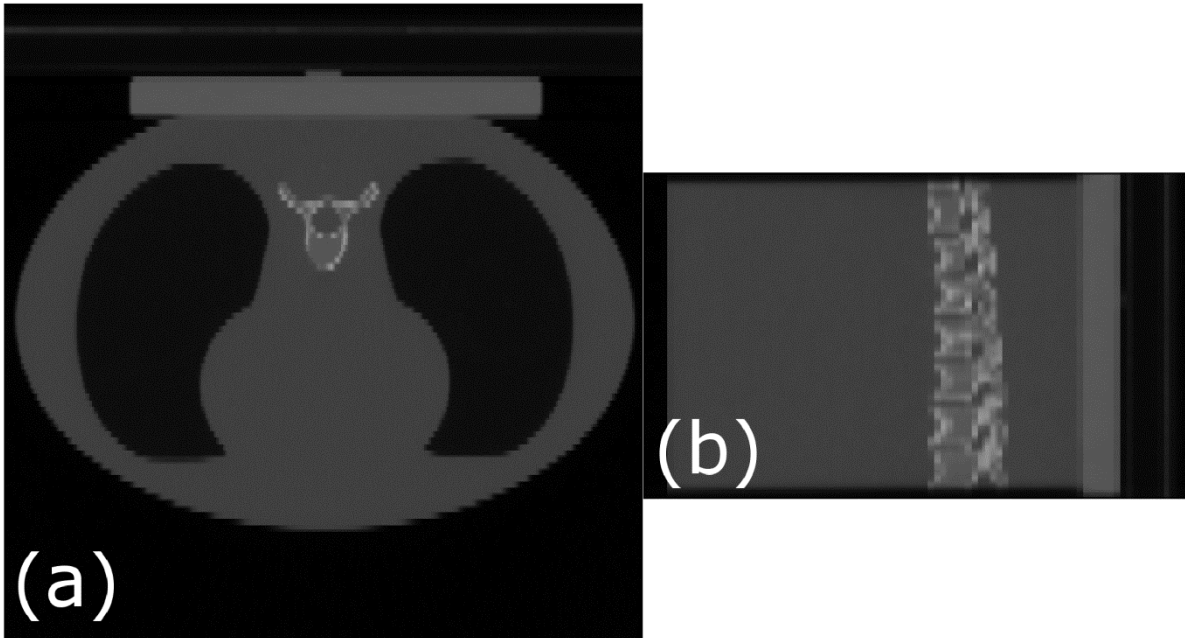


Figure 5.3: CT model of the thorax phantom used in the chest radiography simulation test case. (a): transverse slice; (b): sagittal slice.

5.4.5 Experimental validation of the TLE

Measurements were performed at the biomedical beamline (ID17) of the European Synchrotron Radiation Facility (ESRF, Grenoble, France), pursuing a two-fold objective: (I) evaluating the photon flux, *i.e.* the photon fluence per unit time and per storage ring electron current necessary to estimate the number of histories to be used in the simulations, and (II) determining dose values in different experimental configurations to be compared with dosimetric results simulated by our TLE code.

5.4.5.1 Photon flux measurement protocol

In the simulations, the number of histories n_h needed to compute the total deposited dose is given by $n_h = \phi \cdot I \cdot t \cdot S$, where S is the beam cross-sectional surface area, I is the storage ring electron current, t is the exposure time and ϕ the photon flux (photons/(s·mm²·mA)).

The photon flux was derived from the dose absorbed in water dosimetry measurements, carried out using a ionization chamber connected to a PTW dosimeter (PTW 31010 calibrated by PTB Freiburg, Germany) at different X-ray energies in the range 33.7–72 keV. The active volume of the ionization chamber is 0.125 mm³. As the height of the synchrotron beam is smaller than the chamber size, measurements were performed by vertically scanning the ionization chamber with the photon beam (Prezado et al. 2011). The chamber was positioned perpendicularly to the direction of the beam: in this case no correction concerning

the directional dependence of the device had to be applied. A correction taking into account the energy behaviour of the chamber was applied. The correction factor curves are provided directly by the manufacturer of the chamber. The measurements were repeated twice and the mean value was taken as reference estimate. The photon flux at the point of measurement was evaluated as:

$$\phi_{PTW} = \frac{D\rho}{E\mu_{en}tI} \quad (5.18)$$

where D is the dose recorded by the ionization chamber. Note that eq. 5.18 derives from eq. 5.14 (keeping the same notations), and is valid in the case of a monochromatic X-ray beam with negligible scattering, which is a satisfactory approximation when the ionization chamber is placed in air.

The high-efficiency germanium detector (HEGD) was used to cross-check the results delivered by the PTW dosimeter. The number of counts was determined using the detector-specific energy-dependent photon–counts relation, averaging over repeated acquisitions. From the mean value b of counts (expressed in bits), the photon flux at the point of measurement was calculated as:

$$\phi_{HEGD} = \frac{k \cdot b}{S_{pix}tI} \quad (5.19)$$

where k is the bit–photon conversion factor (corresponding to the number of photons integrated by the HEGD per bit) and S_{pix} is the irradiated pixel surface area (Coan 2006).

5.4.5.2 Dose measurement protocol

Measurements of the dose deposited at different positions within a cylindrical plastic phantom were performed using a CT ionization chamber (Radcal 10X6-3CT, Monrovia, United States) with a read-out connection to a Radcal dosimeter. The Radcal chamber is designed for CT dose measurements and provides dose values in water. The phantom consists in an external layer of polymethylmethacrylate (PMMA) with an outer diameter $D=100$ mm and height of 150 mm, and an internal cylinder of polyethylene (PE) of 60 mm diameter (figure 5.4). Three holes, 13 mm in diameter, make it possible to insert the ionization chamber at different positions (0, 18, 40 mm from the centre). The experiment was carried out with a monochromatic X-ray beam of 60 keV. The phantom was rotated by 360° around its central axis (perpendicular to the beam direction, see arrow in figure 5.4) at a speed of $5^\circ/s$. The X-ray beam used had a parallelepipedal shape with a cross section equal to $2(V) \times 100(H)$ mm². The holes were filled by cylinders of PE, except for the one containing the chamber.

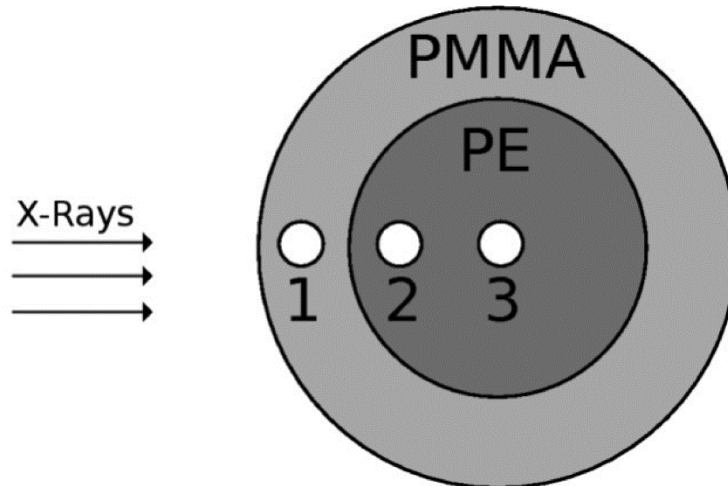


Figure 5.4: Phantom geometry and experimental configuration used in the CT measurements.

5.4.5.3 Simulation parameters

Simulations have been carried out using Geant4 v9.5 with the Penelope physics models, which I have described in the previous sections. An ad-hoc electron cut-off value of 100 keV was used in order to avoid tracking any secondary electron. The distance between the source and the sample was set to 50 cm. The measurements performed with the Radcal chamber on the CT cylindrical phantom were simulated with the active volume of the ionization chamber, 3 cm³, being replaced by a water volume (the chamber provides dose-to-water values). For the simulation, a voxel size of 0.2x0.2x1 mm³ was chosen and the dose estimates were computed by averaging the values obtained in all the voxels contained in the volume of the chamber's active region of. The number of histories chosen for the simulations was 10⁹ in order to obtain a mean statistical uncertainty below 1% in the central irradiated slice.

5.4.6 Performances comparison between TLE and MC dose deposition simulations in complex cases

In order to assess the potential the TLE method to produce dose distributions in complex cases and to evaluate the necessary computing time, I performed two simulations using experimental CT images as inputs for defining the geometry and composition of the volume in which the dose deposition would be evaluated. I considered the CT data of an excised and formalin-fixed human knee joint (one slice: 444x451x1 voxels, with voxel size 0.3x0.3x10 mm³) and of a tumour-bearing human breast (one slice: 321x320x1 voxels, with voxel size 0.3x0.3x10 mm³) acquired at 60 keV by using high-resolution CT

imaging. The images were acquired experimentally using the FReLoN camera detector with the pixel size of $50 \mu\text{m}$.

The parallel X-ray beam had a rectangular cross section of $10 \times 136 \text{ mm}^2$ for the knee joint measurement and of $10 \times 97 \text{ mm}^2$ for the breast measurement. The object was rotated around an axis perpendicular to the beam direction and 200 angular projections over 360° have been simulated. The CT volume of the knee joint has been segmented using a simple thresholding method in order to attribute each voxel to a specific material (solution of 4% formalin in water, muscle and cortical bone). The breast has been segmented into multiple components using a marker-controlled watershed viscous transform (Vachier & Meyer 2005) implemented within the group. By assuming that a 3D image is composed of reliefs, this method is well adapted to the intrinsic nature of the CT images which are characterized by a strong signal on the borders of each feature. The medical *a priori* knowledge of the sample composition was used to assign the following materials to the different regions: adipose tissue, glandular tissue, air and 4% formalin solution in water. In both cases, 10^8 histories were numerically tracked. The simulation parameters were the same as those described in section 5.4.5.3.

In order to test the validity of the local deposition assumption of all energy of the produced secondary electrons, I have repeated the simulations for the breast case with 10^7 events by activating the tracking of the secondary electrons.

5.5 Results

5.5.1 Benchmarking against MC simulation

In the test case described in section 5.4.4, I first verified that our TLE implementation in GATE leads to the same dose distribution computed by the equivalent MC dose actor available in GATE. This is in fact the case within the statistical fluctuations, as shown in figures 5.5 and 5.6. The integrated deposited energy values calculated with the two methods are in agreement within the given uncertainty (table 5.3). The uncertainties are calculated considering the standard deviation of the integrated value of the deposited energy using 20 simulations.

In figure 5.5 and in the profiles in figure 5.6 it is to be noticed that the uncertainty is much larger in the case of the MC simulation because of the slower convergence, as compared to the TLE method.

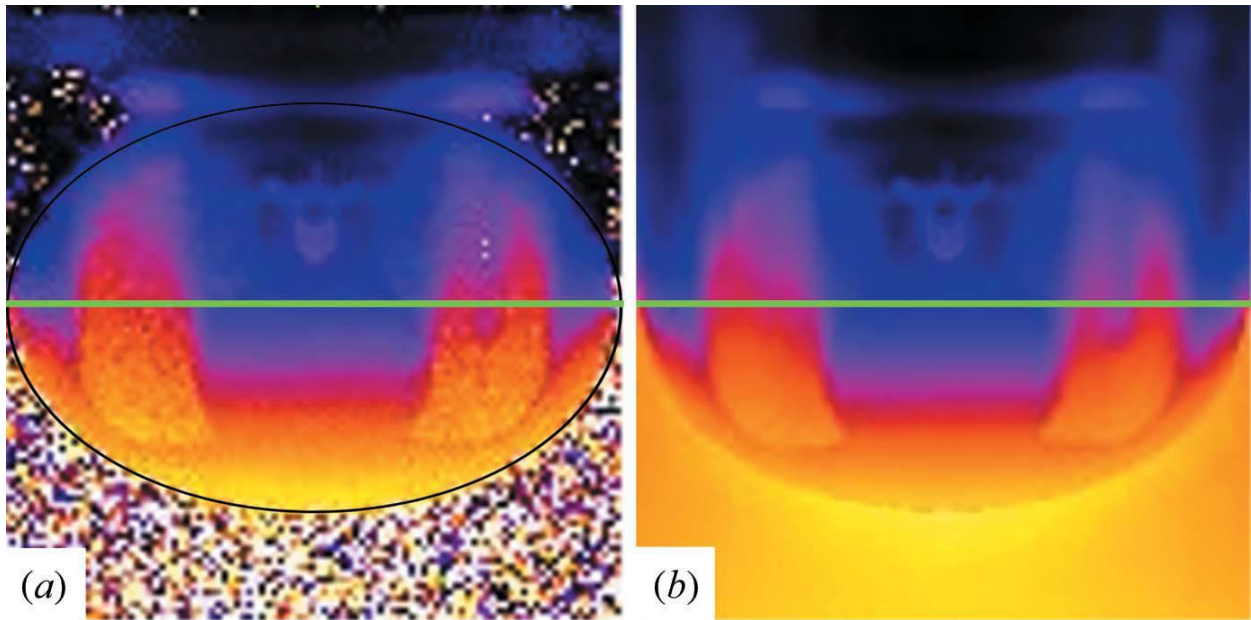


Figure 5.5: Dose distribution maps obtained in the thorax model with the MC method, figure (a), and the TLE method, figure (b). 4×10^8 incident photons were used. The black oval line in figure (a) delimits the region considered for the comparison of the total deposited energy shown in table 5.3.

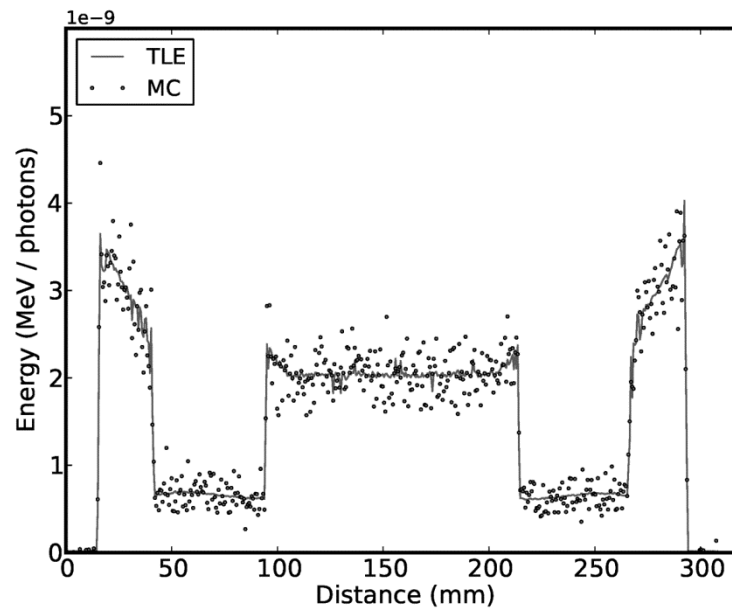


Figure 5.6: Energy deposition profiles in the thorax model simulated with both TLE and MC methods (4×10^8 incident photons). The profiles correspond to the horizontal section marked by the green line in figure 5.5.

MC	TLE	Rel. difference
$3.0404 \times 10^6 \pm 0.009\% \text{ MeV}$	$3.0423 \times 10^6 \pm 0.008\% \text{ MeV}$	0.064 %

Table 5.3: Integrated energy with relative uncertainty in the thorax model, computed with the TLE and the MC method, respectively, under the same simulation conditions (4×10^8 incident photons)

5.5.2 Accuracy test of the TLE method against measurements

The flux values measured with the PTW chamber and the HEGD detector, reported in table 5.4, are in satisfactory agreement. From now on, only the values measured with the PTW are taken into account to assess the photon flux necessary for the simulations.

I have calculated the uncertainties on the HEGD values using the statistical uncertainties on repeated measurements, while for the PTW I considered the uncertainties on both the measurements and the calibration.

Energy	HEGD	PTW
keV	Photons/(mm ² · mA · s)	Photons/(mm ² · mA · s)
33.7	$(1.82 \pm 0.14) \times 10^7$	$(1.84 \pm 0.02) \times 10^7$
45.0	$(1.27 \pm 0.06) \times 10^8$	$(1.26 \pm 0.01) \times 10^8$
50.5	$(1.74 \pm 0.09) \times 10^8$	$(1.71 \pm 0.02) \times 10^8$
65.0	$(1.69 \pm 0.09) \times 10^8$	$(1.60 \pm 0.02) \times 10^8$
72.0	$(1.41 \pm 0.07) \times 10^8$	$(1.33 \pm 0.01) \times 10^8$

Table 5.4: Photon flux values obtained from the measurements at different energies with the HEGD and the PTW chamber.

In table 5.5, the results of the comparison between measured and simulated dose for the CT phantom are reported. The error bars on the simulated values are calculated propagating the uncertainty on the fluence and the statistical error of the simulations. For the measured values, uncertainties are obtained again by propagating the statistical spread of repeated measurements and that of the ionization chamber calibration (this value is provided by the chamber constructor). In figure 5.7, the dose distributions calculated in one transversal slice of the CT phantom are shown, with the CT ionization chamber successively positioned in the three holes. The brighter circular area in the phantom is the volume filled with water (corresponding to the PTW ionization chamber) for which the dose was both measured and simulated.

Position	Measured (Gy)	Simulated (Gy)	% Difference
1	0.262 ± 0.010	0.259 ± 0.007	1.1
1	0.261 ± 0.010	0.259 ± 0.007	0.8
1	0.261 ± 0.010	0.259 ± 0.007	0.8
2	0.264 ± 0.010	0.265 ± 0.007	-0.3
2	0.264 ± 0.010	0.265 ± 0.007	-0.3
2	0.263 ± 0.010	0.265 ± 0.007	-0.7
3	0.261 ± 0.010	0.266 ± 0.007	-1.9
3	0.260 ± 0.010	0.266 ± 0.007	-2.3
3	0.261 ± 0.010	0.266 ± 0.007	-1.9

Table 5.5: Comparison of simulated and measured doses (in Gy) for the CT geometries of figure 5.7. The ionization chamber positions refer to figure 5.4. For each position the computations and the measurements were repeated three times because for each measurement the irradiation time of the chamber is slightly different, thus leading to a different number of photons that have to be entered in the simulations.

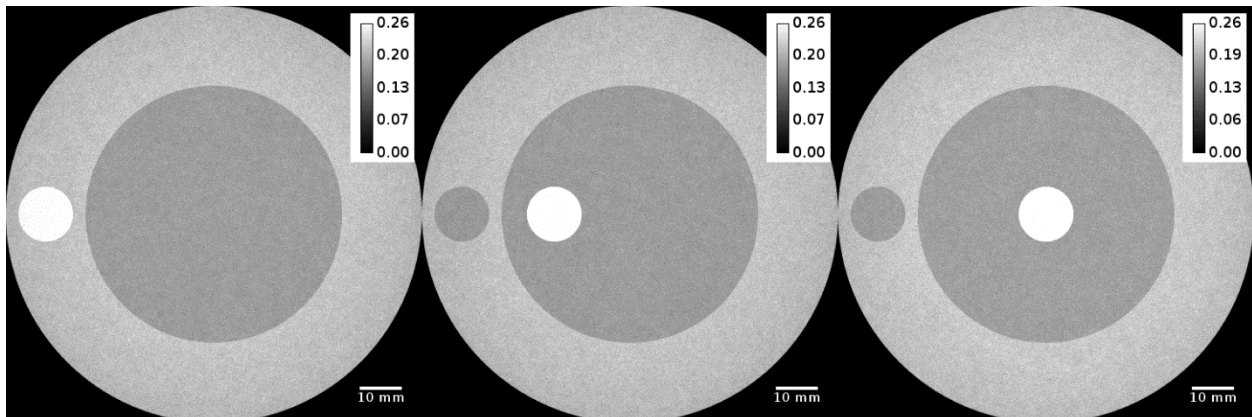


Figure 5.7: Simulated dose distribution maps of a transversal section of the CT phantom corresponding to three different positions of the ionization chamber (the water-filled volume is the white circular area) as reported in figure 5.4. The grey levels correspond to dose values in Gy. The holes not hosting the ionization chamber are filled with PE.

5.5.3 Performances comparison in anatomically complex cases

The results of the simulations carried out with the high-resolution CT volumes of the human knee joint and breast are presented in figure 5.8. Relatively smooth dose maps ($\sim 0.3\%$ mean statistical error per voxel in the whole knee joint volume and $\sim 0.2\%$ in the breast volume) are obtained using the TLE (with 10^8 histories) whereas, for the same number of incident photons, equivalent MC simulations give results affected by very high uncertainty. In fact, for the MC case a large number of voxels are left with no dose information at all and this leads to a mean statistical uncertainty per voxel of $\sim 6.8\%$ in the knee joint and

~5.4% in the breast. Contrary to the standard MC, the use of TLE makes it possible to obtain meaningful dose maps also with a very small number of events (as shown in figure 5.8). For the sake of comparison, I performed the integration over all the voxels composing the sample to work out the average values of the deposited dose. The difference between the average dose values simulated with the standard MC and the TLE method is ~1.2% in the case of the knee joint image and ~0.6% for the breast test case.

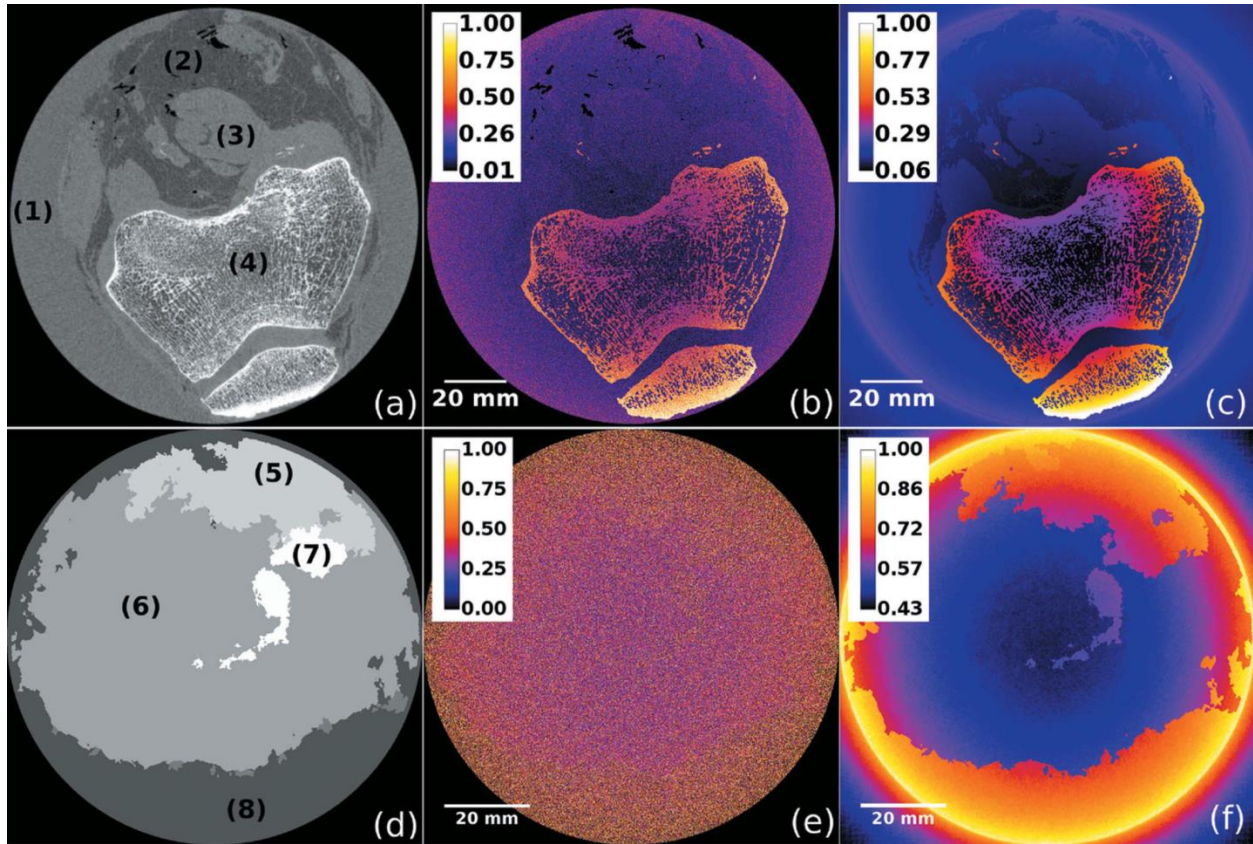


Figure 5.8: Dose distributions obtained in the human knee joint and breast with the MC (centre) and the TLE method (right), with 10^8 incident photon counts. (a), (b) and (c): knee joint; (d), (e) and (f): breast.

(a), (d) are the sample models derived from experimental CT data, (b), (e) are the dose maps obtained with the TLE method, while (c) and (f) are the maps computed with the equivalent MC method. In (a): the region marked with (1) has been assigned to the formalin solution, (2) to the adipose tissue, (3) to muscle and (4) to the cortical and trabecular bone. In (d): (5) has been assigned to glandular tissue, (6) represents the adipose tissue, (7) is the tumour and (8) is the formalin solution. The dose scale in the figures (b), (c), (e) and (f) are normalized to unity.

The total computation time was about 11 h for the knee and 9 h for the breast, using ten 3.3 GHz CPUs for the simulations based on the TLE method, while using the MC method, 10 h are required for the knee and 8 h for the breast. These differences in time are due to several additional operations required within the TLE and related to its coefficients database, see section 5.4.2.

It is possible to estimate the number of events, N_f , required to obtain a statistical error of about σ_f , by means of $N_f = \left(\frac{\sigma_i}{\sigma_f}\right)^2 N_i$, where σ_i and σ_f are the standard deviations with N_i and N_f events, respectively. It is possible to estimate this number in order to recover the same average statistical error as a TLE calculation for a considered region of interest (*i.e.* the entire volume), table 5.6.

Sample	TLE uncertainty	MC uncertainty	Nf/Ni*
Knee	0.3%	6.8%	~460
Breast	0.2%	5.4%	~650

Table 5.6: The value of Nf/Ni has been corrected considering that the TLE method requires about 10% more computation time respect to the MC with the same number of histories. This value can be easily related to the gain in speed of the simulation because of the linear correlation between the computation time and the number of histories used in the simulation.

The reason for this very long time is the great number and the small size of voxels in the two presented cases.

In table 5.7 I have reported the values of the integrated deposited energy calculated with and without forcing the secondary electrons to deposit locally their energy for the breast case scoring 10^7 events: the two estimates are in good agreement within the statistical uncertainty.

TLE*	TLE	Relative difference
$7.982 \times 10^5 \pm 0.015\%$	$7.985 \times 10^5 \pm 0.015\%$	0.033%

Table 5.7: Integrated energy deposition calculated with (asterisk) and without switching the tracking option of the secondary electrons. Values are expressed in MeV.

5.6 Conclusions

The TLE method which has been study in this Thesis work will be implemented in the next release of the open source GATE /Geant4 9.5 simulation platform. As a result, a new software module named *TLEDoseActor* was created, which uses the tables of energy-absorption coefficients which I have generated from the EPDL97 database. The results I produced show that the TLE provides a powerful tool for simulating the dose deposited by photon beams in the keV energy region, when secondary electrons can be deemed to deposit all their energy locally, using a small number of events and without loss of accuracy. Potential applications of this new tool range from CT imaging to nuclear medicine as well as low-energy X-ray external radiotherapy.

In summary, the TLE method makes it possible to simulate dose distributions, with a certain statistical uncertainty, in very complex geometries, like organ volumes imaged with high-resolution CT scans (with the identification of the atomic composition of the tissue assigned to each voxel) in about 2 orders of

magnitude less time with respect to the conventional MC, depending on the used parameters. For the same computational time, analogous MC simulations suffer from much slower statistical convergence.

Chapter 6 - Radiation dose in breast CT imaging with monochromatic X-rays: a simulation study and database

6.1 Introduction.....	137
6.2 Dose database for breast CT	137
6.2.1 Instruments and methods	138
6.2.2 Simulations parameters	139
6.2.2.1 General parameters	139
6.2.2.2 Derivation of a reference dose database.....	141
6.2.2.3 Energy optimization with Gadox- and CdTe-based detection systems.....	141
6.2.2.4 Study of the sample thickness influence	141
6.2.2.5 Study of the tissue composition influence	141
6.2.2.6 Study of the influence of skin and/or PMMA wall to the dose calculation	142
6.2.2.7 Estimation of the accuracy of the approximation factors.....	142
6.2.3 Results.....	142
6.2.3.1 Derivation of a reference dose database.....	142
6.2.3.2 Minimization of the ratio dose/transmittance D_t	144
6.2.3.3 Energy optimization with Gadox-, CdTe-, CsI-based and a-Se imaging detectors	145
6.2.3.4 Study of the sample thickness influence	148
6.2.3.5 Study of the tissue composition influence	150
6.2.3.6 Skin and PMMA wall influence.....	151
6.2.3.7 Calculation of the deposited dose	152
6.2.3.8 Comparison between simulations of test cases and approximated values	152
6.3 Optimization of the radiation dose by adapting the exposure time to sample geometry	153
6.3.1 Instruments and methods:	154
6.3.2 Results and discussion	155
6.3.2.1 Dose and time reduction	155

6.3.2.2 Image quality 159

6.4 Conclusions..... 164

6.4.1 Dose database study..... 164

6.4.2 Optimization of the detector integration time 165

6.1 Introduction

Two of the main problems related to computed tomography (CT) imaging are the dose delivered to the sample and the time required for the acquisition of all the projections. Within our group and this Thesis work, it has been demonstrated that high resolution X-ray phase-contrast imaging (PCI) CT of the breast can be performed at clinically compatible doses either on portions (Keyriläinen et al. 2008) or on whole organs (Zhao et al. 2012). These results despite yet obtained *in vitro*, represent an important step towards the clinical translation of the technique.

A fundamental aspect of this work is the optimization of the CT scan parameters in order to keep both the dose and the acquisition times at clinically compatible values. To this end, I have developed a procedure for a quick estimation of the dose (section 6.2) in CT as well as new methods allowing a reduction of both quantities (section 6.3). The influence of different parameters on the deposited dose distribution, like the breast composition and thickness, the dose deposited to the skin or the sample container (for preclinical tests) have been investigated by means of Monte Carlo (MC) simulations. The results can be generalized to geometries different from that specifically studied, following the applications of some corrections factors that have been tabulated. An energy optimization study is also presented; it considers also the energy dependence of the X-ray detector efficiency. A simple analytical method to estimate the energy that minimizes the dose-transmittance ratio in CT imaging is introduced and compared with the results obtained with simulations.

In section 6.3, I present the study of a method for optimizing both the radiation dose and the image quality by adapting the exposure time following the sample thickness and shape in case of the in-plane PCI-CT geometry. The optimization is performed using only an approximated knowledge of the absorption properties of the imaged object. Results are based on MC simulations (GATE/GEANT4) and on simulations performed with the RIPCIP code which was described in Chapter 3.

6.2 Dose database for breast CT

As previously discussed, a fundamental parameter in X-ray diagnostics and in particular in breast imaging is the radiation dose delivered to the tissue. While the adipose tissue is not considered to be at risk, particular attention is given to the dose deposited into the glandular component part of the breast because of its high radiosensitivity. The typical reference parameter is known as Mean Glandular Dose (MGD) and its precise prediction and calculation has been the subject of a large number of publications (Kulkarni & Supe 1984; Boone 1999; Boone et al. 2001; Boone 2002). Several studies dedicated to the evaluation of the MGD using measurements of the kerma in air are reported in the literature (Boone 1999; Boone 2002; Dance

et al. 2000; Dance 1990), but only few refer to breast CT (Boone et al. 2001) and only a limited number of cases (in terms of breast thickness and composition) are taken into account. Other works studying the influence of different parameters, and the reduction of the dose delivered are related to tomosynthesis (Sechopoulos et al. 2007) or to the organ dose (Rupcich et al. 2012), dose reduction (Rupcich et al. 2013); all these studies consider the radiation issued from X-ray tubes.

In order to thoroughly evaluate the diagnostic relevance of the new imaging approaches proposed in this Thesis, a precise dose assessment study needs to be carried out. However, to the best of our knowledge, no work exists in literature showing a quick and accurate procedure for the estimation of the dose deposition in CT in the case of synchrotron based studies on breast samples.

The aims of the work presented in this next section are 1) to provide a reference database of the dose delivered in breast CT with synchrotron radiation obtained by using MC simulations, considering different breast compositions, thicknesses and X-ray beam energies; 2) to determine the best photon energy for the dose minimization in CT conditions; 3) to introduce a way to easily estimate the average deposited dose (AvD) for generic experimental cases starting from the values calculated and tabulated here. Monochromatic X-rays are considered in this study within the energy range of 15-100 keV. Simulations are performed using the GATE code (Jan et al. 2004; Jan et al. 2011). To accelerate the convergence of the simulations, the TLE technique (Williamson 1987) has been used in GATE as described in Chapter 5 (Mittone et al. 2013).

6.2.1 Instruments and methods

If we consider a cylindrical volume filled with breast, the value of the X-ray energy E_{min} that minimizes the ratio between the deposited dose and the transmittance through the object, in the CPE condition, can be expressed as follows:

$$D_T(E_{min}) = \min\left(\frac{D}{T}\right) \approx \min\frac{E \frac{\mu_{en}}{\rho}}{e^{-\mu l}} \quad (6.1)$$

where D_T is the obtained dose/transmittance ratio, D is the calculated/simulated dose, T the calculated average transmittance after the object, E the photon energy and l indicates the thickness to take into account the traversed material (*i.e.* the mean traversed thickness value). In a realistic case, an additional multiplicative weighting factor has to be used to take into account the imaging detector efficiency.

In figure 6.1, the plot of the ratio D_T as a function of the X-ray energy calculated with equation eq. 6.1 is reported for a cylindrical breast sample of 9 cm in diameter. For the calculation, the cylinder has been approximated in a standard way by a cube whose side is equal to $\pi/4$ times the cylinder in diameter (the side is about 7 cm in this case).

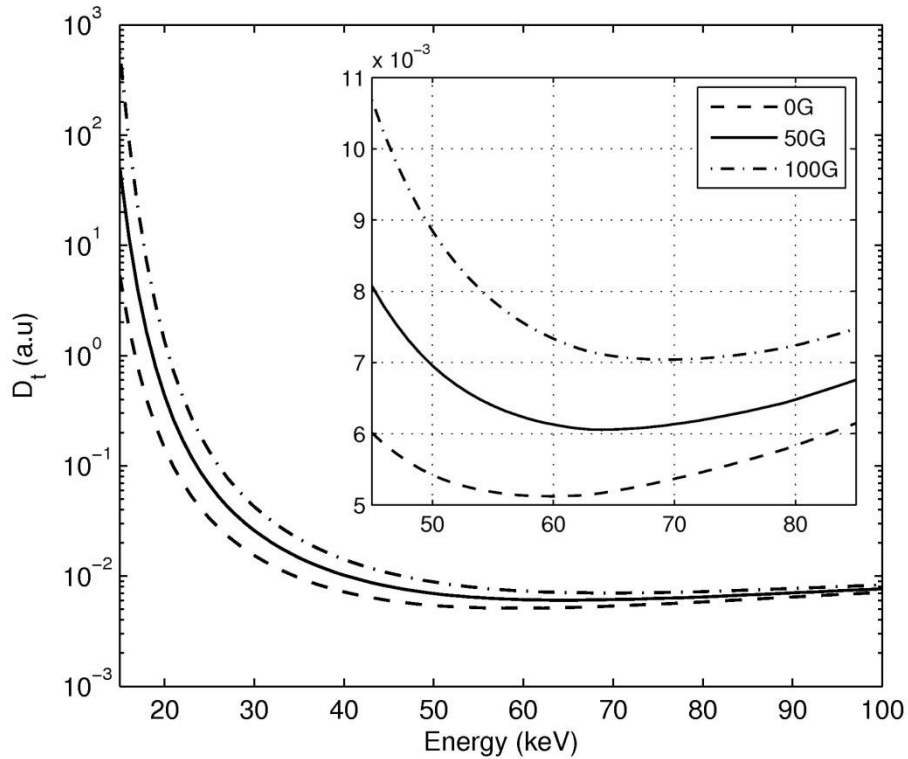


Figure 6.1: Ratio D_t between the deposited dose and the transmittance through the object as a function of the photon energy for a cylindrical breast sample of 9 cm in diameter. The scale is expressed in arbitrary unit (a.u.). The energy values, as it is possible to see in the inset on top right, which minimize these curves (*i.e.* formula 6.1) are respectively 60 keV for 0% glandular tissue (0G), 64 keV for 50% glandular and 50% adipose tissue (50G), and 69 keV for the 100% glandular case (100G).

6.2.2 Simulations parameters

6.2.2.1 General parameters

Simulations were performed using the GATE version 6.1 and the GEANT version 4.9.5 libraries. The used physics models are based on the GEANT implementation of the Penelope code (Salvat & Fernández-Varea 2006). In order to avoid the tracking of all the secondary electrons produced during the interactions, an electron energy cut equal to the maximum energy of these particles (which coincides with the used X-ray energy) is set; a consequent speed up of the simulations is obtained. This choice is justified because, by using the continuous-slowning-down approximation (CSDA), the electron track range is sufficiently small in the energy interval considered in this work. Thus the entire electron energy can be assumed to be deposited locally.

I have simulated a CT imaging setup in which a sample is imaged at different angular views with respect to the rotation axis. The sample was modelled as a homogeneous cylindrical volume of breast tissue. Two hundred angular projections over 360 degrees and a voxel size of $1 \times 1 \times 1 \text{ mm}^3$ were considered. The monochromatic and parallel photon beam has been defined as a rectangular function of area equal to the lateral section of the cylindrical sample (*diameter x height*) for all the presented cases.

The number of primary photons was 5×10^8 in order to keep the statistical uncertainty on the AvD in the entire volume low; an uncertainty below 0.07% for the case corresponding to the thickest sample (*i.e.* 15 cm in diameter) was obtained. In order to calculate the statistical uncertainty on the simulated estimations, per each case, the simulations have been repeated 20 times.

The breast is considered as a mixture of glandular and adipose tissues which can be present with a variable relative percentage. The chemical composition of these tissues is reported in table 6.1 (Hammerstein et al. 1979).

The radiation dose is calculated considering the average value over the entire volume. In order to remove the skin/container influence on the total deposited dose (the skin is not considered radiosensitive and at risk), an external layer of 4 mm of thickness has not been considered for the calculation of the AvD to estimate only the dose deposited in the breast tissue (and ultimately in the glandular fraction, which is considered the most radiosensitive part of the organ).

These dose values have been calculated for various breast compositions. The parameters used in the different phases of this study are described in the following sections. Several correction factors to take into account the influence of the breast composition, thickness and the presence of a skin-or-container layer on the deposited dose have also been derived. These factors will be used to obtain an empirical equation which allows to easily extending the dose estimation to cases other than those considered here, without the need of additional simulations.

Glandular weight fraction %	Tissue density (g/cm ³)	Hydrogen	Carbon	Nitrogen	Oxygen	Phosphorus
0	0.930	0.112	0.619	0.017	0.251	0.001
30	0.963	0.109	0.489	0.021	0.379	0.002
50	0.982	0.107	0.401	0.025	0.464	0.003
70	1.007	0.105	0.315	0.027	0.549	0.004
100	1.040	0.102	0.184	0.032	0.677	0.005

Table 6.1: Breast tissues composition. Values are taken from Hammerstein et al. 1979. Values for the 30% and 70% glandular fractions are calculated by means of a weighted average.

6.2.2.2 Derivation of a reference dose database

Four series of dose simulations have been performed considering four different diameters (6, 9, 12 and 15 cm) and three different compositions (pure adipose, pure glandular and a mix of 50% adipose and 50% glandular tissue) of the breast. The photon beam energy range is 15-100 keV with a step interval of 1 keV. The values of dose presented in this database have been normalized to one single photon.

6.2.2.3 Energy optimization with Gadox- and CdTe-based detection systems

The optimization of the dose/transmittance ratio, D_t , has been studied considering four common detector systems: one based on a Gadox ($\text{Gd}_2\text{O}_3\text{S}$, 60 μm in thickness) screen (*e.g.* FReLoN camera, Coan et al. 2006), and one using a cadmium telluride (CdTe, 1 mm in thickness) screen (*e.g.* Maxipix detector, Ponchut et al. 2011), one based on amorphous selenium and one based on CsI. The effect of the detection system has been calculated by weighting the dose curves, obtained as described in 6.2.2.2, with the efficiency curve $\eta(E)$ of the considered detector. The efficiency of the data acquisition systems (*e.g.* electronics of the detector) are instead assumed equal to 1. Thus, only the efficiency of the layer of the detector screen material is taken into account by using its absorption curve.

6.2.2.4 Study of the sample thickness influence

A series of simulations using the parameters described in section 6.2.2.1 have been performed considering the diameter of the cylindrical sample in the range 60-150 mm with a step of 2 mm. In this case we used a breast sample composed 50% of adipose tissue and 50% of glandular tissue. The considered photon energies are 20 keV, 60 keV and 100 keV. Using the results of these simulations, I have derived an expression to calculate the correction factor R_f , which accounts for the sample thickness.

6.2.2.5 Study of the tissue composition influence

Three series of simulations have been performed varying the composition of a 12 cm-diameter breast. I have considered ten different fractions of glandular tissue, from 0% to 100% with a 10% step, and three different beam energies (30 keV, 60 keV and 90 keV). Using these results a correction factor C_f which accounts for the breast composition and that can be applied for deriving dose values for compositions different from those examined here is derived.

6.2.2.6 Study of the influence of skin and/or PMMA wall to the dose calculation

Simulations in the energy range 15-100 keV, with a 1 keV step, have been performed considering in the simulated geometry a layer of PMMA (2 mm) around the cylindrical sample. The study has been performed considering a geometry consisting of one cylinder of total diameter of 120 mm and height of 50 mm. In this case I used a breast composed 70% of adipose tissue and 30% of glandular tissue in order to consider the average values of a realistic case (Klein et al. 1997).

I performed a second series of simulations considering an external skin layer of 4 mm, using the scheme of a breast used in (Boone et al. 2001). The compositions of the PMMA and the skin used in these simulations are taken from the NIST (<http://physics.nist.gov/>). In these simulations the PMMA and skin layer, respectively, are removed from the sample volume used for the calculation of the AvD.

6.2.2.7 Estimation of the accuracy of the approximation factors

I simulated four different test geometries, described in table 6.2, using the general parameters previously described in section 6.2.2.1.

Geometry name	Diameter (mm)	Tissue	Presence of wall	Energy (keV)
G1	40	40% glandular	2 mm PMMA	20
G2	60	30% glandular	4 mm skin	40
G3	80	20% glandular	4 mm skin	80
G4	130	10% glandular	2 mm PMMA	60

Table 6.2: Parameters list of the test cases used to compare the simulations and the results obtained by using the approximated formula derived in section 6.2.3.7.

I have then compared the results of the simulations obtained for these four test cases with the values calculated by using an approximated formula for the AvD which is introduced in section 6.2.3.7. This formula is based on the dose database and correction factors derived here.

6.2.3 Results

6.2.3.1 Derivation of a reference dose database

The curves of the AvD as a function of the X-ray energy for a cylindrical breast sample of 6, 9, 12 and 15 cm in diameter are reported in figure 6.2 (a-d), respectively. In figure 6.2 (e-f) are shown the profiles of the average dose calculated along the radius (the center is the zero) for the 6 cm and 12 cm in diameter and 50% glandular tissue cases. The values of dose in the following curves are normalized to a single photon.

For each case, I have considered three different breast compositions. All the obtained dose curves present a minimum for a certain energy value falling in the range 57-76 keV.

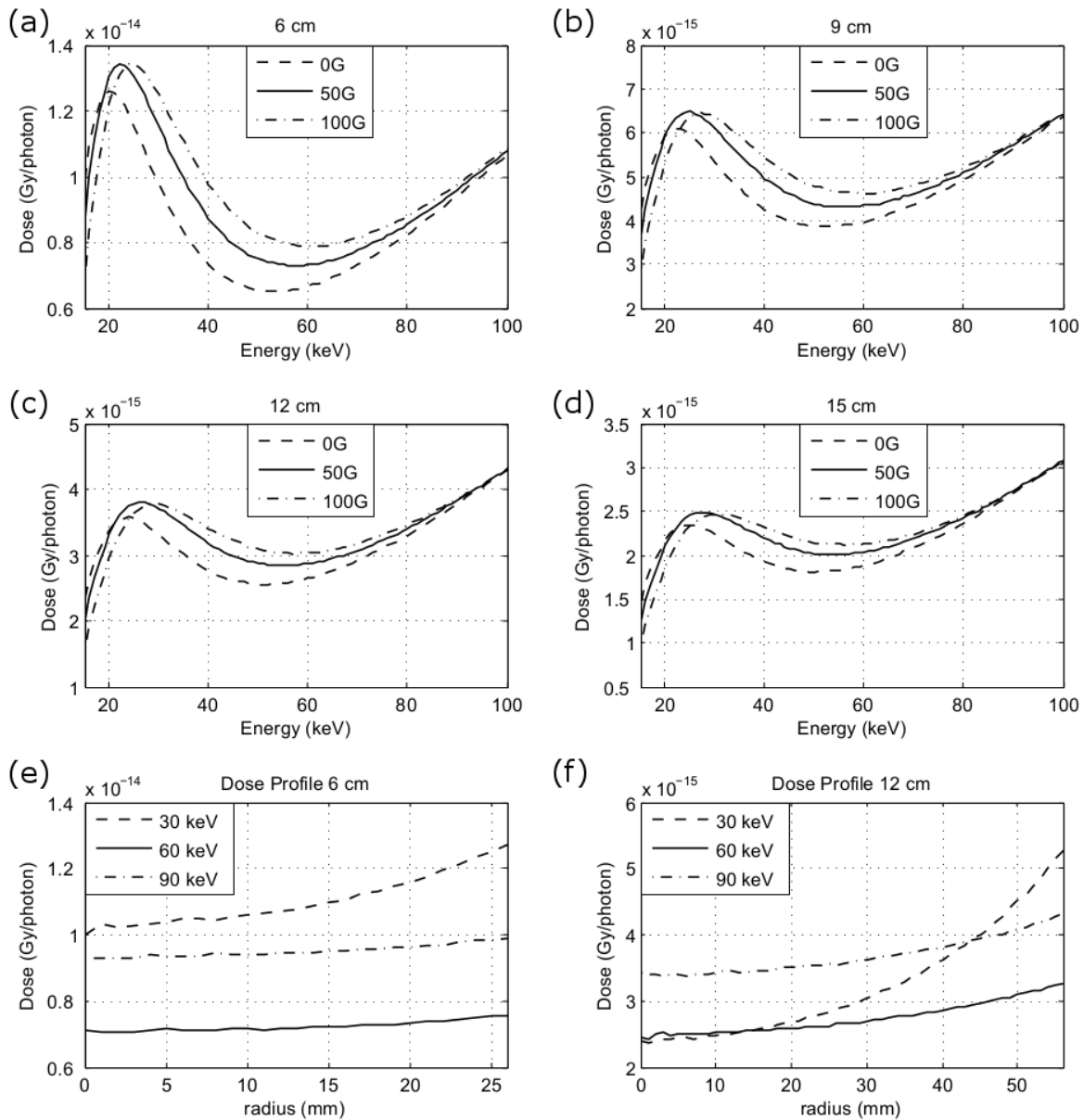


Figure 6.2: Average dose curves for different compositions of the breast. For all the four diameters the curves present a minimum (in the energy range 58-76 keV) as predicted by eq. 6.1. (a) Breasts of 6 cm in diameter, (b) 9 cm, (c) 12 cm and (d) 15 cm. The dose profiles as a function of the radius (starting from the center) for the 6 cm and 12 cm diameter breast cases with 50% of glandular tissue are presented in (e, f).

6.2.3.2 Minimization of the ratio dose/transmittance D_t

The value of the dose obtained for a given energy E_n has been weighted against the mean transmittance through the object at the same E_n . In table 6.3, the values of energy that minimize the ratio of average dose (AvD) to the transmittance obtained from simulations (S) are compared with the minimization energy values calculated (C) by using eq. 6.1. The skin/container effect has not been taken into account for the analytical calculation with eq. 6.1 because for energy values close to the minimization ones (> 50 keV) the deposited dose profiles along the radius in the breast sample are flat (figures 6.2e, 6.2f) and consequently the AvD does not change significantly.

Diameter (mm)	min(S _{0G}) (keV)	min(S _{50G}) (keV)	min(S _{100G}) (keV)	min(C _{0G}) (keV)	min(C _{50G}) (keV)	min(C _{100G}) (keV)
60	57	63	65	58	63	66
90	59	64	70	60	64	69
120	61	68	71	62	66	72
150	63	69	76	63	69	76

Table 6.3: Values of the X-ray energy which minimizes the dose/transmittance ratio for the different breast thickness-composition combinations considered in this study. The “S” columns refer to the results obtained with the simulations, while the “C” columns refer to the calculation performed with equation 4.

The fraction by mass of glandular tissue decreases with increasing compressed breast thickness and age of patient (from 75% at 25 mm to 20% at 80 mm, and from 65% at 20 years to 30% at 75 years). For a medium-sized breast, *i.e.* a compressed breast thickness of 55 mm, the fraction of glandular tissue is about 35% (Klein et al. 1997). We assumed a breast composition of about 30%/70% glandular/adipose tissue in order to consider medium size and middle age female breast cases. Using this consideration and the results reported in table 6.3, the optimal energy range for a breast in the range of 6-15 cm in diameter falls in the interval 60-67 keV.

For low photon energies (< 20 keV), the X-ray transmittance through breast samples with the considered thicknesses is negligible, while for high energies (> 65 keV) the ratio between the dose over the transmittance increases because the contribution of the dose deposited in the sample is larger than the gain obtained in terms of transmittance. The enhancement of the dose deposition follows the rise of the total cross section, mainly due to the Compton scattering in this range of energies. I have reported the AvD values of the curves shown in figure 6.2 in Appendix (tables A2-A5). The statistical uncertainties for the presented simulations are between 0.07% for the 15 cm thick breast and 0.03% for the 6 cm breast.

6.2.3.3 Energy optimization with Gadox-, CdTe-, CsI-based and a-Se imaging detectors

The curves of the dose-transmittance ratio have been normalized with the efficiency (*i.e.* screen absorption curve), indicated by A , of the Gadox-based detector (figure 6.3), CdTe-based (figure 6.4), CsI-based (figure 6.5) and a-Selenium (figure 6.6).

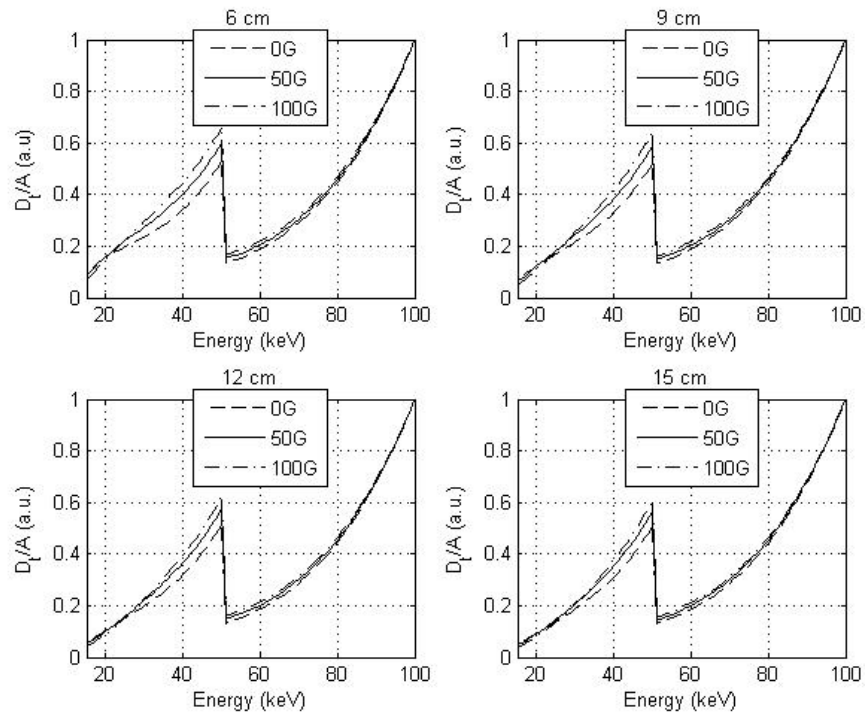


Figure 6.3: Dose-transmittance ratio curves normalized to the efficiency (*i.e.* screen absorption curve, A) of a Gadox-based detector for four different breast sample diameters and three different breast compositions. The scale is expressed in arbitrary unit (a.u.).

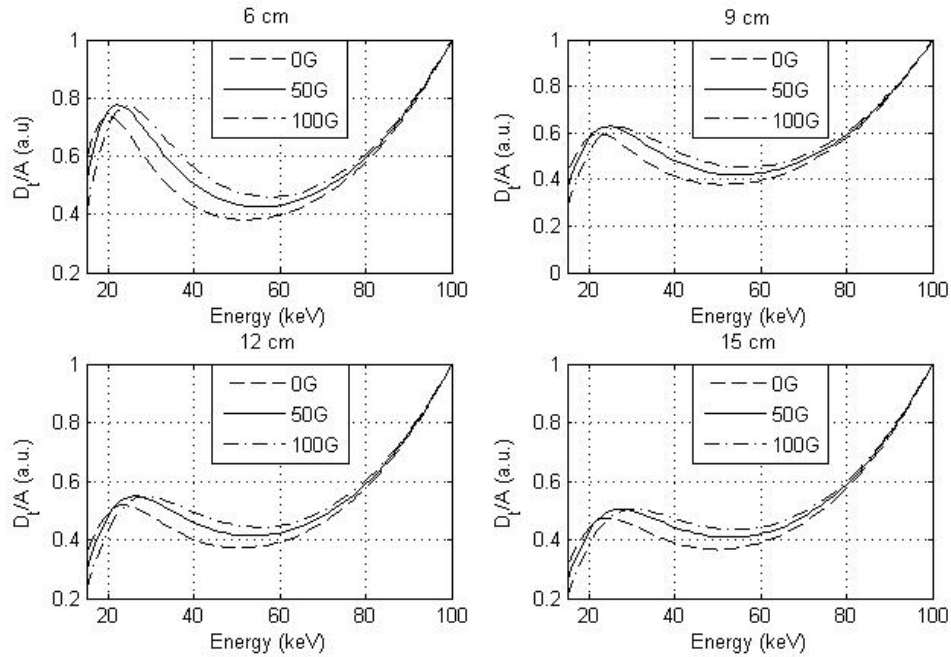


Figure 6.4: Dose-transmittance ratio curves normalized on the efficiency (*i.e.* screen absorption curve, A) of a CdTe-based detector for four different breast sample diameters and three different breast compositions. The scale is expressed in arbitrary unit (a.u.).

Results are shown in figure 6.4 and indicate that the detector properties, in terms of efficiency, may appreciably influence the radiation dose curves. The optimal energies are immediately above the K-edge of the gadolinium (~ 51 keV) for the Gadox-based detector and fall in the range 50-60 keV for the CdTe-based detector.

Nowadays, a-Selenium and CsI based detectors are becoming very common in clinical mammography. If we considered these kinds of detectors, the energies that minimize the dose/transmittance ratio lie in the range 50-55 keV for the a-Selenium (figure 6.5) and around 55-60 keV for the CsI (figure 6.6).

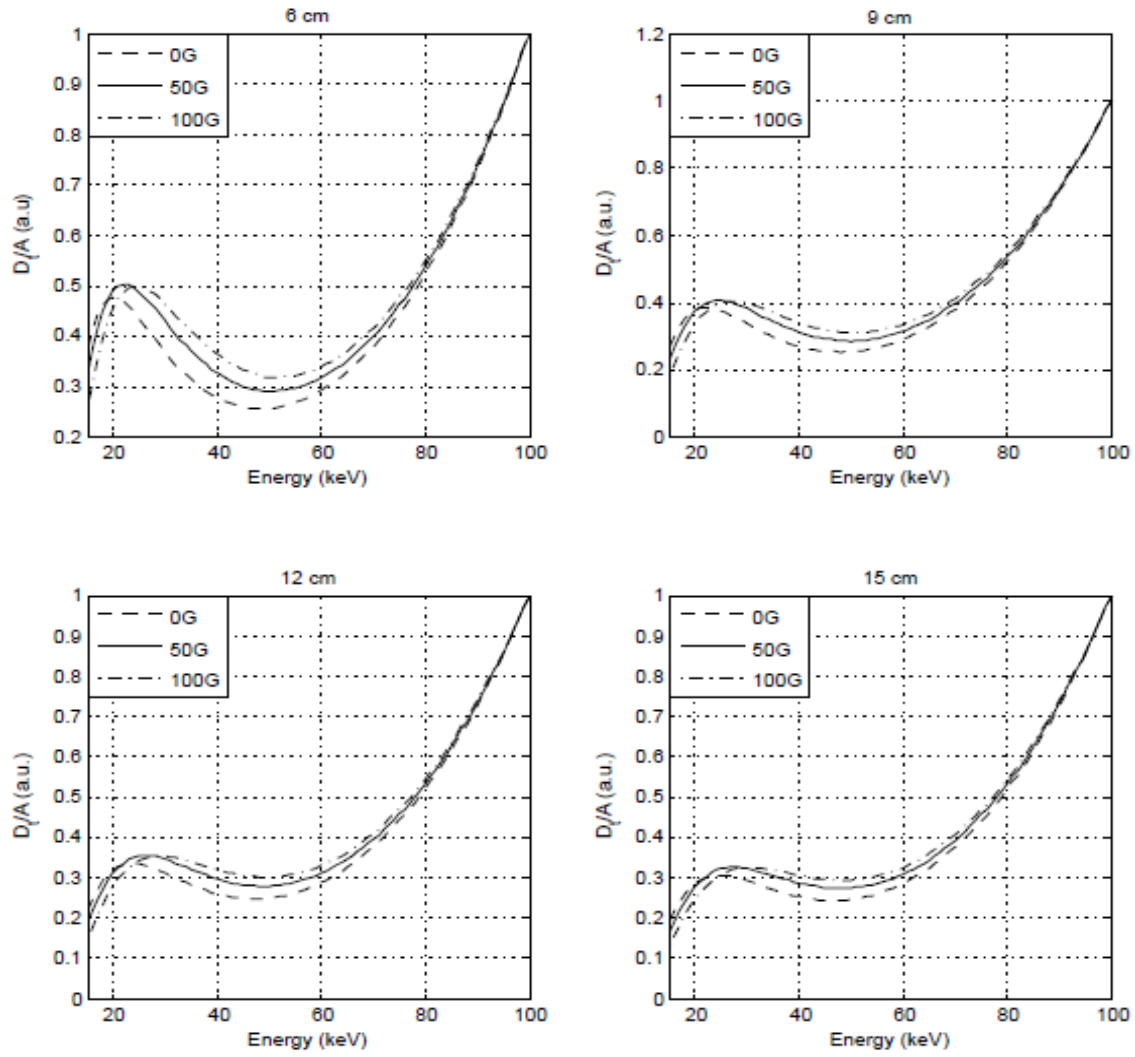


Figure 6.5: Dose-transmittance ratio curves normalized on the efficiency (*i.e.* screen absorption curve, A) of a Selenium detector for four different breast sample diameters and three different breast compositions. The scale is expressed in arbitrary units (a.u.).

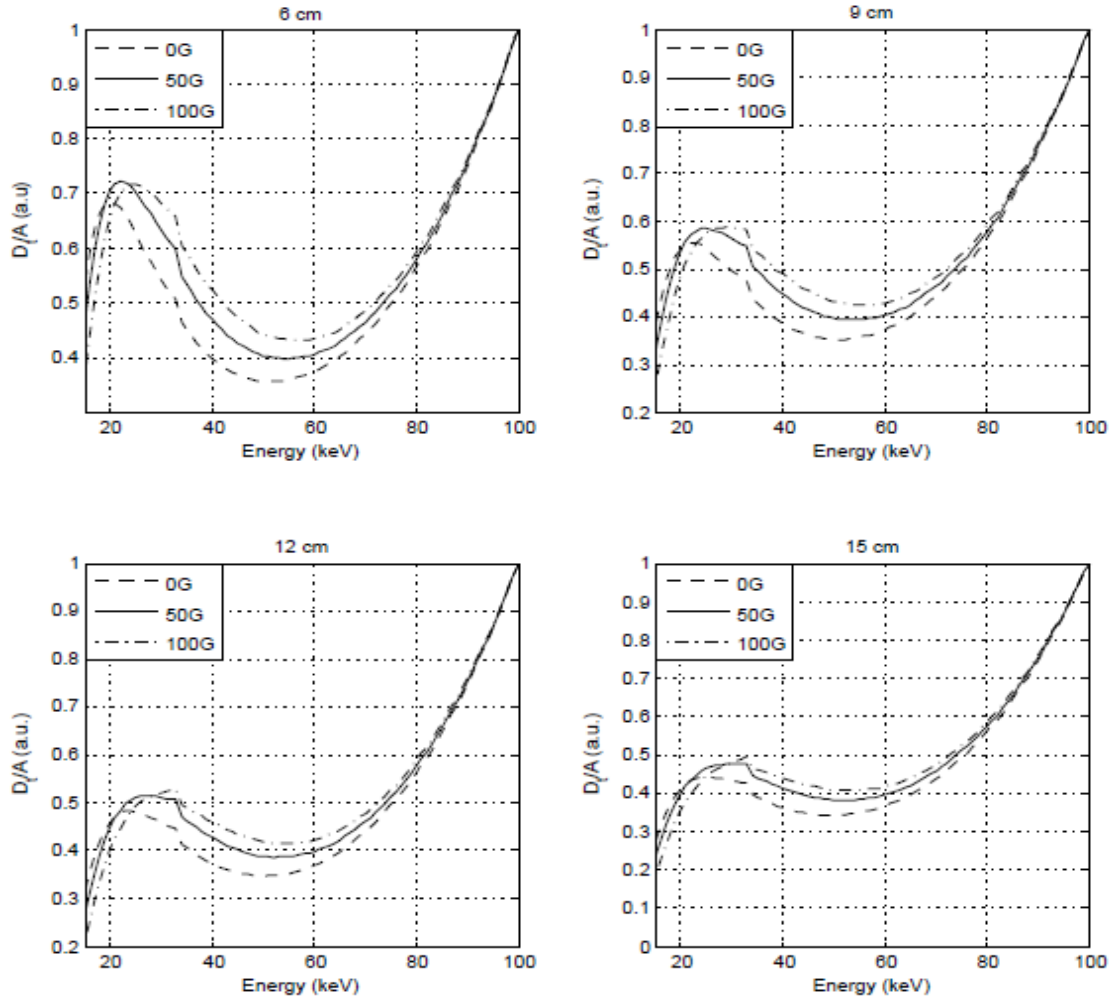


Figure 6.6: Dose-transmittance ratio curves normalized on the efficiency (*i.e.* screen absorption curve, A) of a CsI detector for four different breast sample diameters and three different breast compositions. The scale is expressed in arbitrary units (a.u.).

6.2.3.4 Study of the sample thickness influence

In figure 6.7, I present the value of the AvD as a function of the breast thickness (*i.e.* diameter of the cylindrical sample) considering three different photon energies (20 keV, 60 keV, 100 keV).

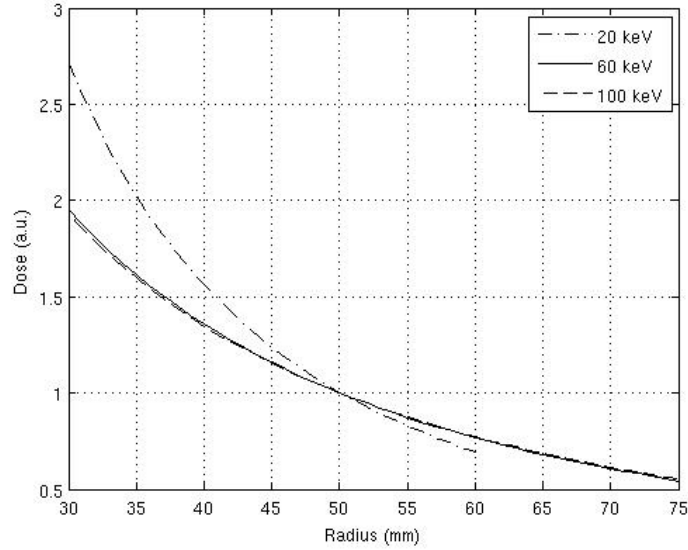


Figure 6.7: Average dose as a function of the breast sample thickness (*i.e.* radius of the cylindrical model). Three energies have been considered: 20, 60 and 100 keV. The dose is normalized on the AvD value corresponding to a radius of 50 mm (for making the plot easier to the reader). The curve at 60 keV presents lower dose deposition values. This energy is in fact closer to the value of energy that minimizes the dose, according to figure 6.2. Only values corresponding to a transmittance through the sample > 1% are reported for the 20 keV case.

For higher photon energies (e.g. 60 and 100 keV), the effect of the sample radius (*i.e.* thickness) on the AvD diminishes because of two different effects: 1) the dose deposition is less energy-dependent as shown in figure 6.2 (e-f) due to the rapid photoelectric fall-off and the weaker energy dependence of the Compton effect; 2) the volume over which the energy deposition is averaged is larger. The dose curves presented in figure 6.7 have been fitted using an exponential function with a quadratic exponent (interpolated dose): $D_{int} = e^{p_1x^2+p_2x+p_3}$. In table 6.4 the fit parameters and the coefficient of determination (R2) are reported for the dose curves of figure 6.7.

Energy (keV)	p ₁	p ₂	p ₃	R2
20	4.6120E-4	-8.6550E-2	3.1733	0.9968
60	1.9500E-4	-4.8458E-2	1.9370	0.9993
100	1.9721E-4	-4.8051E-2	1.9102	0.9998

Table 6.4: Fit parameters of the exponential polynomial interpolations of the curves presented in figure 6.7.

These interpolation parameters can be used to calculate the value of the dose for cases that differ from the ones presented in the reference database I have calculated. The correction factor, to take into account the effect of the diameter on the dose, can be obtained as $R_f = D_{int}/D_{ref}$, where D_{ref} can be taken directly

from tables A2-A5 in Appendix (*i.e.* corresponding to figures 6.2(a-d)), while D_{int} can be calculated using the exponential interpolation with the coefficients of table 6.4.

6.2.3.5 Study of the tissue composition influence

In figure 6.8 the AvD curves as a function of the breast sample composition are reported for 30, 60 and 90 keV.

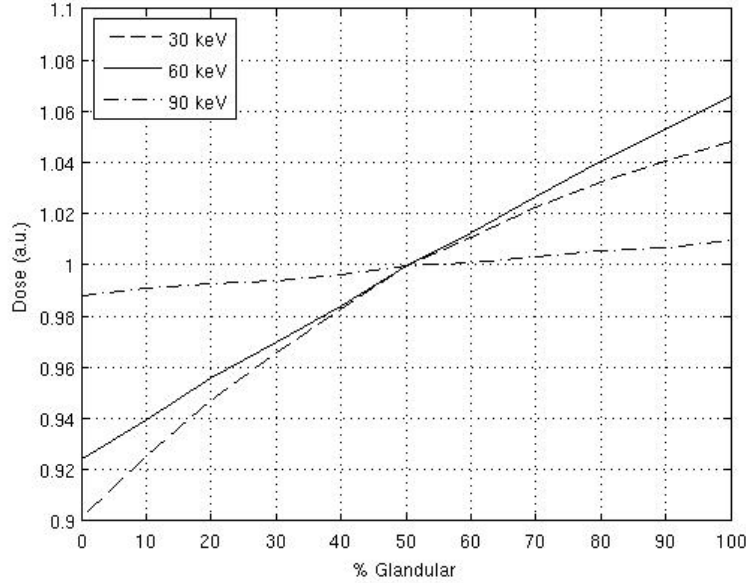


Figure 6.8: Average dose curves as a function of the percentage of glandular tissue within the breast sample for three different photon energies. The values of dose are normalized considering the points at 50% of glandular as reference values (for making the plot easier to the reader).

I have interpolated the curves using a quadratic function expressed as: $D_{int} = p_1x^2 + p_2x + p_3$. The interpolation parameters are reported in table 6.5.

Energy (keV)	p_1	p_2	p_3	R2
30	-9.5110E-06	2.4030E-3	9.0195E-1	0.9996
60	-1.5810E-06	1.5766E-3	9.2410E-1	0.9999
90	-1.0859E-07	2.2637E-4	9.8793E-1	0.9931

Table 6.5: Parameters of the quadratic fits used to interpolate the dose curves shown in figure 6.8.

The correction factor which takes into account the effect of a different breast composition, with respect to the cases here reported, can be obtained as $C_f = D_{int}/D_{ref}$. D_{ref} represents the reference dose value (from tables A2-A5 in Appendix) for the closest case in terms of X-ray energy, breast diameter and composition, while D_{int} is the value calculated using the interpolation function for the wanted breast composition. The AvD increases with the percentage of glandular tissue in the breast because the fractions of high Z elements (*i.e.* Oxygen) increase with it (table 6.1) and because of the dependence of the Compton scattering cross

section on Z. The influence of a different composition on the AvD decreases at higher energies (figure 6.2). This is mainly due to the fact that at higher energies the Compton scattering prevails over the photoelectric effect. Owing to the lower dependence on Z of the Compton scattering with respect to the photoelectric effect, the small discrepancies in the mean value of Z (*i.e.* corresponding to different breast compositions) determine negligible variations in the dose.

6.2.3.6 Skin and PMMA wall influence

In figure 6.9 are presented, as a function of the photon energy, the ratios between the AvD simulated by considering an additional skin or a container wall, respectively and the reference AvD (*i.e.* case simulated without wall) for a total external breast diameter of 12 cm.

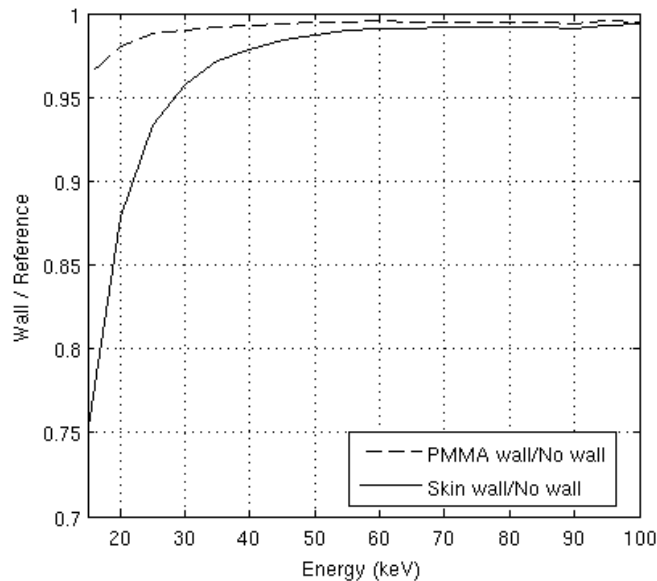


Figure 6.9: As a function of the photon energy are reported the ratios between the AvD curve obtained by including a PMMA/skin wall layer and the reference AvD curve for a 12 cm in diameter.

To correct the reference dose values for the presence of a wall layer, it is sufficient to multiply them by the ratio value derived from the curves in figure 6.2 for the corresponding photon energies. The presence of a PMMA (container) wall, as it is possible to see in figure 6.9, can be neglected during the calculation of the dose with an error < 3% for energies < 30 keV and a constant difference of ~1% for the other energies in the considered range. The presence of a skin layer instead plays a more important role for energies < 20 keV (~25% for 15 keV), while for higher energies, > 50 keV, the contribution becomes smaller (< 2%) and can be neglected. For low energies, photons deposit most of their energy in the external layers of the sample which are not considered in the calculation while, at high energies, the profile of dose is flat (figure 6.2) and for this reason the influence on the AvD of the skin layer is smaller.

6.2.3.7 Calculation of the deposited dose

The deposited dose for a generic case can be easily calculated by taking as starting point the reference values reported in the Appendix (*i.e.* tables A2-A5). One can consider the “nearest” tabulated case in terms of breast tissue thickness, composition and photon energy, and then apply the previously calculated correction factors (C_F , R_F , and W_F , see sections 6.2.3.4, 6.2.3.5 and 6.2.3.6). The resulting formula is:

$$D_c = D_{ref} C_F R_F W_F Ph \quad (6.2)$$

where Ph represents the number of photons used during the experimental irradiation or of the wanted (to be calculated) case. In order to calculate the correct value of Ph it is necessary to consider the height of the irradiated sample and the height used to model the simulated phantom. This results in multiplying the obtained number of photons for the ratio between the simulated height (5 cm) and the experimental irradiated height. For an estimation of the MGD an additional factor G_f has to be considered. This factor can be defined as following, for $f_g \neq 0$:

$$G_f = \frac{\left(\frac{\mu_{en}}{\rho}\right)_g}{f_g \cdot \left(\frac{\mu_{en}}{\rho}\right)_g + f_a \cdot \left(\frac{\mu_{en}}{\rho}\right)_a} \quad (6.3)$$

where f_g is the fraction of glandular tissue and f_a the fraction of the adipose tissue, respectively, in the case to be calculated. The MGD can be estimated as $MGD = D_c G_f$. Several values of G_f for different energies and compositions are reported in table A6 in the Appendix.

6.2.3.8 Comparison between simulations of test cases and approximated values

The results of the dose simulations for four test cases (table 6.2) have been compared to the results obtained by using the tabulated values D_{ref} (Appendix, tables A2-A5) and the calculated correction factors of table 6.6. D_{calc} is the dose so calculated using eq. 6.2, while D_{sim} is the dose value obtained from the direct simulation of the considered test geometries.

Geometry	D _{ref} (Gy/ph)	C _F	D _F	W _F	Ph	D _{calc} (Gy)	D _{sim} (Gy)	Difference %
G1	1.30E-14	0.99	1.89	0.98	5.00E+08	1.19E-05	1.29E-05	8
G2	8.72E-15	0.97	1	0.97	5.00E+08	4.10E-06	4.03E-06	1.7
G3	4.92E-15	1.02	1.17	0.99	5.00E+08	2.91E-06	2.90E-06	0.3
G4	2.65E-15	1.02	0.89	0.99	5.00E+08	1.19E-06	1.19E-06	~0

Table 6.6: Comparison of the results obtained by using eq. 6.2 and the results obtained with direct simulations, see section 6.2.2.7. The correction factors are calculated using the interpolation curves and the values from figure 6.2.

The difference between the direct simulation and the estimated value is $< 2\%$ for the cases 2-3-4. The first case presents a larger difference, $\sim 8\%$, because the approximation used for correcting for the different diameter does not describe in a sufficiently precise way the behaviour of the dose deposition in diameters smaller than 60 mm (which is anyway a rather small, and therefore not realistic, diameter for a female human breast). In order to better describe the breast thickness effect for such small samples a higher order of the polynomial interpolation should be considered. The correction factor for low diameters (< 60 mm) derived by using the exponential function with a quadratic exponent leads to an underestimation of the deposited dose. The level of accuracy of the results for the cases 2-3-4, which represent more realistic anatomical conditions, demonstrate that the approximated method I derive in this work (*i.e.* equation 6.2) correctly predicts the deposited dose.

6.3 Optimization of the radiation dose by adapting the exposure time to sample geometry

This part of the simulation work is dedicated to the optimization of the radiation dose (and examination time) by using a modulated X-ray flux for imaging the breast tissues when the rotation axis lies in the plane of the beam. This modulation is obtained by varying the detector exposure time depending on the geometry of the sample.

In clinics, a similar method, applied to conventional X-ray tube sources, and based on the modulation of the intensity of the current of the X-ray tube, is already applied to significantly reduce the dose delivered to the patient (McCollough et al. 2006). Here, a parallel monochromatic beam has been considered (as the typical synchrotron beam) but the method can be applied to any X-ray spectrum. Simulations have been performed using the software GATE v6.2 (Jan et al. 2011). The comparison of the results obtained with and without the proposed optimization of the exposure time is presented. The modulation of the detector exposure time is equivalent to consider a different amount of photons depending on the thickness (and composition if necessary) of the sample at different stages of its illumination, as shown in figure 6.10.

6.3.1 Instruments and methods:

The simulation software GATE v6.2 has been used together with the TLE method in the same way as described in section 6.2.

The two samples modelled for these simulations are obtained from experimental data acquired at the ESRF. I performed the segmentation of the acquired images (previously reconstructed using the RGVF approach as described in Chapter 3) using a threshold method following a priori medical knowledge of the sample composition to assign the materials to the different regions. Four different materials composing the samples and their environment have been considered: adipose tissue, glandular tissue, 4% formalin solution in water and skin. The two modelled samples have two different diameters: 84 mm and 45 mm. In both cases the sample height has been considered to be of 10 mm. The voxel size is $0.184 \times 0.184 \times 10 \text{ mm}^3$ for the 84 mm sample, and $0.092 \times 0.092 \times 10 \text{ mm}^3$ for the 45 mm one. The simulated X-ray beam has been defined as a rectangular function of area $1 \times 10 \text{ mm}^2$ (*i.e.* laminar beam). For the 84 mm breast X-ray energies of 60 keV and 100 keV have been used, while for the 45 mm 30 keV and 60 keV, for a total of four study cases (table 6.7).

Simulated case	Diameter (mm)	Energy (keV)
Case 1	84	60
Case 2	84	100
Case 3	45	30
Case 4	45	60

Table 6.7: summary of the cases considered in this study.

The sample performs a rotation around a central axis perpendicular to the beam direction according to figure 6.10. During the acquisition, the laminar beam impinges at each step on a different region of the sample (of 1 mm of height in this particular case); several vertical displacements are needed to image the entire sample. In the simulations presented, each step considers a priori knowledge of the sample thickness that is used to optimize the exposure time of the detection system. The optimization is done considering the average absorption of the irradiated region. To calculate the mean absorption I used the values of the absorption coefficient for breast tissue provided by the NIST (NIST). For each simulation 5×10^7 primary photons have been used, in order to keep the statistical uncertainty per voxel always $< 1\%$, and 200 angular projections have been acquired over 360° . To obtain the final distribution of the dose $D_{Tot}(x,y)$ the results of all simulations weighted on the absorption curve have been successively summed up using $D_{Tot}(x,y) = \sum_i^{BS} (D_i(x,y) \cdot A_{w,i})$, where BS indicates the total number of steps, $D_i(x,y)$ is the dose distribution at the i -th step and $A_{w,i}$ is the sample absorption for the i -th step. This value has been then compared with the corresponding image obtained without modulation of the exposure time. This optimization is equivalent at

each step of the irradiation to weighting the exposure time for the sample absorption. The simulations without an optimized X-ray exposure time have been performed with the same parameters used in the optimized cases (and described at the beginning of this section) with the exception of the beam geometry. In the first case an X-ray beam area of $84 \times 10 \text{ mm}^2$ has been considered while in the second modelled sample a $45 \times 10 \text{ mm}^2$ beam area has been used.

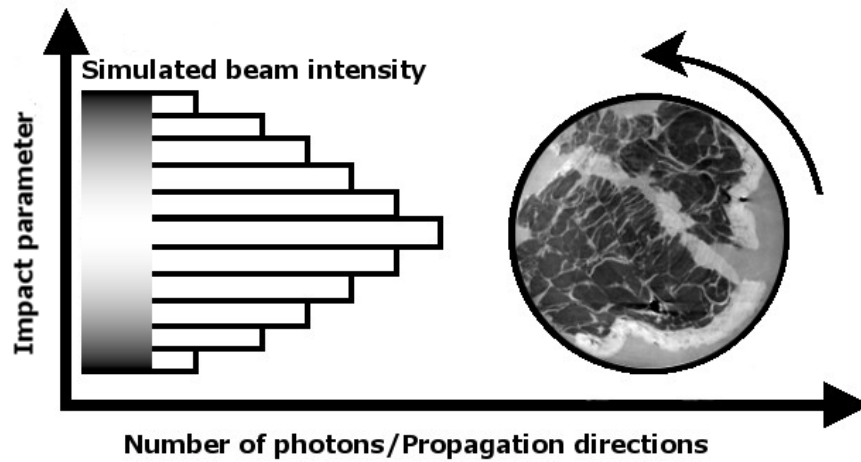


Figure 6.10: Geometry of the X-ray beam used for the optimization of the sample irradiation in CT. The histogram of intensity represents the modelled beam that is used for the dose simulations presented in the next sections.

6.3.2 Results and discussion

6.3.2.1 Dose and time reduction

In figure 6.10 are shown the results of the simulations using the beam modelled as in figure 6.10 and obtained by modulation of the exposure time are compared with the results produced by using a flat beam profile (*i.e.* constant exposure time).

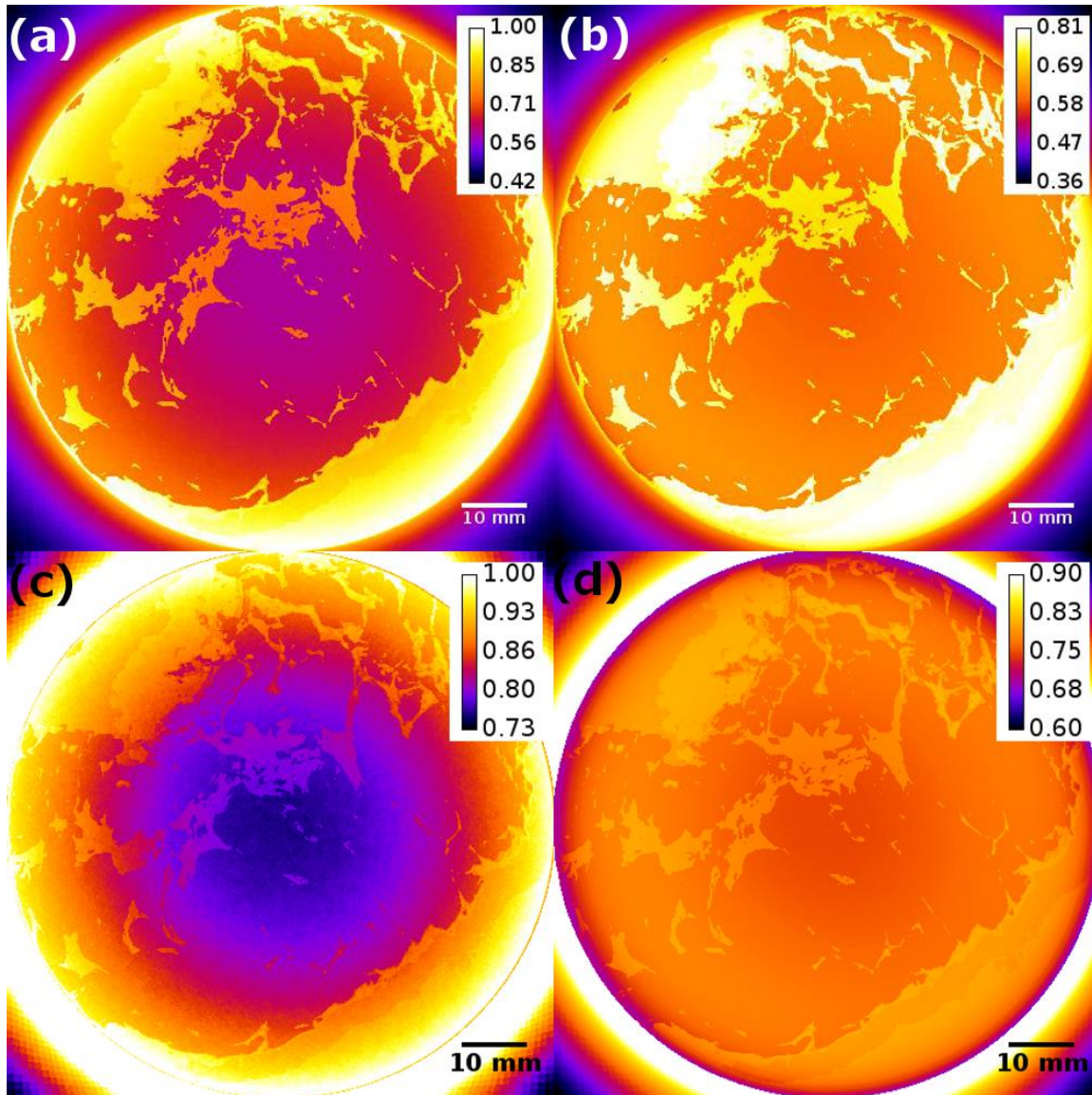


Figure 6.11: Normalized dose distributions for the modelled breast samples of 84 mm of diameter. (a) without an intensity modulated 60 keV X-ray beam (*i.e.* flat beam profile), (b) with an intensity-modulated 60 keV X-ray beam, (c) without an intensity-modulated 100 keV X-ray beam, (d) with an intensity-modulated 100 keV X-ray beam.

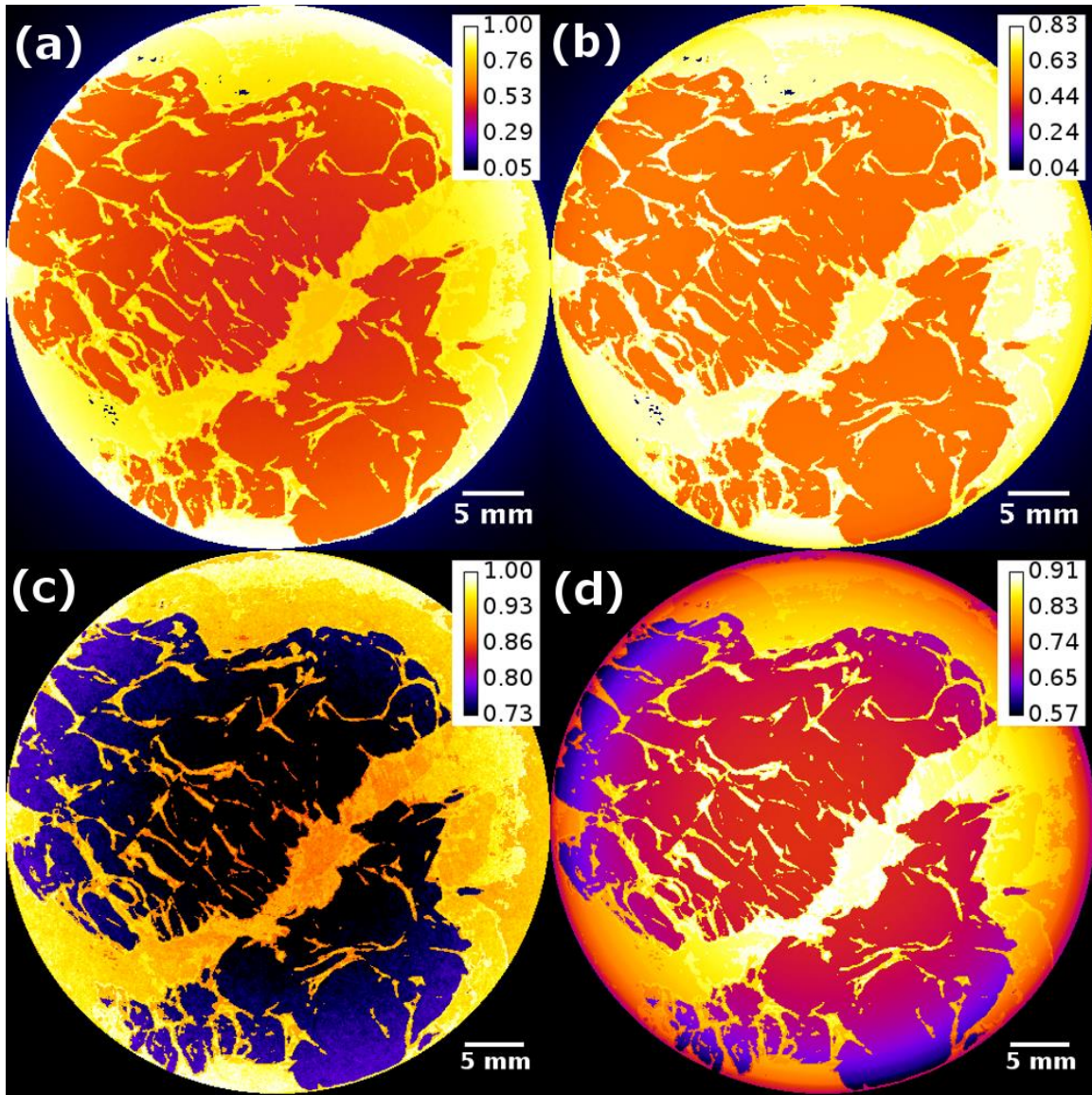


Figure 6.12: Normalized dose distributions for the modelled breast samples of 45 mm of diameter (a) with non-modulated 30 keV beam, (b) with modulated 30 keV beam, (c) with non-modulated 60 keV beam, (d) with modulated 60 keV beam.

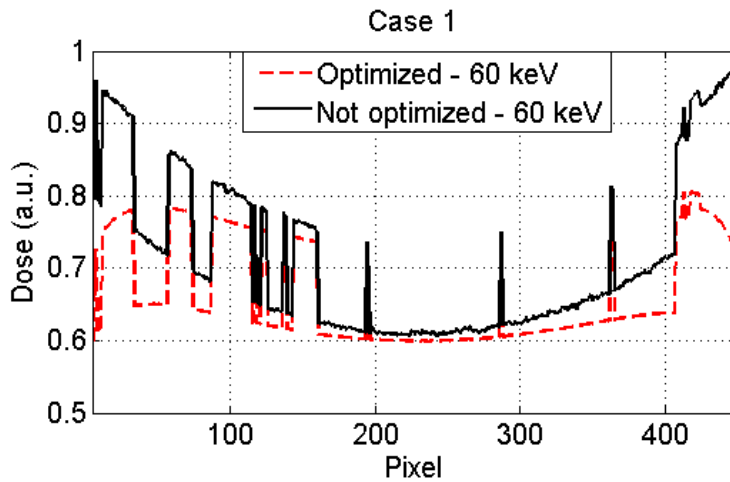


Figure 6.13a: Profiles along the central horizontal lines of figure 6.11a, b for the 84 mm diameter breast and a 60 keV X-ray beam. The averaged dose reduction in the whole sample is ~11%.

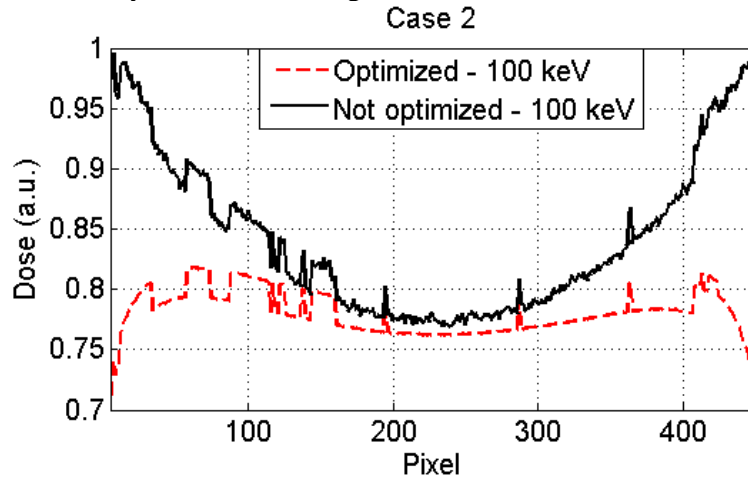


Figure 6.13b: profiles along the central horizontal lines of figure 6.11c, d for the 84 mm breast and a 100 keV X-ray beam. The averaged dose reduction in the whole sample is ~16%.

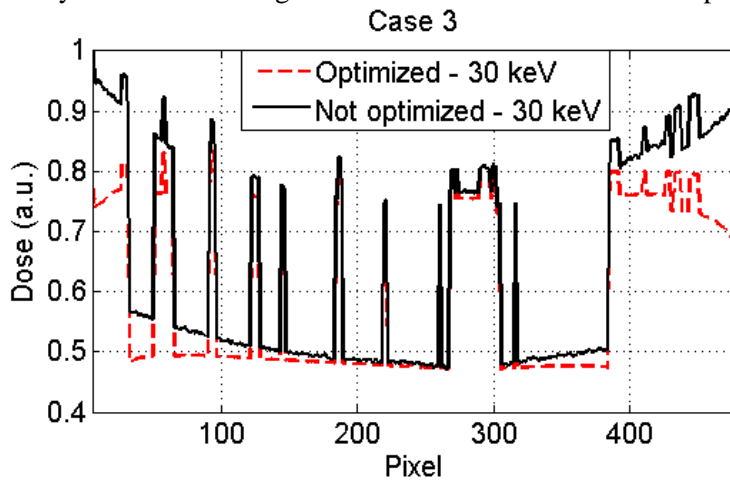


Figure 6.13c: profiles along the central horizontal lines of figure 6.12c, d for the 45 mm breast and a 30 keV X-ray beam. The averaged dose reduction in the whole sample is ~11%.

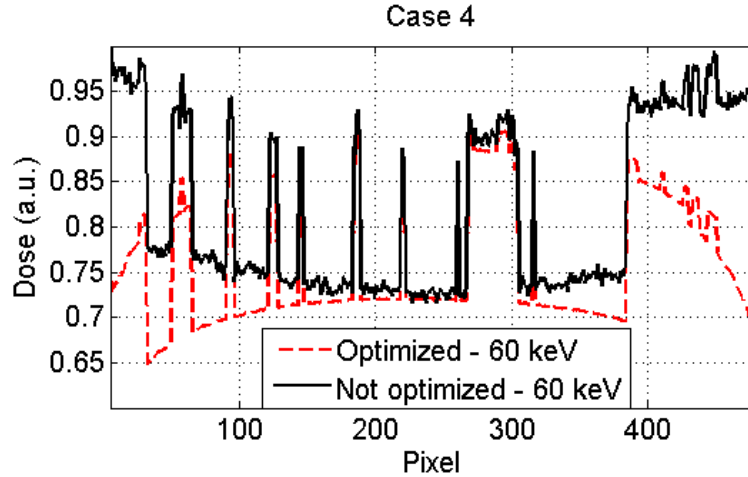


Figure 6.13d: profiles along the central horizontal lines of figure 6.12c, d for the 45 mm breast and a 60 keV X-ray beam. The averaged dose reduction in the whole sample is ~17%.

These results show how the modulation of the X-ray beam profile (*i.e.* exposure time) allows reducing the overall dose deposited in the volume. For a modulated X-ray beam (figures 6.11a, 6.11d, 6.12a, 6.12d) we have a flat distribution of the dose in the imaged volume in contrary to the case of a non-modulated beam. The gain is obtained owing to a reduced dose delivered. The exposure is usually chosen in order to have a sufficient transmission from the largest portions of the sample, therefore the exposure results excessive for the thinner parts of the object. Calculating the average dose deposited in figures 6.11a, b, c, d we obtain an overall dose reduction of ~11% for the cases 1, 3 and ~16-17% for cases 2, 4 with a maximum of ~25% of reduction in dose in the external layers. The reduction can be calculated in a first approximation by using the ratio of the total number of photons for the case of a non-modulated X-ray beam and the number of photons for the modulated beam. The reductions obtained with the simulations are smaller than the analytically calculated values due to the effect of the scattering in the external layers. By optimizing the irradiation time the total acquisition time is also reduced.

6.3.2.2 Image quality

The influence of the proposed optimization procedure has been also studied in terms of the resulting image quality by means of simulations; calculations have also been completed by experimental results. The simulations have been performed using the complex breast modelled sample with a voxel size in these cases of $50 \times 50 \times 1000 \mu\text{m}^3$ described in Chapter 3. I performed simulations of the geometries in both the analyser-based imaging (ABI), figure 6.14, and the propagation-based imaging (PBI) techniques, figure 6.16. The simulations parameters used for the ABI case are the same as described in Chapter 3. For the PBI simulations the propagation of waves is considered by calculating the Fresnel integral with a propagation

distance of 10 m. The number of photons used for both the ABI and the PBI simulations is 10^4 per pixel. All the remaining simulations parameters (beam, input models, and detector) are the same as used in the ABI simulations described in Chapter 3. The experimental results (figure 6.15) concern two different excised breast samples in formalin solution (~ 10 cm and ~ 6 cm of diameter, respectively) imaged using the ABI technique at ID17 (ESRF). In one case the exposure time was modulated as described above while in the second case a flat X-ray flux profile has been used. Both the images acquired using the ABI have been acquired using the in-plane geometry (Chapter 2). Two sets of images have been acquired for each breast sample at a position $\pm\theta$ with respect to the Bragg angle of the analyser RC. In this case the chosen θ was at the 50% of the maximum of the curve. The EDEI algorithm, described in Chapter 3 (Maksimenko 2007), has been used to extract the refraction angle signal. The reconstructions have been performed using the RGVF approach for the ABI data and with the filtered backprojection with the ramp filter in the case of PBI simulations. The results of the optimized and not-optimized methods have been compared, for both the experimental and simulated images, by calculating the Figure Of Merit (FOM) in a defined region of the reconstructed images. The FOM is defined as $FOM = SNR/\sqrt{D}$, where D is the delivered dose to obtain the considered image. In this case I used, instead of the delivered dose, the number of photons employed during the acquisitions of the projections. The Signal to Noise Ratio (SNR) is calculated by using $SNR = \rho/\sigma$, where ρ is the average density value calculated in the considered region and σ its standard deviation. In figure 6.14 (ABI simulations) the image obtained with the modulation of the exposure time presents a FOM=2.62 while in the image without modulation a FOM=2.86 is instead obtained. In figure 6.15 the experimental results obtained by applying the ABI-CT technique are presented. In figures 6.15a, b the results of a ~ 6 cm a ~ 10 cm in diameter breasts, respectively, are shown. The images reconstructed using the optimized and not optimized exposure time present a difference between the FOMs smaller than 2%. In the case of the PBI simulations, figure 6.16, the FOMs calculated in the two different regions present similar values. The results obtained demonstrate how the image quality in the studied cases is preserved while there is a gain in term of average dose delivered.

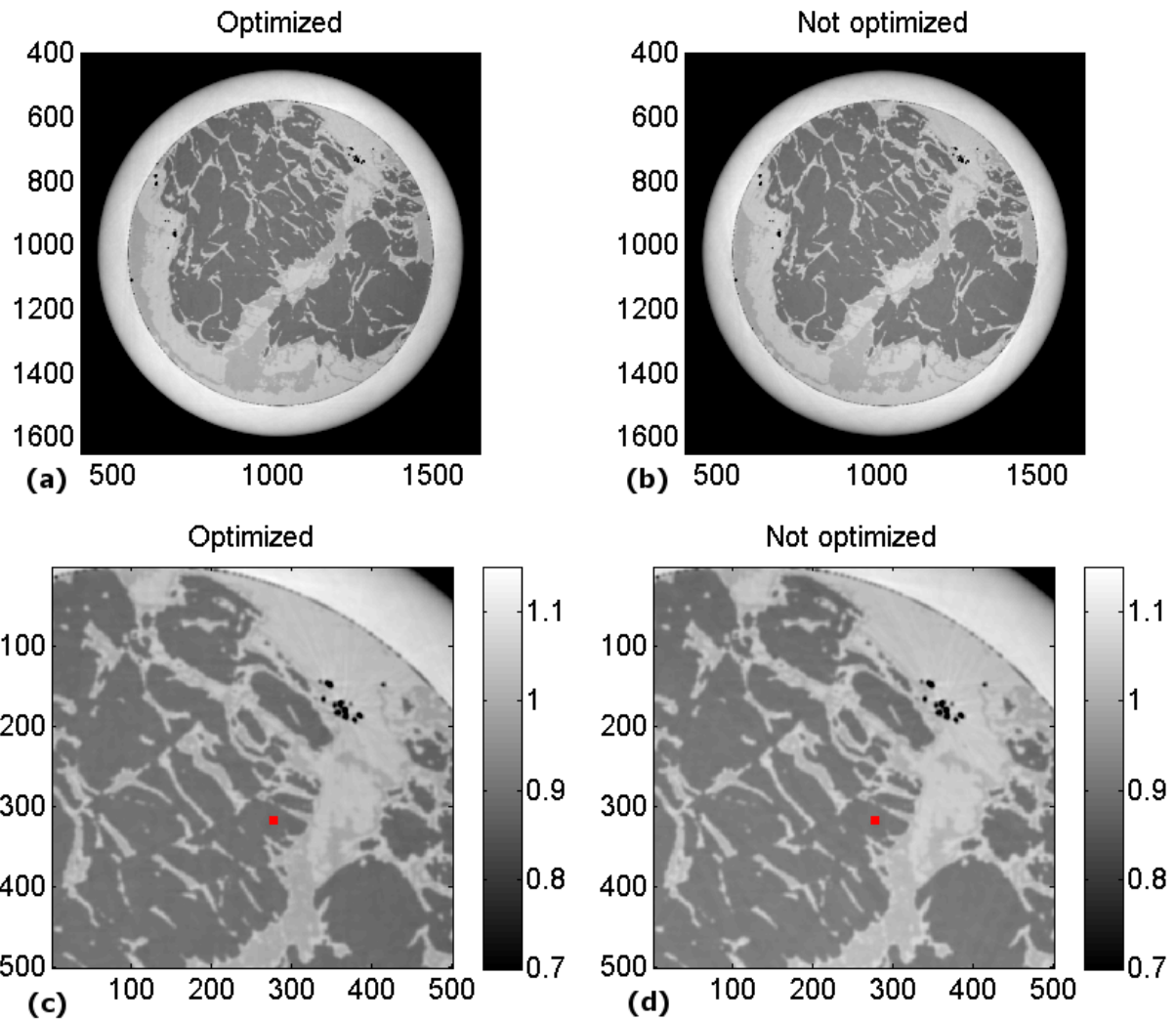


Figure 6.14: Results of the simulations of an ABI experiment. The refraction angle image has been obtained using the EDEI algorithm; the reconstruction of the distribution of δ (converted in density, according to the procedure described in Chapter 3) is obtained using the RGVF approach. (a) CT image simulated by using a modulated X-ray beam intensity profile, (b) CT image obtained without the optimization. (c) and (d): zoomed views within a CT slice reconstructed of images (a) and (b). The Image with the modulate exposure time presents a FOM=3.0, while the one without modulation has a FOM=2.1. Each region used for the FOMs calculation consists in 20x20 pixels.

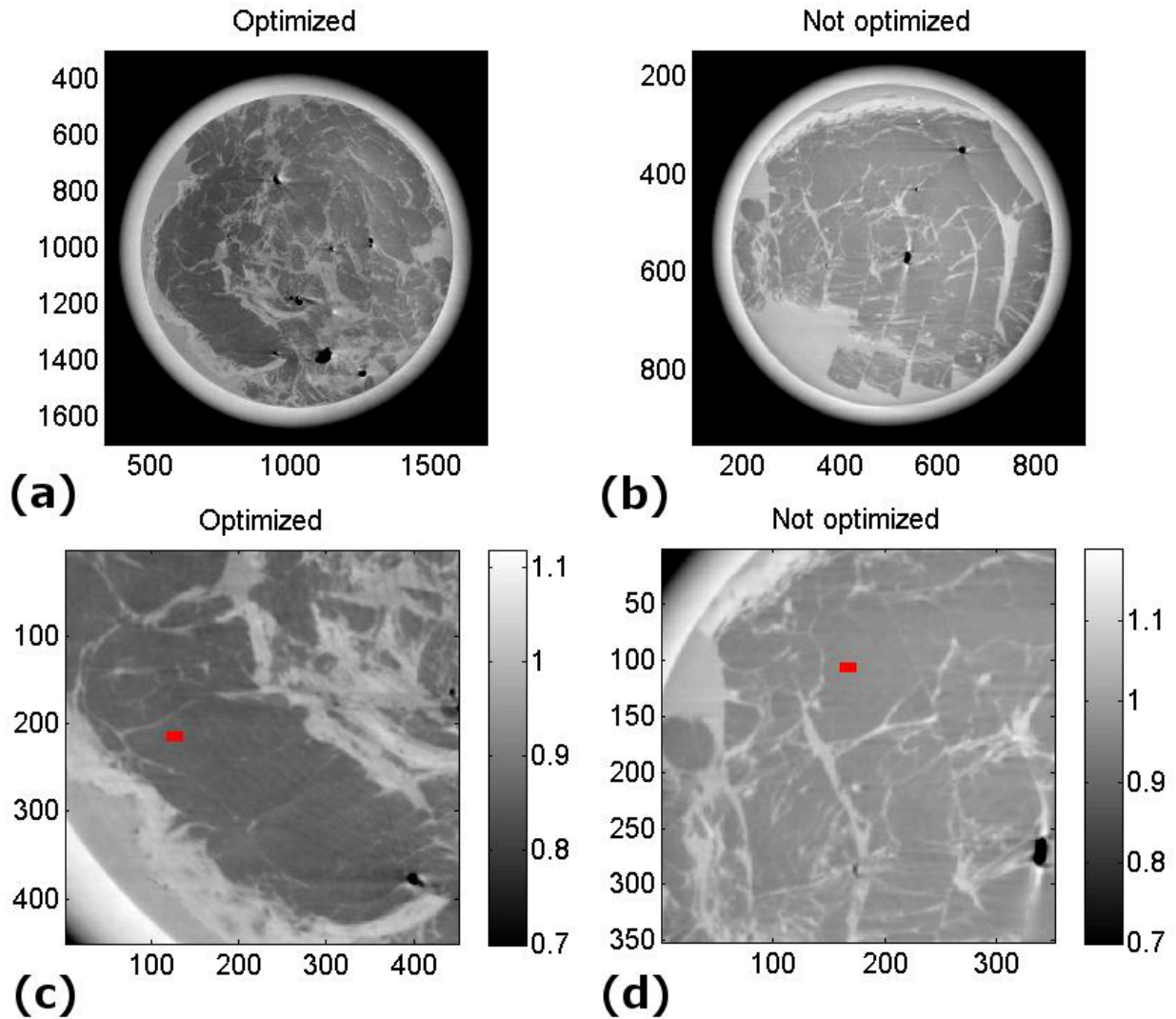


Figure 6.15: CT reconstruction of experimental data of two different breast samples acquired at ID17 (ESRF). Image (a) has been obtained with and (b) without the exposure modulation. (c), (d): zoomed views within a CT slice reconstructed of image (a) and (b). Image (a) presents a FOM=5.27, while in image (b) the FOM=5.18. The FOMs have been calculated considering the region marked by the red parallelepipeds in figures (c) and (d). Each region consists of 10x5 pixels. The reconstructed quantity is the δ , converted to densities, (grey colour bar). No post-processing has been applied to the images.

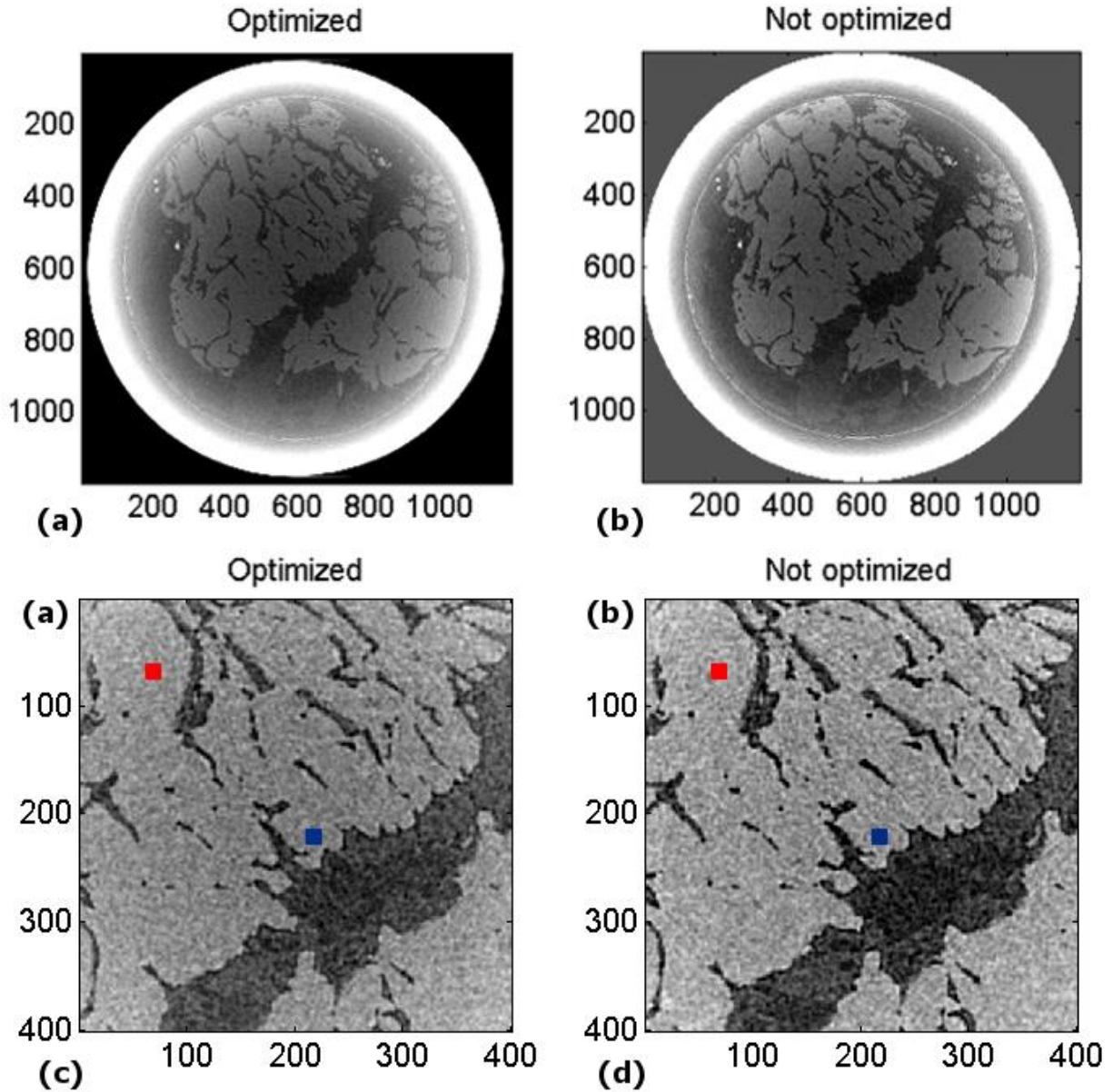


Figure 6.16: Results of the simulation of a PBI experiment with a propagation distance of 10 m and a pixel size of $50 \times 50 \mu\text{m}^2$. Simulated reconstructed image (a) with and (b) without modulation of the X-ray intensity profile. (c), (d): Zoomed views of within a CT slice reconstructed of image (a) and (d) of image (b). The FOMS have been calculated in the regions marked by the red and blue squares (c), (d). The obtained values are, for image (c), $\text{FOM}_{\text{blue}}=0.10$, $\text{FOM}_{\text{red}}=0.15$; for image (d) $\text{FOM}_{\text{blue}}=0.11$, $\text{FOM}_{\text{red}}=0.14$. Each region used for the FOM calculation consists in 10×10 pixels.

6.4 Conclusions

6.4.1 Dose database study

In this chapter a **database of dose curves versus the photon energy for a monochromatic X-ray CT imaging configuration for breast CT is provided**. Studied parameters include **a range of energies of 15-100 keV a breast diameter ranging between 60 and 150 mm and different breast compositions**. The obtained database is reported in the Appendix. **The analytical way proposed (eq. 6.1) shows a good agreement (2 keV of maximum difference) with simulations to estimate the optimal photon energy to minimize the ratio dose/transmittance**. These small discrepancies are attributable to the approximation introduced to describe the sample geometry for the analytic calculation. The results of the influence of the breast composition, of the total breast thickness and of the presence of an additional external wall layer (skin or PMMA) are also presented.

It is possible to notice that for energies higher than ~ 70 keV the dose/transmittance ratio starts to slowly increase because the contribution due to the gain in transmittance becomes less important with respect to the increase in dose deposition resulting from the rise of the total photon cross section. The value of the energy which minimizes the dose/transmittance ratio has been also studied considering four realistic detection system based on a Gadox, CsTe, Se and CsI screens, respectively. **Results show that the best energies for the CdTe system (for the considered geometries) fall in the energy range of 50-60 keV, 50-55 keV for the a-Selenium, around 55-60 keV for the CsI. For the Gadox-based detector the best energies are immediately above the gadolinium K-edge (~ 51 keV).**

Several correction factors were calculated using interpolations of the simulated values for the different (in terms of breast composition, thickness and of the presence of an external layer) studied cases. These factors can be used to estimate the AvD, using the values presented in the database, for geometries and cases which are not included among those reported here.

At high photon energies (≥ 90 keV) the influence of the breast composition plays a negligible role ($<2\%$) on the AvD, while it becomes more important at lower energies (*i.e.* differences up to 8% for 60 keV and up to 10% for 30 keV). If the MGD is considered, the composition represents a crucial factor because the final contribution has to be weighted by the factor Gf (eq. 6.3), reported in table A6 of the Appendix.

The effect of the presence of an external wall composed of light elements (PMMA) can be neglected with an error of few percentages for energies > 25 keV. At low energies (~ 15 keV) the effect of the skin plays an important role (with errors up to $>25\%$), but it can be neglected for energies > 50 keV.

The results of the comparison between the simulated test cases and the approximated calculation using the presented reference database and the correction factors (*i.e.* eq. 6.3) show a good agreement for the cases

of sample geometries with a diameter > 60 mm. In the case of lower breast thicknesses the error on the estimated doses increases, as discussed above.

The current work is useful for CT imaging studies using monochromatic parallel synchrotron radiation beams since it allows to easily assessing the average delivered dose with a good accuracy in pre-clinical breast imaging research. This work provides a simple and fast way to optimize the value of the X-ray energy for given experimental parameters and breast sample characteristics. I demonstrated that this method works in a large variety of experimental cases in terms of breast thickness, composition and photons energies. The results of this study are also been published (Mittone et al. 2014).

6.4.2 Optimization of the detector integration time

In this simulation study I demonstrated how it is possible **to reduce the dose deposited into the sample by ~11-17% with a simple modulation of the exposure time of the detection system** (corresponding to a modulation of the X-ray beam flux profile). The gain in deposited dose is related to the geometrical properties and composition of the considered sample and also to the radiation energy. The overall reduction of the average dose deposited is due to a reduction of the energy deposited in the external layers of the sample. The resulting profile along the breast thickness is flat, in contrary to the non-modulated beam case where the dose is higher in the layers close to the surface. **The optimization of the exposure time proved, in the considered cases, that the image quality, studied in term of FOM, is preserved using both the ABI and PBI technique.** In conclusion the modulation of the exposure time allows an overall reduction of the dose deposited in the irradiated samples without loss in terms of image quality. I believe that the application of the proposed method can be interesting especially for applications where the deposited dose plays a crucial role.

Conclusions

In this chapter a summary of the work and results obtained within this Thesis work is reported following the structure of the manuscript. The theoretical and experimental work performed within this Thesis was dedicated to the development and application of advanced quantitative CT methods for reconstructing the distribution of the index of refraction in biological samples by using X-ray phase-contrast imaging and in particular the analyser-based technique. While results reported in the literature before this Thesis were limited to small objects, the objective of the work I have performed was to extend the potential of the index of refraction CT to the case of complex and large medical specimens (*i.e.* full organs) in this work

For this purpose several simulations studies and experiments have been carried out. All these studies have aimed at optimizing the experimental setup, acquisition procedure and the image reconstruction algorithms by taking also into account different sources of image artefacts. An important part of the work was dedicated to compare two different CT acquisition configurations for the analyser-based imaging technique by identifying their limits and advantages. This was done with simulations and experiments, as well. To improve the quality of the CT reconstructed images a deconvolution procedure has been also studied.

The other important focus of my work has concerned the problem of the estimation and optimization of the radiation dose in CT. For an accurate knowledge of the deposited dose normally Monte Carlo (MC) simulations are employed, but they are very expensive in terms of computational resources and time. One of the objectives was to create a tool allowing performing fast and accurate simulations of the dose deposited during the CT imaging sessions. To this end the Track Length Estimator (TLE) method has been implemented in the open-source software GATE and the results have been benchmarked versus the conventional MC method and experimental measurements. In addition, a new dose database for breast CT with a monochromatic radiation and a study for optimizing the X-ray energy in order to minimize the dose deposited in the sample and maximize the signal on the detector have been produced.

7.1 Optimization of the ABI CT imaging setup for quantitative analysis

7.1.1 Simulation studies: analysis of experimental errors and comparison of different CT geometries

In the framework of my Thesis, a series of simulations have been performed by using a code developed within our group to optimize the experimental setup and parameters for ABI CT imaging.

In order to study the effect on images of different experimental sources of noise, artefacts or errors I have implemented in the code a series of functions for simulating those cases.

It has been proved how the influence of interfaces between materials showing very different optical properties (for example the interface between air and the sample) may quantitatively affect the CT reconstructions of the index of refraction (differences up to 50% in the calculated density maps) and reduce the visibility in terms of image contrast. Several simulations have been also performed to compare the results produced with two different CT acquisition geometries (in-plane and out-of-plane configurations) for ABI. A qualitative comparison has been performed by reconstructing the refraction angle distributions using, first, the EDEI algorithm to separate the refraction and the absorption components of the signal and, successively, the FBP algorithm to reconstruct the refraction angle images. The quantitative comparison of the two CT configuration has been done by retrieving δ , the real part of the index of refraction. The distributions of δ have been then converted in material/tissue density maps. Using the in-plane geometry more accurate results are obtained in the quantitative reconstructions, while a better qualitative depiction of the internal structures is obtained using the out-of-plane geometry, when the reconstructions of the refraction angle are compared. In general the in-plane geometry provides higher contrast due to its sensitivity along two directions (*i.e.* the two axes in the axial view) while the out-of-plane geometry is sensitive only along one direction (the direction of the sensitivity of the diffraction plane of the crystal analyser, *i.e.* the vertical axis in the sagittal views shown in the Thesis for this CT geometry). This leads to better results in terms of depiction of the internal features in the investigated samples in the case of axial views when using the in-plane geometry and in the sagittal views when using the out-of-plane geometry.

For the extraction of quantitative information, and therefore the reconstruction of physical quantities such as the index of refraction or the material density, **the main limitation of the out-of-plane geometry is related to the definition of the boundary conditions necessary for the phase-retrieval.** It is often difficult to have the proper experimental configuration that allows a proper definition of the boundaries. **Another advantage of using the in-plane configuration is related to the possibility of reconstructing**

the distribution of the δ (and then of the density) using several alternative different approaches (for instance, the Gradient Filtered Backprojection for gradient projections, the Refractive Gradient Vector Field and the phase-retrieval performed on the refraction angle projections as described in Chapter 3). On the contrary, for the out-of-plane configuration the only procedure to be used is the one based on a phase-retrieval algorithm. It is possible to find a comparison of the results using the three different approaches in case of the in-plane geometry for the reconstruction of the distribution of δ in our work Gasilov et al. 2014. **For a qualitative investigation of the samples both CT acquisition geometries produce good results and can be used.** In this case the geometry must be chosen according to the direction in which the structures of interest are oriented in the sample. For quantitative reconstruction the use of the in-plane geometry is strongly suggested.

All the results of the simulations performed considering models of biological tissues are obtained at clinical compatible doses (*i.e.* few mGy).

7.1.2 Experimental comparison of the two CT acquisition geometries for the analyser-based imaging

The results of the experimental comparison of the two CT acquisition geometries are presented in Chapter 4 of this Thesis work. The results of the reconstruction of the index of refraction in a large breast sample (11 cm of diameter) using the in-plane geometry are also compared with the corresponding absorption CT image. These results have been reported in Gasilov et al. 2013 and another manuscript is in preparation. The obtained results show that it is possible to reconstruct the distribution of the index of refraction (or density) for large and complex sample, while previous results reported in the literature were limited to small objects.

By comparing the results of the reconstruction obtained by using the in-plane geometry with the absorption CT images of the same sample, it has been demonstrated that the values of density (derived from the distribution of δ values) are more accurate in terms of both SNR and average value, if compared to the corresponding tabulated values. The use of the in-plane geometry leads to a better depiction of the different tissues because of a reduced overall noise in the reconstructed image. Moreover the CT images of δ have been obtained using a dose ~ 3 times smaller compared to the one delivered in the case of absorption CT. However, despite the dose remains high respect to the values used in clinical examinations, some solutions exist to reduce it. For instance detectors with higher efficiency (which is now very low) can be used and the number of projections used in the reconstruction can be further reduced (special iterative CT algorithms have been implemented in our team but were not used in this Thesis).

Moreover, considering the high SNR of the images we produced, an additional reduction of the dose can be obtained by reducing the exposure time (*i.e.* reduction of statistics)

The experimental comparison of the two acquisition geometries confirms the results of the simulation study: the in-plane geometry offers much more accurate quantitative results with respect to the out-of-plane geometry. However, as previously mentioned, the choice of the geometry to be used has to be made depending on the characteristics of the sample to be inspected.

7.1.3 Deconvolution procedure

In the last part of the Chapter 4 I have investigated how to improve the quality of the reconstructed images by deconvolving experimental data with the spatial resolution (*i.e.* the point-spread function) of the imaging detection system. I have implemented a deconvolution procedure whose application to experimental CT data determined **an improved image sharpness and the preservation of the SNR.** However, the procedure requires a preliminary denoising step. In this work, the wavelet decomposition has been used in order to avoid the amplification of the noise and a consequent decrease of the SNR during the deconvolution procedure. The deconvolution has been applied to different stages of the CT image reconstruction process and the results have been compared. The best results are obtained by applying the deconvolution to the refraction angle projections. In the studied case, it has also been shown how the use of a slightly incorrect PSF does not produce any significant qualitative or quantitative image degradation.

7.2 Simulations of the dose deposition

7.2.1 Implementation and validation of the Track length estimator

In this Thesis work the TLE method has been implemented in collaboration with the INSA institute of Lyon in the open-source platform GATE. **The implementation of this method has been benchmarked against analogous MC dose calculations. No significant difference has been found between the results obtained with the two methods in terms of total deposited energy.** In addition, the spatial distributions of the deposited energy were also found to be in agreement within statistical fluctuations. However, the TLE method provides the substantial advantage of exhibiting a strong variance reduction in comparison to equivalent MC simulations, with no significant loss of accuracy. **In an anatomically complex case (as shown in Chapter 5) we found that MC computations required about 500 times more events to reach the same averaged statistical uncertainty per voxel as the TLE method, using the same parameters.**

The TLE dose calculations were also validated experimentally in the case of a CT dosimetry experiment with a cylindrical phantom irradiated with 60 keV monochromatic synchrotron X-rays. **Differences between experiment and simulation lower than 2.3 % has been found.**

The applicability of the TLE method is however currently limited to an energy range between 1 keV and 1 MeV because of the limited range of the pre-calculated mass-energy absorption coefficients in the database created within this work and the need of keep the validity of the introduced approximations. Nevertheless this energy range is already wider than the one needed for biomedical imaging applications. The (highest) energy limit for applying the TLE approach is fixed by the assumption that the electron transport can be neglected (local energy deposit), with no significant energy escape in form of secondary radiation, *i.e.* the energy-transfer and energy-absorption coefficients are assumed to coincide, this limitation becoming more stringent in the case of high-Z elements.

In summary, the TLE method, integrated in the GATE platform, has been proved to be a powerful tool allowing simulation of dose distributions in very complex geometries, like organ volumes imaged by high-resolution CT scans (with the identification of the atomic composition of the tissue assigned to each voxel) in several hours, depending on the used parameters, whereas analogous MC simulations requiring equivalent amounts of processing time suffer from much slower statistical convergence. Potential applications of this new tool range from CT imaging to nuclear medicine as well as low-energy X-ray external radiotherapy. The results of this work are published in Mittone et al., 2013.

7.2.2 Creation of a dose database for CT mammography using monochromatic radiation

This study aimed at providing a fast way to estimate the dose deposited in breast CT with monochromatic X-rays. For this purpose **a database of dose curves versus the photon energy for a range of energies of 15-100 keV has been created for breast samples with a diameter ranging between 60 and 150 mm and characterized by different tissue compositions** (the tables with the results are reported in the Appendix). The database is obtained from MC simulations combined with the TLE method to accelerate the convergence. **An analytical formula is proposed in this work to estimate the optimal photon energy to minimize the ratio dose/transmittance.** Results obtained with this formula show a **good agreement (2 keV of maximum difference) with the dose values computed with MC simulations.** Some discrepancies are attributable to the approximation introduced to describe the sample geometry for the analytic calculation.

It has been demonstrated how for energies higher than ~ 70 keV the dose/transmittance ratio starts to slowly increase. Four realistic **detection systems based on Gadox, CsTe, Se and CsI screens**, respectively, have

been considered. Results show that **the best energies, considering certain/common sample geometries, fall in the energy range of 50-60 keV for all the four studied cases.** In order to extend the applicability of these results, several correction factors were calculated to adapt the values presented in the database depending on the composition and thickness of the breast and of the presence of an external wall layer (PMMA/skin) for cases different from those included in our tables.

The influence of the breast composition plays a negligible role at high energies (>90 keV) while for low energies it has to be taken into account. Also the presence of an external wall composed of light elements (PMMA) can be neglected with an error of few percentages for energies > 25 keV.

It is possible to calculate the Mean Glandular Dose from the values provided in the database by weighting the reported values by a factor accounting the different radiosensitivity of the different tissues composing the breast. The values of this correction factor are reported in the Appendix.

In order to evaluate the accuracy of the results of the database I have created, simulations considering four test cases have been carried out. The results have then been compared with the ones obtained by using the database. Good agreements for breast geometries with a diameter > 60 mm have been found. In case of smaller diameters the error on the estimated doses increase, as discussed in Chapter 4.

In conclusion the results presented in this part of the work may be useful in case of CT imaging studies using monochromatic parallel radiation X-ray beams. **The database presented allows easily assessing the average delivered dose with a good accuracy in pre-clinical breast imaging research.** Thanks to the introduction of the correction factors a large variety of experimental cases can be studied using the presented method. The results of this study have been published in Mittone et al. 2014.

7.2.3 Optimization of the radiation dose by adapting the exposure time to the sample geometry

In the second section of Chapter 6, it has been demonstrated, using a MC simulation study, the possibility of reducing the average dose deposited in a CT imaged volume by suitably spatially modulating the flux of the laminar X-ray beam depending on the shape and composition of the sample. **A reduction of about ~11/17% in terms of deposited dose has been obtained for the case of breast CT by simply adapting the exposure time of the detection system for the thickness of the imaged part of the specimen,** and also, by selecting the optimal X-ray energy (this advantage is due to the use of tunable and monochromatic radiation). The dose reduction reaches ~30% in the external layers of the sample and this is what mainly determined the overall decrease of the average dose. The resulting profile of the distribution of the dose in the sample along the breast thickness is flat, in contrary to the case in which a non-modulated beam is used. In the latter case, the deposited dose is higher in the external parts of the imaged volume. **Experimental**

(by using the ABI technique) and simulations (by considering both ABI and PBI methods) results show that the X-ray flux modulation does not produce appreciable effects in the quantitative PCI-CT reconstructions. The quality of the images is also preserved in terms of SNR values with both ABI and PBI methods. We believe that the use of the proposed method can be of particular interest for those applications where the deposited dose plays a crucial role and an accurate delineation of small features is important.

7.3 Concluding remarks

The work and results produced in this Thesis not only represent an important step towards a wider application of phase-contrast CT techniques in the biomedical field, but also open to new stimulating scientific questions. Further research and developments can use these results as a starting point. **New investigations and methods are required for reducing again both the radiation delivered to the tissues and the time required to perform a complete CT scan.** Improvements of aspects concerning both hardware (for examples: better efficiency of the detectors, wider X-ray beam, optimized optical elements) and algorithms (reconstruction using a reduced amount of projections and image post-processing) are possible and desirable. **Additional work is also required in order to further improve the accuracy of the quantitative results in index of refraction CT.** To this end, a more precise extraction of the refraction angles and a reduction of CT reconstruction artefacts are required.

The methods and results proposed in this work can be partially translated also to other PCI techniques. For example to the edge-illumination technique that has, as demonstrated, many similarities with the ABI.

One of the main limitations of the application of PCI in clinics is the time required for an exam, because all the PCI techniques only use part of the beam delivered by a conventional X-ray source. **A promising solution is presented by the compact X-ray source technologies.** The aim of these new sources is to deliver a quasi-monochromatic X-ray beam with flux densities that are intermediate between the one of Synchrotron Radiation facilities and the clinical X-ray generators. **The usage of these machines may boost the implementation towards clinics of PCI.** This is particularly true for those methods, as for instance the edge-illumination technique, which can be applied with divergent and polychromatic beams.

References

- Afanas'ev, A.M. & Kohn, V.G., 1971. Dynamical theory of X-ray diffraction in crystals with defects. *Acta Crystallographica Section A*, 27(5), pp.421–430.
- Agostinelli, S. et al., 2003. Geant4—a simulation toolkit. *Nuclear Instruments and Methods in Physics Research Section A: Accelerators, Spectrometers, Detectors and Associated Equipment*, 506(3), pp.250–303.
- Akio, Y. et al., 2008. Quantitative comparison of imaging performance of x-ray interferometric imaging and diffraction enhanced imaging. *Medical Physics*, 35(10), p.4724.
- Allison, J. et al., 2006. Geant4 developments and applications. *IEEE Transactions on Nuclear Science*, 53(1), pp.270–278.
- Ando, M. et al., 2001. A New Optics for Dark-Field Imaging in X-Ray Region 'Owl'. *Japanese Journal of Applied Physics*, 40(Part 2, No. 8A), pp.L844–L846.
- Ando, M. et al., 2008. Refraction-based 2D, 2.5D and 3D medical imaging: stepping forward to a clinical trial. *European journal of radiology*, 68(3 Suppl), pp.S32–6.
- Arfelli, F. et al., 1999. Improvements in the field of radiological imaging at the SYRMEP beamline.
- Arfelli, F. et al., 1998. Low-dose phase contrast x-ray medical imaging. *Physics in Medicine and Biology*, 43(10), pp.2845–2852.
- Arfelli, F. et al., 2000. Mammography with synchrotron radiation: phase-detection techniques. *Radiology*, 215(1), pp.286–93.
- Arhatari, B.D. et al., 2004. Phase contrast radiography: Image modeling and optimization. *Review of Scientific Instruments*, 75(12), p.5271.
- Attix, F.H., 2004. Introduction to radiological physics and radiation dosimetry.
- Authier, A., 2001. *Dynamical Theory of X-ray Diffraction*,
- Azároff, L. V., 1968. *Elements of X-ray crystallography*,
- Battistoni, G. et al., 2007. The FLUKA code: description and benchmarking. In *AIP Conference Proceedings*. AIP, pp. 31–49.
- Baym, G., 1974. *Lectures on Quantum Mechanics*,
- Bech, M. et al., 2010. Advanced contrast modalities for X-ray radiology: Phase-contrast and dark-field imaging using a grating interferometer. *Zeitschrift für medizinische Physik*, 20(1), pp.7–16.

- Op de Beeck, M., Dyck, D. V & Coene, W., 1996. Wave function reconstruction in HRTEM: the parabola method. *Ultramicroscopy*, 64, pp.167–183.
- Beltran, M.A. et al., 2010. 2D and 3D X-ray phase retrieval of multi-material objects using a single defocus distance. *Optics Express*, 18(7), p.6423.
- Berger, J. & Zucker, M., 2004. ESTAR, PSTAR, and ASTAR: Computer Programs for Calculating Stopping-Power and Range Tables for Electrons, Protons, and Helium Ions (version 1.2.2). Available: <http://physics.nist.gov/Star>. *National Institute of Standards and Technology*.
- Berger, M.J., 1963. Monte Carlo calculation of the penetration and diffusion of fast charged particles.
- Berger, M.J. & Hubbell, J.H., 1987. *XCOM: Photon cross sections on a personal computer*, Oak Ridge, TN.
- Berger, M.J. & Seltzer, S.M., 1972. Response functions for sodium iodide scintillation detectors. *Nuclear Instruments and Methods*, 104(2), pp.317–332.
- Bevins, N. et al., 2012. Multicontrast x-ray computed tomography imaging using Talbot-Lau interferometry without phase stepping. *Medical physics*, 39(1), pp.424–8.
- Boone, J.M. et al., 2001. Dedicated Breast CT: Radiation Dose and Image Quality Evaluation. *Radiology*, 221(3), pp.657–667.
- Boone, J.M., 1999. Glandular breast dose for monoenergetic and high-energy X-ray beams: Monte Carlo assessment. *Radiology*, 213(1), pp.23–37.
- Boone, J.M., 2002. Normalized glandular dose (DgN) coefficients for arbitrary X-ray spectra in mammography: computer-fit values of Monte Carlo derived data. *Medical physics*, 29(5), pp.869–75.
- Born, M. & Wolf, E., 1999. *Principles of optics: electromagnetic theory of propagation, interference and diffraction of light* 7th ed. C. U. Press, ed., Cambridge.
- Bravin, a et al., 2007. A numerical wave-optical approach for the simulation of analyzer-based x-ray imaging. *Optics express*, 15(9), pp.5641–5648.
- Bravin, A., 2003. Exploiting the X-ray refraction contrast with an analyser: the state of the art. *Journal of Physics D: Applied Physics*, 36, pp.A24–A29.
- Bravin, A., Coan, P. & Suortti, P., 2013. X-ray phase-contrast imaging: from pre-clinical applications towards clinics. *Physics in Medicine and Biology*, 58(1), pp.R1–R35.
- Brooks, T.F. & Humphreys, W.M., 2006. A deconvolution approach for the mapping of acoustic sources (DAMAS) determined from phased microphone arrays. *Journal of Sound and Vibration*, 294(4-5), pp.856–879.
- Bushuev, V.A., Beliaevskaya, E.A. & Ingal, V.N., 1997. Wave optical description of x-ray phase contrast images of weakly absorbing non crystalline objects. *Il Nuovo Cimento*, 19D, pp.513–520.

- Bushuev, V.A., Ingal, V.N. & Beliaevskaya, E.A., 1998. Wave theory of X-ray phase-contrast radiography. *Crystallography Reports*, 43(4), pp.538–547.
- Carlsson, G.A., 1971. A criticism of existing tabulations of mass energy transfer and mass energy absorption coefficients. *Health physics*, 20(6), pp.653–5.
- Carlsson., G.A., 1985. Theoretical Basis for Dosimetry. In *Theoretical Basis for Dosimetry, Chap. 1 in The Dosimetry of Ionizing Radiation, Vol. 1*, K.R. Kase, B.E. Båjrngard and F.H. Attix, eds. Academic Press, Orlando, pp. 1–75.
- Castelli, E. et al., 2007. Clinical mammography at the SYRMEP beam line. *Nuclear Instruments and Methods in Physics Research Section A: Accelerators, Spectrometers, Detectors and Associated Equipment*, 572(1), pp.237–240.
- Castelli, E. et al., 2011. Mammography with synchrotron radiation: first clinical experience with phase-detection technique. *Radiology*, 259(3), pp.684–94.
- Chan, H.-P. & Doi, K., 1983. The validity of Monte Carlo simulation in studies of scattered radiation in diagnostic radiology. *Physics in Medicine and Biology*, 28(2), pp.109–129.
- Chapman, D. et al., 1997. Diffraction enhanced x-ray imaging. *Physics in Medicine and Biology*, 42(11), pp.2015–2025.
- Chapman, D. et al., 1996. Mammography imaging studies using a Laue crystal analyzer. *Rev Sci Instrum*, 67(9), pp.1–5.
- Chibani, O. & Williamson, J.F., 2005. MCPI: a sub-minute Monte Carlo dose calculation engine for prostate implants. *Medical physics*, 32(12), pp.3688–98.
- Chou, C.Y. et al., 2007. An extended diffraction-enhanced imaging method for implementing multiple-image radiography. *Physics in Medicine and Biology*, 52(7), pp.1923–1945.
- Cloetens, P. et al., 2002. 3D imaging using coherent synchrotron radiation. *Image Anal. Stereol.*, 21((Suppl. 1)), pp.S75–S85.
- Cloetens, P., 1999. *Contribution to Phase Contrast Imaging, Reconstruction and Tomography with hard Synchrotron Radiation. Principles, Implementation and Applications*. Vrije Universiteit Brussel.
- Cloetens, P. et al., 1996. Phase objects in synchrotron radiation hard X-ray imaging. *Journal of Physics D: Applied Physics*, 29, pp.133–146.
- Coan, P., 2006. *Development and application of the analyzer-based imaging technique with hard synchrotron radiation*. Joseph Fourier.
- Coan, P. et al., 2006. Evaluation of imaging performance of a taper optics CCD; FReLoN' camera designed for medical imaging. *Journal of synchrotron radiation*, 13(Pt 3), pp.260–70.
- Coan, P. et al., 2005. Phase-contrast X-ray imaging combining free space propagation and Bragg diffraction. *Journal of synchrotron radiation*, 12(Pt 2), pp.241–5.

- Coan, P., Bravin, A. & Tromba, G., 2013. Phase-contrast x-ray imaging of the breast: recent developments towards clinics. *Journal of Physics D: Applied Physics*, 46(49), p.494007.
- Cromer, D.T., 1970. Relativistic Calculation of Anomalous Scattering Factors for X Rays. *The Journal of Chemical Physics*, 53(5), p.1891.
- Cullen, D.E., Hubbell, J.H. & Kissel, L., 1997. EPDL97: the Evaluated Photon Data Library, '97 Version.
- Dance, D.R. et al., 2000. Additional factors for the estimation of mean glandular breast dose using the UK mammography dosimetry protocol. *Physics in medicine and biology*, 45(11), pp.3225–40.
- Dance, D.R., 1990. Monte Carlo calculation of conversion factors for the estimation of mean glandular breast dose. *Physics in medicine and biology*, 35(9), pp.1211–9.
- David, C. et al., 2002. Differential x-ray phase contrast imaging using a shearing interferometer. *Applied Physics Letters*, 81(17), p.3287.
- Davis, T.J., 1996. X-ray diffraction imaging using perfect crystals. *Journal of X-ray Science and Technology*, 6, pp.317–342.
- Davis, T.J. et al., 1995. X-ray image contrast from a simple phase object. *Phys. Rev. Lett.*, 74(16), pp.3173–3176.
- Demarco, J.J., Wallace, R.E. & Boedeker, K., 2002. An analysis of MCNP cross-sections and tally methods for low-energy photon emitters. *Physics in medicine and biology*, 47(8), pp.1321–32.
- Dhawan, A.P., 2003. *Medical image analysis*,
- Diemoz, P.C., Bravin, A., Langer, M., et al., 2012. Analytical and experimental determination of signal-to-noise ratio and figure of merit in three phase-contrast imaging techniques. *Optics express*, 20(25), pp.27670–90.
- Diemoz, P.C., 2011. *Experimental and theoretical contributions to X-ray phase-contrast techniques for medical imaging*. Université de Grenoble.
- Diemoz, P.C. et al., 2013. Improved sensitivity at synchrotrons using edge illumination X-ray phase-contrast imaging. *Journal of Instrumentation*, 8(06), pp.C06002–C06002.
- Diemoz, P.C., Bravin, A. & Coan, P., 2012. Theoretical comparison of three X-ray phase-contrast imaging techniques: propagation-based imaging, analyzer-based imaging and grating interferometry. *Optics express*, 20(3), pp.2789–805.
- Durfee, S.M. et al., 2000. Sonographic Evaluation of Clinically Palpable Breast Cancers Invisible on Mammography. *The breast journal*, 6(4), pp.247–251.
- Elder, F. et al., 1947. Radiation from Electrons in a Synchrotron. *Physical Review*, 71(11), pp.829–830.

- Elleume, H. et al., 1999. Instrumentation of the ESRF medical imaging facility. *Nuclear Instruments and Methods in Physics Research Section A: Accelerators, Spectrometers, Detectors and Associated Equipment*, 428(2-3), pp.513–527.
- Endrizzi, M. et al., 2013. Edge illumination and coded-aperture X-ray phase-contrast imaging: increased sensitivity at synchrotrons and lab-based translations into medicine, biology and materials science. In R. M. Nishikawa & B. R. Whiting, eds. *SPIE Medical Imaging*. International Society for Optics and Photonics, pp. 866812–1.
- Faris, G.W. & Byer, R.L., 1988. Three-dimensional beam-deflection optical tomography of a supersonic jet. *Applied optics*, 27(24), pp.5202–12.
- Fedorenko, R.P., 1962. A relaxation method for solving elliptic difference equations. *USSR Computational Mathematics and Mathematical Physics*, 1(4), pp.1092–1096.
- Fernández, M. et al., 2005. Human breast cancer in vitro: matching histo-pathology with small-angle x-ray scattering and diffraction enhanced x-ray imaging. *Physics in medicine and biology*, 50(13), pp.2991–3006.
- Fernández, M. et al., 2008. USAXS and SAXS from cancer-bearing breast tissue samples. *European Journal of Radiology*, pp.89–94.
- Ferrari, A. et al., 2005. FLUKA: A multi-particle transport code (Program version 2005).
- Förster, E., Goetz, K. & Zaumseil, P., 1980. Double crystal diffractometry for the characterization of targets for laser fusion experiments. *Kristall und Technik*, 15(8), pp.937–945.
- Fragoso, M. et al., 2008. Experimental verification and clinical implementation of a commercial Monte Carlo electron beam dose calculation algorithm. *Medical physics*, 35(3), pp.1028–38.
- Freud, N. et al., 2008. A Hybrid Approach for Fast Simulation of Dose Deposition in Stereotactic Synchrotron Radiotherapy. *IEEE Transactions on Nuclear Science*, 55(3), pp.1008–1017.
- Gasilov, S. et al., 2013. On the possibility of quantitative refractive-index tomography of large biomedical samples with hard X-rays. *Biomedical optics express*, 4(9), pp.1512–8.
- Gasilov, S. et al., 2014. Tomographic reconstruction of the refractive index with hard X-rays: an efficient method based on the gradient vector-field approach. *Opt. Express*, 22(5), pp.5216–5227.
- Geant4, 2013. Geant4 physics reference manual. Available at: www.cern.ch/geant4.
- Gureyev, T.E. et al., 1999. Hard x-ray quantitative non-interferometric phase-contrast microscopy. *Journal of Physics D: Applied Physics*, 32(5), pp.563–567.
- Gureyev, T.E. et al., 2004. Optical phase retrieval by use of first Born- and Rytov-type approximations. *Applied optics*, 43(12), pp.2418–30.
- Gureyev, T.E. & Wilkins, S.W., 1997a. Regimes of X-ray phase-contrast imaging with perfect crystals. *II Nuovo Cimento D*, 19(2-4), pp.545–552.

- Gureyev, T.E. & Wilkins, S.W., 1997b. Regimes of X-ray phase-contrast imaging with perfect crystals. *Il Nuovo Cimento D*, 19(2-4), pp.545–552.
- Hammerstein, G.R. et al., 1979. Absorbed radiation dose in mammography. *Radiology*, 130(2), pp.485–91.
- Hasnah, M.O. et al., 2005. Mass density images from the diffraction enhanced imaging technique. *Medical physics*, 32(2), pp.549–52.
- Hayward, E. & Hubbell, J., 1954. The Albedo of Various Materials for 1-Mev Photons. *Physical Review*, 93(5), pp.955–956.
- Heitler, W., 1954. *The Quantum Theory of Radiation*,
- Henke, B.L., Gullikson, E.M. & Davis, J.C., 1993. X-Ray Interactions: Photoabsorption, Scattering, Transmission, and Reflection at $E = 50\text{--}30,000$ eV, $Z = 1\text{--}92$. *Atomic Data and Nuclear Data Tables*, 54(2), pp.181–342.
- Herman, G.T., 2009. *Fundamentals of Computerized Tomography: Image Reconstruction from Projections*,
- Hignette, O. et al., 2003. Hard X-ray microscopy with reflecting mirrors status and perspectives of the ESRF technology. *Journal de Physique IV (Proceedings)*, 104, pp.231–234.
- Hu, C. et al., 2008. Comparison of refraction information extraction methods in diffraction enhanced imaging. *Optics Express*, 16(21), p.16704.
- Hubbell, J.H., Gimm, H.A. & Overbo, I., 1980. Pair, Triplet, and Total Atomic Cross Sections (and Mass Attenuation Coefficients) for 1 MeV–100 GeV Photons in Elements $Z=1$ to 100. *Journal of Physical and Chemical Reference Data*, 9(4), p.1023.
- Hubbell, J.H. and Seltzer, S.M., 2004. Tables of X-ray mass attenuation coefficients and mass energy absorption coefficients (version 1.4). *National Institute of Standards and Technology, Gaithersburg, MD*.
- ICRU, 1984. *Report 37. Stopping Powers for Electrons and Positrons*,
- ICRU, 1989. *Report 44. Tissue Substitutes in Radiation Dosimetry and Measurement*,
- Ignatyev, K. et al., 2011. A New Generation of X-ray Baggage Scanners Based on a Different Physical Principle. *Materials*, 4(12), pp.1846–1860.
- ImageJ, ImageJ. Available at: <http://imagej.nih.gov/ij/>.
- Ingal, V.N. & Beliaeskaya, E.A., 1995. X-ray plane-wave topography observation of the phase contrast from a non-crystalline object. *Journal of physics. D, Applied physics*, 28(11), pp.2314–2317.
- Ivanchenko, V. et al., 2011. Recent Improvements in Geant4 Electromagnetic Physics Models and Interfaces. In *3th Monte Carlo Conference MC2010*. pp. 898–903.
- Jackson, J.D., 1975. *Classical Electrodynamics*. In Wiley, ed. New York.

- Jan, S. et al., 2011. GATE V6: a major enhancement of the GATE simulation platform enabling modelling of CT and radiotherapy. *Physics in medicine and biology*, 56(4), pp.881–901.
- Jan, S. et al., 2004. GATE: a simulation toolkit for PET and SPECT. *Physics in Medicine and Biology*, 49(19), pp.4543–4561.
- Jemal, A. et al., 2010. Global cancer statistics. *CA: a cancer journal for clinicians*, 61(2), pp.69–90.
- Jenkins, T.M., Nelson, W.R. & Rindi, A., 1988. *Monte Carlo transport of electrons and photons*,
- Kak, A.C. & Slaney, M., 1988. *Principles of Computerized Tomographic Imaging*, New York: IEEE Press.
- Keyriläinen, J. et al., 2008. Toward high-contrast breast CT at low radiation dose. *Radiology*, 249(1), pp.321–7.
- Keyriläinen, J., Fernández, M. & Suortti, P., 2002. Refraction contrast X-ray imaging. *Nucl Instr Meth A*, 488, pp.419–427.
- Kitchen, M.J. et al., 2007. Analyser-based phase contrast image reconstruction using geometrical optics. *Physics in Medicine and Biology*, 52(14), pp.4171–4187.
- Klein, R. et al., 1997. Determination of average glandular dose with modern mammography units for two large groups of patients. *Physics in medicine and biology*, 42(4), pp.651–71.
- Kulkarni, R.N. & Supe, S.J., 1984. Radiation dose to the breast during mammography: a comprehensive, realistic Monte Carlo calculation. *Physics in medicine and biology*, 29(10), pp.1257–64.
- L. D. Landau, E.M.L., 1974. *Theoretical physics. Volume 8. Electrodynamics of continuous media (2nd edition)*,
- Lagomarsino, S. et al., 1997. Phase contrast hard x-ray microscopy with submicron resolution. *Applied Physics Letters*, 71(18), p.2557.
- Lewis, R., 1997. Medical applications of synchrotron radiation x-rays. *Physics in Medicine and Biology*, 42(7), pp.1213–1243.
- Ljungberg, M. & Strand, S.-E., 1989. A Monte Carlo program for the simulation of scintillation camera characteristics. *Computer Methods and Programs in Biomedicine*, 29(4), pp.257–272.
- Maksimenko, A. et al., 2005. Computed tomographic reconstruction based on x-ray refraction contrast. *Applied Physics Letters*, 86(12), p.124105.
- Maksimenko, A., 2007. Nonlinear extension of the x-ray diffraction enhanced imaging. *Applied Physics Letters*, 90(15), p.154106.
- Marenzana, M. et al., 2012. Visualization of small lesions in rat cartilage by means of laboratory-based x-ray phase contrast imaging. *Physics in medicine and biology*, 57(24), pp.8173–84.

- McCollough, C.H., Bruesewitz, M.R. & Kofler, J.M., 2006. CT dose reduction and dose management tools: overview of available options. *Radiographics : a review publication of the Radiological Society of North America, Inc*, 26(2), pp.503–12.
- Miao, J., Förster, F. & Levi, O., 2005. Equally sloped tomography with oversampling reconstruction. *Physical Review B*, 72(5), p.052103.
- Mittone, A. et al., 2013. An efficient numerical tool for dose deposition prediction applied to synchrotron medical imaging and radiation therapy. *Journal of synchrotron radiation*, 20(Pt 5), pp.785–92.
- Mittone, A., Bravin, A. & Coan, P., 2014. Radiation dose in breast CT imaging with monochromatic x-rays: simulation study of the influence of energy, composition and thickness. *Physics in Medicine and Biology*, 59(9), pp.2199–2217.
- Momose, A. et al., 2009. High-speed X-ray phase imaging and X-ray phase tomography with Talbot interferometer and white synchrotron radiation. *Optics Express*, 17(15), p.12540.
- Momose, A. et al., 2006. Phase Tomography by X-ray Talbot Interferometry for Biological Imaging. *Japanese Journal of Applied Physics*, 45(6A), pp.5254–5262.
- Momose, A. et al., 1996. Phase-contrast X-ray computed tomography for observing biological soft tissues. *Nature Medicine*, 2(4), pp.473–475.
- Momose, A., 2003. Phase-sensitive imaging and phase tomography using X-ray interferometers. *Optics Express*, 11(19), p.2303.
- Munro, P.R.T. et al., 2013. A simplified approach to quantitative coded aperture X-ray phase imaging. *Optics express*, 21(9), pp.11187–201.
- Munro, P.R.T. et al., 2012. Phase and absorption retrieval using incoherent X-ray sources. *Proceedings of the National Academy of Sciences of the United States of America*, 109(35), pp.13922–7.
- Munro, P.R.T. et al., 2010. Source size and temporal coherence requirements of coded aperture type x-ray phase contrast imaging systems. *Optics express*, 18(19), pp.19681–92.
- Nesterets, Y.I. et al., 2006. On qualitative and quantitative analysis in analyser-based imaging. *Acta crystallographica. Section A, Foundations of crystallography*, 62(Pt 4), pp.296–308.
- Nesterets, Y.I. et al., 2004. Quantitative diffraction-enhanced X-ray imaging of weak objects. *Journal of Physics D: Applied Physics*, 37, pp.1262–1274.
- Nesterets, Y.I., Gureyev, T. & Wilkins, S., 2005. Polychromaticity in the combined propagation-based/analyser-based phase-contrast imaging. *Journal of Physics D: Applied Physics*, 38(24), pp.4259–4271.
- NIST, National institute of standards and technology. Available at: <http://www.nist.gov/>.
- Nock, R. & Nielsen, F., 2004. Statistical region merging. *IEEE transactions on pattern analysis and machine intelligence*, 26(11), pp.1452–8.

- Olivo, A. et al., 2001. An innovative digital imaging set-up allowing a low-dose approach to phase contrast applications in the medical field [In Process Citation]. *Med Phys*, 28(8), pp.169–1610.
- Olivo, A., Diemoz, P.C. & Bravin, A., 2012. Amplification of the phase contrast signal at very high x-ray energies. *Optics letters*, 37(5), pp.915–7.
- Olivo, A. & Speller, R., 2007. Modelling of a novel X-ray phase contrast imaging technique based on coded apertures. *Phys. Med. Biol.*, 52(22), pp.6555–6573.
- Oltulu, O. et al., 2003. Extraction of extinction, refraction and absorption properties in diffraction enhanced imaging. *J. Phys. D: Appl. Phys.*, 36, pp.2152–2156.
- Paganin, D. et al., 2004. Phase retrieval using coherent imaging systems with linear transfer functions. *Optics Communications*, 234, pp.87–105.
- Paganin, D. et al., 2002. Simultaneous phase and amplitude extraction from a single defocused image of a homogeneous object. *Journal of Microscopy*, 206(1), pp.33–40.
- Paganin, D.M., 2006. *Coherent X-ray optics* J. Chikawa, J. R. Helliwell, & S. W. Lovesey, eds., Oxford University Press.
- Pagot, E. et al., 2003. A method to extract quantitative information in analyzer-based x-ray phase contrast imaging. *Applied Physics Letters*, 82(20), p.3421.
- Parham, C. et al., 2009. Design and implementation of a compact low-dose diffraction enhanced medical imaging system. *Academic radiology*, 16(8), pp.911–7.
- Pavlov, K.M. et al., 2004. Linear systems with slowly varying transfer functions and their application to x-ray phase-contrast imaging. *J. Phys. D: Appl. Phys.*, 37, pp.2746–2750.
- Pelowitz, D.B., 2005. MCNPX user's manual, version 2.5.0. Technical Report LA-CP-05-0369. *Los Alamos National Laboratory*, p.473. Available at: <http://www.oecd-nea.org/tools/abstract/detail/ccc-0730> [Accessed February 20, 2014].
- Peterzol, A. et al., 2003. Image quality evaluation of the angiography imaging system at the European synchrotron radiation facility. *Nucl. Instr. Meth. A*, 510, pp.45–50.
- Pinsker, Z.G., 1978. Dynamical scattering of X-rays in crystals. In S. S. in S. S. Physics, ed. Berlin.
- Pisano, E.D. et al., 2000. Human breast cancer specimens: diffraction-enhanced imaging with histologic correlation--improved conspicuity of lesion detail compared with digital radiography. *Radiology*, 214(3), pp.895–901.
- Podurets, K.M., Somenkov, V.A. & Shilstein, Ss., 1989. Refraction-contrast radiography. *Sov Phys - Tech Phys*, 34(6), pp.654–657.
- Pogany, A., Gao, D. & Wilkins, S.W., 1997. Contrast and resolution in imaging with a microfocus x-ray source. *Rev. Sci. Instrum.*, 68(7).

- Ponchut, C. et al., 2011. MAXIPIX, a fast readout photon-counting X-ray area detector for synchrotron applications. *Journal of Instrumentation*, 6(01), pp.C01069–C01069.
- Press, W.H. et al., 1992. *Numerical recipes in C (2nd ed.): the art of scientific computing*, Cambridge University Press.
- Prezado, Y. et al., 2011. Dosimetry protocol for the forthcoming clinical trials in synchrotron stereotactic radiation therapy (SSRT). *Medical physics*, 38(3), pp.1709–17.
- Protopopov, V. V et al., 2002. X-ray imaging of microobjects using dark field refraction-contrast method with resonantly absorbing multilayer mirrors. In *SPIE Medical Imaging*. S. Diego: SPIE, pp. 277–285.
- Raven, C., Snigirev, A. & Snigireva, I., 1996. Phase-contrast microtomography with coherent high-energy synchrotron X rays. *Appl. Phys. Lett.*, 69(13), pp.1826–1828.
- Ribberfors, R., 1983. X-ray incoherent scattering total cross sections and energy-absorption cross sections by means of simple calculation routines. *Physical Review A*, 27(6), pp.3061–3070.
- Ries, L.A.G., Melbert, D. & Krapcho, M., 2004. *SEER Cancer statistics review, 1975-2004*, National Cancer Institute, Bethesda, MD.
- Rigon, L. et al., 2003. A new DEI algorithm capable of investigating sub-pixel structures. *J. Phys. D: Appl. Phys.*, 36, pp.A107–A112.
- Rigon, L. et al., 2002. Diffraction Enhanced Imaging Utilizing crystal reflections at Elettra and NSLS. In A. and Yaffe, ed. *SPIE Medical Imaging*. S. Diego: SPIE, pp. 255–266.
- Rigon, L., Arfelli, F. & Menk, R.H., 2007. Three-image diffraction enhanced imaging algorithm to extract absorption, refraction, and ultrasmall-angle scattering. *Applied Physics Letters*, 90, p.114102.
- Del Río, M.S., 2004. XOP 2.1 — A New Version of the X-ray Optics Software Toolkit. In *AIP Conference Proceedings*. AIP, pp. 784–787.
- Robert Dougherty, OptiNav, I., 2005. Extensions of DAMAS and Benefits and Limitations of Deconvolution in Beamforming (AIAA). *11th AIAA/CEAS Aeroacoustics Conference*.
- Rupcich, F. et al., 2012. A database for estimating organ dose for coronary angiography and brain perfusion CT scans for arbitrary spectra and angular tube current modulation. *Medical physics*, 39(9), pp.5336–46.
- Rupcich, F. et al., 2013. Reducing radiation dose to the female breast during CT coronary angiography: a simulation study comparing breast shielding, angular tube current modulation, reduced kV, and partial angle protocols using an unknown-location signal-detectability metric. *Medical physics*, 40(8), p.081921.
- Sakurai, J.J., 2006. *Advanced Quantum Mechanics*,

- Saloman, E.B., Hubbell, J.H. & Scofield, J.H., 1988. X-ray attenuation cross sections for energies 100 eV to 100 keV and elements $Z = 1$ to $Z = 92$. *Atomic Data and Nuclear Data Tables*, 38(1), pp.1–196.
- Salvat, F., Fernández-Varea, J. & Sempau, J., 2011. PENELOPE-2011: A code system for Monte Carlo simulation of electron and photon transport. *Workshop Proceedings*.
- Salvat, F. & Fernández-Varea, J.M., 2009. Overview of physical interaction models for photon and electron transport used in Monte Carlo codes. *Metrologia*, 46(2), pp.S112–S138.
- Salvat, F. & Fernández-Varea, J.M., 2006. PENELOPE-2008: A Code System for Monte Carlo Simulation of Electron and Photon Transport.
- Schulz-Wendtland, R. et al., 2009. Digital mammography: an update. *European journal of radiology*, 72(2), pp.258–65.
- Sechopoulos, I. et al., 2007. Computation of the glandular radiation dose in digital tomosynthesis of the breast. *Medical physics*, 34(1), pp.221–32.
- Smans, K. et al., 2010. Simulation of image detectors in radiology for determination of scatter-to-primary ratios using Monte Carlo radiation transport code MCNP/MCNPX. *Medical physics*, 37(5), pp.2082–91.
- Snigirev, A. et al., 1995. On the possibilities of x-ray phase contrast microimaging by coherent high-energy synchrotron radiation. *Review of Scientific Instruments*, 66(12), p.5486.
- Snigirev, A. et al., 1995. On the possibility of x-ray phase contrast microimaging by coherent high-energy synchrotron radiation. *Rev. Sci. Instrum.*, 66(12), pp.5486–5492.
- Snigirev, A. et al., 1996. On the requirements to the instrumentation for the new generation of the synchrotron radiation sources. Beryllium windows. *Nucl. Instr. Meth.*, A 370(2-3), pp.634–640.
- Somenkov, V.A., Tkalich, A.K. & Shilshtein, Ss., 1991. Refraction contrast in X-ray introscopy. *Sov. Phys. Tech. Phys.*, 36(11), pp.1309–1311.
- Stampanoni, M. et al., 2011. The first analysis and clinical evaluation of native breast tissue using differential phase-contrast mammography. *Investigative radiology*, 46(12), pp.801–6.
- Sztrókay, A. et al., 2012. High-resolution breast tomography at high energy: a feasibility study of phase contrast imaging on a whole breast. *Physics in medicine and biology*, 57(10), pp.2931–2942.
- Takeda, Y. et al., 2007. X-Ray Phase Imaging with Single Phase Grating. *Japanese Journal of Applied Physics*, 46(No. 3), pp.L89–L91.
- Talbot, H.F., 1836. Facts relating to optical science. No. IV. *Phil. Mag.*, 9, pp.401–407.
- Taylor, R.E.P., Yegin, G. & Rogers, D.W.O., 2007. Benchmarking brachydose: Voxel based EGSnrc Monte Carlo calculations of TG-43 dosimetry parameters. *Medical physics*, 34(2), pp.445–57.

- Thüring, T. et al., 2011. Non-linear regularized phase retrieval for unidirectional X-ray differential phase contrast radiography. *Optics express*, 19(25), pp.25545–58.
- Tsai, W.L. et al., 2002. Building on bubbles in metal electrodeposition. *Nature*, 417, p.139.
- Vachier, C. & Meyer, F., 2005. The Viscous Watershed Transform. *Journal of Mathematical Imaging and Vision*, 22(2-3), pp.251–267.
- Van Cittert, P., 1934. Die Wahrscheinliche Schwingungsverteilung in Einer von Einer Lichtquelle Direkt Oder Mittels Einer Linse Beleuchteten Ebene. *Physica*, 1(1-6), pp.201–210.
- Weitkamp, T. et al., 2005. X-ray phase imaging with a grating interferometer. *Optics Express*, 13(16), pp.6296–6304.
- Wernick, M.N. et al., 2006. Computation of mass-density images from X-ray refraction-angle images. *Phys Med. Biol.*, 51, pp.1769–1778.
- Wernick, M.N. et al., 2003. Multiple-image radiography. *Phys Med. Biol.*, 48(23), pp.3875–3895.
- Wilkins, S.W. et al., 1996. Phase-contrast imaging using polychromatic hard X-rays. *Nature*, 384, pp.335–338.
- Williamson, J.F., 1987. Monte Carlo evaluation of kerma at a point for photon transport problems. *Medical physics*, 14(4), pp.567–76.
- Williamson, J.F., Monte Carlo evaluation of kerma at a point for photon transport problems. *Medical physics*, 14(4), pp.567–76.
- Ye, S.-J., Ove, R. & Naqvi, S.A., 2006. Doppler broadening effect on low-energy photon dose calculations using MCNP5 and PENELOPE. *Health physics*, 91(4), pp.361–6.
- Zachariasen, W.H., 1945. Theory of X-ray diffraction in crystals. In J. W. & S. Inc., ed. New York.
- Zee, W. van der, Hogenbirk, A. & Marck, S.C. van der, 2005. ORANGE: a Monte Carlo dose engine for radiotherapy. *Physics in Medicine and Biology*, 50(4), pp.625–641.
- Zhao, Y. et al., 2012. High-resolution, low-dose phase contrast X-ray tomography for 3D diagnosis of human breast cancers. *Proceedings of the National Academy of Sciences of the United States of America*, 109(45), pp.18290–4.
- Zhifeng, H., Kejun, K. & Yigang, Y., 2007. Extraction methods of phase information for X-ray diffraction enhanced imaging. *Nuclear Instruments and Methods in Physics Research Section A: Accelerators, Spectrometers, Detectors and Associated Equipment*, 579(1), pp.218–222.
- Zhong, Z. et al., 2000. Implementation of diffraction-enhanced imaging experiments: at the NSLS and APS. *Nucl Instr and Meth A*, 450, pp.556–567.
- Zienkiewicz, O.C. & Morgan, K., 2006. *Finite elements and approximation*,

Appendix

A.1 Coefficients calculation code (Mu_Calc)

This code is composed of several classes and methods dedicated to read the EPDL97 database (Cullen et al. 1997) and to calculate several coefficients like the mass attenuation coefficient μ/ρ , the mass-energy absorption coefficient μ_{en}/ρ and the optical constant δ and β for single materials and for compounds. I wrote the code in the ANSI/ISO C++ language. A brief description of the methods used for calculating the different coefficients is presented in the next sections. This code has been written to produce the tables required for the dose computation with the GATE *TLEDoseActor*. No easily accessible databases of such coefficients (especially for X-ray energies > 30 keV), were available.

A.1.1 The Mass Attenuation Coefficient

The mass attenuation coefficient μ/ρ gives the measurement of the strength of the absorption or scattering of photons at a given wavelength, per unit mass, by an element or a substance. A narrow beam of monoenergetic photons with an incident intensity I_0 , penetrating a layer of material with thickness x and density ρ , emerges with intensity I given by the exponential attenuation law:

$$I = I_0 e^{-\mu/\rho x \rho} \quad (\text{A.1})$$

The μ/ρ , the photon interaction cross sections and related quantities are functions of the photon energy. The total cross section can be written as the sum over contributions from the principal photon interactions:

$$\sigma_{tot} = \sigma_{pe} + \sigma_{coh} + \sigma_{incoh} + \sigma_{pair} + \sigma_{trip} + \sigma_{ph,n} \quad (\text{A.2})$$

where σ_{pe} is the atomic photoelectric cross section, σ_{coh} and σ_{incoh} are the coherent (Rayleigh) and the incoherent (Compton) scattering cross sections, respectively, σ_{pair} and σ_{trip} are the cross sections for electron-positron production in the fields of the nucleus and of the atomic electrons, respectively, and $\sigma_{ph,n}$ is the photonuclear cross section. The mass attenuation absorption coefficient can be then calculated using:

$$\frac{\mu}{\rho} = \frac{\sigma_{tot}}{uA} \quad (\text{A.3})$$

Where u is the atomic mass unit (1/12 of the mass of an atom of the nuclide ^{12}C) and A is the relative atomic mass of the target element. In case of mixtures and compounds the coefficient can be calculated using:

$$\left(\frac{\mu}{\rho}\right)_{mix} = \sum_i w_i \left(\frac{\mu}{\rho}\right)_i \quad (\text{A.4})$$

Where w_i is the fraction by weight of the i^{th} atomic constituent, and the $(\mu/\rho)_i$ is the value of the mass absorption coefficient for the i -element composing the mixture.

A.1.2 The Mass Energy-Absorption Coefficient

The mass energy-transfer coefficient, μ_{tr}/ρ , when multiplied by the photon energy fluence, gives the dosimetric quantity kerma (Carlsson 1985). Thus μ_{tr}/ρ takes into account the escaped energy of the secondary photon radiations produced at the initial photon-atom interaction site, plus, by convention, the quanta of radiation from the annihilation of positrons (assumed to have come to rest) originating in the initial pair- and triplet-production interactions. Hence μ_{tr}/ρ is defined as:

$$\frac{\mu_{tr}}{\rho} = (f_{pe}\sigma_{pe} + f_{incoh}\sigma_{incoh} + f_{pair}\sigma_{pair} + f_{trip}\sigma_{trip})/uA \quad (\text{A.5})$$

In this formula (eq. A.5), coherent scattering has been omitted because of the negligible energy transfer associated with it. The factors f represents the average fractions of the photon energy E that is transferred to kinetic energy of charged particles in the remaining types of interactions, and uA represents the atomic mass of the element. These energy-transfer fractions are given by:

$$f_{pe} = 1 - X/E \quad (\text{A.6})$$

where X is the average energy of the fluorescence radiation (characteristic X-rays) emitted per absorbed photon;

$$f_{incoh} = 1 - (\langle E' \rangle + X)/E \quad (\text{A.7})$$

where $\langle E' \rangle$ is the average energy of the Compton-scattered photon;

$$f_{pair} = 1 - 2mc^2/E \quad (\text{A.8})$$

where mc^2 is the rest energy of the electron, and

$$f_{trip} = 1 - (2mc^2 + X)/E \quad (\text{A.9})$$

The fluorescence energy X in eq. A.6, eq. A.7, and eq. A.9 depends on the distribution of atomic-electron vacancies produced in the process under consideration and is in general evaluated differently for photoelectric absorption, incoherent scattering, and triplet production. Moreover, X is assumed to include the emission of "cascade" fluorescence X-rays associated with the complete atomic relaxation process initiated by the primary vacancy (Carlsson 1971).

As only the characteristics of the target atom are involved in calculating μ_{tr}/ρ , the mass energy-transfer coefficient for homogeneous mixtures and compounds can be obtained in a manner analogous (eq. A.4) to that for μ/ρ :

$$\frac{\mu_{tr}}{\rho} = \sum_i w_i \left(\frac{\mu_{tr}}{\rho} \right)_i \quad (\text{A.10})$$

The mass energy-absorption coefficient involves the further emission of radiation produced by the charged particles traveling through the medium, and is defined as:

$$\frac{\mu_{en}}{\rho} = (1 - g) \frac{\mu_{tr}}{\rho} \quad (\text{A.11})$$

The factor g in eq. A.11 represents the average fraction of the kinetic energy of secondary charged particles (produced in all types of interactions) that is subsequently lost in photon-emitting (Bremsstrahlung, atomic de-excitation following ionization due to electron impacts processes).

The distance covered by electrons in the matter is always much smaller than the voxel size and thus can be neglected. For example, at 80 keV the electron range in water is 98 μm (calculated using the continuous slowing-down approximation). As electrons follow wiggly trajectories due to multiple scattering, the projected range (average penetration depth measured along the initial direction of the particle) is generally much smaller than the above calculated range.

The Bremsstrahlung emission of photons during the slowing-down of electrons can be neglected as well, because collisional energy losses are by far the dominating process.

Taking into account all these considerations, for low- Z material and low energy, we can consider $g \approx 0$. Using this approximation, the formulas used in the software for the calculation are the following eq. A.12-A.13:

$$\frac{\mu_{en}}{\rho} = (f_{pe}\sigma_{pe} + f_{incoh}\sigma_{incoh})/uA \quad (\text{A.12})$$

$$\frac{\mu}{\rho} = (\sigma_{pe} + \sigma_{coh} + \sigma_{incoh})/uA \quad (\text{A.13})$$

The results are validated versus the reference values (please refer to figures 4.2 and 4.3 of Chapter 4).

A.1.3 Calculations of the optical constants

For the calculation of the optical constants used in the presented work the following formulations have been used:

$$\delta = \frac{r_e \lambda^2 Z \rho N_A}{2\pi A} \quad (\text{A.14})$$

where r_e is the electron radius, λ the wavelength, Z the atomic number, A the mass number and N_A is the Avogadro's number. The absorption term can be related to the absorption coefficient (Snigirev et al. 1996):

$$\beta = \frac{\mu \lambda}{4\pi} \quad (\text{A.15})$$

In case of compounds a simple sum rule is employed:

$$\left(\frac{\delta}{\beta}\right)_{mix} = \sum_i w_i \frac{\delta_i}{\beta_i} \frac{\rho_{mix}}{\rho_i} \quad (\text{A.16})$$

Where w_i is the mass/mass fraction of the i -element composing the compound. The results have been validated with the values obtained by Henke (Henke et al. 1993), as shown figures A1, A2. The comparison is done only for a restricted range of energies (<30 keV), because the values provided in the Henke table are only for this energy range [0-30 keV].

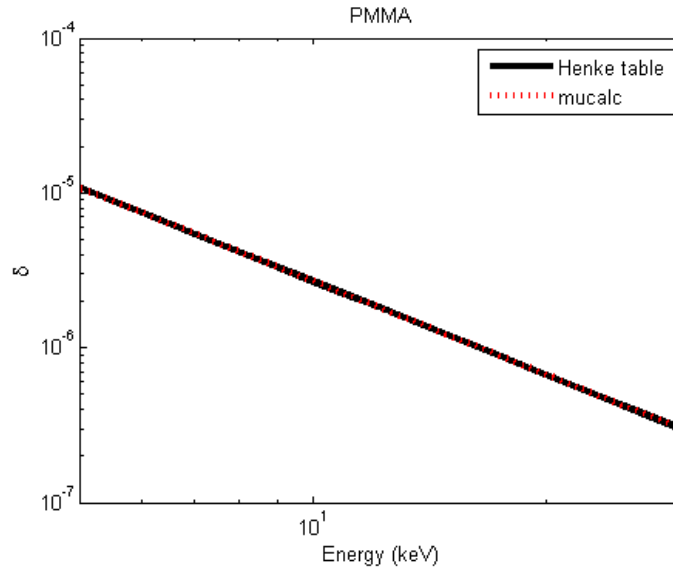


Figure A.1: comparison between the values of δ for PMMA calculated with the *Mu_calc* software and the values provided by Henke et al. 1993.

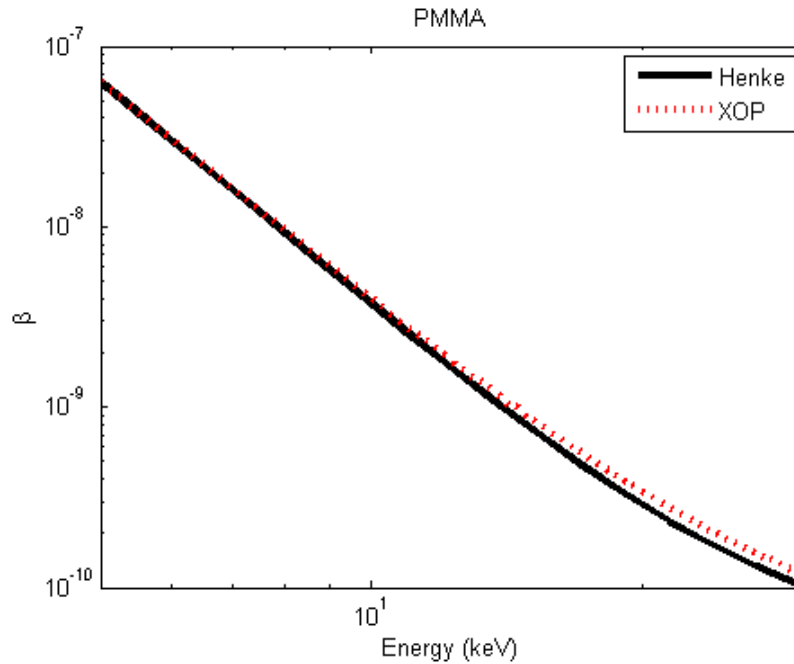


Figure A.2: comparison between the values of β for PMMA calculated with the *Mu_calc* software and the values provided by Henke et al. 1993. The results coincide with the one calculated using X-POWER of XOP, for this reason only the XOP results are reported in the comparison (del Río 2004).

A.2 Dose database for breast CT

The reference database obtained in the study presented in Chapter 6 is here reported:

Energy (keV)	μ_{en}/ρ 0% Glandular (cm ² /g)	μ_{en}/ρ 30% Glandular (cm ² /g)	μ_{en}/ρ 50% Glandular (cm ² /g)	μ_{en}/ρ 70% Glandular (cm ² /g)	μ_{en}/ρ 100% Glandular (cm ² /g)
15	7.65E-01	9.05E-01	1.00E+00	1.10E+00	1.24E+00
20	3.06E-01	3.63E-01	4.02E-01	4.41E-01	4.98E-01
25	1.53E-01	1.81E-01	2.00E-01	2.19E-01	2.47E-01
30	8.98E-02	1.05E-01	1.16E-01	1.26E-01	1.42E-01
35	5.95E-02	6.88E-02	7.53E-02	8.17E-02	9.11E-02
40	4.36E-02	4.96E-02	5.39E-02	5.80E-02	6.41E-02

45	3.50E-02	3.90E-02	4.19E-02	4.47E-02	4.88E-02
50	2.98E-02	3.27E-02	3.47E-02	3.67E-02	3.96E-02
55	2.69E-02	2.90E-02	3.05E-02	3.19E-02	3.40E-02
60	2.51E-02	2.67E-02	2.78E-02	2.89E-02	3.04E-02
65	2.41E-02	2.53E-02	2.61E-02	2.70E-02	2.82E-02
70	2.37E-02	2.46E-02	2.52E-02	2.59E-02	2.68E-02
75	2.34E-02	2.41E-02	2.46E-02	2.51E-02	2.59E-02
80	2.33E-02	2.39E-02	2.43E-02	2.47E-02	2.53E-02
85	2.35E-02	2.40E-02	2.43E-02	2.46E-02	2.51E-02
90	2.38E-02	2.41E-02	2.44E-02	2.46E-02	2.50E-02
95	2.40E-02	2.43E-02	2.45E-02	2.47E-02	2.50E-02
100	2.42E-02	2.44E-02	2.46E-02	2.48E-02	2.50E-02

Table A1: mass-energy absorption coefficient for breast tissue calculated following the composition presented in Chapter 6. The values are calculated using the EPDL97 database (Cullen et al. 1997).

Energy (keV)	Dose (Gy/photon)		
	0% Glandular	50% Glandular	100% Glandular
15	9.93E-15	8.76E-15	7.00E-15
17	1.17E-14	1.11E-14	9.55E-15
19	1.25E-14	1.26E-14	1.15E-14
21	1.26E-14	1.33E-14	1.27E-14
23	1.21E-14	1.34E-14	1.33E-14
25	1.15E-14	1.30E-14	1.34E-14
27	1.08E-14	1.25E-14	1.32E-14
29	1.01E-14	1.18E-14	1.27E-14
31	9.41E-15	1.12E-14	1.22E-14

33	8.81E-15	1.05E-14	1.16E-14
35	8.29E-15	9.91E-15	1.10E-14
37	7.88E-15	9.40E-15	1.05E-14
39	7.50E-15	8.93E-15	1.00E-14
41	7.20E-15	8.53E-15	9.57E-15
43	6.96E-15	8.21E-15	9.20E-15
45	6.79E-15	7.95E-15	8.88E-15
47	6.66E-15	7.73E-15	8.62E-15
49	6.56E-15	7.55E-15	8.34E-15
51	6.52E-15	7.44E-15	8.21E-15
53	6.52E-15	7.38E-15	8.10E-15
55	6.53E-15	7.32E-15	7.99E-15
57	6.57E-15	7.29E-15	7.92E-15
59	6.63E-15	7.31E-15	7.88E-15
61	6.71E-15	7.35E-15	7.88E-15
63	6.80E-15	7.38E-15	7.89E-15
65	6.94E-15	7.48E-15	7.94E-15
70	7.32E-15	7.76E-15	8.14E-15
75	7.75E-15	8.12E-15	8.45E-15
80	8.24E-15	8.55E-15	8.80E-15
85	8.81E-15	9.05E-15	9.27E-15
90	9.42E-15	9.61E-15	9.77E-15
95	1.00E-14	1.02E-14	1.03E-14
100	1.07E-14	1.08E-14	1.08E-14

Table A2: Average dose database for a breast of 6 cm of diameter for different breast compositions. The dose values refer to a single photon.

Energy (keV)	Dose (Gy/photon) 0% Glandular	Dose (Gy/photon) 50% Glandular	Dose (Gy/photon) 100% Glandular
15	4.28E-15	3.70E-15	2.92E-15
17	5.20E-15	4.81E-15	4.06E-15
19	5.77E-15	5.63E-15	4.98E-15
21	6.07E-15	6.17E-15	5.68E-15
23	6.08E-15	6.43E-15	6.14E-15
25	5.95E-15	6.48E-15	6.37E-15
27	5.72E-15	6.39E-15	6.44E-15
29	5.46E-15	6.20E-15	6.41E-15
31	5.19E-15	5.96E-15	6.28E-15
33	4.94E-15	5.72E-15	6.11E-15
35	4.71E-15	5.49E-15	5.92E-15
37	4.51E-15	5.27E-15	5.72E-15
39	4.32E-15	5.06E-15	5.52E-15
41	4.19E-15	4.88E-15	5.33E-15
43	4.07E-15	4.73E-15	5.17E-15
45	3.98E-15	4.60E-15	5.05E-15
47	3.92E-15	4.50E-15	4.92E-15
49	3.88E-15	4.42E-15	4.83E-15
51	3.86E-15	4.36E-15	4.76E-15
53	3.87E-15	4.33E-15	4.69E-15
55	3.88E-15	4.31E-15	4.65E-15
57	3.90E-15	4.31E-15	4.63E-15
59	3.95E-15	4.32E-15	4.62E-15
61	4.00E-15	4.35E-15	4.62E-15
63	4.06E-15	4.38E-15	4.64E-15

65	4.14E-15	4.43E-15	4.68E-15
70	4.37E-15	4.62E-15	4.81E-15
75	4.63E-15	4.83E-15	4.99E-15
80	4.92E-15	5.08E-15	5.20E-15
85	5.27E-15	5.40E-15	5.49E-15
90	5.65E-15	5.73E-15	5.79E-15
95	6.01E-15	6.08E-15	6.11E-15
100	6.38E-15	6.44E-15	6.44E-15

Table A3: Average dose database for a breast of 9 cm of diameter for different breast compositions. The dose values refer to a single photon.

Energy (keV)	Dose (Gy/photon)		
	0% Glandular	50% Glandular	100% Glandular
15	2.35E-15	2.02E-15	1.59E-15
17	2.89E-15	2.65E-15	2.21E-15
19	3.27E-15	3.14E-15	2.74E-15
21	3.49E-15	3.48E-15	3.15E-15
23	3.57E-15	3.70E-15	3.45E-15
25	3.56E-15	3.79E-15	3.64E-15
27	3.49E-15	3.80E-15	3.75E-15
29	3.38E-15	3.75E-15	3.77E-15
31	3.25E-15	3.66E-15	3.75E-15
33	3.12E-15	3.55E-15	3.70E-15
35	3.00E-15	3.44E-15	3.63E-15
37	2.90E-15	3.34E-15	3.55E-15
39	2.80E-15	3.23E-15	3.45E-15
41	2.73E-15	3.13E-15	3.37E-15
43	2.66E-15	3.05E-15	3.29E-15
45	2.62E-15	2.99E-15	3.23E-15

47	2.59E-15	2.94E-15	3.17E-15
49	2.57E-15	2.89E-15	3.11E-15
51	2.56E-15	2.87E-15	3.08E-15
53	2.56E-15	2.86E-15	3.05E-15
55	2.58E-15	2.85E-15	3.04E-15
57	2.60E-15	2.85E-15	3.03E-15
59	2.63E-15	2.86E-15	3.03E-15
61	2.67E-15	2.89E-15	3.04E-15
63	2.71E-15	2.91E-15	3.05E-15
65	2.77E-15	2.95E-15	3.08E-15
70	2.92E-15	3.07E-15	3.18E-15
75	3.10E-15	3.23E-15	3.31E-15
80	3.30E-15	3.40E-15	3.46E-15
85	3.54E-15	3.61E-15	3.65E-15
90	3.78E-15	3.83E-15	3.85E-15
95	4.04E-15	4.06E-15	4.07E-15
100	4.29E-15	4.32E-15	4.30E-15

Table A4: Average dose database for a breast of 12 cm of diameter for different breast compositions. The dose values refer to a single photon.

Energy (keV)	Dose (Gy/photon)		
	0% Glandular	50% Glandular	100% Glandular
15	1.48E-15	1.27E-15	9.96E-16
17	1.84E-15	1.67E-15	1.39E-15
19	2.08E-15	1.98E-15	1.73E-15
21	2.25E-15	2.22E-15	2.00E-15
23	2.33E-15	2.37E-15	2.20E-15

25	2.34E-15	2.46E-15	2.34E-15
27	2.32E-15	2.49E-15	2.42E-15
29	2.27E-15	2.48E-15	2.46E-15
31	2.20E-15	2.45E-15	2.46E-15
33	2.13E-15	2.40E-15	2.45E-15
35	2.06E-15	2.33E-15	2.42E-15
37	2.01E-15	2.28E-15	2.39E-15
39	1.95E-15	2.22E-15	2.34E-15
41	1.91E-15	2.16E-15	2.29E-15
43	1.86E-15	2.12E-15	2.25E-15
45	1.84E-15	2.08E-15	2.22E-15
47	1.82E-15	2.05E-15	2.18E-15
49	1.81E-15	2.03E-15	2.15E-15
51	1.83E-15	2.02E-15	2.14E-15
53	1.82E-15	2.01E-15	2.13E-15
55	1.83E-15	2.01E-15	2.12E-15
57	1.85E-15	2.02E-15	2.12E-15
59	1.87E-15	2.03E-15	2.12E-15
61	1.90E-15	2.04E-15	2.14E-15
63	1.93E-15	2.06E-15	2.15E-15
65	1.97E-15	2.09E-15	2.17E-15
70	2.09E-15	2.19E-15	2.25E-15
75	2.22E-15	2.30E-15	2.34E-15
80	2.36E-15	2.42E-15	2.45E-15
85	2.53E-15	2.57E-15	2.59E-15
90	2.70E-15	2.74E-15	2.74E-15
95	2.89E-15	2.90E-15	2.89E-15

100	3.08E-15	3.08E-15	3.06E-15
-----	----------	----------	----------

Table A5: Average dose database for a breast of 15 cm of diameter for different breast compositions. The dose values refer to a single photon.

Energy (keV)	30% Glandular	50% Glandular	70% Glandular
15	1.37	1.24	1.13
30	1.35	1.23	1.12
45	1.25	1.16	1.09
60	1.14	1.10	1.06
75	1.07	1.05	1.03
90	1.03	1.02	1.01
100	1.02	1.02	1.01

Table A6: G_f values for tissues containing 30%, 50% and 70% of glandular tissue. The remaining fraction is constituted by adipose tissue.

Eidesstattliche Versicherung

Name, Vorname

Ich erkläre hiermit an Eides statt,
dass ich die vorliegende Dissertation mit dem Thema

selbständig verfasst, mich außer der angegebenen keiner weiteren Hilfsmittel bedient und alle Erkenntnisse, die aus dem Schrifttum ganz oder annähernd übernommen sind, als solche kenntlich gemacht und nach ihrer Herkunft unter Bezeichnung der Fundstelle einzeln nachgewiesen habe.

Ich erkläre des Weiteren, dass die hier vorgelegte Dissertation nicht in gleicher oder in ähnlicher Form bei einer anderen Stelle zur Erlangung eines akademischen Grades eingereicht wurde.

Ort, Datum

Unterschrift Doktorandin/Doktorand